REPUBLIC OF TURKEY

YILDIZ TECHNICAL UNIVERSITY

GRADUATE SCHOOL OF SCIENCE AND ENGINEERING

LANTHANIDE AND/OR QUANTUM DOT DOPED LUMINESCENT GLASSES/GLASS NANOCOMPOSITES AS WAVELENGTH CONVERTORS FOR ADVANCED OPTO ELECTRONIC APPLICATIONS

Orhan KIBRISLI

DOCTOR OF PHILOSOPHY THESIS

Department of Metallurgical and Materials Engineering

Extractive Metallurgy Program

Supervisor

Assoc. Prof. Dr. Ali Erçin ERSUNDU

May, 2022

REPUBLIC OF TURKEY

YILDIZ TECHNICAL UNIVERSITY

GRADUATE SCHOOL OF SCIENCE AND ENGINEERING

LANTHANIDE AND/OR QUANTUM DOT DOPED LUMINESCENT GLASSES/GLASS NANOCOMPOSITES AS WAVELENGTH CONVERTORS FOR ADVANCED OPTO ELECTRONIC APPLICATIONS

A thesis submitted by Orhan KIBRISLI in partial fulfillment of the requirements for the degree of DOCTOR OF PHILOSOPHY is approved by the committee on 26.05.2022 in Department of Metallurgical and Materials Engineering, Extractive Metallurgy Program.

Assoc. Prof. Dr. Ali Erçin ERSUNDU
Yıldız Technical University
Supervisor

Approved By the Examining Committee

Assoc. Prof. Dr. Ali Erçin ERSUNDU, Supervisor
Yıldız Technical University _____

Prof. Dr. Necmettin MARAŞLI, Member
İstanbul Aydın University _____

Prof. Dr. M. Lütfü ÖVEÇOĞLU, Member
İstanbul Technical University _____

Prof. Dr. Cengiz KAYA, Member
Yıldız Technical University _____

Asst. Prof. Dr. Fatih AKYOL, Member
Yıldız Technical University _____

I hereby declare that I have obtained the required legal permissions during data collection and exploitation procedures, that I have made the in-text citations and cited the references properly, that I haven't falsified and/or fabricated research data and results of the study and that I have abided by the principles of the scientific research and ethics during my Thesis Study under the title of Lanthanide and/or Quantum Dot Doped Luminescent Glasses/Glass Nanocomposites as Wavelength Convertors for Advanced Opto Electronic Applications supervised by my supervisor, Assoc. Prof. Dr. Ali Erçin ERSUNDU. In the case of a discovery of false statement, I am to acknowledge any legal consequence.

Orhan KIBRISLI

Signature

This study was supported by the Scientific and Technological Research Council of Turkey (TUBITAK) BIDEB 2211-C Ph.D. Scholarship for Underlying Research Fields, BIDEB 2214 Visiting Researcher Scholarship for Ph.D. Students, ARDEB projects 120N754 and 117M206, The Council of Higher Education (YOK) 100/2000 Ph.D. scholarship and YTU Scientific Research Projects (BAP) FDK-2020-3935 and FDK-2021-4543.

Our virtues and our failings are inseparable, like force and matter.
When they separate, man is no more.

Nikola Tesla

ACKNOWLEDGEMENTS

It is a privilege to express my deepest gratitude to my thesis director Assoc. Prof. Dr. Ali Erçin Ersundu for giving me the opportunity to be a part of his group even before the group was formed! His conscientious guidance, tremendous friendliness, continuous encouragements, trust in me and the valuable freedom he gave me helped me to complete my Ph.D. Without a doubt, there is a lot for me to learn from him as a scholar even after eight years.

I am also extremely indebted to Assoc. Prof. Dr. Miray Çelikbilek Ersundu who provided me valuable guidance and deep scientific insights. Her deep knowledge and gracious approach towards the subject have always helped me immensely to overcome the challenges faced during my Ph.D. Countless fruitful discussions lead to formation of innovative ideas even beyond this thesis.

I have been very fortunate to have a number of great friends with brilliant minds that have also been a source of support through the years at YTU Glass Research Group. There is much overlap between social and work circles and it has made work a true pleasure. During my Ph.D., I had the opportunity to observe Naji who is one of my best friends become a successful researcher even if he resisted a lot in the beginning. My experience would have been significantly poorer without you. Thanks to Erdinç's strong will and hardworking personality, solving problems or coming up with new ones was never really a problem. This work wouldn't have been as comprehensive as it is now without your contributions. I'll always remember your banana rule but I cannot promise to follow. Utku the incorrigible collector, keep up your outstanding performance as a fresh researcher. It is a pleasure to have a versatile friend like you who can keep up with my odd hobbies. Ulaş who is the most colorful guy in our group definitely deserves an apology from me about the spatula. Sorry mate, it wasn't the best day of my life. Beyza the crispy outside crunchy inside, sorry for all the inappropriate talk that you are subjected during our socials. I am glad that you let me sneak through your walls. I had a perfect work environment thanks to you guys. I will always miss the synergy and the fun we had and I know it is irreplaceable.

I would like to thank the Scientific and Technological Research Council of Turkey (TUBITAK) for their financial support under BIDEB 2211-C Ph.D. Scholarship for Underlying Research Fields, BIDEB 2214 Visiting Researcher Scholarship for Ph.D. Students, ARDEB projects 120N754 and 117M206, the Council of Higher Education (YOK) for 100/2000 Ph.D. scholarship and YTU Scientific Research Projects (BAP) for their financial support under FDK-2020-3935 and FDK-2021-4543.

I would like to express my appreciation to Yıldız Technical University and all of its staff. It has been my home for last twelve years and provided me a great research environment.

I would also like to extend my gratitude with a deep sense of reverence towards my family who has supported me since the beginning of my journey.

Any omission in this acknowledgement does not mean lack of gratitude.

Orhan KIBRISLI

TABLE OF CONTENTS

LIST OF SYMBOLS x

LIST OF ABBREVIATIONS xii

LIST OF FIGURES xiv

LIST OF TABLES xviii

ABSTRACT xx

ÖZET xxii

1 INTRODUCTION 1

1.1 Literature Review 1

1.2 Objective of the Thesis 3

1.3 Original Contribution 3

2 THEORETICAL INFORMATION 6

2.1 Basic Principles of Luminescence 6

2.2 Energy Transfer Mechanisms 9

2.2.1 Excited State Absorption 10

2.2.2 Energy Transfer Upconversion 10

2.2.3 Photon Avalanche 11

2.2.4 Cooperative Energy Transfer 11

2.2.5 Energy Migration-Mediated Up-Conversion 11

2.3 Photoluminescent Materials 12

2.3.1 Organics 12

2.3.2 Transition Metals 13

2.3.3 Lanthanide Ions 13

2.3.4 Quantum Dots 16

2.4 Photonic and Opto-Electronic Applications of Photoluminescent Glasses 18

3 Dy^{3+} DOPED TELLURITE GLASSES FOR SOLID-STATE LIGHTING: AN INVESTIGATION THROUGH PHYSICAL, THERMAL, STRUCTURAL AND OPTICAL SPECTROSCOPY STUDIES 20

3.1 Introduction 20

3.2 Experimental procedure 23

3.2.1 Glass Synthesis 23

3.2.2 XRD, Physical and Thermal Investigations 24

3.2.3 FTIR, Optical Absorption and Emission Spectra Investigations 25

3.2.4 Judd-Ofelt Analysis, Radiative Properties and Decay Profiles 27
3.3 Results and Discussion 30
3.3.1 Physical Properties 30
3.3.2 Thermal Properties 34
3.3.3 Structural Properties 36
3.3.4 Absorption Spectra and Bonding Parameters 37
3.3.5 Judd-Ofelt Analysis 39
3.3.6 Photoluminescence Spectra and Radiative Properties 41
3.3.7 Colorimetric Properties 45
3.3.8 Decay Profiles 48
3.4 Conclusions 49
4 ROBUST $CsPbBr_3$ AND CdSe / Dy^{3+}+CdSe QUANTUM DOT DOPED GLASS NANOCOMPOSITE HYBRID COUPLING AS COLOR CONVERTER FOR SOLID-STATE LIGHTING APPLICATIONS 51
4.1 Introduction 51
4.2 Experimental procedure 54
4.3 Results and discussion 57
4.3.1 Structural and thermal analysis 57
4.3.2 Optical properties and particle size determination 59
4.3.3 Photoluminescence properties 62
4.3.4 Thermal, chemical and photo stability 67
4.3.5 Blue LED excited white light generation 71
4.4 Conclusions 73
5 CdSe AND $CsPbBr_3$ QUANTUM DOTS CO-DOPED MONOLITHIC GLASSES AS TUNABLE WAVELENGTH CONVERTORS 74
5.1 Introduction 74
5.2 Experimental procedure 75
5.2.1 Glass synthesis 75
5.2.2 Characterization studies 77
5.3 Results and discussions 78
5.4 Conclusions 85
6 INSTANTANEOUS COLOR TUNING OF UP-CONVERSION EMISSION IN A NOVEL LANTHANIDE DOPED MONOLITHIC GLASS VIA EXCITATION MODULATION 86
6.1 Introduction 86
6.2 Experimental Section 88

6.2.1 Glass Synthesis 88
6.2.2 Measurements and Characterization Studies: 89
6.3 Results and Discussion 91
6.3.1 Judd-Ofelt Analysis and Radiative Properties 92
6.3.2 Modulation of Up-conversion Emission Spectrum 97
6.3.3 Time Resolved Photoluminescence Spectra 99
6.3.4 Quantum Yield 101
6.4 Conclusions 102
7 NONINVASIVE OPTICAL TEMPERATURE SENSING BEHAVIOR OF Ho^{3+} AND Ho^{3+}/Er^{3+} DOPED TELLURITE GLASSES THROUGH UP AND DOWN-CONVERTED EMISSIONS 104
7.1 Introduction 104
7.2 Experimental Section 107
7.2.1 Glass Synthesis 107
7.2.2 Measurements and Characterization Studies 107
7.3 Results and Discussion 110
7.3.1 Physical, Thermal and Structural Properties 110
7.3.2 Absorption Spectra, Judd-Ofelt Analysis and Radiative Properties 113
7.3.3 Room-temperature Photoluminescence Measurements 119
7.3.4 Optical Temperature Sensing 122
7.4 Conclusions 127
8 RESULTS AND DISCUSSIONS 129
REFERENCES 132
A SUPPORTING INFORMATION 154
PUBLICATIONS FROM THE THESIS 164

LIST OF SYMBOLS

S_A	Absolute sensitivity
ω	Angular frequency
J	Angular momentum
N_A	Avogadro number
E_g	Band gap
$E_{g,bulk}$	Bulk band gap
f_{cal}	Calculated oscillator strength
e	Charge of an electron
T_c	Crystallization onset temperature
T_p	Crystallization peak temperature
ρ	Density
ε	Dielectric constant
m_h	Effective mass of a hole
m_e	Effective mass of an electron
S_{ED}	Electric dipole linestrength
A_{ED}	Electric dipole radiative transition probability
I	Emission intensity
F	Field strength
T_g	Glass transition temperature
R_i	Interionic distance
N	Ionic concentration
Ω_λ	Judd-Ofelt parameters
τ	Lifetime
S_{MD}	Magnetic dipole linestrength
A_{MD}	Magnetic dipole radiative transition probability
f_{meas}	Measured oscillator strength
M	Metallization factor
α_m	Molar electronic polarizability
R_m	Molar reflection
V_M	Molar volume
r	Nanoparticle radius

β	Nephelauxetic ratio
σ	Optical bandwidth gain
Λ	Optical basicity
ε_{opt}	Optical dielectric constant
V_O	Oxygen molar volume
h	Planck constant
R_p	Polaron radius
p	Population inversion rate
η	Quantum efficiency
A_R	Radiative transition probability
R_L	Reflection loss
S_R	Relative sensitivity
m	Rest mass of an electron
δ_{rms}	Root mean square
c	Speed of light
S	Surface area
T	Temperature
λ	Wavelength

LIST OF ABBREVIATIONS

CCT	Correlated color temperature
CET	Cooperative energy transfer
CIE	International Commission on Illumination
COD	Crystallography Open Database
CRI	Color rendering Index
CW	Continuous wave
DR	Dissolution rate
DS	Downshifting
DSC	Differential scanning calorimetry
EMA	Effective mass approximation
EMU	Energy migration-mediated up-conversion
ESA	Excited state absorption
ETU	Energy transfer up-conversion
FIR	Fluorescence intensity ratio
FTIR	Fourier transform IR spectroscopy
FWHM	Full width half max
GNC	Glass nanocomposite
GRR	Green to red ratio
IC	Internal conversion
ISC	Intersystem crossing
JCPDS	Joint Committee on Powder Diffraction Standards
J-O	Judd-Ofelt
LED	Light emitting diode
LER	Luminescence efficacy
LO	Longitudinal optical
NIR	Near infrared
NTCL	Non-thermally coupled energy level
OD	Optical density

OPD	Oxygen packing density
PA	Photon avalanche
PLE	Photoluminescence excitation
PLQY	Photoluminescence quantum yield
QC	Quantum cutting
QD	Quantum dot
SHG	Second harmonic generation
TCL	Thermally coupled energy level
TPA	Two photon absorption
UC	Up-conversion
UCQY	Up-conversion quantum yield
UHD	Ultra high definition
UV	Ultraviolet
XRD	X-ray diffraction

LIST OF FIGURES

Figure 2.1 Schematic diagram of the luminescence process a) electron in lowest energy state b) excited state and c) light emission.....6

Figure 2.2 A sample Jablonski diagram 8

Figure 2.3 Schematic representation of UC corresponding to a) ESA, b) ETU, c) PA, d) CET and e)EMU 10

Figure 2.4 Effect of Coulomb, spin-orbit, crystal field and magnetic field perturbation 14

Figure 2.5 Diagram of energy levels with corresponding term symbols for Ln(III) 15

Figure 2.6 Schematic energy diagrams for the electronic structures of atoms, molecules/clusters, small and large QDs and bulk semiconductors.....17

Figure 2.7 Electron-hole pair generation and emission of photon by semiconductor. 18

Figure 3.1 XRD diffractograms of glass samples.....31

Figure 3.2 Macro photos of synthesized glass samples a) under daylight b) under blue light 32

Figure 3.3 DSC curves of glass samples 35

Figure 3.4 Fourier-transform IR spectra of glass samples (inset shows deconvoluted FTIR spectrum of TWLD3 glass sample) 37

Figure 3.5 Optical absorption spectra of glass samples in Vis-NIR region (inset shows Tauc plot of TWLD01 glass sample) 38

Figure 3.6 Photoluminescence excitation spectrum of TWLD1 glass sample recorded at 575 nm 39

Figure 3.7 Photoluminescence emission spectra of Dy^{3+} ion doped TWLD glasses pumped at 453 nm 42

Figure 3.8 Partial energy level diagram of Dy^{3+} ion 43

Figure 3.9 CIE chromaticity coordinates of Dy^{3+} ion doped TWLD glasses.....46

Figure 3.10 Decay rates for the transition from $^4F_{9/2}$ to $^6H_{15/2}$ in Dy^{3+} ion doped TWLD glasses 49

Figure 4.1 Macro photos of a) $CsPbBr_3$, b) CdSe, and c) Dy^{3+}+CdSe doped GNCs along with as-cast samples under daylight.....53

Figure 4.2 XRD patterns of a) P-575-8h and b) C-545-12h samples, c) Raman spectra of C-545-12h and DC-525-48h samples. 54

Figure 4.3 Optical absorption spectra of a) $CsPbBr_3$, b) CdSe, and c) Dy^{3+}+CdSe doped GNCs along with as-cast samples. 59

Figure 4.4 Room temperature PL spectra and PLQY values of a,d) $CsPbBr_3$, b,e) CdSe and c,e) Dy^{3+}+CdSe doped GNCs, respectively. 62

Figure 4.5 Macro photos of a) $CsPbBr_3$ b) CdSe and c) Dy^{3+}+CdSe doped GNCs along with as-cast samples under UV LED excitation. 63

Figure 4.6 (a, b, c) Stokes shift spectra and (d, e, f) two-dimensional excitation-emission mapping for P-575-8h, C-545-12h, and DC-525-48h samples, respectively.....65

Figure 4.7 (a, b, c) Time-dependent PL spectra and (d, e, f) PL intensities of first heating and last cooling cycles for P-575-8h, C-545-12h, and DC-525-48h samples, respectively. 67

Figure 4.8 a) Macro photos and b) PLQY values of selected P-575-8h (green), C-545-12h (red), and DC-525-48h (yellow) GNCs immersed in water up to 60 days. 69

Figure 4.9 PL spectra of a) P-575-8h and b) C-545-12h and c) DC-525-48h samples under 5 W/cm^2 442 nm irradiation up to 30 min. 70

Figure 4.10 Emission spectra of a) blue LED chip, b) P-575-8h, c) C-545-12h, and d) DC-525-48h samples. Schematic illustration of e) WLED1 f) WLED2 devices. EL (electroluminescence) + PL spectra of constructed g) WLED1 and h) WLED2 devices (insets show macro photos of setups). 72

Figure 4.11 CIE diagram showing color coordinates of LED chip, selected samples and constructed WLED devices.....73

Figure 5.1 DSC thermogram of CdSe and $CsPbBr_3$ QDs co-doped as-cast sample (coded as D-as cast).....76

Figure 5.2 Macro photos of prepared glasses a), c) under daylight and b), d) under UV light. 78

Figure 5.3 Absorbance spectra of QDs a) co-doped and b) singly-doped glass samples.....78

Figure 5.4. a) XRD and b) Raman spectra of selected glass samples 79

Figure 5.5 Tauc plots of a) C-530-10h and b) P-530-10h samples. Band gaps are calculated as 2.62 eV and 2.39 eV, respectively. 81

Figure 5.6 Emission spectra of singly QD doped a) C-530-10h and b) P-530-10h samples under 325 and 425 nm excitation. 81

Figure 5.7 Excitation wavelength dependent (325-425 nm) a), c), e), g), i), k) emission spectra and b), d), f), h), j), l) CIE color diagrams of QDs co-doped glass samples. Excitation wavelength intervals are set as 20 nm and 5 nm for emission spectra and CIE color diagram, respectively. 84

Figure 6.1 Absorption and emission spectra of a) Tm^{3+} and b) Ho^{3+} ions and calculated gain coefficients of c) Tm^{3+} and d) Ho^{3+} ions for red, green and blue emissions in G1 sample.....96

Figure 6.2 (a) Emission spectra of G1 sample under 973 nm laser irradiation showing varying G/R ratios upon different excitation characteristics. Pictures

show the colors of the emission upon related excitation. (b) Color coordinates of the obtained emissions with respect to excitation characteristics. Inner triangle-like shape shows the color gamut achievable in the current study and outer triangle defines the Rec. 2020 standard for 4K UHD TVs. 97

Figure 6.3 Partial Jablonski diagram of Ho^{3+}, Tm^{3+} and Yb^{3+} ions demonstrating radiative and non-radiative transitions along with energy transfer among different ions. Adapted with permission [210]. 2019, Elsevier. 97

Figure 6.4 Schematic illustration of excitation source, pulse modulator and galvanometer setup. A plus sign was constructed by scanning the glass sample with a 973 nm laser beam. Different colored lines were obtained by instantaneously modulating the pulse frequency. 99

Figure 6.5 Time resolved PL spectra of G1 sample upon two different excitation frequencies for three emission bands. Left hand side illustrates rising and right hand side illustrates decay profiles. 101

Figure 6.6 PL spectra recorded in the integrated sphere and calculated UCQY values under CW irradiation operating at 13 W cm^{-2} power density. 101

Figure 7.1 Macro photos of transparent samples under daylight. 111

Figure 7.2 a) XRD patterns and b) DSC curves of studied samples confirming their glassy nature 112

Figure 7.3. FTIR spectra of glass samples revealing broad peaks and shoulders originated from glass structure. 113

Figure 7.4 Absorbance spectra of glass samples exposing characteristic electronic transitions of Ho^{3+} and Er^{3+} ions along with absorption edge of the glass matrix. 114

Figure 7.5 a) Room temperature PL spectra of glass samples (inset shows emission colors of samples) b) Possible up- and down-conversion mechanisms in partial Jablonski diagram of Er^{3+} and Ho^{3+} ions. 119

Figure 7.6 a) Pump power dependent PL spectra of G-Ho/Er sample b) Log-Log plot of pump power versus UC emission intensities of G-Ho/Er sample under 973 nm laser irradiation. 120

Figure 7.7 Time-resolved PL spectra of prepared samples a) under 487 nm excitation for G-Ho and G-Ho/Er glass samples b) under 973 nm for G-Ho/Er glass sample. 121

Figure 7.8 Temperature dependent PL spectra of a) G-Ho and b) G-Ho/Er samples under 487 nm excitation and c) G-Ho/Er sample under 973 nm (0.70 W) excitation d) Temperature dependent variation of FIRs alternating between measured maximum and minimum temperatures (inset shows temperature dependent emission mapping of G-Ho/Er sample under 973 nm excitation after 5 heating-cooling cycles) 122

Figure 7.9 Experimentally measured and fitted FIR graphs corresponding to a) $I_{550/660}$ b) $I_{546/660}$ c) $I_{546/533}$ d) $I_{660/533}$ intensity ratios. 123

Figure 7.10 Calculated S_A and S_R values corresponding to a) $I_{550/660}$ b) $I_{546/660}$ c) $I_{546/533}$ d) $I_{660/533}$ intensity ratios. 127

LIST OF TABLES

Table 2.1 Classification of luminescence.....7

Table 2.2 Commonly observed emission transitions for the emissive Ln(III) ions 16

Table 3.1 Equations used to calculate physical properties of glasses.....25

Table 3.2 Physical parameters of Dy^{3+} ion doped TWLD glasses.....34

Table 3.3 Measured (f_{meas}, 10^{-6}) and calculated (f_{cal}, 10^{-6}) oscillator strengths and r.m.s deviation ($\delta_{rms,}$ 10^{-6}) of Dy^{3+} ions in TWLD glasses.....40

Table 3.4 Judd-Ofelt intensity parameters Ω_2, Ω_4, Ω_6 (10^{-20} cm^2), comparison of their magnitude and Ω_4/Ω_6 (spectroscopic quality factor) of Dy^{3+} ion doped TWLD glasses along with some previously reported glass systems.....41

Table 3.5 Radiative transition probability (A_R), stimulated emission cross-section (σ), optical bandwidth gain ($\sigma\times\Delta\lambda_{eff}$) and calculated ($\beta_{cal}$) and measured ($\beta_{meas}$) branching ratios of Dy^{3+} ion doped TWLD glasses along with some previously reported glass systems 44

Table 3.6 Colorimetric properties of TWLD glasses along with some other Dy^{3+} doped glasses.....47

Table 3.7 Calculated (τ_{cal}) and measured (τ_{meas}) lifetime, quantum efficiency (η) and non-radiative transition rate (W_{NR}) values of Dy^{3+} ion doped TWLD glasses along with some previously reported glass systems 48

Table 4.1 First excitonic absorption peak center wavelengths, band gap and particle radii values for prepared GNCs. 61

Table 4.2 Colorimetric properties of selected samples excited with LED chip, constructed WLED devices and LED chip itself.....69

Table 5.1 Sample codes and applied heat-treatment conditions. 77

Table 5.2 Raman peak assignments for selected D-530-5h sample 80

Table 5.3 FWHM, peak wavelength, color coordinates and PLQY values of prepared glass samples. Excitation wavelengths are indicated on related columns for each feature. 83

Table 6.1. Judd-Ofelt intensity parameters Ω_2, Ω_4, Ω_6, their trend and spectroscopic quality factor (Ω_4/Ω_6) of G1 sample along with the literature data 94

Table 6.2 Radiative properties of G1 sample calculated through Judd-Ofelt analysis for selected transitions 95

Table 7.1 Physical parameters of synthesized glass samples. 110

Table 7.2 Linestrengths of the transitions used in Judd-Ofelt analysis. 115

Table 7.3 Judd-Ofelt intensity parameters Ω_2, Ω_4, Ω_6 (10^{-20} cm^2), their trend and spectroscopic quality factor (Ω_4/Ω_6) of prepared glass samples along with the literature data.....117

Table 7.4 Radiative properties of the prepared glass samples for selected transitions.....118

Table 7.5 Absolute sensitivity, S_A, relative sensitivity, S_R, and temperature range of applied intensity ratios along with different Ho^{3+} and Er^{3+} doped materials. 125

ABSTRACT

Lanthanide and/or Quantum Dot Doped Luminescent Glasses/Glass Nanocomposites as Wavelength Convertors for Advanced Opto Electronic Applications

Orhan KIBRISLI

Department of Metallurgical and Materials Engineering

Doctor of Philosophy Thesis

Supervisor: Assoc. Prof. Dr. Ali Erçin ERSUNDU

In this thesis, different lanthanide ion and/or QD doped glasses/glass nanocomposites are developed and their optical and photoluminescence properties are specifically investigated for their integration in advanced opto electronic applications thanks to their wavelength converting properties. Structure-property relations are linked and thermal, chemical and photo stability features are determined under exaggerated conditions to test the suitability of such materials for practical applications. Proof-of-concept prototypes are constructed for solid-state lighting, 3D display and temperature sensing applications.

The thesis itself is composed of eight chapters including introduction, theoretical background, five core sections and results and discussions. The first study demonstrates an investigation on novel Dy^{3+} doped tellurite glasses for solid-state lighting applications. The second study presents two alternative white LED device constructions by coupling $CsPbBr_3$ doped silicate-based glass nanocomposite layer with CdSe and Dy^{3+}+CdSe doped layers on top of a blue LED chip to improve

emission properties of single Dy^{3+} doped glasses. Third study introduces a novel approach where CdSe and $CsPbBr_3$ QDs are formed together in a silicate glass matrix for the first time to eliminate the disadvantages of multi-layered LED design. In the fourth study, instantaneous tuning of emission color by the modulation of excitation frequency in monolithic tellurite glasses doped with $Ho^{3+}/Tm^{3+}/Yb^{3+}$ ions are demonstrated for 3D display applications. Finally, temperature dependent up- and down-converted photoluminescence emissions of Ho^{3+} and Ho^{3+}/Er^{3+} doped tellurite glasses are investigated in terms of fluorescence intensity ratio (FIR) method for their use in noninvasive optical temperature sensing applications.

This thesis reveals favorable properties and drawbacks of the new generation luminescent glass/glass nanocomposite-based wavelength convertors and also contributes to the integration of these novel materials into high-end applications. Development and evaluation of new generation glass-based opto-electronic materials will pave the way for performance enhancement of existing applications as well as discovery of the new ones.

Keywords: Lanthanide ion, quantum dot, WLED, temperature sensing, volumetric display

ÖZET

İleri Opto Elektronik Uygulamalar için Dalga Boyu Dönüştürücüler Olarak Lantanit ve/veya Kuantum Nokta Katkılı Luminesan Cam ve Cam Nanokompozitler

Orhan KIBRISLI

Metalürji ve Malzeme Mühendisliği Anabilim Dalı

Doktora Tezi

Danışman: Doç. Dr. Ali Erçin ERSUNDU

Bu tez çalışmasında, dalgaboyu dönüştürücü özelliğine sahip lantanit iyonu ve/veya kuantum nokta katkılı camlar/cam nanokompozitler geliştirilmiş ve optik ve fotolüminesans özellikleri ileri seviye opto elektronik uygulamalara entegrasyonu açısından incelenmiştir. Hem fotolüminesan malzemeler için hem de konak malzemeler için yapı-özellik ilişkileri kurulmuştur. Isıl, kimyasal ve foto dayanım özellikleri ekstrem koşullar altında incelenmiş ve katı-hal aydınlatma, üç boyutlu ekran ve temassız sıcaklık ölçüm uygulamaları için prototip cihazlar geliştirilmiştir.

Tez çalışması giriş, teorik bilgi, beş ana bölüm ve sonuçlar ve tartışmalar kısmı olmak üzere toplam sekiz bölümden oluşmaktadır. İlk çalışmada yeni nesil Dy^{3+} katkılı tellürit camlar geliştirilmiş ve katı-hal aydınlatma uygulamalarında kullanım potansiyelleri değerlendirilmiştir. İkinci çalışmada, Dy^{3+} katkılı tellürit camların ışıma özelliklerini geliştirmek adına, $CsPbBr_3$ ve $CdSe/Dy^{3+}+CdSe$ katkılı silika cam nanokompozitlerin katmanlar halinde mavi LED çipi üzerinde konumlandırılması ile beyaz ışık yayan iki farklı LED geliştirilmiştir. Üçüncü

çalışmada, yeni bir yaklaşım olarak, CdSe ve $CsPbBr_3$ QD'ler aynı cam konak malzeme içerisinde sentezlenerek katmanlı yapının dezavantajları ortadan kaldırılmaya çalışılmıştır. Dördüncü çalışmada, $Ho^{3+}/Tm^{3+}/Yb^{3+}$ lantanit iyonları katkılı tellürit camların ışıma rengi, uyarım kaynağının frekansının değiştirilmesi ile anlık ve geçici olarak ayarlanmış ve bu camların hacimsel ekran uygulamalarında kullanım potansiyelleri değerlendirilmiştir. Son olarak, Ho^{3+} ve Ho^{3+}/Er^{3+} katkılı tellürit camların floresans şiddet oranı yöntemi ile temassız sıcaklık ölçümü uygulamalarında kullanım potansiyelinin değerlendirildiği deneysel çalışmalara yer verilmiştir.

Sonuç olarak, bu tez çalışması yeni nesil lüminesan cam/cam nanokompozit esaslı dalga boyu dönüştürücülerin avantajlı ve geliştirilmesi gereken özelliklerini ortaya koyarken aynı zamanda pratik uygulamalara entegrasyonunu da ele almaktadır. Dolayısıyla, cam esaslı yeni nesil opto elektronik malzemelerin geliştirilmesi ve değerlendirilmesi, mevcut uygulamalarda kullanılan malzemelerinin performanslarının arttırılmasının yanı sıra özgün malzemeler kullanarak yeni uygulamaların geliştirilmesi için de gereken bilgi birikimine katkı sağlamaktadır.

Anahtar Kelimeler: Lantanit iyonu, kuantum nokta, beyaz LED, sıcaklık algılama, hacimsel ekran

1
INTRODUCTION

1.1 Literature Review

Through the history, we have come a long way in imitating rays of our beloved star Sun. Obviously, not as strong as it shines but we can artificially cover specific wavelengths of the electromagnetic spectrum for desired applications such as lighting (Vis), communication (radio), cooking (micro), sanitization (UV), measuring (IR) etc. Despite the importance of the whole electromagnetic spectrum, Vis region stands out since it is the only portion that our eyes can decode and we need to see what is around while Sun is shining up through the opposite hemisphere or when we are stuck indoors without windows. Technological developments have enabled humankind to achieve artificial light generation by using different techniques such as, fire, incandescent bulbs and luminescent materials but eventually development of more advanced techniques and materials became inevitable. Since our society depends on energy in almost every sense, scientists are always working on to develop more efficient approaches and topics — Vis light generation is not an exception. Environmental concerns are the most important motivation behind this tremendous research area. Moreover, recent scientific and technological advancements demand optical features that traditional light sources cannot meet. At this point, new generation light sources which are using vast number of luminescent materials have taken the center stage.

In late 1930s, fluorescent bulbs made a huge impact in lighting industry by replacing substantial number of incandescent bulbs after their commercialization. They are more energy efficient compared to incandescent bulbs but they have their own problems such as toxicity and excessive blue light. By all means, real revolution in lighting technology came to life by the introduction of LEDs into our daily life. LEDs almost wiped out all other lighting technologies due to their outstanding features such as vivid colors with flexible tuning, long lifetime, environmental friendliness, high energy efficiency and high brightness. This

revolution was not only limited to lighting applications but also invaded numerous high-end photonic and opto-electronic applications such as lasers, solar cells, displays and sensors.

A wide variety of materials and living organisms demonstrating luminescent behavior can be categorized according to their triggering mechanism such as electroluminescence, bioluminescence, triboluminescence and photoluminescence — the protagonist of this thesis. Among various photoluminescent materials which will be mentioned in detail in the upcoming chapters, lanthanide ions and QDs are the most promising/popular photoluminescent materials. Each of them possesses divergent properties compared to each other enabling favorable features for different photonic and opto-electronic applications. Abundant 4f-4f or 5d-4f emission transitions and shielding effect of outer 5s and 5p orbitals and their durability make lanthanide ions versatile photoluminescent materials. On the other hand, size dependent band gap and emission wavelength tunability are the showcase features of QDs. Achievable PLQY values for both materials are more than satisfying which set their potential significantly high in the game. Notwithstanding, their overall performance highly rely on the material in which they are encapsulated. Therefore, selection of the encapsulation material for the desired application is as important as the selection of the photoluminescent material itself. Studies on polymer encapsulation of colloidal QDs or lanthanide ion complexes are relatively matured but still cannot meet the desired mechanical, thermal, chemical and optical resistivity rates for numerous practical applications. Another approach is integration of glasses to provide outstanding resistance against aforementioned environmental conditions. Nevertheless, formation of lanthanide ions and QDs are challenging tasks if favorable properties such as PLQY and wavelength tunability should not be sacrificed in return of robust protection. Thus, searching of ideal encapsulation materials for specific applications is a hot topic in materials science and engineering community.

In this thesis, different tellurite and silicate glass matrices are meticulously tailored to exploit favorable properties of lanthanide ions and QDs by considering the target applications such as solid-state lighting, 3D display and non-invasive

temperature sensing. For each application, structure-property relations are investigated and proof-of-concept prototypes are constructed to develop ideal luminescent materials for aforementioned applications.

1.2 Objective of the Thesis

High-end photonic and opto-electronic applications such as solid-state lighting, 3D display and non-invasive temperature sensing require photoluminescent materials with unique emission properties and resistance features against environmental conditions. For this reason, in this thesis, different types of glass matrices are designed and synthesized to host lanthanide ions and QDs. Therefore, optical, photoluminescence, structural, thermal and resistance (chemical, thermal and photo) properties are investigated. Moreover, proof-of-concept prototypes are constructed for aforementioned applications. The objective of this thesis is utilization of novel lanthanide ion and QD doped glasses/glass nanocomposites in solid-state lighting, 3D display and non-invasive temperature sensing applications. According to the experimental results, lanthanide ion/QD doped glasses/glass nanocomposites are evaluated to possess high potentiality to be used in high-end photonic and opto-electronic applications.

1.3 Original Contribution

Since the thesis itself is composed of 5 different scientific journal papers, novelty of the thesis can be given for each paper separately. In the third chapter, Dy^{3+} lanthanide ion doped tellurite glasses in the TeO_2-WO_3-Li_2O (TWL) system were synthesized. Favorable properties of TWL system for solid-state lighting applications such as low absorption and scattering losses, good transmittance in Vis region, high crystallization resistance and high lanthanide ion solubility are well-known. There are a few studies on the spectroscopic and structural properties on lanthanide ion doped TWL glasses having different compositions. However, no such study exist on the investigation of TWL glasses for solid state lighting applications especially for white light generation. Therefore, in this study physical, thermal, structural and optical properties of Dy^{3+} doped tellurite glasses were investigated through differential scanning calorimetry (DSC), Fourier-transform IR spectroscopy (FTIR), Vis-NIR absorption, Judd-Ofelt (J-O), photoluminescence

and decay analyses. Consequently, the results obtained in this work were discussed and compared with other reported Dy^{3+} doped glasses with the aim of revealing spectroscopic properties of Dy^{3+} ions in TWL glass system to evaluate their suitability for solid-state lighting applications. In the fourth chapter, robust $CsPbBr_3$ and CdSe / Dy^{3+}+CdSe doped silicate glass nanocomposite (GNC) layers exhibiting green and broadband emission covering red end of the visible spectrum (red / yellow), respectively were synthesized, and coupled to be placed on top of a blue LED chip as a proof-of-concept demonstration of two alternative WLED devices. PLQY of the glass encapsulated CdSe QDs were enhanced significantly by the addition of Dy^{3+} ions for the first time. Moreover, exceptional colorimetric properties and long-term stability were obtained by the layering of two different types of glass encapsulated QDs. In the fifth chapter, CdSe and $CsPbBr_3$ QDs were formed together in a monolithic silicate glass for the first time and emission color was tuned by regulating intensity of PL bands of both QDs upon changing excitation wavelength. Leverageable PLQY values were obtained for CdSe and $CsPbBr_3$ QDs revealing the high potential of QDs co-doped monolithic glasses for tunable wavelength convertors. In the sixth chapter, a comprehensive investigation on the relation between excitation modulation and emission properties of a $Ho^{3+}/Tm^{3+}/Yb^{3+}$ triply doped monolithic tellurite glass was given to achieve the precise manipulation of PL spectra. Radiative properties of the proposed systems were investigated accordingly in terms of PL measurements, J-O analysis and PLQY of related transitions. Instantaneous color change was shown for the first time by varying the frequency of excitation source attached to a galvanometer. Demonstrated proof-of-concept prototype revealed the potential of synthesized glasses to be used in full-color laser-based volumetric displays or color tunable monolithic multiwavelength lasers. In the seventh chapter, a special tellurite glass composition doped with Ho^{3+} and Er^{3+} ions were designed for obtaining high spectroscopic quality factors to enable favorable emission properties. Four different emission band pairs were comprehensively investigated in the frame of non-invasive temperature sensing through fluorescence intensity ratio (FIR) technique. Highest absolute and relative sensitivity values were

calculated as 0.0172 K^{-1} and 2.48% K^{-1}, respectively which are competitive values for non-invasive temperature sensing in the 298 – 558 K range.

2
THEORETICAL INFORMATION

2.1 Basic Principles of Luminescence

The term “luminescence” is coined in 1884 by German physicist Eilhardt Wiedemann from Latin *lumen* (light) + *escence* (denoting a state) to discriminate light emission phenomena which are not solely originated by increment in temperature as opposed to incandescence [1]. Thus, incandescence is often referred as “hot light” whereas luminescence is “cold light”. Luminescent materials which emit light have been known to mankind since antiquity as a weak glow from insects, mushrooms, sea algae, rotting wood and aurora borealis. Some of the earliest information about these materials can be found in Aristotle’s books [2]. Luminescence can be described as light emission occurring from electronically excited states (see Figure 2.1) of any substance and genre of luminescence are classified according to the method of excitation (see Table 2.1).

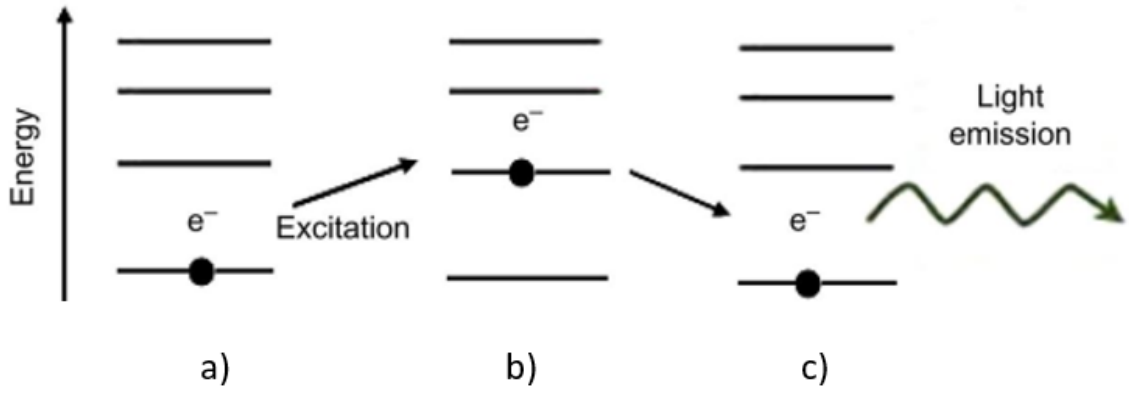


Figure 2.1 Schematic diagram of the luminescence process a) electron in lowest energy state b) excited state and c) light emission [3]

Photoluminescence, as a subcategory of luminescence, refers to light emission from a molecule or an atom by absorption of electromagnetic radiation [4]. Formally, it is divided into two categories as fluorescence and phosphorescence according to nature of excited states. Fluorescence occurs in excited singlet state which electron in the ground state is paired with an electron in excited state

spinning in reverse direction. Since return to ground state is spin allowed, fluorescence occurs expeditiously after the absorption of photon. Therefore, emission lifetimes generally take place in the range of nano to microseconds. On the contrary, phosphorescence arises between the triplet states in which the electron in the ground state has same spin orientation as the excited state electron. Emission rates are slow (10^3 to 10^0 s^{-1}) due to the forbidden transition and therefore, phosphorescence lifetimes are typically in the range of milliseconds to seconds [5].

Table 2.1 Classification of luminescence [3]

Phenomenon	Definition	Applications
Photoluminescence	It is the phenomenon in which emission of light takes place from any form of matter after absorption of photons.	Fluorescent lamps, display devices
Radioluminescence	It is the phenomenon in which light is created in the material after bombarding with ionizing radiation.	X-ray imaging, scintillation
Electroluminescence	It is the phenomenon in which, typically a semiconductor emit light in response to an electrical current or a strong electric field.	LEDs, laser diodes
Chemiluminescence	It is the phenomenon in which two chemicals react to form an excited intermediate, breaks down releasing some of its energy as photons of light to reach its ground state.	Chemical analysis
Thermoluminescence	It is the luminescence, displayed by certain crystalline materials, where the previously absorbed energy from electromagnetic radiation or other ionizing radiation is re-emitted as light when the material is triggered by temperatures above a certain threshold.	Dosimetry of ionizing radiation
Mechanoluminescence	It is a type of luminescence induced by any mechanical action in solids by elastic deformation, plastic deformation and fracture of solids.	Piezoelectric materials
Crystalloluminescence	It is defined as the emission of light during the crystallization of certain salts from liquid solution or from the fused phase.	-

Photoluminescence as a photophysical phenomenon can conveniently be described with Jablonski diagrams. A common Jablonski diagram of a photoluminescent system is given in Figure 2.2. As depicted in the Jablonski diagram, the electrons promoted to an excited state once the system absorbs

photons. Prior to radiative transition (photoluminescence), excited state electron often relaxes to the first vibrational level of S_1 state and dissipates heat. This transition is called internal conversion (IC) and also known as Kasha's rule [6]. After that, excited electron may fully relax to the ground state through another thermal dissipation occurrence or radiative transition which results in photon emission that is called fluorescence. On the other hand, the electron may change its spin angular momentum to jump a lower energy triplet state (intersystem crossing, ISC). This jump may be followed by another relaxation to S_0 state as IC which is also followed by a triplet radiative decay resulting in phosphorescence emission.

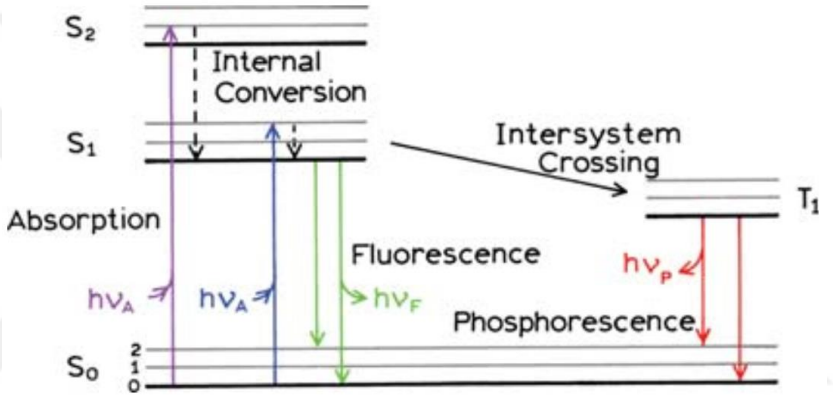


Figure 2.2 A sample Jablonski diagram [5]

Photoluminescence usually occurs when luminescent material is excited at shorter wavelengths or higher energies. This phenomenon was explained by Sir. G. G. Stokes for the first time in 1852 through a quinine solution. In that experiment, UV excitation was provided by sunlight harnessing blue glass as a selective filter for wavelengths below 400 nm. Incident light was blocked by a yellow glass of wine in order to keep it away from the detector which is a pair of eyes. Quinine fluorescence (450 nm) was detected easily thereafter. Fluorescent molecules in solution undergo energy losses between excitation and emission on a consistent basis. The rapid decay to the lowest vibrational stage of S_1 is a typical cause of the Stokes transition. Furthermore, fluorophores decay to higher S_0 vibrational levels, resulting in further excitation energy loss due to thermalization of the excess vibrational energy.

2.2 Energy Transfer Mechanisms

Downshifting (DS) luminescence of Ln^{3+} is a Stokes process where one photon with high energy is absorbed by the luminescent material and converted into a low energy photon. If the absorbed photon is converted into two or more photons with lower energies, then the quantum values larger than unity is obtained and this process is called quantum cutting QC [7, 8]. The concept of obtaining quantum yields larger than 100% was first proposed by Dexter in 1957 via cutting a single photon into two photons with lower energies. Later in 1974, Sommerdijk et al. [9] showed that a single UV photon of Pr^{3+} (∼210 nm) is converted into two visible photons in YF_4 and α-$NaYF_4$ hosts.

Up-conversion (UC) luminescence is a nonlinear process, known as anti-Stokes emission, in which the consecutive absorption of two or more low-energy photons results in the emission of high-energy photons. The UC concept was first devised by Bloembergen in 1959 but the lack of a coherent light source lingered the generation of upconverted visible emission until the advent of laser. After the breakthrough experiment realized by Auzel in 1966, anti-Stokes emission obtained through the conversion of near infrared (NIR) photons to visible (Vis) photons prompted the development of NIR upconverters for a vast number of applications. In a study described by Dexter before 1966, it was assumed that all energy transfers took place from excited state of first ion to the ground state of second ion [11]. However, by observing the UC in a Yb^{3+}-Er^{3+} doped system, Auzel initially suggested that energy transfer between ions can occur between two ions both being at excited state and not only absolute energy but also energy differences can be exchanged among ions [12, 13]. As shown in Figure 2.3, the UC process for lanthanide-based systems is generally divided into five categories: excited state absorption (ESA), energy transfer up-conversion (ETU), photon avalanche (PA), cooperative energy transfer (CET) and energy migration-mediated up-conversion (EMU) [10].

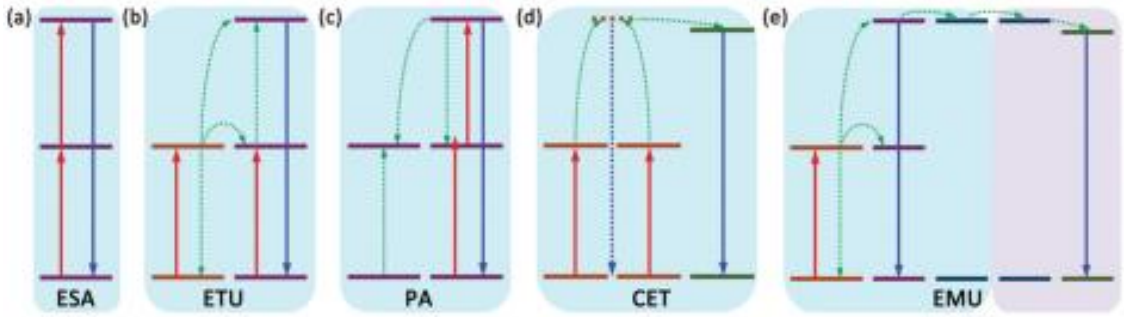


Figure 2.3 Schematic representation of UC corresponding to a) ESA, b) ETU, c) PA, d) CET and e)EMU [10]

2.2.1 Excited State Absorption

ESA is a single ion process where two excitation photons are sequentially absorbed by an ion having multiple stable intermediate energy levels. If the first absorbed photon lives long enough in the intermediate level, the absorption of the second photon promotes the ion to a higher excited energy level and eventually as a result of de-excitation an up-converted photon will be emitted (see Figure 2(a)). Due to the sequential absorption of two photons, this process is also called two-step absorption. High power density, dopants with large absorption cross-section and low doping concentration is needed to realize ESA. This is because non-radiative cross-relaxations occurring at high doping concentrations could diminish the emission intensity.

2.2.2 Energy Transfer Upconversion

APTE (French acronym for Addition de Photons par Transfert d'Energie) which was later named as ETU is the most common mechanism in Ln^{3+} doped systems. ETU is generally occurring in a system with a sensitizer (usually Yb^{3+} due to its large absorption cross section) and an activator (Ho^{3+}, Er^{3+}, Tm^{3+} etc.) and it is the most efficient mechanism among other five mechanisms given in Figure 2. In ETU, following the excitation, sensitizer ions non-radiatively transfer their energy to activator ions via dipole-dipole resonant interaction and causing the activator ions to get pumped to their excited states (see Figure 2(b)). It is worth to mention that the energy transfer from sensitizer not only populates the emitting levels of activators but also the intermediate levels [14]. The high absorbance of activator at the emission wavelength of the sensitizer could possibly lead ETU with higher

efficiencies like Yb^{3+} (sensitizer) and Er^{3+} (activator) couple excited at 980 nm. In case of diminutive energy mismatch between the absorption wavelength of activator and emission wavelength of sensitizer such as in the case of Yb^{3+}-Tm^{3+} or Yb^{3+}-Ho^{3+} couples, it could be compensated by the phonons of the host and this process is called phonon assisted energy transfer [15].

2.2.3 Photon Avalanche

In PA process, the energy between ground and intermediate states of the ion is not identical to the energy of excitation photon (see Figure 2(c)). Therefore, some electrons are promoted to an intermediate state and the ion experiences an ESA process and populates a higher excited state (super excited). Afterwards, the intermediate levels of the ion and a neighboring ion is occupied by a cross relaxation process. This process continues to happen as long as the depletion of super excited ions is less than the ground state ions [16].

2.2.4 Cooperative Energy Transfer

CET process is similar to an ETU process. However, in this process the activators are lack of real intermediate energy levels. Therefore, two sensitizers are pumped to a virtual excited state and afterwards the energy simultaneously transferred to the activator (see Figure 2(d)). This process is widely studied in glasses, polymers, bulk materials, and nanomaterials [17, 18].

2.2.5 Energy Migration-Mediated Up-Conversion

Wang et al. proposed energy migration-mediated up-conversion (EMU) method in 2011 as an attempt to further increase the efficiency of UC emissions where the appropriate intermediate levels of activators are missing. In this process four luminescent centers of sensitizer, accumulator, migrator, and activator are incorporated into separate layers. Firstly, the higher energy levels of accumulator are populated via ETU. Afterwards, energy from the excited state of the accumulator is transferred to the migrator and energy from migrators in the core is transferred to the ones lying in the shell. Eventually the energy is absorbed by the activator and the radiative emission is observed from the excited state of the accumulator and activator to their ground states (see Figure 2(e)) [19].

2.3 Photoluminescent Materials

Visible light covers a tiny fraction — about 0.0035 percent — of the electromagnetic spectrum and it is the only portion that human eye can decode. Therefore, technological developments have led to the emergence of a wide range of artificial visible light sources over time including fire, incandescent bulbs and the most lately luminescent materials. Fire and incandescent bulbs have served us well mainly to illuminate our surroundings but eventually development of more advanced materials and techniques have become inevitable due to the increasing demands of our society not only for lighting purposes but also for various high-tech applications. At this point, photoluminescent materials have taken the center stage due to their outstanding features to meet challenging requirements of scientific and technological developments.

Photoluminescent materials can be categorized as organic and inorganic in the first order. Plenty of organic substances are known for their photoluminescent behavior so it is not practical to cover all of them in this thesis which focuses on inorganic photoluminescent materials. Therefore, the most common organic compounds will be mentioned briefly in the next section and the focus will be mostly on inorganic photoluminescent materials especially lanthanide ions and QDs.

2.3.1 Organics

Organic fluorophores can be classified broadly into two categories as intrinsic and extrinsic. Natural fluorophores are known as intrinsic photoluminescent materials such as NADH, aromatic amino acids, derivatives of pyridoxyl, flavins and chlorophyll. However, the intrinsic photoluminescence is usually insufficient for desired applications because of its low intensity. On the contrary, specially designed extrinsic photoluminescent materials such as rhodamine, fluorescein and dansyl provide favorable emission features for wide variety of applications [5]. Even tough, organic substances are widely used in bio-applications due to their flexible bio compatibility features, their poor thermal, photo and chemical resistance values prevent their utilization into applications which take place in extreme environmental especially thermal conditions. At this point, lanthanide

and quantum dot based inorganic photoluminescent materials have taken the center stage due to their outstanding thermal, chemical and photo resistivity along with favorable emission properties.

2.3.2 Transition Metals

Transition metals have their *d* subshells partially filled or incomplete which can give rise to cations. PL in transition metal containing compounds is most likely occurs due to two types of electronic transitions: (1) Ligand to metal charge transfer in which an electron can jump from a ligand orbital to transition metal orbital. (2) *d-d* orbital transitions occurs as an electron jump between *d* orbitals. Low oxidation state of the metal ions promotes such transitions. Emissions with large FWHM can be obtained through aqueous solutions of transition metal ions. PL applications of transition metals (Nb, V, Zr, Mn and Cr) are mostly focused on their coupling with metal organic frameworks as chemical sensors [20].

2.3.3 Lanthanide Ions

Rare earth materials are categorized into two groups as actinides and lanthanides distinguished by the progressive filling of 5f (actinides) or 4f (lanthanides) shells of their electronic configurations, from thorium to lawrencium and from cerium to lutecium, respectively. Amongst actinides, uranium was extremely popular due to its charming green emission back in the past for wide variety of photoluminescence applications. However, radioactive behavior of actinides cut out their utilization into our daily life. On the contrary, outstanding emission features of lanthanide ions without radioactive features make them extremely favorable for diverse applications which requires photoluminescence such as solid-state lighting, 3D display, non-invasive optical temperature sensing, laser gain medium and optical fiber amplifiers [21].

Unique features of lanthanide electronic structure mainly relies on quantum theory of atomic spectroscopy and crystal-field interaction which can be used to treat all cumulative solid-state effects as a perturbation. Shielding effect of electrons in outer 5s and 5p shells over partially occupied 4f shell prevent interactions with the ligands. Therefore, lanthanide ions take little amount of participation in chemical bond formation. 4f orbitals of lanthanide ions are

significantly less extended compared to 5s and 5p orbitals ultimately resulting in electronic transitions which possess atomic-like characteristics and sharp emission lines [21]. The spectroscopic properties of lanthanide ions in an electronic structure such as $4f^{N-1}5d$ are strongly influenced when a 4f electron is excited to a 5d shell that extends beyond the 5s and 5p orbitals. Thus, electronic transitions between $4f^N$ and $4f^{N-1}5d$ states results in absorption or emission of photons and become significantly different from transitions within $4f^N$ configuration. A modified crystal-field theory is mandatory for modelling stronger lattice-ion interactions to analyze energy level splitting and excited state dynamics. The overall emission properties of a lanthanide ion may be explained by evaluating interactions in different forms given in Figure 2.4 [22].

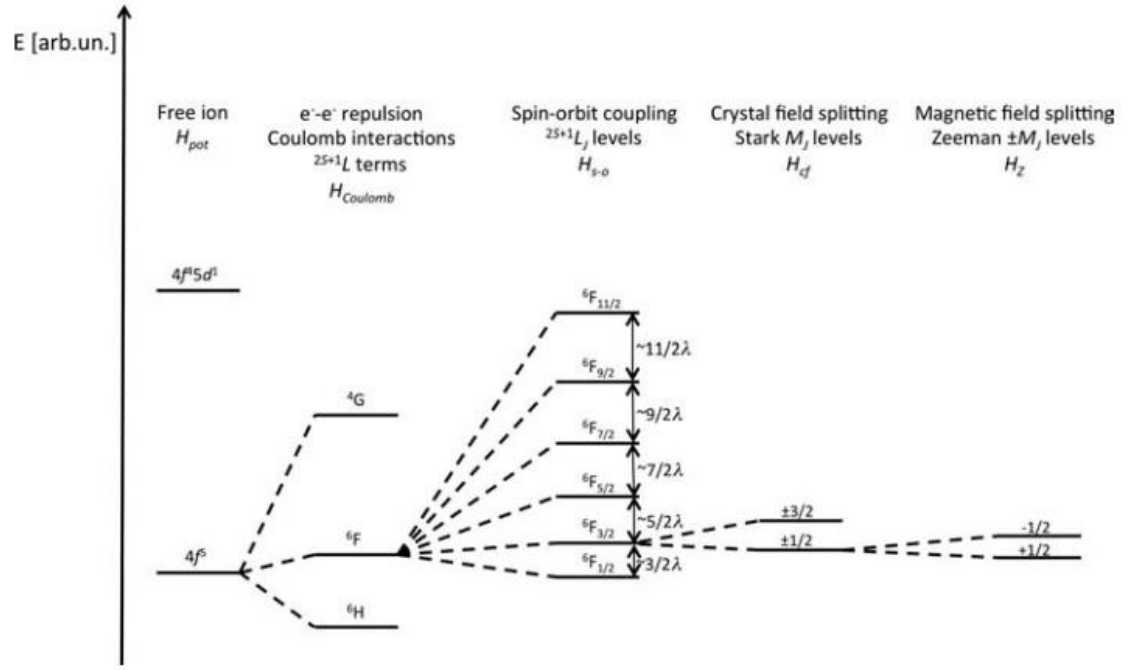


Figure 2.4 Effect of Coulomb, spin-orbit, crystal field and magnetic field perturbation [22]

A complete diagram, showing the ground and excited states of all lanthanide ions in the +III oxidation state with corresponding term symbols, is displayed in Figure 2.5. Table 2.2 summarizes the most commonly observed emission transitions for the emissive Ln(III) ions [22].

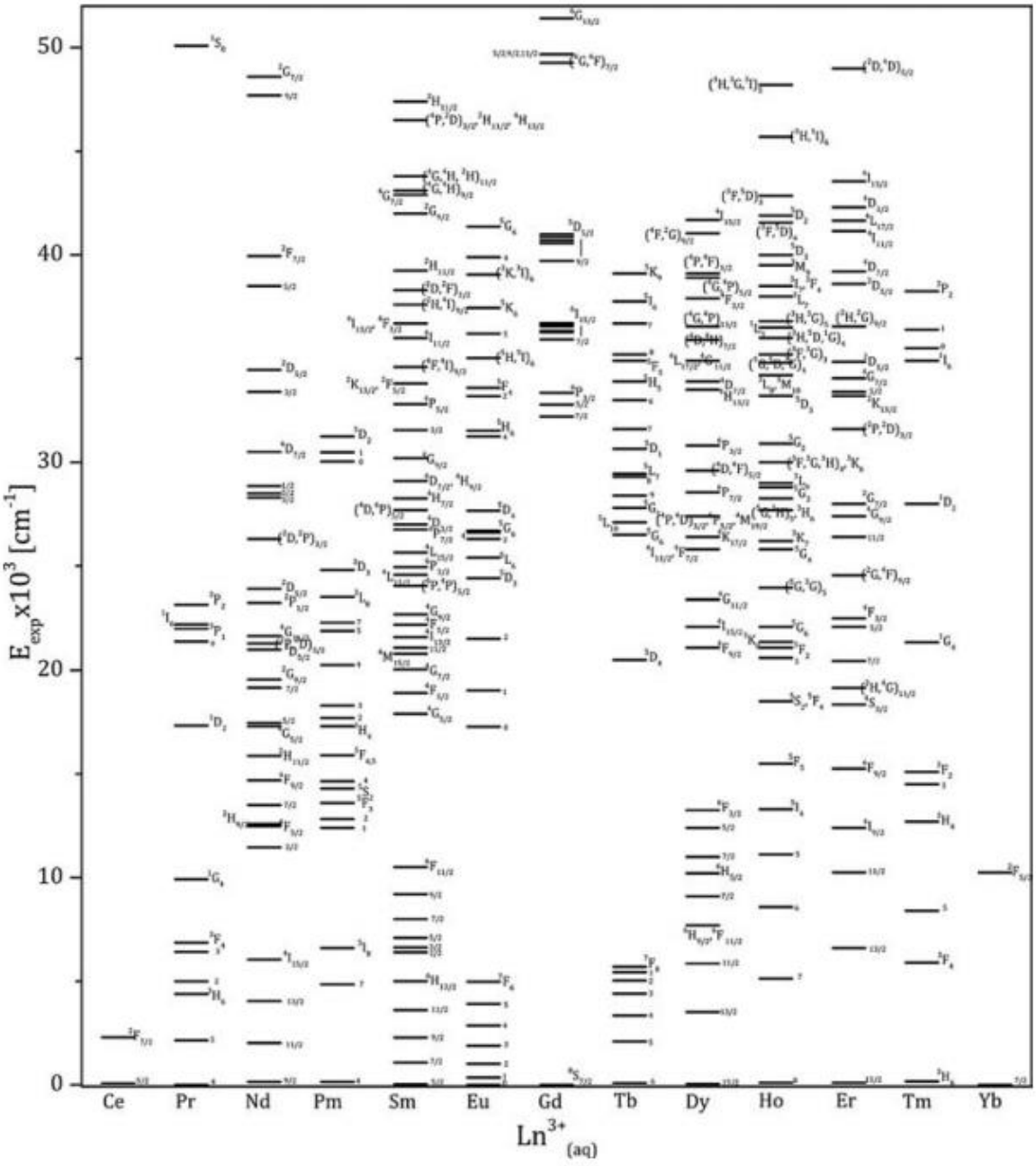


Figure 2.5 Diagram of energy levels with corresponding term symbols for Ln(III) [22]

Table 2.2 Commonly observed emission transitions for the emissive Ln(III) ions

Ln	Transition	λ (nm)
Pr	$^1D_2 \rightarrow {}^3F_4$ $^1D_2 \rightarrow {}^1G_4$ $^1D_2 \rightarrow {}^3H_J$ (J=4, 5) $^3P_0 \rightarrow {}^3H_J$ (J=4 – 6) $^3P_0 \rightarrow {}^3F_J$ (J=2 – 4)	1000 1440 600, 690 490, 545, 615, 640 700, 725
Nd	$^4F_{3/2} \rightarrow {}^6H_J$ (J=9/2 – 13/2)	900, 1060, 1350
Sm	$^4G_{5/2} \rightarrow {}^4I_J$ (J=5/2 – 13/2) $^4G_{5/2} \rightarrow {}^6F_J$ (J=1/2 – 9/2)	560, 595, 640, 700, 775 870, 887, 926, 1010, 1150
Eu	$^5D_0 \rightarrow {}^7F_J$ (J=0 – 6)	580, 590, 615, 650, 720, 750, 820
Gd	$^6P_{7/2} \rightarrow {}^8S_{7/2}$	315
Tb	$^5D_4 \rightarrow {}^7F_J$ (J=6 – 0)	490, 540, 580, 620, 650, 660, 675
Dy	$^4G_{5/2} \rightarrow {}^4I_J$ (J=5/2 – 13/2) $^4G_{5/2} \rightarrow {}^6F_J$ (J=1/2 – 9/2)	475, 570, 660, 750 455, 540, 615, 695
Ho	$^5S_2 \rightarrow {}^5I_J$ (J=8, 7) $^5F_5 \rightarrow {}^5I_J$ (J=8, 7)	545, 750 650, 965
Er	$^4S_{3/2} \rightarrow {}^4I_J$ (J=15/2, 13/2) $^4F_{9/2} \rightarrow {}^4I_{15/2}$ ^4I_J (J=9/2, 13/2) $\rightarrow {}^4I_{15/2}$	545, 850 660 810, 1540
Tm	$^1D_2 \rightarrow {}^3F_4, {}^3H_4, {}^3F_J$ (J=3, 2) $^1G_4 \rightarrow {}^3H_6, {}^3F_4, {}^3H_5$ $^3H_4 \rightarrow {}^3H_6$	450, 650, 740, 775 470, 650, 770 800
Yb	$^2F_{5/2} \rightarrow {}^2F_{7/2}$	980

2.3.4 Quantum Dots

Nano-structured materials have drawn tremendous attention in the last few decades since R. Feynman emphasized as "…there is plenty of room at the bottom … in the science of ultra-small structures." in his famous talk at CalTech on December 29, 1959. QDs are one of the most popular nanomaterials which can be considered as semi-conductor nanocrystals as small as a few nanometers in radius length. Their size tunable band gap, narrow and symmetric PL spectra, broad absorption profile and high PLQY features make them promising materials for various opto-electronic applications which require conversion of photons into photons in different wavelengths. More than forty years of academic research finally led to commercialization of them through QD containing TVs in 2013 [23].

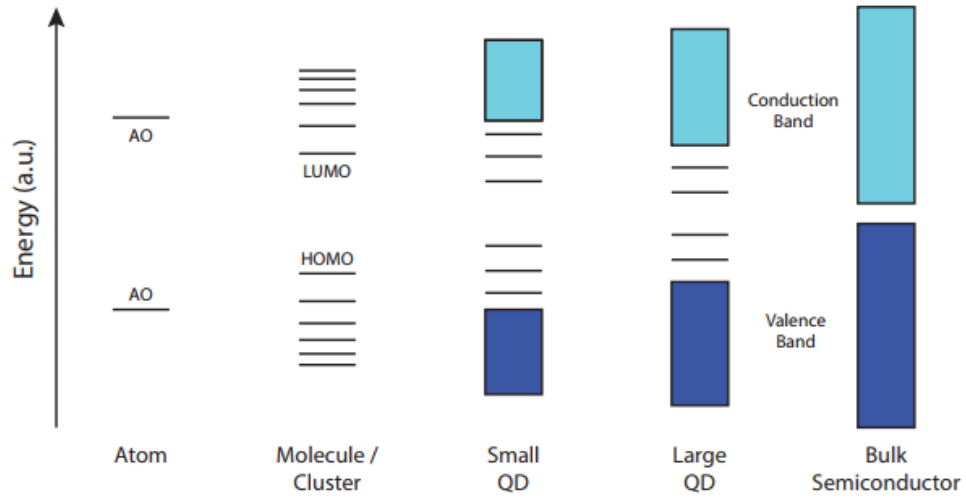


Figure 2.6 Schematic energy diagrams for the electronic structures of atoms, molecules/clusters, small and large QDs and bulk semiconductors

Electrons can only exist in discrete energy bands of materials. Without any external excitation, electrons prefer to sit in lowest possible energy level (see Figure 2.6). According to Pauli Exclusion Principle, every energy level is allowed to contain finite number of electrons. Therefore, the outermost valence and conduction bands determine the electronic properties of the material. Valance band of metals are full and the electrons in the conduction band can move freely which allow them to conduct charge. Energy difference between valence and conduction bands is named as band gap energy. An electron requires to absorb an amount of energy at least equal or more energy travel between different energy states. Conduction band of an insulating material is empty when it is in ground state and large band gap makes their electrons difficult to be excited from valence band to conduction band. In case of semiconductors, their electronic behavior is substantially similar to insulators but with a smaller band gap energy value in the order of 1 eV which allows photons to excite electrons from valence band to conduction band. Absorbed photon should be carrying an amount of energy, $h\upsilon$, at least equal to the band gap energy to excite the electron.

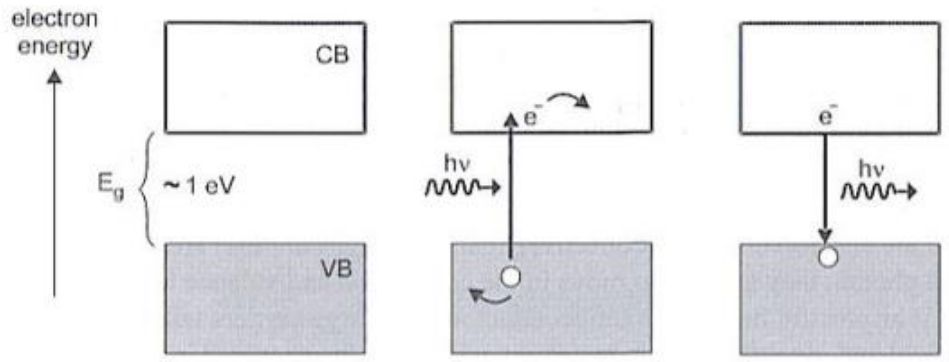


Figure 2.7 Electron-hole pair generation and emission of photon by semiconductor

A positively charged hole is formed when an electron is excited to the conduction band after the absorption of the incident photon. Electron and hole relaxes through releasing their excess energy by inelastic collisions and settle to the lowest and the highest level, respectively in their current bands. When the material returns to its ground state, the electron and the hole recombines and emits a photon with the same energy of band gap (see Figure 2.7).

2.4 Photonic and Opto Electronic Applications of Photoluminescent Glasses

Aforementioned photoluminescent materials are usually sensitive to environmental conditions. Therefore, a proper encapsulation is mandatory for their utilization into engineering applications. Polymer materials are commonly used in encapsulation of lanthanide ions and QDs. However, limited thermal, chemical and photo resistivity of polymer hosts make them insufficient for extreme environmental conditions or high powered electromagnetic radiation. At this point, glass families such as silicates and tellurites step forward as promising encapsulation media for optically active materials due to their excellent thermal and chemical stability providing reliable protection to favorable emission properties. Glass hosts are easy to manufacture and possess high lanthanide and QD solubility compared to crystals and powders. Additionally, high optical transmittance in broad wavelengths and producibility in bulk, powder and fiber forms are among other favorable properties of glasses. Hereof, amid different glass hosts, tellurite glasses step forward owing to their outstanding properties such as relatively low phonon energy, good chemical and thermal stability, good

lanthanide solubility and low melting temperature whilst silicate glasses offer a little bit more transmittance at UV edge of the electromagnetic spectrum and superior thermal and chemical resistance [24].

Lanthanide ions usually demonstrate better PL features inside host materials that have lower phonon energy values whilst whole synthesis process of QDs in glass hosts is significantly challenging. Due to different chemical environments of varying glass hosts, finding appropriate host material for the desired QD is a tedious task. Therefore, in this thesis, silicate and tellurite glass matrices were chosen and tuned through different network modifiers and intermediate oxides to synthesize the most ideal host material for the chosen PL material by taking the needs of the application into account. Besides single doping of lanthanide ions and QDs, their combinations are also investigated.

Nowadays, photoluminescent glasses are considered as a hot topic in materials science. Especially QD doped glasses have drawn tremendous attention to take place in advanced opto-electronic applications since 2017. Even though there are numerous studies in the literature, there is also a lot of missing knowledge which lingers their commercialization. Therefore, studies in the engineering framework as well as fundamental scientific studies are urgently needed. To sum up, in this thesis, optical and photoluminescence properties of lanthanide ion and/or QD doped glasses/glass nanocomposites are specifically investigated for different target applications due to their color converting properties. Structure-property relations are linked both for photoluminescent materials, i.e., lanthanides and/or QDs, and glass hosts. Thermal, chemical and photo stability features are determined under exaggerated conditions to test the suitability of such materials for practical applications. Proof-of-concept prototypes are constructed for solid-state lighting, 3D display and non-invasive temperature sensing applications.

3
Dy^{3+} DOPED TELLURITE GLASSES FOR SOLID-STATE LIGHTING: AN INVESTIGATION THROUGH PHYSICAL, THERMAL, STRUCTURAL AND OPTICAL SPECTROSCOPY STUDIES

O. Kıbrıslı, A. E. Ersundu, and M. Ç. Ersundu, "Dy^{3+} doped tellurite glasses for solid-state lighting: An investigation through physical, thermal, structural and optical spectroscopy studies," *Journal of Non-Crystalline Solids,* vol. 513, pp. 125-136, 2019.

3.1 Introduction

Electricity is an essential part of modern life and very important to the world economy. Electricity is used for several purposes such as lighting, heating, cooling, refrigeration, operating appliances, and public transportation systems. Lighting accounts for approximately 15 percent of global electricity consumption and 5 percent of worldwide greenhouse gas emissions. Therefore, development of new energy-saving lighting devices has recently drawn great importance as part of sustainable energy strategies. Among energy-saving lighting strategies, solid-state lighting devices outshine due to their unique properties such as high energy efficiency, high brightness, longer lifetime, excellent low temperature performance, good reliability, and added benefits like maintenance savings and environmental friendliness. Moreover, thanks to these favorable properties light emitting diodes (LEDs), as the best-known solid-state lighting devices, make smart lighting possible. Recent studies showed that being exposed to artificial light without the ideal color balance (excessive blue light and poor imitation of daylight) induces circadian phase shifts, melatonin suppression and increasing alertness in humans [25]. Hence, smart lighting with ideal color balance can simulate the variations of daylight and improve environmental lighting. Owing to these features, commercially available white light emitting diodes (WLEDs) have

begun to replace lighting devices such as incandescent, fluorescent, halogen and xenon bulbs [26-28].

Conventional WLEDs are mostly consist of three components: a crystalline phosphorus (e.g. Ce^{3+}: YAG), an ultraviolet LED chip (e.g. InGaN) and epoxy resin. However, temperature increment due to the flowing current through LED chip might lead to deterioration of the resin that encapsulates conventional LEDs and ultimately reduces the quality and intensity of the emitted light [29]. In addition, large refractive index difference between resin and phosphor increases the amount of scattered light and also poor heat resistance of resin decreases the overall lifetime of the device [30]. Therefore, rare earth ion-doped glasses have recently drawn much attention as an alternative to phosphor-based WLED systems owing to their several advantageous properties such as, chemical durability, better transparency and heat resistance, homogeneous emission, low cost, and simpler manufacture procedure [31, 32].

Abundant 4f-4f or 5d-4f emission transitions and shielding effect of the outer 5s and 5p orbitals make rare earth ions excellent luminescent materials. For this reason, they find use in numerous fields of applications: e.g. holographic and optical storage, solid-state lasers, LEDs, optical amplifiers, color displays, sensors, photovoltaics [33, 34]. Among trivalent lanthanide ions, Dy^{3+} offers promising features for solid-state lighting applications especially for white light generation [35]. Under UV excitation Dy^{3+} doped materials emit blue light at 470–500 nm and yellow light at 570–600 nm related to $^4F_{9/2} \rightarrow {}^6H_{15/2}$ and $^4F_{9/2} \rightarrow {}^6H_{13/2}$ transitions, respectively [36]. The ratio of yellow to blue emission depends on host material because of the hypersensitivity of $^4F_{9/2} \rightarrow {}^6H_{13/2}$ transition that obeys the selection rule $\Delta L = \pm 2$ and $\Delta J = \pm 2$. It is possible to tune the ratio of yellow to blue emission by changing host material, concentration of Dy^{3+} ions and varying the pumping wavelength [37, 38].

It is well known that the selection of host material for rare earth ion doping is of a crucial importance to obtain better emission properties with long durability. Hence, Dy^{3+} ion doping for white light emission has been studied and reported in different host materials such as oxyfluoride [32], phosphate [38], borate [39, 40],

tellurite [41-62], silicate [63] and germanate [64] glasses. Among various host materials tellurite glasses step forward with their advantageous properties, such as relatively low phonon energy, good non-linear optical properties, low scattering and absorption losses, high refractive index, high dielectric constant, good IR transmissivity, low melting temperature, good thermal and chemical stability and high devitrification resistance [65-67]. Recent studies have also shown that tellurite glasses offer promising spectroscopic properties for solid-state lasers and white LEDs that are comparable or better than other glass systems [36, 68, 69]. Therefore, investigating luminescent properties of different tellurite-based glasses has become crucial to evaluate their potentiality as durable and efficient luminescent materials for solid-state lighting applications.

The position of rare earth energy levels is identical for different hosts while the intensity of the emissions changes with the phonon energy and the local crystal field of the host matrix. Therefore, a thermally and chemically stable tellurite glass composition in the TeO_2-WO_3-Li_2O (TWL) system was selected as host material for various amount of Dy^{3+} doping. The favorable properties of TWL system for solid-state lighting applications such as low absorption and scattering losses, good transmittance in Vis region, high crystallization resistance and high rare earth solubility was reported in our previous works [70, 71]. There are a few studies on the spectroscopic and structural properties of rare earth element doped glasses having different compositions in the TWL system [72-74], however to the best of our knowledge, no such study exists solely on the investigation of TWL glasses for solid-state lighting applications especially for white light generation. Therefore, in this study physical, thermal, structural and optical properties of Dy^{3+} doped tellurite glasses were investigated through differential scanning calorimetry (DSC), Fourier-transform IR spectroscopy (FTIR), Vis-NIR absorption, Judd-Ofelt (J-O), photoluminescence and decay analyses. Consequently, the results obtained in this work have been discussed and compared with other reported Dy^{3+} doped glasses with the aim of revealing spectroscopic properties of Dy^{3+} ions in TeO_2-WO_3-Li_2O glass system to evaluate its suitability for solid-state lighting applications.

3.2 Experimental procedure

3.2.1 Glass Synthesis

Glasses in the (50-x)TeO_2-25WO_3-25Li_2O-$x$$Dy_2O_3$ (x = 0, 0.1, 0.25, 0.5, 1, 2, 3 mol%) system were synthesized using conventional melt quenching technique. The preparing of glasses by means of melt quenching technique is historically the most established and it is still the most widely used in the synthesis of tellurite glasses. The melt-quenching technique is usually adopted in the preparation of bulk tellurite glasses, whereas the sol-gel method could be an alternative to produce high-quality amorphous thin films.

Synthesized glasses were coded according to Dy_2O_3 content (in mol%) in batch composition as presented below:

TWL: 50TeO_2-25WO_3-25Li_2O (base glass)

TWLD01: 49.9TeO_2-25WO_3-25Li_2O-0.01Dy_2O_3

TWLD025: 49.75TeO_2-25WO_3-25Li_2O-0.25Dy_2O_3

TWLD05: 49.5TeO_2-25WO_3-25Li_2O-0.5Dy_2O_3

TWLD1: 49TeO_2-25WO_3-25Li_2O-1Dy_2O_3

TWLD2: 48TeO_2-25WO_3-25Li_2O-2Dy_2O_3

TWLD3: 47TeO_2-25WO_3-25Li_2O-3Dy_2O_3

For glass synthesis, high purity chemicals (Alfa Aesar) of TeO_2 (99.99%), WO_3 (99.8%), Li_2CO_3 (99%) and Dy_2O_3 (99.99%) were weighed and thoroughly mixed in an agate mortar with a pestle to ensure complete homogeneity. Batches of 7 g were placed into a platinum crucible with a closed lid and the mixtures were melted in an electrical furnace at 800 °C for 30 min. The melts were occasionally stirred to avoid the formation of bubbles and to ensure homogeneity. Subsequently, glass samples were obtained by pouring the melts into pre-heated stainless-steel molds. Immediately afterwards, glass samples were annealed below the glass transition temperature at 290 °C for 3 h and cooled down to room temperature with 1 °C/min cooling rate to remove residual internal stress resulted from the rapid cooling of the glass melt. Finally, glass samples were ground and

polished to obtain plan-parallel surfaces having an average thickness of 1.5 mm for further characterization studies.

3.2.2 XRD, Physical and Thermal Investigations

Amorphous nature of synthesized samples was checked by X-ray diffraction (XRD) analysis in a Philips/PANalytical X'pert Pro XRD instrument using CuK_α radiation at 45kV and 40 mA in the 2θ range from 20°-80° with a step size of 0.02°. Density, ρ, measurements were performed at room temperature by the Archimedes' principle using deionized water as immersion liquid with a digital balance of sensitivity 10^{-4} g. Measurements were repeated five times on each sample and the density values were determined with an error of ±1%. Density calculations were made according to the following equation:

$$\rho = \frac{W_{air}}{W_{air} - W_{liquid}} \tag{3.1}$$

where W_{air} and W_{liquid} are the weight of the glass sample in air and deionized water, respectively. Chemical durability of glasses was checked through dissolution rate (DR) calculations by using the following relation:

$$DR = \Delta W / (S \times t) \tag{3.2}$$

where ΔW is the difference between initial and final weight, S is the total surface area of the sample and t is the immersion time. TWL samples were precisely weighed and placed in 200 ml beaker full of boiling deionized water. Glass sample was removed after 100 min, washed with acetone and was dried (at 80 °C, for 1 h) subsequently in an oven for final weighing. Measurement was repeated for five times with different samples and average values were recorded with an error of ±0.001 g/cm^2.min. Refractive index values of glass samples were measured by using Brewster angle method with a resolution of 0.05°/step [75]. In addition, using measured density and refractive index values, various physical properties of glasses were calculated according to the equations given in Table 3.1. Thermal characteristics of glass samples were studied by using DSC analysis in a Netzsch DSC 204F1 (limit of detection: <0.1μV, with an error estimate of ± 1°C) instrument. DSC analysis was performed with a constant sample weight of 25 ± 1 mg in aluminum pans, under 25 ml/min flowing argon gas atmosphere with a

heating rate of 10 °C/min. Accordingly, glass transition onset (T_g), crystallization onset and peak temperatures (T_c/ T_p) were determined. Additionally, values of thermal difference, ΔT, were determined through the calculations of $\Delta T = T_c - T_g$ to evaluate the thermal stability of glasses.

Table 3.1 Equations used to calculate physical properties of glasses

Parameter	Equation	Definition	Reference
Molar Volume, V_M (cm^3mol^{-1})	$V_M = \frac{M}{\rho}$	M: molecular weight	[70]
Oxygen Molar Volume, V_O (cm^3mol^{-1})	$V_O = V_M \times \left(\frac{1}{\sum x_i n_i}\right)$	x_i: molar fraction n_i: number of oxygen atoms in each oxide	[70]
Oxygen Packing Density, OPD ($molL^{-1}$)	$OPD = 1000C\left(\frac{\rho}{M}\right)$	C: number of oxygen atoms per each comp.	[70]
Molar Refraction, R_m (cm^3)	$R_m = \frac{(n^2-1)}{(n^2+2)} \times V_M$	n: refractive index	[76]
Reflection Loss, R_L (%)	$R_L = \left[\frac{(n-1)}{(n+1)}\right]^2$		[29]
Molar Electronic Polarizability, α_m ($10^{-24}.cm^3$)	$\alpha_m = \frac{R_m}{2.52}$		[29]
Dielectric Constant, ε	$\varepsilon = n^2$		[29]
Optical Dielectric Constant, ε_{opt}	$\varepsilon = n^2 - 1$		[77]
Ionic Concentration, N (10^{20} ions/cm^3)	$N = \frac{N_A \times \rho}{M} \times \%mol\ R.E.I$	$R.E.I$: Rare earth ion	[29]
Polaron Radius, R_p (Å)	$R_p = \frac{1}{2} \times \left(\frac{\pi}{6N}\right)^{\frac{1}{3}}$		[29]
Inter Ionic Distance, R_i (Å)	$R_i = \left(\frac{1}{N}\right)^{\frac{1}{3}}$		[29]
Field Strength, F $\times 10^{16}$ (cm^{-2})	$F = \left(\frac{Z}{R_p^2}\right)$	Z: Atomic number	[29]
Metallization Factor, M	$M = 1 - \frac{R_m}{V_M}$		[29]
Optical Basicity, Λ	$\Lambda = \sum x_i \Lambda_i$	Λ_i: Basicity value of constituent oxide	[78]

3.2.3 FTIR, Optical Absorption and Emission Spectra Investigations

Structural investigations were realized by Fourier transform infrared (FTIR) spectroscopy using reflection technique in the wavenumber range 400 - 1000 cm^{-1} with a resolution of 1 cm^{-1} in a Bruker Hyperion 3000 FTIR spectrometer.

Optical absorption spectrum of each glass sample was recorded using Shimadzu UV 3600 UV-Vis-NIR spectrophotometer in the wavelength range 400 - 2000 nm at room temperature with a resolution of 0.5 nm. Subsequently, optical band gap values of glass samples were calculated using the following equation proposed by Davis and Mott [79]:

$$\alpha(\omega) = \frac{A(\hbar\omega - E_{opt})^p}{\hbar\omega} \quad (3.3)$$

where A is a constant named band tailing parameter, α is absorption coefficient, ω is angular frequency, $\hbar\omega$ is photon energy, E_{opt} is optical band gap energy in eV and p is an index depending on the nature of the electronic transition responsible for absorption. For amorphous materials, indirect transitions are valid according to the Tauc relation, therefore in this work p was taken as 2. According to the Tauc relation, the band gap energy of the glasses was determined by extrapolating the absorption coefficient to zero absorption in the $(\alpha\hbar\omega)^{1/2}$ vs $\hbar\omega$ plot [71].

The bonding nature of the Dy^{3+} and ligand bond was investigated through nephelauxetic ratios and bonding parameters. The nephelauxetic ratio, β, of related transitions were calculated by using the following relation [80]:

$$\beta = \frac{\overline{\nu}_c}{\overline{\nu}_a} \quad (3.4)$$

where $\overline{\nu}_c$ and $\overline{\nu}_a$ are peak positions of the related transition of Dy^{3+} ion in glass matrix and aqua ion, respectively [81]. The bonding parameter, δ, was determined from the average value of nephelauxetic ratio, $\overline{\beta}$, by using the following relation [82]:

$$\delta = \frac{1-\overline{\beta}}{\overline{\beta}} \times 100 \quad (3.5)$$

Photoluminescence excitation and emission spectra of glass samples were measured in a Perkin Elmer LS55 spectrofluorometer (resolution: 0.5 nm) with a pulsed xenon arc lamp of 20 kW as radiation source in the wavelength ranges 325-525 and 450-700 nm, respectively. The International Commission on Illumination (CIE) 1931 chromaticity coordinates were determined by using photoluminescence emission data using following equations [38]:

$$x = \frac{X}{X+Y+Z} \tag{3.6}$$

$$y = \frac{Y}{X+Y+Z} \tag{3.7}$$

$$z = \frac{Z}{X+Y+Z} \tag{3.8}$$

where X, Y, Z are the tristimulus values which are related to the three basic colors red, green and blue. X, Y and Z are defined as: $X = \int E(\lambda)\,\overline{x}(\lambda)d\lambda$, $Y = \int E(\lambda)\,\overline{y}(\lambda)d\lambda$, $Z = \int E(\lambda)\,\overline{z}(\lambda)d\lambda$ where $\overline{x}$, $\overline{y}$ and $\overline{z}$ are matching functions of CIE. Artificial colors indicated by X, Y and Z can be added to produce real spectral colors. Correlated color temperature (CCT) values were determined by using McCamy empirical formula [83]:

$$CCT = -449n^3 + 3525n^2 - 6823n + 5520.3 \tag{3.9}$$

where $n = \frac{X-X_e}{Y-Y_e}$ and the chromaticity epicenter is $X_e = 0.332$ and $Y_e = 0.186$. Color purity values were evaluated from the following expression [30]:

$$Color\ purity = \frac{\sqrt{(x-x_{ee})^2+(y-y_{ee})^2}}{\sqrt{(x_d-x_{ee})^2+(y_d-y_{ee})^2}} \tag{3.10}$$

where (x, y), (x_{ee}, y_{ee}) and (x_d, y_d) are the chromaticity coordinates of samples, equal energy point and dominant wavelength, respectively. Color rendering index (CRI) values were calculated by using OSRAM LED ColorCalculator software.

3.2.4 Judd-Ofelt Analysis, Radiative Properties and Decay Profiles

Measured oscillator strengths (f_{meas}) were obtained from absorbance spectra by using subsequent equation to calculate phenomenological Judd-Ofelt parameters:

$$f_{meas} = \frac{2.303mc^2}{N_A\pi e^2}\int \varepsilon(\nu)d\nu = 4.318 \times 10^{-9}\int \varepsilon(\nu)d\nu \tag{3.11}$$

where c is the velocity of light in vacuum, m and e are the rest mass and charge of an electron, respectively, N_A is Avogadro's number, $\varepsilon(\nu)$ is the molar absorptivity of the related absorption band at wavenumber ν (in cm^{-1}) [84]. Theoretical oscillator strengths (f_{cal}) for the induced electric dipole transitions from the ground state (ΨJ) of Dy^{3+} ions to various excited states ($\Psi' J'$) were calculated based on the Judd–Ofelt theory [85, 86] using the following relation:

$$f_{cal} = \frac{8\pi^2 mc\nu}{3he^2(2J+1)} \times \frac{(n^2+2)^2}{9n}\left(\sum_{\lambda=2,4,6}\Omega_\lambda\left(\Psi J\|U^\lambda\|\Psi' J'\right)^2\right) \tag{3.12}$$

where $\sum_{\lambda=2,4,6} \Omega_\lambda \left(\Psi J \| U^\lambda \| \Psi' J'\right)^2$ is the line strength of electric-dipole transitions, J and J' are the total angular momentum of the ground state and excited states, h is Planck's constant, ν (cm^{-1}) is the wavenumber of the transition from initial state ΨJ to the excited state Ψ'J', n is the refractive index of the sample, Ω_λ ($\lambda = 2, 4, 6$) are the Judd-Ofelt intensity parameters and $||U^\lambda||^2$ are the doubly reduced matrix elements of the unit tensor operator of the rank $\lambda = 2, 4, 6$. Doubly reduced matrix elements depend on neither host nor local environment so the values were directly taken from the literature data [87]. Judd-Ofelt parameters were calculated according to Judd-Ofelt theory by using least square fitting for the equations of *fcal* and *fmeas* values. Root mean square deviations, δ_{rms}, of f_{cal} and f_{meas} values were calculated via the following equation:

$$\delta_{rms} = \sum \left\{ \frac{(f_{exp} - f_{meas})^2}{N} \right\}^{\frac{1}{2}} \tag{3.13}$$

where N is the number of transitions used. δ_{rms} indicates the quality of the fit between the equations (11) and (12) and the accuracy of the Judd-Ofelt parameters.

Next step of J-O analysis is determination of radiative properties such as A_R, radiative transition probability, β, branching ratio, $\sigma \times \Delta\lambda_{eff}$, optical bandwidth gain, τ_{cal}, calculated lifetime and σ, stimulated emission cross-section. A_R values were calculated according to following relation [88]:

$$A_R\,(\Psi J, \Psi' J') = \frac{64\pi^4 \nu^3 e^2}{3h(2J+1)} \left[\frac{n(n^2+2)^2}{9} S_{ED} + n^3 S_{MD} \right] \tag{3.14}$$

where S_{ED} (electric dipole) and S_{MD} (magnetic dipole) are line strengths of related transition. S_{ED} and S_{MD} values were determined via subsequent equations [88]:

$$S_{ED}(\Psi J, \Psi' J') = e^2 \left(\sum_{\lambda=2,4,6} \Omega_\lambda \left(\Psi J \| U^\lambda \| \Psi' J'\right)^2 \right) \tag{3.15}$$

and

$$S_{MD}(\Psi J, \Psi' J') = \left(\frac{e^2}{4m^2c^2} \right) \Omega_\lambda (\Psi J \| L + 2S \| \Psi' J')^2 \tag{3.16}$$

β_{cal} values were obtained by using the following relation [88]:

$$\beta_{cal}(\Psi J, \Psi' J') = \frac{A_R(\Psi J, \Psi' J')}{A_T(\Psi' J')} \tag{3.17}$$

where A_T (total radiative transition probability) is the summation of all A_R from $^4F_{9/2}$ state to various excited states. β_{meas} values were evaluated from ratio of integrated area of corresponding emission band to total integrated area of the emission. τ_{cal} values were obtained from the following relation [88]:

$$\tau_{cal} = \frac{1}{A_T(\Psi' J')} \tag{3.18}$$

Stimulated emission cross section values, σ, were calculated for each emission peak wavelength according to below given equation [86]:

$$\sigma(\lambda_p)(\Psi J, \Psi' J') = \frac{\lambda_p^4}{8\pi c n^2 \Delta\lambda_{eff}} A_R(\Psi J, \Psi' J') \tag{3.19}$$

where $\Delta\lambda_{eff}$ is the effective bandwidth of corresponding emission band calculated by dividing the band area by height.

Decay profiles were measured to find the lifetime values and quantum efficiencies of synthesized glasses. Experimental lifetime values of glass samples were determined through time resolved photoluminescence measurements by using Edinburgh Instruments FLS 1000 spectrometer equipped with a microsecond xenon lamp (45 W, 100 Hz). Single exponential decay profiles were fitted by using the following expression:

$$I_t = I_0 e^{-t/\tau} \tag{3.20}$$

while non-exponential decay profiles were fitted according to below given equation [89]:

$$I = I_0 + A_1 \exp\left(-\frac{t}{\tau_1}\right) + A_2 \exp\left(-\frac{t}{\tau_2}\right) \tag{3.21}$$

where I_0 and I_t are emission intensities at t=0 and t=t, respectively. τ_1 and τ_2 are lifetime values of two channels contributing to decay processes and A_1 and A_2 values are decay constants. Non-exponential lifetime values were found according to following equation [90]:

$$\tau_{meas} = \frac{A_1\tau_1^2 + A_1\tau_2^2}{A_1\tau_1 + A_2\tau_2} \tag{3.22}$$

Quantum efficiency, η, is expressed as the ratio of number of photons emitted to the number of photons absorbed. η value can be calculated by the following relation for rare earth ion doped glasses [91]:

$$\eta = \frac{\tau_{meas}}{\tau_{cal}} \times 100 \tag{3.23}$$

Lastly, non-radiative transition rates, W_{NR}, were obtained from the subsequent expression [68]:

$$W_{NR} = \frac{1}{\tau_{meas}} - \frac{1}{\tau_{cal}} \tag{3.24}$$

3.3 Results and Discussion

3.3.1 Physical Properties

The XRD patterns of synthesized samples are given in Figure 3.1 and it was proven that the samples have amorphous character. Photographs of optically polished samples under daylight and blue light are presented in Figure 3.2. All synthesized samples were obtained visually transparent and optically clear (see Figure 3.2a). It was observed that the color of samples is pale yellow, and no significant change in color was detected with varying Dy^{3+} ion concentration. It is well known that the color change has a direct impact on visible absorption spectrum and the position of absorption edge. Therefore, the transmittance values of synthesized glasses did not show significant alteration with varying Dy^{3+} ion concentration reaching around 75% for all compositions. In addition, the short wavelength absorption edge was located around 400 nm for all glasses.

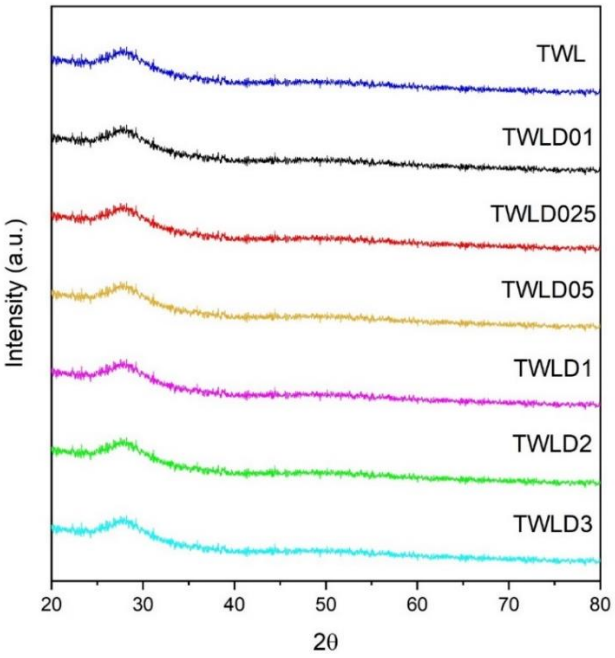


Figure 3.1 XRD diffractograms of glass samples

Physical properties of glasses exhibit significant modification with the slight change of glass network. Therefore, different physical properties of glasses were calculated by using measured density and refractive index values and the obtained results are tabulated in Table 3.2.

Density values of prepared samples showed an increase with increasing Dy^{3+} content at the expense of TeO_2 due to the larger density value of Dy_2O_3. Similarly, molar volume, V_M, values increased with the replacement of Dy_2O_3 with TeO_2. This behavior can be explained due to the increase in the number of oxygen atoms which have the highest ionic radius in the glass structure. Therefore, it can be said that the increasing oxygen content in glass composition leads to formation of excess free volume by increasing the molar volume and opens up the glass structure. Additionally, increment of oxygen molar volume, V_O, and decrement of oxygen packing density, OPD, with increasing Dy_2O_3 content was attributed to the replacement of higher field strength Te^{4+} ions with lower field strength Dy^{3+} ions which results less tightly packing of the glass network.

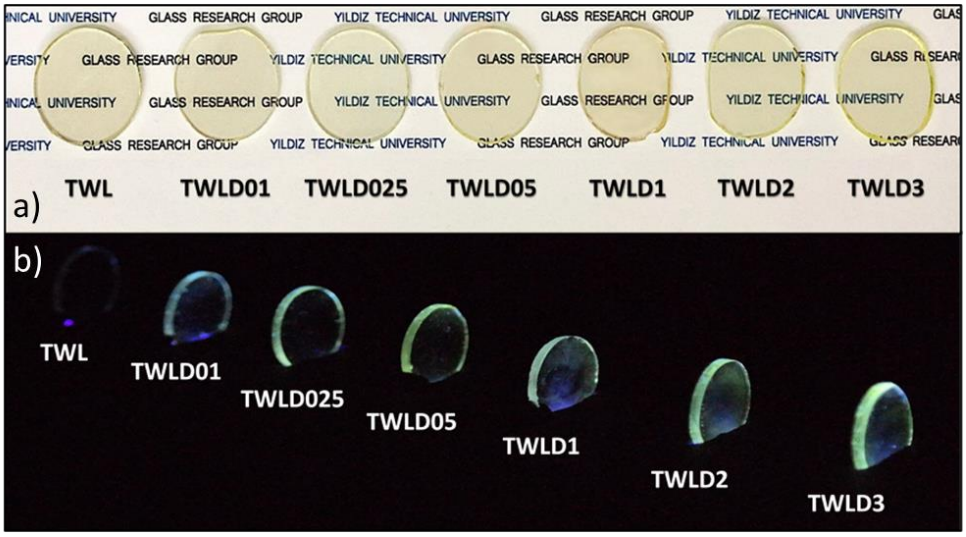


Figure 3.2 Macro photos of synthesized glass samples a) under daylight b) under blue light

Molar refraction, R_M, is a measure of the total polarizability of a mole of material. Less tightly packing of glass structure results in increment of R_M and molar electronic polarizability (α_m) that defines the magnitude of electrons responding to an electric field [76]. Increment of electronic polarizability values is also responsible for the increase of dielectric and optical dielectric values and so refractive index [92]. Reflection losses (R_L) of synthesized glasses were found to be in the scale of 10-12%. This behavior refers that most of the radiation impinging on the sample is transmitted through the glass. The increment of Dy^{3+} ions in glass composition resulted a decrease in interionic distance (r_i) and polaron radius (r_p) indicating an increase in non-radiative losses [57]. r_p values were found to be smaller compared to r_i values revealing high field strength (F) for prepared glasses [58]. Metallization factor (M) is an empirical equation that determines the tendency for metallization. According to Herzfeld's theory, refractive index becomes infinite for the condition $R_M/V_M = 1$ in the Lorentz-Lorenz equation [27]. If the R_M/V_M value equals or greater than unity one can say that material have mobile electrons and considered as metal. On the occasion of $R_M/V_M < 1$, material can be considered to have non-metallic nature. Taking calculated M values into account, it was observed that R_M/V_M values are smaller than unity indicating the amorphous nature of synthesized samples and also supports the XRD results.

Optical basicity indicates the electron donating power of the oxygen in oxide glasses that controls the effectiveness of cation hosting which is very important for photonic and opto-electronic applications such as laser gain mediums. Optical basicity of each oxide in the glass composition was used (Λ_{TeO_2} = 0.93 [76], Λ_{WO_3} = 1.05 [59], Λ_{Li_2O} = 0.87 [59], $\Lambda_{Dy_2O_3}$ = 0.945 [93]) to calculate optical basicity values of glasses (see Table 3.2) and a slight increase in the Λ was observed with increasing Dy^{3+} content at the expense of TeO_2 in glass composition.

Dissolution rate, *DR*, of TWL glass was calculated as 1.75×10^{-6} ± 0.001 (g/cm^2.min). In general, a small value of *DR* indicates good chemical durability of glasses. *DR* of TWL glass is approximately one order of magnitude higher compared to soda-lime glass that refers good chemical durability and non-hygroscopicity of this glass composition.

Table 3.2 Physical parameters of Dy^{3+} ion doped TWLD glasses

Parameter	TWLD01	TWLD025	TWLD05	TWLD1	TWLD2	TWLD3
Molecular Weight, M (g/mol)	158.31	158.63	159.17	160.23	162.37	164.50
Density (g/cm^3)	5.46	5.47	5.48	5.50	5.54	5.57
Band Gap, E_g (eV)	2.91	2.89	2.88	2.87	2.86	2.85
Refractive Index	1.95	1.97	2.01	2.04	2.07	2.09
Molar Volume, V_M (cm^3/mol)	28.981	29.011	29.017	29.089	29.301	29.494
Oxygen Molar Volume, V_O ($cm^3.mol^{-1}$)	15.46	15.48	15.50	15.56	15.71	15.86
Oxygen Packing Density, OPD ($mol.L^{-1}$)	64.68	64.59	64.53	64.29	63.65	63.06
Molar Refraction, R_m (cm^3)	13.997	14.212	14.605	14.926	15.315	15.599
Reflection Loss, R_L (%)	10.371	10.667	11.259	11.704	12.148	12.443
Molar Electronic Polarizability, α_m ($10^{-24}.cm^3$)	0.555	0.564	0.579	0.592	0.607	0.619
Dielectric Constant, ε	3.803	3.881	4.040	4.162	4.285	4.368
Optical Dielectric Constant	2.803	2.881	3.040	3.162	3.285	3.368
Ionic Concentration, N (10^{20} ions/cm^3)	0.176	0.441	0.885	1.778	3.577	5.401
Polaron Radius, r_p (Å)	15.480	11.402	9.041	7.165	5.676	4.948
Inter Ionic Distance, r_i (Å)	38.420	28.298	22.437	17.783	14.087	12.279
Field Strength, F $\times 10^{16}$ (cm^{-2})	0.275	0.508	0.808	1.285	2.049	2.696
Metallization Factor, M	0.517	0.510	0.497	0.487	0.477	0.471
Optical Basicity, Λ	0.9450	0.9450	0.9451	0.9452	0.9453	0.9455

3.3.2 Thermal Properties

DSC thermograms of synthesized glasses are given in Figure 3.3. All samples showed a shallow broad endothermic hump corresponding to the glass transition temperature. T_g values slightly shifted to higher temperatures from 323 °C to 326 °C for lower Dy^{3+} doping rates (from 0.1 to 0.5 mol%) while the shift in T_g became more apparent with increasing doping rates reaching up to 343 °C. The increment

in T_g with increasing Dy_2O_3 content was attributed to the partial substitution of TeO_2 by Dy_2O_3 of greater number of cations per mol and average cross-linking density. Additionally, it can also be explained that increasing number of bonds per unit volume increases with increasing Dy_2O_3 content which ultimately results an increase in T_g [65]. At relatively elevated temperatures exothermic peaks related to the crystallization and/or transformation of different phases from glassy matrix was detected. First crystallization onset temperatures were found to lie in the range of 470 to 496 °C. T_c values initially exhibited an increase up to 0.5 mol% Dy_2O_3 doping and subsequently showed a slight decrease with further increment of Dy_2O_3 content. The temperature difference between T_g and exothermic peak onset T_c, ΔT, indicating the glass stability against crystallization was found to vary between 127 and 170 °C. It was reported in the literature that the ΔT should usually be larger than 100 °C to obtain thick glass samples with good thermal stability [94]. Hence, all glasses prepared in this work were found suitable for use in a wider temperature range without crystallization.

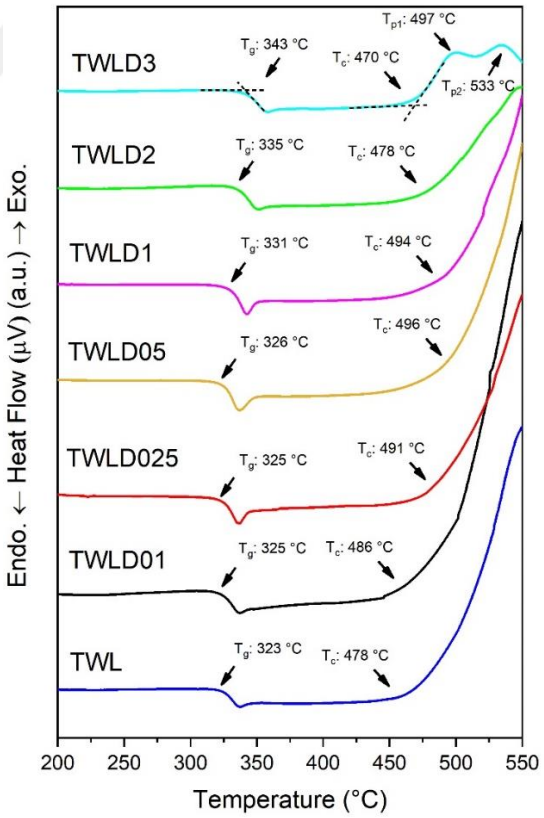


Figure 3.3 DSC curves of glass samples

3.3.3 Structural Properties

FTIR spectra of studied samples are given in Figure 3.4. In general, FTIR spectra show broad peaks and shoulders due to the disorder nature (lack of long-range periodicity) of glass structure. Therefore, FTIR spectra were deconvoluted into several symmetrical Gaussian functions (see inset of Figure 3.4). FTIR bands were then assigned by considering the IR spectra of each raw material and compared with reported IR data. For TWLD glasses the peaks at around 613-617 cm^{-1} and 643-697 cm^{-1} are due to the stretching vibrations of Te–O–Te linkages in trigonal bipyramid units, while the peak at around 776–791 cm^{-1} is attributed to the asymmetric stretching vibrations of TeO_3 trigonal pyramid or TeO_{3+1} polyhedral units. The shoulder appearing at around 833–846 cm^{-1} is assigned to the stretching vibrations of W–O–W linkages and the peak at 922 cm^{-1} is attributed to the stretching vibrations of $W–O^-$ and W═O linkages in tetrahedral WO_4 or octahedral WO_6 units. According to the literature, the narrow bands located at around 536 cm^{-1} were possibly arisen due to asymmetric vibrations of Te–O–Te linkages, stretching vibrations of Te–O–W or bending vibrations of Dy–O linkages [29, 34, 93, 95-97]. Since the intensity of this band increases with the increasing Dy_2O_3 content, it is more likely that the band located around 536 cm^{-1} in this study represents the bending vibrations of Dy–O linkages. FTIR bands were found to be almost at the same positions for all glasses showing very slight changes towards the higher wavenumber values with the increment of Dy_2O_3 content.

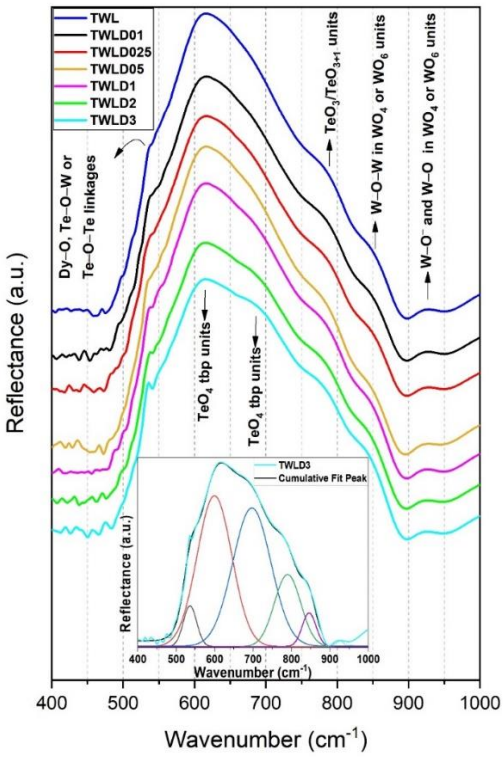


Figure 3.4 Fourier-transform IR spectra of glass samples (inset shows deconvoluted FTIR spectrum of TWLD3 glass sample)

3.3.4 Absorption Spectra and Bonding Parameters

Optical absorption spectra of glasses recorded in the UV-Vis-NIR region are illustrated in Figure 3.5. Each spectrum exhibited eight absorption bands centered around 451, 474, 754, 803, 902, 1096, 1280 and 1689 nm related with the f-f induced electric dipole transitions from $^6H_{15/2}$ ground state to the various excited states: $^4I_{15/2}$, $^4F_{9/2}$, $^6F_{3/2}$, $^6F_{5/2}$, $^6F_{7/2}$, $^6F_{9/2}$, $^6F_{11/2}$ and $^6H_{11/2}$, respectively [98].

Bands located in the range of 450 to 500 nm were weaker in intensity due to the strong absorption of the glass matrix near the absorption edge. Strong absorption band related to the transition from $^6H_{15/2}$ to $^6F_{11/2}$ around 1280 nm is hypersensitive as it obeys the selection rule, $|\Delta S|=0$, $|\Delta L| \leq 2$ and $|\Delta J| \leq 2$ [99]. Therefore, any changes in the local structure around Dy^{3+} ions may strongly affect the intensity of the peak at around 1280 nm. Consequently, intensities of all absorption bands increased with the increment of Dy_2O_3 content.

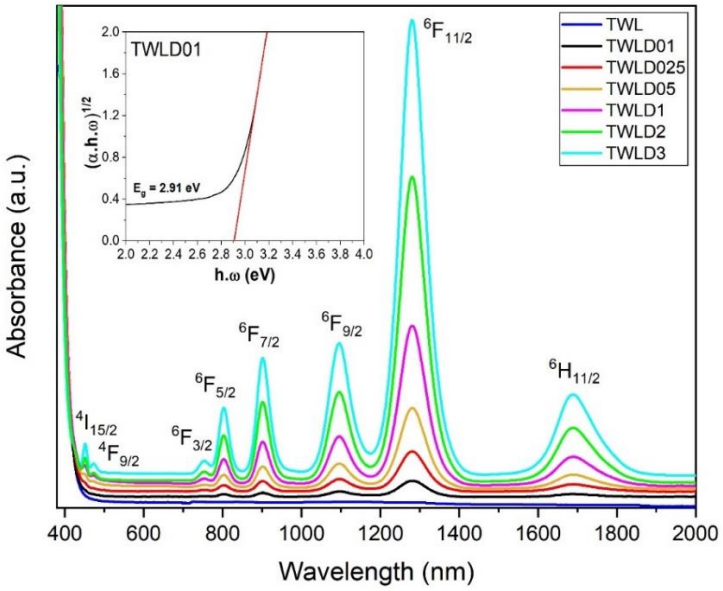


Figure 3.5 Optical absorption spectra of glass samples in Vis-NIR region (inset shows Tauc plot of TWLD01 glass sample)

The bonding nature of Dy^{3+} ions with its surrounding ligands can be identified from the negative or positive magnitude of δ value. There was no considerable shift of absorption bands as a result of the increment of Dy_2O_3 content in the glass composition, hence δ value was calculated as -0.49 for all compositions. Consequently, glasses prepared in this study exhibited negative bonding parameters referring to the ionic nature of Dy–O bonds [58, 100]. Inset of Figure 3.5 represents the Tauc plot for selected TWLD01 sample and the calculated band gap values are tabulated in Table 3.2 for all glasses. In general, optical band gap values showed a decrease with the increasing amount of Dy_2O_3 in glass structure. This decrement was attributed to the increase in the degree of electron localization that increases donor centers in glass matrix [29].

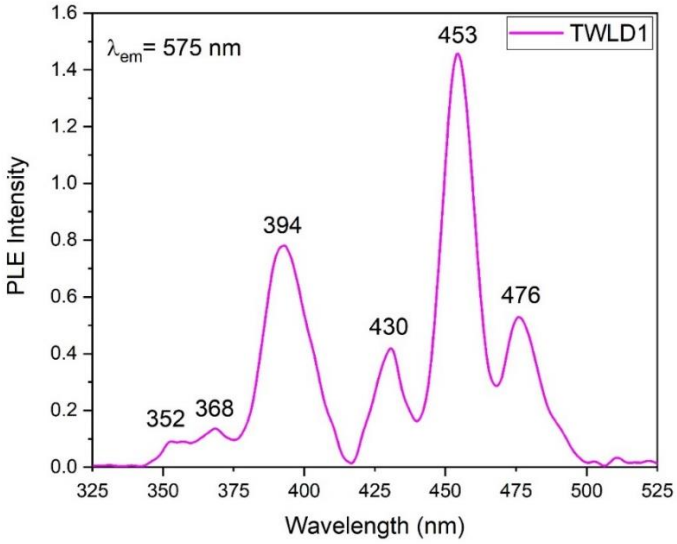


Figure 3.6 Photoluminescence excitation spectrum of TWLD1 glass sample recorded at 575 nm

3.3.5 Judd-Ofelt Analysis

The absorption spectra of rare earth ions comprise information about electronic transitions and radiative properties [58]. In order to reveal this information f_{meas} and f_{cal} values were calculated and given in Table 3.3 along with root mean square deviations. As clearly seen from Table 3.3, oscillator strength of the transition from ground state ($^6H_{15/2}$) to excited state ($^6F_{11/2}$) is the strongest among all transitions due to the hypersensitive nature of this transition. Three J–O parameters are very useful to investigate local structure around the lanthanide ion in a glass matrix. Therefore, Ω_2, Ω_4 and Ω_6 values were calculated according to J–O theory by using the least square fitting of f_{meas} and f_{cal} values.

Table 3.3 Measured (f_{meas}, 10^{-6}) and calculated (f_{cal}, 10^{-6}) oscillator strengths and r.m.s deviation ($\delta_{rms,}$ 10^{-6}) of Dy^{3+} ions in TWLD glasses

From $^6H_{15/2}$	TWLD01		TWLD025		TWLD05		TWLD1		TWLD2		TWLD3	
	f_{meas}	f_{cal}	f_{meas}	f_{cal}	f_{meas}	f_{cal}	f_{meas}	f_{cal}	f_{meas}	f_{cal}	f_{meas}	f_{cal}
$^4I_{15/2}$	0.03	0.13	0.04	0.15	0.05	0.20	0.07	0.29	0.17	0.70	0.26	1.03
$^4F_{9/2}$	0.01	0.04	0.02	0.09	0.03	0.10	0.04	0.17	0.09	0.37	0.13	0.49
$^6F_{3/2}$	0.01	0.01	0.01	0.02	0.02	0.05	0.06	0.14	0.18	0.44	0.23	0.54
$^6F_{5/2}$	0.03	0.09	0.06	0.16	0.16	0.38	0.34	0.79	0.73	1.67	1.02	2.28
$^6F_{7/2}$	0.06	0.14	0.16	0.36	0.36	0.76	0.77	1.60	1.64	3.31	2.30	4.57
$^6F_{9/2}$	0.16	0.29	0.33	0.60	0.68	1.19	1.49	2.53	3.06	5.08	4.30	7.03
$^6F_{11/2}$	0.56	0.87	1.58	2.43	2.96	4.43	6.53	9.52	12.27	17.44	17.70	24.75
$^6H_{11/2}$	0.14	0.17	0.37	0.43	0.69	0.78	1.59	1.75	3.29	3.54	4.68	4.96
δ_{rms}	±0.01		±0.05		±0.17		±0.69		±2.18		±4.04	

Calculated J–O values of Dy^{3+} ion doped TWLD glasses, their trends and spectroscopic quality factors are given in Table 3.4 along with some previously reported glass systems. Ω_2 value indicates the asymmetry level of the environment around Dy^{3+} ions. Ω_4 and Ω_6 values refer to bulk properties such as rigidity and viscosity [101]. The trend of J-O values was found in following order: $\Omega_2 > \Omega_4 > \Omega_6$ for the studied glass system and such behavior represents good quality of glass host for optical device applications [39]. Ω_2 values showed an increment with increasing Dy_2O_3 content that indicates higher asymmetry around Dy^{3+} ions [91]. The ratio between Ω_4 and Ω_6 values (Ω_4/Ω_6) can be defined as spectroscopic quality factor that used to describe the stimulated emission of the rare earth ions in various hosts [102]. In this study, Ω_4/Ω_6 values tend to decrease with increasing Dy_2O_3 indicating a decreasing behavior in spectroscopic quality factor. However, spectroscopic quality factors calculated in this study were found to be in good

agreement with other Dy^{3+} doped glasses reported in the literature revealing that these values are suitable for opto electronic device fabrication [33].

Table 3.4 Judd-Ofelt intensity parameters Ω_2, Ω_4, Ω_6 (10^{-20} cm^2), comparison of their magnitude and Ω_4/Ω_6 (spectroscopic quality factor) of Dy^{3+} ion doped TWLD glasses along with some previously reported glass systems

Sample codes	Ω_2	Ω_4	Ω_6	Ω_λ trend	Ω_4/Ω_6	Reference
TWLD01	0.470 ± 0.02	0.116 ± 0.01	0.11 ± 0.01	$\Omega_2 > \Omega_4 > \Omega_6$	1.045	Present work
TWLD025	1.436 ± 0.07	0.216 ± 0.03	0.265 ± 0.03	$\Omega_2 > \Omega_6 > \Omega_4$	0.815	Present work
TWLD05	2.637 ± 0.1	0.465 ± 0.04	0.538 ± 0.04	$\Omega_2 > \Omega_6 > \Omega_4$	0.864	Present work
TWLD1	5.895 ± 0.23	0.931 ± 0.12	1.220 ± 0.17	$\Omega_2 > \Omega_6 > \Omega_4$	0.763	Present work
TWLD2	11.036 ± 0.42	1.708 ± 0.26	2.664 ± 0.32	$\Omega_2 > \Omega_6 > \Omega_4$	0.641	Present work
TWLD3	16.002 ± 0.53	2.395 ± 0.37	3.750 ± 0.41	$\Omega_2 > \Omega_6 > \Omega_4$	0.638	Present work
TSWD2	12.404	3.458	5.224	$\Omega_2 > \Omega_6 > \Omega_4$	0.662	[40]
BTLND2D	6.006	1.866	1.252	$\Omega_2 > \Omega_4 > \Omega_6$	1.490	[76]
2DZTFB	4.279	2.284	1.819	$\Omega_2 > \Omega_4 > \Omega_6$	1.256	[9]
TeWLi	11.58	9.058	1.268	$\Omega_2 > \Omega_4 > \Omega_6$	7.143	[64]
TTWD01	2.86	0.32	0.89	$\Omega_2 > \Omega_6 > \Omega_4$	0.35	[12]
Oxyfluoride	6.41	1.02	2.25	$\Omega_2 > \Omega_6 > \Omega_4$	0.45	[75]
Phosphate	4.628	0.774	0.794	$\Omega_2 > \Omega_6 > \Omega_4$	0.97	[78]
Silicate	8.32	2.14	2.75	$\Omega_2 > \Omega_6 > \Omega_4$	0.78	[61]
Borate	11.30	3.30	2.60	$\Omega_2 > \Omega_4 > \Omega_6$	1.26	[79]

3.3.6 Photoluminescence Spectra and Radiative Properties

Photoluminescence (PL) spectra of rare earth ions depend on excitation wavelength. Figure 3.6 shows the photoluminescence excitation (PLE) spectrum of selected TWLD1 sample by monitoring an emission at 575 nm. The observed excitation peaks were assigned to transitions from $^6H_{15/2}$ to $^6P_{7/2}$, $^6P_{5/2}$, $^4F_{7/2}$, $^4G_{11/2}$, $^4I_{15/2}$, $^4F_{9/2}$, respectively [103]. The transition from $^6H_{15/2}$ to $^4I_{15/2}$ located at 453 nm was found to have the highest intensity and therefore this transition wavelength was selected to be used for excitation in PL measurements.

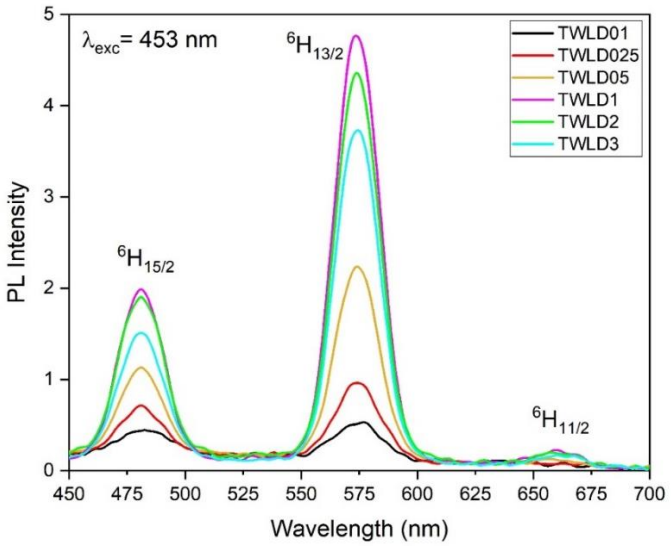


Figure 3.7 Photoluminescence emission spectra of Dy^{3+} ion doped TWLD glasses pumped at 453 nm

PL spectra of prepared glasses are illustrated in Figure 3.7. The spectra exhibited two intense emission bands. The first band was at 481 nm related to $^4F_{9/2}$ to $^6H_{15/2}$ transitions due to magnetic dipole and the second band was at 575 nm belonging to $^4F_{9/2}$ to $^6H_{13/2}$ transitions due to electric dipole. Moreover, a weaker emission band was observed around 661 nm referring to $^4F_{9/2}$ to $^6H_{11/2}$ transitions. Intensity of the emission bands tended to increase with increasing Dy^{3+} concentration up to 1 mol% and then decreased for higher Dy^{3+} concentrations, while the peak positions remained unchanged. This behavior was attributed to the PL quenching effect at higher Dy^{3+}concentrations. This is resulted due to higher possibility of non-radiative transitions such as cross relaxation and resonance energy transfer of shorter average distance between Dy^{3+} ions in glass matrix [35]. The PL quenching effect becomes more prominent when the interaction between ions are stronger as a result of the smaller distance between Dy^{3+} ions.

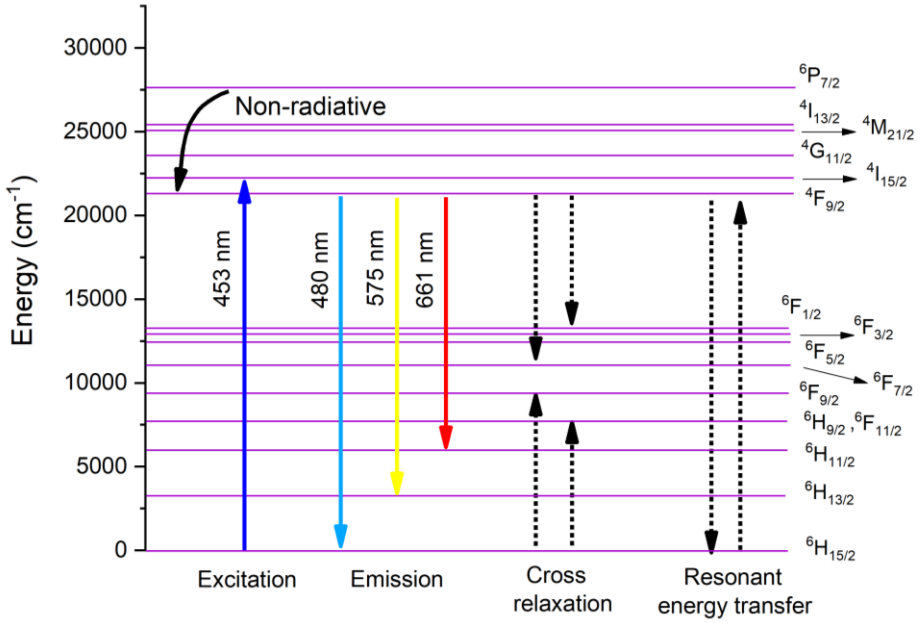


Figure 3.8 Partial energy level diagram of Dy^{3+} ion

Hypersensitive transition located at 575 nm obeys the selection rule $\Delta L = \pm 2$ and $\Delta J = \pm 2$. Hypersensitive transitions significantly interact with the ligand environment and dominate other emission transitions [104]. Partial energy diagram of Dy^{3+} ion in TWLD glasses are shown in Figure 3.8. In general, transitions between $^6P_{7/2}$ and $^4F_{9/2}$ exhibit non-radiative nature as the ion jumps to its lower energy levels without emitting any radiation due to small energy gaps between the energy levels. Transitions of Dy^{3+} ions from $^4F_{9/2}$ to lower energy levels such as $^6H_{15/2}$, $^6H_{13/2}$ and $^6H_{11/2}$ emitting radiations of wavelength at 480, 575 and 661 nm cause yellow, blue and red emissions, respectively. The possible non-radiative transition modes of Dy^{3+} ions such as resonant energy transfer and the cross-relaxation channels are also depicted in Figure 3.8. The non-radiative transition modes are resulted due to the strong interaction among the Dy^{3+} ions when the separation between the ions decreases.

The luminescence behavior of TWLD glasses was also evaluated in terms of radiative properties. Accordingly, the radiative transition probability, A_R, branching ratio, β, stimulated emission cross section, σ, optical bandwidth gain, $\sigma \times \Delta\lambda_{eff}$, parameters were calculated and given in Table 3.5. The larger the A_R values, the higher is the probability of Dy^{3+} ions to return from excited level to the ground state: $^4F_{9/2}$ [103]. Taking this into account, it was observed that the

transition between $^4F_{9/2}$ and $^6H_{13/2}$ has greater A_R values among other radiative transitions of Dy^{3+} ion in synthesized glasses. The value of branching ratio of a transition is a measure of attaining stimulated emission.

Table 3.5 Radiative transition probability (A_R), stimulated emission cross-section (σ), optical bandwidth gain ($\sigma \times \Delta\lambda_{eff}$) and calculated ($\beta_{cal}$) and measured ($\beta_{meas}$) branching ratios of Dy^{3+} ion doped TWLD glasses along with some previously reported glass systems

Sample codes	Transitions	A_R (s^{-1})	σ (10^{-21} cm^2)	$\sigma \times \Delta\lambda_{eff}$ (10^{-28} cm^3)	β_{cal}	β_{meas}	Reference
					(10^{-28} cm^3)		
TWLD01	$^4F_{9/2}$ - $^6H_{11/2}$	3.511	0.01	0.66	0.07	0.27	Present work
	$^4F_{9/2}$ - $^6H_{13/2}$	36.403	0.45	13.90	0.63	0.59	
	$^4F_{9/2}$ - $^6H_{15/2}$	8.158	0.11	5.44	0.14	0.08	
TWLD025	$^4F_{9/2}$ - $^6H_{11/2}$	10.367	0.07	1.90	0.07	0.36	Present work
	$^4F_{9/2}$ - $^6H_{13/2}$	103.745	1.52	38.80	0.69	0.62	
	$^4F_{9/2}$ - $^6H_{15/2}$	18.861	0.16	12.32	0.12	0.07	
TWLD05	$^4F_{9/2}$ - $^6H_{11/2}$	19.254	0.14	3.39	0.07	0.34	Present work
	$^4F_{9/2}$ - $^6H_{13/2}$	195.163	3.07	70.12	0.70	0.67	
	$^4F_{9/2}$ - $^6H_{15/2}$	38.558	0.54	24.19	0.13	0.05	
TWLD1	$^4F_{9/2}$ - $^6H_{11/2}$	42.956	0.27	7.34	0.07	0.29	Present work
	$^4F_{9/2}$ - $^6H_{13/2}$	435.326	6.10	151.84	0.71	0.65	
	$^4F_{9/2}$ - $^6H_{15/2}$	86.19	1.75	52.50	0.14	0.04	
TWLD2	$^4F_{9/2}$ - $^6H_{11/2}$	81.365	0.55	13.50	0.06	0.31	Present work
	$^4F_{9/2}$ - $^6H_{13/2}$	839	12.36	284.22	0.70	0.64	
	$^4F_{9/2}$ - $^6H_{15/2}$	184.922	3.21	109.40	0.15	0.07	
TWLD3	$^4F_{9/2}$ - $^6H_{11/2}$	117.586	0.77	19.13	0.06	0.19	Present work
	$^4F_{9/2}$ - $^6H_{13/2}$	1207.64	17.43	401.31	0.71	0.66	
	$^4F_{9/2}$ - $^6H_{15/2}$	260.213	3.82	151.01	0.15	0.05	
Tellurite	$^4F_{9/2}$ - $^6H_{11/2}$	286.33	0.91	16.31	0.081	0.050	[68]
	$^4F_{9/2}$ - $^6H_{13/2}$	2586.05	5.87	82.74	0.730	0.572	
	$^4F_{9/2}$ - $^6H_{15/2}$	669.78	0.69	10.83	0.189	0.378	
Oxyfluoride	$^4F_{9/2}$ - $^6H_{11/2}$	72	-	-	-	0.07	[105]
	$^4F_{9/2}$ - $^6H_{13/2}$	729	-	-	-	0.68	
	$^4F_{9/2}$ - $^6H_{15/2}$	194	-	-	-	0.18	
Phosphate	$^4F_{9/2}$ - $^6H_{11/2}$	29.29	-	-	-	-	[106]
	$^4F_{9/2}$ - $^6H_{13/2}$	268.29	0.880	-	0.71	-	
	$^4F_{9/2}$ - $^6H_{15/2}$	4.84	1.250	-	0.12	-	
Silicate	$^4F_{9/2}$ - $^6H_{11/2}$	98.48	0.7894	-	0.07	0.02	[91]
	$^4F_{9/2}$ - $^6H_{13/2}$	877.78	4.8265	-	0.63	0.62	
	$^4F_{9/2}$ - $^6H_{15/2}$	235.54	0.5837	-	0.17	0.34	
Borate	$^4F_{9/2}$ - $^6H_{11/2}$	-	-	-	-	-	[107]
	$^4F_{9/2}$ - $^6H_{13/2}$	830.7	32.25	-	0.83	0.378	
	$^4F_{9/2}$ - $^6H_{15/2}$	169.9	3.15	-	0.169	0.621	

The β_{cal} and β_{meas} parameters have similar values for electric dipole transition from $^4F_{9/2}$ to $^6H_{13/2}$ since the J–O analysis is more accurate for electric dipole transitions. On the other hand, β values differ from each other for $^4F_{9/2}$ - $^6H_{15/2}$ transition due to the magnetic nature of this dipole transition [103]. β values greater than 0.5 usually refers to high lasing power properties [108]. The branching ratio of the emission transition from $^4F_{9/2}$ to $^6H_{13/2}$ of all TWLD glasses were found to be higher than 0.5 proving the suitability of synthesized samples for lasing applications.

Furthermore, higher magnitude of σ value indicates lower laser threshold that results in higher ratio of energy extraction for a laser. In addition, $\sigma \times \Delta\lambda_{eff}$ parameter is a useful tool to predict optical amplification ability of rare earth ion doped medium [107]. From all transitions of Dy^{3+} ion, $^4F_{9/2} \rightarrow {}^6H_{13/2}$ transition had the highest emission cross-section and among all concentrations of Dy^{3+} doping, 3 mol% Dy^{3+} doped glass (TWLD3) showed the highest emission cross-section. Consequently, greater values of A_R, β, σ and $\sigma \times \Delta\lambda_{eff}$ parameters for $^4F_{9/2} \rightarrow {}^6H_{13/2}$ transition in TWLD glasses are comparable with other Dy^{3+} doped glasses reported in the literature revealing high potentiality of prepared glasses in this study for lasing and solid-state lighting applications [80].

3.3.7 Colorimetric Properties

Color properties of the emitted light from Dy^{3+} doped glasses were investigated through CIE 1931 chromaticity color coordinates (x, y), color purity, yellow to blue emission intensity ratios (Y/B), CCT and CRI. CIE chromaticity coordinates of Dy^{3+} ion doped TWLD glasses are shown in Figure 3.9 and the calculated colorimetric parameters are given in Table 3.6. As clearly seen from Figure 3.9, color coordinates of TWLD01 and TWLD025 samples are very close to the equal energy point (x=0.33, y=0.33). Emission at yellow region (575 nm) is highly affected by the local environment due to its hypersensitivity. In general, it is known that hypersensitive transitions suppress other transitions. Thus, color coordinates shifted towards the yellow region of the CIE diagram with increasing Dy_2O_3 content since the intensity of yellow emission increased excessively above 0.25 mol% Dy^{3+} content, however the blue emission was suppressed and showed a lower increase in intensity. Therefore, only lower Dy^{3+} doping rates resulted color coordinates closer to the pure white light. This phenomenon could be

explained due to the inhomogeneous spectral power distribution and hypersensitivity of the emission at yellow region which is the main reason behind the failure of reaching pure white light. Improvement in color properties could be achieved by several factors, e.g. using a higher pumping power excitation source and co-doping with different rare earth elements or nanoparticles [42, 44, 46, 54, 109-118].

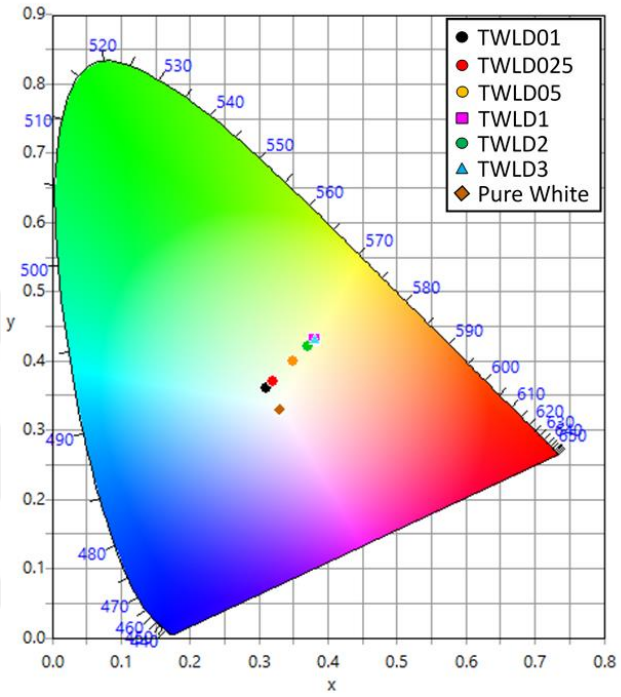


Figure 3.9 CIE chromaticity coordinates of Dy^{3+} ion doped TWLD glasses

Additionally, Figure 3.2b is given to reveal the photoluminescence behavior of TWLD glasses under blue light in a dark room. From Figure 3.2b, it can clearly be observed that all glasses doped with Dy^{3+} show white light emission except for TWL base glass composition with no rare-earth ion addition.

Color purity of the standard white light is 0% [28]. Therefore, color purity values should be as low as possible to achieve pure white emission. In this work, TWLD01 and TWLD025 samples exhibited the lowest color purity values among all prepared samples as 7.2 and 12.2, respectively. Moreover, an increment in color purity values was observed with increasing Dy_2O_3 content due to the yellow shift of the emission. Y/B ratio values of glass samples were found to lie in the range of 1.18 to 2.46 indicating the possibility of white light generation upon blue

excitation [58]. Furthermore, TWLD01 and TWLD025 samples showed Y/B ratios that are very close to unity representing white light generation.

Table 3.6 Colorimetric properties of TWLD glasses along with some other Dy^{3+} doped glasses

Sample codes	x	y	CCT (K)	CRI	Purity (%)	Y/B	Reference
TWLD01	0.31	0.36	6325	58	7.2	1.18	Present work
TWLD025	0.32	0.37	5660	42	12.2	1.35	Present work
TWLD05	0.35	0.40	4810	22	28.5	1.97	Present work
TWLD1	0.38	0.43	4221	7	44.8	2.40	Present work
TWLD2	0.37	0.42	4378	11	39.6	2.28	Present work
TWLD3	0.38	0.43	4217	8	45.9	2.46	Present work
TSWD2	0.35	0.40	4917	-	-	1.51	[68]
BTLND2D	0.39	0.45	4034	-	-	1.88	[100]
2DZTFB	0.36	0.41	4610	-	-	1.07	[33]
TeWLi	0.34	0.39	5261	-	-	1.45	[92]
TTWD01	0.33	0.38	-	-	-	1.93	[36]
Silicate	0.41	0.42	4344	-	-	1.66	[91]
Borate	0.28	0.32	-	-	-	0.5	[107]

Commercial white LEDs are usually delivered with CCT and CRI ratings for better understanding of their color properties by end-users [91]. The CCT of a light source is quantified as the surface temperature (K) of an ideal blackbody that emits light having the same color tint as the light source. CCT values that calculated in this study were found in the range of 4217-6325 K referring to natural daylight (3500-6500 K). CRI is the ability of the light source to make colors look natural and it takes values in the range of 0 to 100. Thus, incandescent lamps and natural daylight have the best CRI values (accepted as 100). CRI values of synthesized glasses in this study were relatively low due to the inhomogeneous spectral power distribution and absence of red emission. In Table 3.6, the colorimetric properties of synthesized glasses were compared with other glass

systems reported in the literature and it was observed that glasses prepared in this study showed comparable or better colorimetric properties. Thus, these glasses have potentiality to be used as luminescent material for white LEDs.

Table 3.7 Calculated (τ_{cal}) and measured (τ_{meas}) lifetime, quantum efficiency (η) and non-radiative transition rate (W_{NR}) values of Dy^{3+} ion doped TWLD glasses along with some previously reported glass systems

Sample codes	τ_{cal} (μs)	τ_{meas} (μs)	η (%)	W_{NR} (s^{-1})	Reference
TWLD01	2017	257	12	3395	Present work
TWLD025	772	229	29	3071	Present work
TWLD05	419	200	47	2613	Present work
TWLD1	190	168	88	689	Present work
TWLD2	98	60	61	6462	Present work
TWLD3	75	45	60	8888	Present work
TSWD2	282	195	69	1582	[40]
HGT-Dy-0.1	-	279	62	1367	[22]
0.5DPTFB	-	230	46	2368	[70]
Oxyfluoride	938	472	50	1052	[77]
Phosphate	584	420	71	668	[78]
Silicate	773	573	74	451	[61]
Borate	999	162	16	5171	[79]

3.3.8 Decay Profiles

The PL lifetime decay profiles of Dy^{3+} doped glasses were obtained by monitoring an excitation at 453 nm and an emission at 575 nm related to the transition from $^4F_{9/2}$ to $^6H_{13/2}$. Figure 3.10 illustrates the logarithmic plots of normalized decay profiles of Dy^{3+} ion doped TWLD glasses. Recorded decay profiles showed single exponential behavior up to 0.5 mol% Dy^{3+} doping (TWLD05) and then changed to non-exponential behavior for higher Dy^{3+} doping rates. The non-exponential behavior became more prominent with increasing Dy^{3+} ion concentration due to the increasing energy transfer between donor and acceptor ions in glass structure.

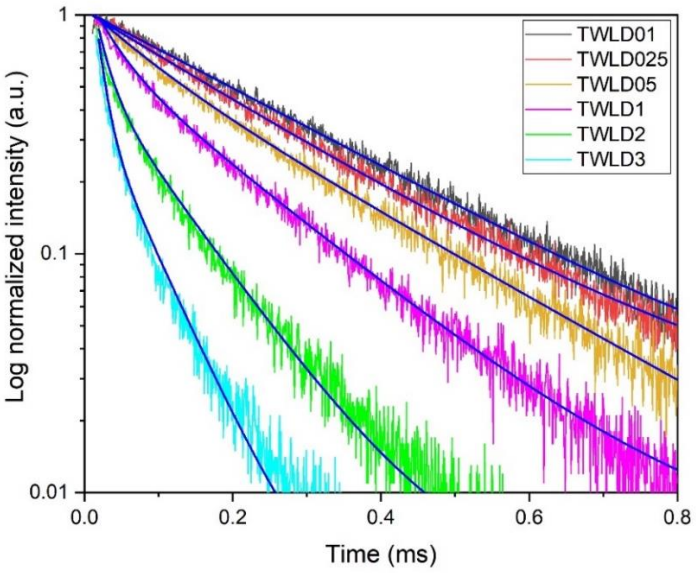


Figure 3.10 Decay rates for the transition from $^4F_{9/2}$ to $^6H_{15/2}$ in Dy^{3+} ion doped TWLD glasses

The calculated values of lifetime, quantum efficiency and non-radiative transition rate of Dy^{3+} ion doped TWLD glasses are given in Table 3.7 along with some previously reported glass systems. Increasing rate of cross-relaxation between Dy^{3+} ions resulted a decrement in τ_{cal} and τ_{meas} values [100]. Additionally, τ_{cal} values were found greater than τ_{meas} values and this behavior was attributed to the non-radiative cross-relaxation or multi-phonon relaxation of Dy^{3+} ions [33]. W_{NR} values decreased up to 1 mol% Dy^{3+} ion content and then increased for higher doping rates. The reason for obtaining weaker emission bands in photoluminescence analysis for TWLD2 and TWLD3 samples was also related to the higher W_{NR} values. On the contrary, the value of η increased up to 1 mol% Dy^{3+} ion concentration and then decreased for higher Dy^{3+} doping concentrations [80]. Consequently, lifetime, quantum efficiency and W_{NR} values of glasses prepared in this study were found to be comparable with other Dy^{3+} doped glasses reported in literature indicating the potentiality of TWLD glasses as solid-state lighting materials.

3.4 Conclusions

In summary, glasses with $50TeO_2$-$25WO_3$-$25Li_2O$ mol% composition were doped with various amount of Dy_2O_3 (from 0.1 to 3 mol%) to investigate the effect of Dy^{3+} on physical, thermal, structural and optical spectroscopy properties of

tellurite glasses. All glasses were obtained optically clear and transparent and transmittance values were found around 75% independent from the composition. Physical and structural properties did not show a significant change with varying concentration. However, density, molar volume and oxygen molar volume values showed a slight increase, while oxygen packing density values decreased with increasing Dy^{3+} content. Therefore, the increment of Dy^{3+} ion content was attributed to the formation of excess free volume resulting less tightly packing of the glass network. FTIR analysis confirmed the presence of TeO_4, TeO_3, TeO_{3+1}, WO_4, WO_6 structural units and formation of Dy–O linkages in the glass structure. All glasses showed suitable thermal properties with high glass stability values ranging from 127 to 170 °C. Photoluminescence studies showed that $^4F_{9/2} \rightarrow {}^6H_{13/2}$ transition (575 nm) possesses the highest radiative properties such as A_R, σ, β and $\sigma \times \Delta\lambda_{eff}$ for all glasses. In addition, luminescence quenching effect was observed at above 1 mol% Dy^{3+} ion concentrations. Among all studied glass compositions, TWLD01 (x=0.31, y=0.36) and TWLD025 (x=0.32, y=0.37) samples revealed the closest CIE color coordinate values to pure white light coordination and they also showed the lowest color purity and highest CCT and CRI values indicating good potentiality to be used as luminescent material for WLED applications. Consequently, the obtained optical spectroscopy results in this study were found to be comparable or better compared to other glass systems in the literature and it was concluded that for an improved color property, quantum efficiency and non-radiative transition rate in this glass system, lower Dy_2O_3 content would be necessary.

4
ROBUST $CsPbBr_3$ AND CdSe / Dy^{3+}+CdSe QUANTUM DOT DOPED GLASS NANOCOMPOSITE HYBRID COUPLING AS COLOR CONVERTER FOR SOLID-STATE LIGHTING APPLICATIONS

O. Kıbrıslı, E. Erol, M. Çelikbilek Ersundu, and A. E. Ersundu, "Robust $CsPbBr_3$ and CdSe / Dy^{3+}+CdSe quantum dot doped glass nanocomposite hybrid coupling as color converter for solid-state lighting applications," *Chemical Engineering Journal,* vol. 420, p. 130542, 2021.

4.1 Introduction

In the last decade, tremendous attention has been devoted to the research on solid-state lighting devices, especially white-light-emitting diodes (WLEDs), due to their favorable properties such as long lifetime, high efficiency, and environmental friendliness [119, 120]. Conventional WLEDs are generally structured by combination of blue LED chips and phosphor materials i.e., yellow emitting YAG:Ce^{3+} [121]. However, low chemical and thermal stability of phosphor materials along with low color rendering index (CRI) values due to lack of red emission triggered researchers to integrate quantum dots (QDs) into the solid-state lighting applications [122]. Facile emission wavelength tunability through band gap engineering and high photoluminescence (PL) quantum yield (QY) values are among advantageous optoelectronic features of QDs that make them promising materials for laser [123], solar cell [124], sensor [125], biological imaging [126], display [127, 128], and solid-state lighting applications [129]. However, high surface energy of colloidal QDs results in exalted vulnerability against temperature, air, and water that limits and hinders their consolidation with practical applications as commercial products [130]. Therefore, numerous encapsulation and surface modification methods have been developed to overcome stability issues of various QDs [131-135]. Despite the fact that colloidal

$CsPbX_3$ (X=Br^-, Cl^-, I^-) perovskite QDs and IIB-VIA (CdSe, ZnSe, CdS, ZnS, ZnTe and CdTe) QDs are widely investigated, long term stability with ideal emission properties have not been achieved yet. At this point, glasses step forward as promising encapsulation media for optically active QDs due to their excellent thermal and chemical stability providing reliable protection to favorable emission properties [136, 137]. So far, $CsPbBr_3$ and CdSe QDs have been successfully synthesized in different glass systems such as phosphate [138, 139], silicate [140, 141] and tellurite [142, 143], in which the effect of glass host on luminescence properties of QDs as well as their chemical and thermal stabilities have been investigated in detail. However, the main limitation of tellurite-based systems are high-cost due to expensive raw materials [144], while the poor chemical and thermal stability of phosphate glasses [130, 145] remain as an obstacle to the long-term durability of QDs. The silicate glass systems, on the other hand, generally offer the highest thermal, chemical, and mechanical stability features [146, 147]. $CsPbX_3$ QDs embedded glasses have already been demonstrated as promising spectral converters for WLEDs [142, 144, 148]. Efficient green emission can be obtained from $CsPbBr_3$ QDs (PLQY: ~85 %), while it is still challenging to obtain high efficiency red emission using $CsPbI_3$ perovskite QDs (PLQY: ~5 %) [130, 149]. Red emission can also be generated using ceramic based phosphor materials such as $CaAlSiN_3:Eu^{2+}$. However, optical transparency of these ceramic-based materials is quite far from meeting the expectations of LED standards [121]. Another approach would be using CdSe QDs as red emission source along with $CsPbBr_3$ QDs to achieve ideal white light due to reddish broadband emission of CdSe QDs originating from surface defects when they are embedded in glass matrices. Even tough broadband emission is a favorable feature to acquire high CRI values, it has a strong negative effect on PLQY values of CdSe QDs [150]. Therefore, CdSe/$Cd_{1-x}Zn_xSe$ core/shell structures are successfully engineered in glass matrices to enhance PLQY values by Xia et al. [137, 151] and Han et al. [152] revealing their potential to be used as luminescent materials in solid-state lighting applications. Since constructing core/shell structures in a dense medium, i.e., glass, is a more challenging task compared to colloidal counterparts, PLQY enhancement in glasses through lanthanide ion doping along with QDs arises as a

simple and promising alternative [153]. In this respect, Dy^{3+} ions are favorable due to $^{6}H_{15/2} \rightarrow {}^{4}F_{9/2}$ (485 nm) transition which triggers radiative energy transfer from Dy^{3+} ions to CdSe ions.

In this work, robust $CsPbBr_3$ and CdSe / Dy^{3+}+CdSe doped glass nanocomposite (GNC) layers exhibiting green and broadband emission covering red end of the visible spectrum (red / yellow), respectively are synthesized, and coupled to be placed on top of a blue LED chip as a proof-of-concept demonstration of two alternative WLED devices. Emission color properties and PLQY values reveal the potential of proposed system in long-term stable solid-state lighting applications with superior opto-electronic properties.

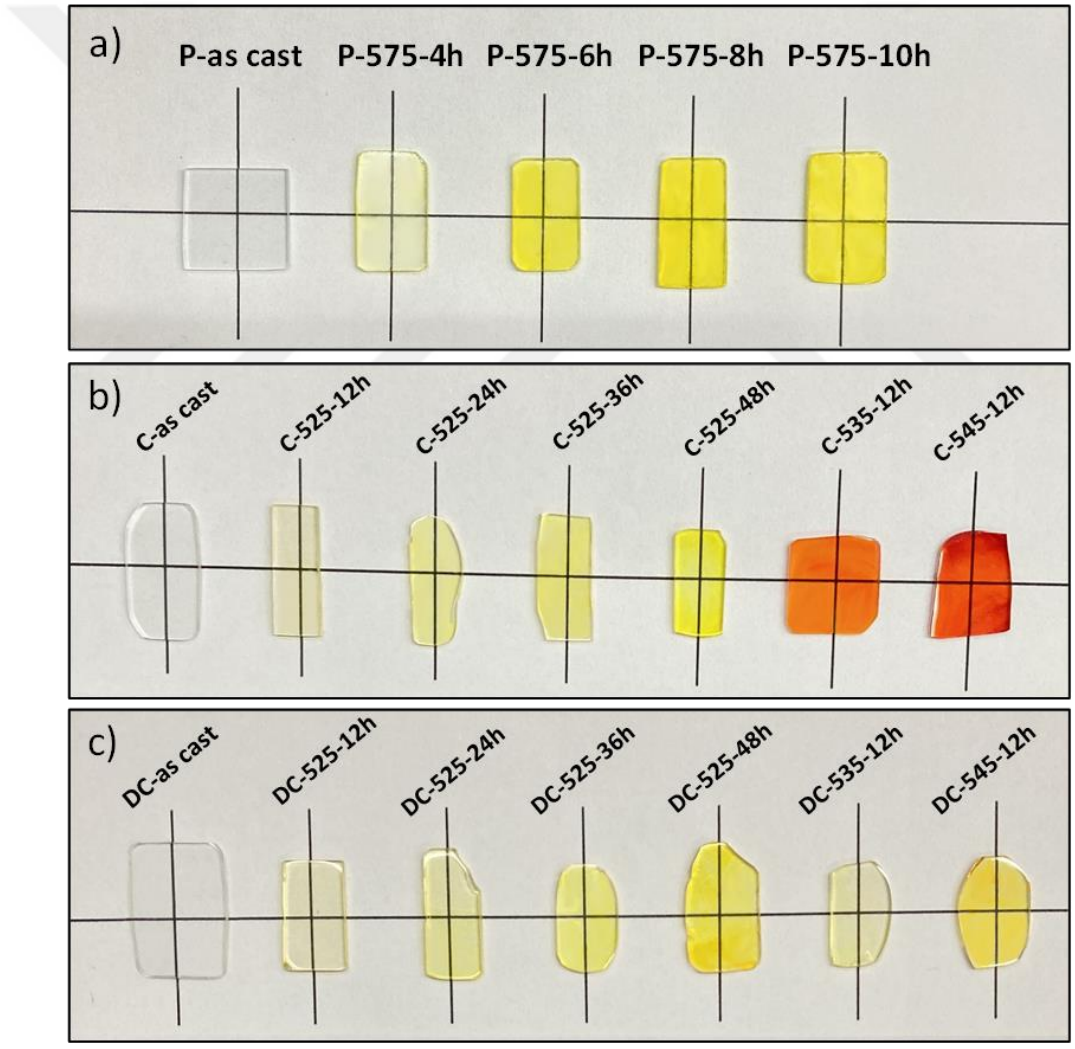


Figure 4.1 Macro photos of a) $CsPbBr_3$, b) CdSe, and c) Dy^{3+}+CdSe doped GNCs along with as-cast samples under daylight

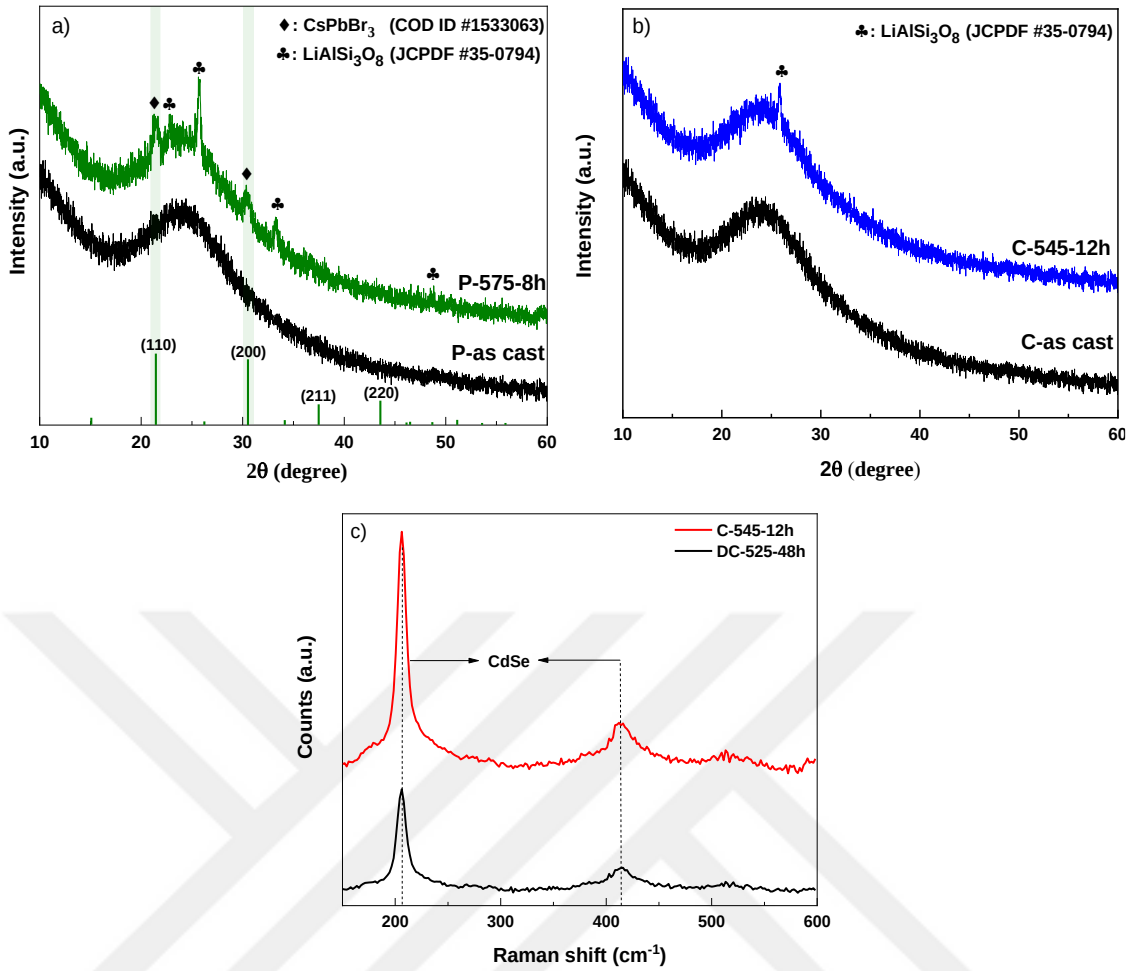


Figure 4.2 XRD patterns of a) P-575-8h and b) C-545-12h samples, c) Raman spectra of C-545-12h and DC-525-48h samples

4.2 Experimental procedure

In this work, a special silicate base glass composition is designed for solid-state lighting applications with the chemical composition of $60SiO_2$-$25Li_2O$-$5Al_2O_3$-10ZnO (in mol%). The base glass is then doped with 3CsBr-$6PbBr_2$, 1CdO-0.5ZnSe and $0.25Dy_2O_3$+1CdO-0.5ZnSe (all in mol%) to obtain $CsPbBr_3$, CdSe and Dy^{3+}+CdSe doped glass samples, respectively by using conventional melt-quenching method with analytical grade starting chemicals. The schematic representation of GNC synthesis is given in Figure. A.1. The starting materials are weighed with utmost care using a high precision scale (10^{-4} g) and mixed in an agate mortar using a pestle for 15 min to attain complete homogeneity. Thereafter, batches of 10 g are placed into alumina crucibles and melted at 1350 °C for 10 to 60 min in an electrical furnace. The melts are then poured into

preheated stainless-steel molds and pressed with another steel plate to obtain as-cast samples (see Figure A.1). After melting and rapid cooling, the cations and anions constituting the $CsPbBr_3$ (i.e., Cs^+, Pb^{2+}, Br^-) and CdSe (i.e., Cd^{2+} and Se^{2-}) have no time to bond with each other and are distributed homogeneously in as-cast samples. The as-cast samples are immediately annealed at 350 °C for 3 h to prevent formation of internal stresses originating from rapid cooling. Afterwards, the annealed glass samples are cooled down to room temperature (cooling rate: 1 °C/min) inside the furnace. Subsequently, samples are heat-treated at varying temperatures and durations to produce GNCs. The nucleation and growth of QDs in glass simultaneously occur with the diffusion-controlled heat treatment process, which lowers the energy of QDs embedded glass reaching to a more stable state compared to the metastable glassy state. With the heat treatment process the ions of Cs^+, Pb^{2+}, Br^-, and Cd^{2+}, Se^{2-} gradually diffuse, bond together, and form $CsPbBr_3$ and CdSe QDs, respectively [154]. Heat-treatment temperatures are selected above the glass transition temperature (T_g) and below the crystallization onset temperature (T_c) of base glass that are determined from the DTA analysis at around 460 °C and 586 °C, respectively (see Figure A.2). Finally, the obtained samples are undergone grinding and polishing processes to obtain high quality surfaces and to fix their thickness at 0.9 mm. Samples are coded according to the incorporated dopants (P: $CsPbBr_3$, C: CdSe, and DC: Dy^{3+}+CdSe) and heat-treatment conditions (temperature °C – duration h). Macro photos of prepared samples are shown in Figure 4.1 along with their codes.

25±1 mg of powdered base glass sample is placed in sealed aluminum pan to realize differential scanning calorimetry (DSC) measurements using Netzsch DSC-204F1 with a heating rate of 10 °C/min under argon gas atmosphere. Phase analysis of selected samples are conducted through X-ray diffraction (XRD) analysis using a Philips/PANalytical X'pert Pro diffractometer. The average wavelength of Cu $K\alpha_1$ and Cu $K\alpha_2$ radiations (λ = 1.5418 Å) is used at 45 kV and 40 mA in the 2θ range from 10 to 80° with a scanning step size of 0.02°. Raman analysis are realized in Renishaw Invia Raman microscope under 532 nm laser excitation in the 150-600 cm^{-1} wavenumber range. Absorbance spectra are recorded in the UV-Vis region between 300 and 700 nm with a resolution of 1 nm

in Edinburgh Instruments FS5 spectrofluorometer. Steady-state/time resolved photoluminescence (PL) and absolute quantum yield (PLQY) measurements are also conducted by using the same spectrofluorometer (equipped with 150 W xenon lamp) in the wavelength range of 420-900 nm with a signal to noise ratio of water Raman signal >6000:1 and 0.5 nm spectral resolution. After meticulous excitation-emission mapping studies (see Figure A.8), PLQY values are measured at 345 nm (optimal excitation wavelength for QDs with the highest PLQY values) in an integrated sphere (150 mm internal spherical cavity, politetrafloroetilen coated). The PLQY values are characterized with an estimated error rated of ± 5% via the following equation [129]:

$$PLQY = \frac{number\ of\ emitted\ photons}{number\ of\ absorbed\ photons} = \frac{L_{sample}}{E_{reference} - E_{sample}} \tag{4.1}$$

where $E_{reference}$ and E_{sample} are the scattering intensities of excitation light not absorbed by reference and sample, respectively, L_{sample} is emission intensity obtained by integrating the area under calibrated emission spectra. Blank samples are used to obtain references values. The number of absorbed photons is defined by the difference in scattering integrated areas between reference and sample. External quantum efficiency (EQE) values are calculated as the ratio of number of photons emitted and number of electrons injected. The recorded decay curves are fitted using bi-exponential equation to achieve the converging χ^2 values to unity as formulated below:

$$I(t) = A_1 e^{\left(\frac{-t}{\tau_1}\right)} + A_2 e^{\left(\frac{-t}{\tau_2}\right)}, \tag{4.2}$$

where, $I(t)$ defines the emission intensity, τ_1 and τ_2 are the lifetime values and A_1 and A_2 are decay constants. Average lifetime of each transition is calculated using the following expression:

$$\tau_{meas} = \frac{A_1\tau_1^2 + A_2\tau_2^2}{A_1\tau_1 + A_2\tau_2} \tag{4.3}$$

Temperature dependent PL measurements up to 275 °C are carried out by placing a heated solid transmission apparatus from Pike Technologies in the spectrofluorometer. Photostability measurements are conducted using 442 nm He-Cd laser, 1/8 m spectrograph, TE cooled CCD and 600 Line/mm grating setup. Direct band gaps (E_g) of GNCs are calculated through $(\alpha\hbar\omega)^2$ vs $\hbar\omega$ plots according to Tauc relation by extrapolating linear part of the plots where $\hbar\omega$ is photon

energy and α is absorption coefficient (see Figure A.3, Figure A.4 and Figure A.5). The size of $CsPbBr_3$ and CdSe QDs formed in GNCs are estimated through effective mass approximation (EMA) according to the following relation [129, 155]:

$$E_g(r) = E_{g,bulk} + \frac{h^2}{8r^2}\left(\frac{1}{m_e^*} + \frac{1}{m_h^*}\right) - \frac{1.8e^2}{4\pi\varepsilon_0\varepsilon_r r}, \quad (4.4)$$

where, $E_{g,bulk}$ (CdSe: 1.74 eV, $CsPbBr_3$: 2.3 eV) is the bulk band gap, r is nanoparticle radius, m_e^* (CdSe: $0.13m_e$, $CsPbBr_3$: $0.15m_e$) and m_h^* (CdSe: $0.45m_e$, $CsPbBr_3$: $0.14m_e$) are effective mass of electron and hole, respectively, ε_0 is the vacuum permittivity, ε (CdSe: 9.53, $CsPbBr_3$: 4.797) is relative permittivity, $\hbar$ is Planck's constant and e is charge of the electron. Additionally, particle size of CdSe QDs are also estimated by another theoretical model proposed by Yu et al. as given below to confirm results obtained through EMA method:

$$D = (1.6122 \times 10^{-9})\lambda^4 - (2.6575 \times 10^{-6})\lambda^3 + (1.6242 \times 10^{-3})\lambda^2 - (0.4277)\lambda + (41.57), \quad (4.5)$$

where D is particle diameter and λ is the center wavelength of first excitonic absorption peak [156]. Colorimetric properties such as, color coordinates, CRI, correlated color temperature (CCT) and color purity values are calculated via OSRAM ColorCalculator software. Luminous efficacy values (LER) are calculated according to the following equation [157]:

$$LER = \left(683\frac{lm}{W_{opt}}\right)\frac{\int P_{opt}(\lambda)v(\lambda)d\lambda}{P_{opt}(\lambda)d\lambda}, \quad (4.6)$$

where (v) is eye sensitivity function, P_{opt} (λ) is spectral density.

4.3 Results and discussion

4.3.1 Structural and thermal analysis

XRD measurements are performed to check the amorphous nature of as-cast samples and to identify the crystallized phases in selected GNCs (see Figure 4.2). Typical broad halos appearing in the XRD patterns of as-cast samples verify the amorphous structure of glasses. As given in Figure 4.2a, after heat-treatment of $CsPbBr_3$ doped glasses at 575 °C for 8 h (P-575-8h sample), definite diffraction peaks at 2θ values of 21.38° and 30.41° superimpose over the amorphous halo and are assigned to (110) and (200) crystalline planes of the cubic $CsPbBr_3$ phase

(COD database code: 1533063). Additionally, further peaks observed at 2θ values of 22.8°, 25.7°, 33.1°, 48.4° are due to the formation of tetragonal $LiAlSi_3O_8$ phase (JCPDS no. 00-035-0794) that crystallizes as a second phase from the base glass composition during heat treatment. $LiAlSi_3O_8$ — a type of β-quartz phase — is already reported to exhibit some superior properties such as low thermal expansion coefficient, high thermal durability, good mechanical strength, and transparency in Li_2O-Al_2O_3-SiO_2 based glass-ceramics [158, 159]. Therefore, formation of such crystalline phase would be beneficial as long as it does not hinder the transparency of GNCs. Figure 4.2b shows XRD pattern of selected CdSe doped glass (C-545-12h) after heat-treatment at 545 °C for 12h. However, presence of CdSe could not be detected via XRD analysis possibly due to extremely small amount of dopant ratio. Furthermore, compared to $CsPbBr_3$ doped sample due to lower heat-treatment temperature only a single peak appears at 2θ value of 22.8° corresponding to the tetragonal $LiAlSi_3O_8$ phase resulting from the crystallization of base glass. Therefore, detection of CdSe QDs are realized through Raman analysis and recorded spectra for selected samples (C-545-12h and DC-525-48h) are given in Figure 4.2c. Characteristic Raman shift peak originated from longitudinal optical (LO) mode of CdSe QDs and its overtone appear for both selected samples at 206 cm^{-1} and 412 cm^{-1}, respectively. Intensity of Raman peaks are higher in C-545-12h sample compared to DC-525-48h sample due to formation of larger CdSe QDs upon higher heat-treatment temperature. Absence of Raman shift peak of Se^{2-} at around 320 cm^{-1} indicates that majority of Se atoms involve in the formation of CdSe QDs. Doubled doping ratio of CdO (1 mol%) compared to ZnSe (0.5 mol%) in the glass composition plays a key role in the aforementioned situation as denoted by Lee et al. [160]. Authors also performed significant effort to provide TEM analysis results for the confirmation of QDs in GNCs. However, non-conductive nature of glass samples and significant amount of Li_2O content in the glass composition caused unwanted crystallization reactions under high energy electron beam and ultimately hindered to obtain reliable results.

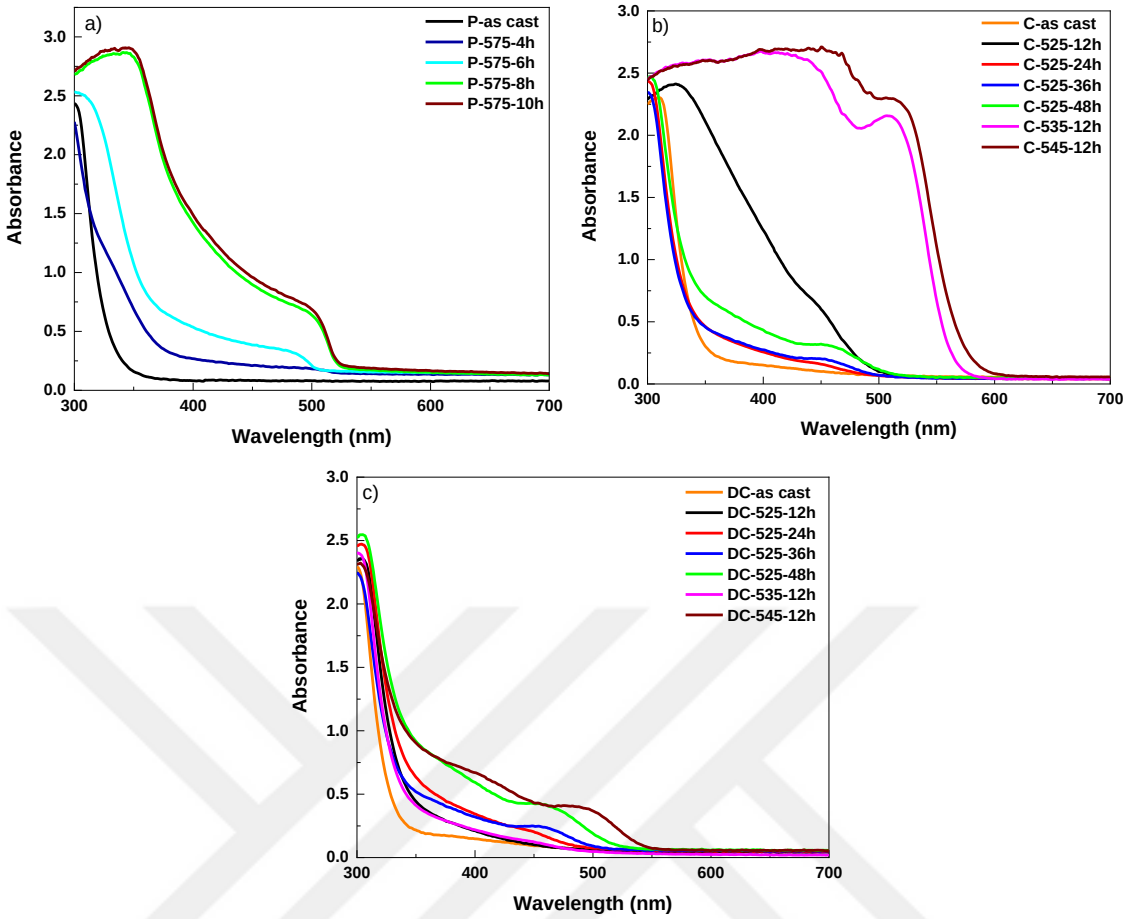


Figure 4.3 Optical absorption spectra of a) $CsPbBr_3$, b) CdSe, and c) Dy^{3+}+CdSe doped GNCs along with as-cast samples

4.3.2 Optical properties and particle size determination

Optically clear and highly transparent glasses obtained after casting and annealing processes reveal the absence of QDs before heat-treatment (see Figure 4.1). In general, GNCs demonstrate a color change with increasing heat-treatment temperature and duration, i.e., from pale yellow to vivid yellow for $CsPbBr_3$ doped samples and from pale yellow to red for CdSe doped samples with a dramatic color shift at heat-treatment temperatures higher than 525 °C. Dy^{3+}+CdSe doped samples also change their color with respect to varying heat-treatment condition. However, with the incorporation of Dy^{3+} ions only yellow color is observed even for high temperatures and longer durations. The color change has a direct impact on absorption spectra and the position of absorption edge of GNCs as depicted in Figure 4.3. Characteristic ground state excitonic transition of $CsPbBr_3$ and CdSe QDs due to formation of electron-hole pairs induced by photons are detected in

GNCs. Center wavelengths of the absorption bands are determined in the range of 486-498 nm and 449-515 nm for $CsPbBr_3$ and CdSe QDs, respectively (see details in Table 4.1). However, P-575-4h, DC-525-12h, and DC-535-12h samples do not show any detectable peaks due to insufficient heat-treatment conditions i.e., lesser temperature or duration. Notably, gradual red shift of the center wavelengths confirms the increasing size and decreasing band gap of formed QDs. Band gap values are calculated in the range of 2.33-2.37 eV and 2.22-2.60 eV for $CsPbBr_3$ and CdSe QDs, respectively (see Table 4.1). Blue shifted band gap values confirm the strong quantum confinement effect since the bulk band gap energy of $CsPbBr_3$ and CdSe QDs are 2.3 eV (539 nm) and 1.73 eV (716 nm), respectively [72-74]. The average particle size calculation for $CsPbBr_3$ and CdSe QDs in GNCs are realized using EMA method (see Table 4.1). Average radii of QDs in $CsPbBr_3$ doped GNCs are found to lay in the range of 5.63-6.98 nm. $CsPbBr_3$ QDs are more sensitive to heat-treatment conditions compared to CdSe QDs. Therefore, heat-treatments are applied in a narrower duration range with 2h intervals to obtain desired emission color properties and quantum yield values. The radii of QDs in CdSe doped GNCs gradually increase from 2.04 to 2.23 nm with increasing duration for the samples heat-treated at 525°C. Moreover, radii of CdSe QDs dramatically increase to 2.70 and 2.79 nm for samples heat-treated at temperatures of 535°C and 545°C, respectively. On the other hand, average radii of QDs in Dy^{3+}+CdSe doped samples range between 2.08 and 2.52 nm. When Dy^{3+} ions are introduced to GNCs, CdSe QDs form in a smaller size under the same heat-treatment conditions. This is possibly due to increasing number of bonds per unit volume with the incorporation of Dy_2O_3 that ultimately results slowing down the crystallization process [26]. Another theoretical model proposed by Yu et al. [67] is applied to confirm estimated radii of QDs in CdSe and Dy^{3+}+CdSe doped GNCs and calculations show that both approaches are in a good match with slight differences for larger particles as depicted in study of Rodríguez-Mas et al. [75].

Table 4.1 First excitonic absorption peak center wavelengths, band gap and particle radii values for prepared GNCs

Samples	First Excitonic Absorption Peak (nm)	Band gap (eV)	Particle Radius, EMA (nm)	Particle Radius, Yu model (nm)
C-525-12h	450	2.60	2.04	2.10
C-525-24h	452	2.57	2.08	2.11
C-525-36h	454	2.53	2.14	2.13
C-525-48h	463	2.47	2.23	2.18
C-535-12h	510	2.25	2.70	2.50
C-545-12h	515	2.22	2.79	2.54
DC-525-12h	N/A	N/A	N/A	N/A
DC-525-24h	449	2.57	2.08	2.09
DC-525-36h	462	2.49	2.20	2.17
DC-525-48h	465	2.33	2.49	2.19
DC-535-12h	N/A	N/A	N/A	N/A
DC-545-12h	495	2.32	2.52	2.39
P-575-4h	N/A	N/A	N/A	N/A
P-575-6h	486	2.37	5.63	N/A
P-575-8h	491	2.34	6.54	N/A
P-575-10h	498	2.33	6.98	N/A

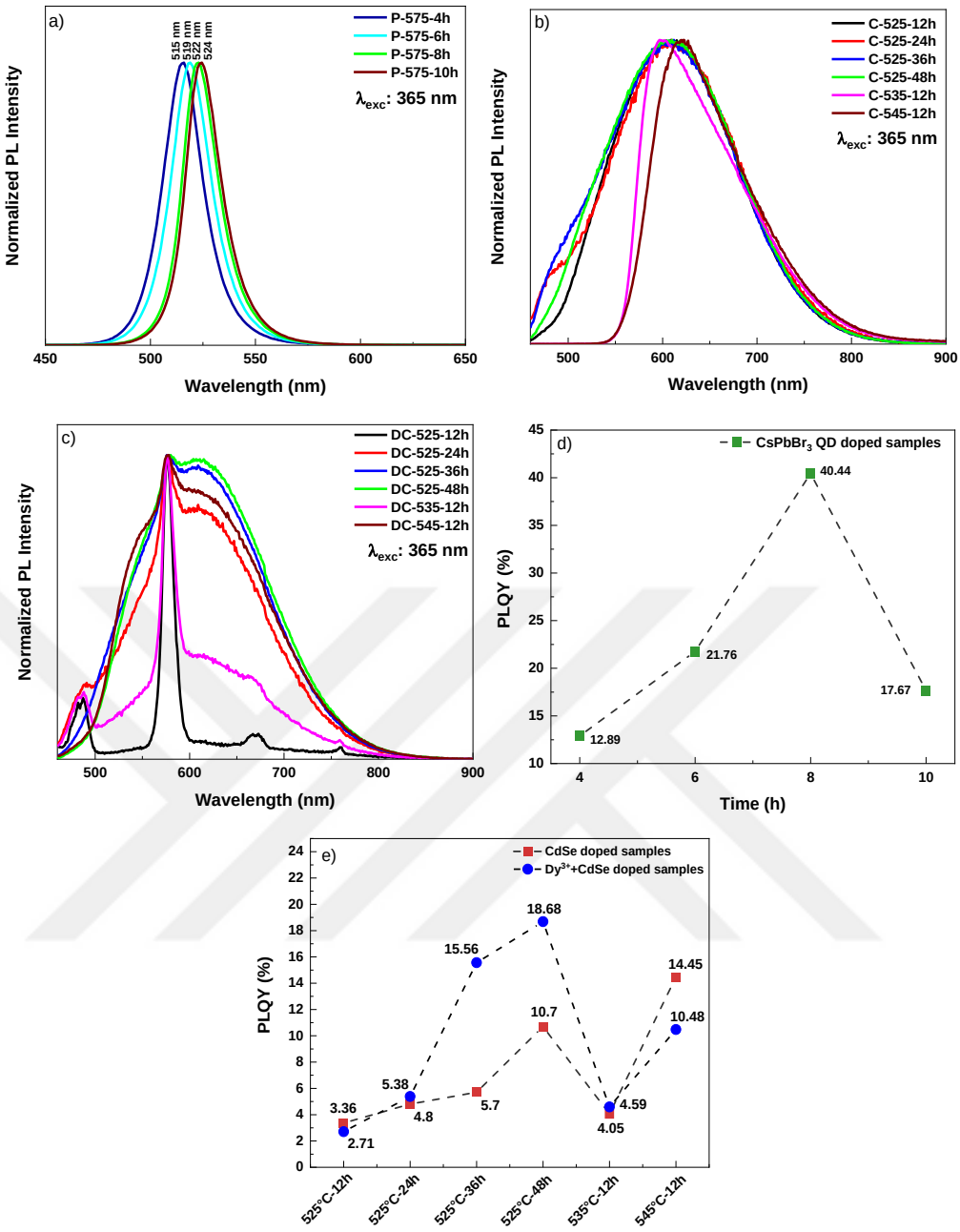


Figure 4.4 Room temperature PL spectra and PLQY values of a,d) $CsPbBr_3$, b,e) CdSe and c,e) Dy^{3+}+CdSe doped GNCs, respectively

4.3.3 Photoluminescence properties

PL spectra of prepared GNCs are given in Figure 4.4. All PL curves are normalized to provide better comparison. Emission bands of $CsPbBr_3$ QDs doped GNCs show narrow FWHM values. FWHM values gradually decrease from ~ 27 nm to ~ 22 nm and peaks of the PL bands show a slight red shift from 519 nm to 524 nm upon increasing heat-treatment duration. These tunable PL spectra along with a narrow FWHM value reveal that $CsPbBr_3$ perovskite QDs doped GNCs can emit high color

purity green light (see Figure 4.5). CdSe doped GNCs heat-treated at 525 °C for different durations demonstrate broad emission bands centered at around 608 nm with FWHM values in the range of 157-167 nm due to inhomogeneous size distribution and surface defects. When the heat-treatment temperature rises to 535 °C and 545 °C, peaks with central wavelengths of 599 and 622 nm, respectively exhibit a more asymmetrical form. FWHM values of emission bands reduce to 116 and 111 nm for 535 °C and 545 °C, respectively due to narrower size distribution of CdSe QDs formed in GNCs at elevated heat-treatment temperatures. The highest FWHM value is calculated for DC-525-48h sample as 163 nm amongst Dy^{3+}+CdSe doped samples. Emission bands of Dy^{3+} ions at 485, 575, 670 and 759 nm wavelengths are significantly visible in DC-525-12h sample. However, these emission bands fade away gradually when heat-treatment temperature and/or duration increases. Only the emission band at 575 nm remains visible at relatively higher temperatures and durations. Interestingly, the peak at 485 nm becomes invisible when duration hits 36h at 525 °C and 12h at 545 °C. This behavior is possibly observed due to sufficient formation of CdSe QDs to absorb Dy^{3+} emission strongly at 485 nm. Close first excitonic absorption peak center wavelength values of CdSe QDs also confirm this behavior.

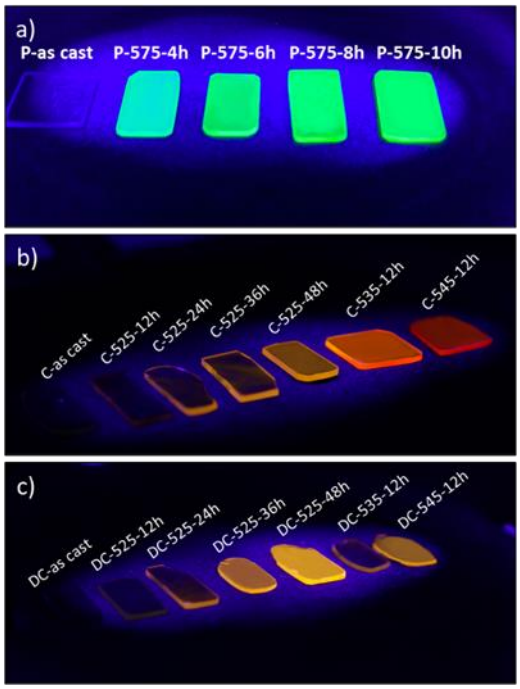


Figure 4.5 Macro photos of a) $CsPbBr_3$ b) CdSe and c) Dy^{3+}+CdSe doped GNCs along with as-cast samples under UV LED excitation

Absolute PLQY values of GNCs are given in Figure 4.4d and 4.4e. For $CsPbBr_3$ QDs doped GNCs absolute PLQY values ranging between 12-40% are obtained for different heat-treatment durations (see Figure 4.4d). The P-575-4h sample shows the lowest PLQY value (12.89%) indicating that shorter heat-treatment time could not provide sufficient activation energy for the complete crystallization of $CsPbBr_3$ QDs. Distinctly, the P-575-8h sample has the maximum PLQY value (44.44%). However, further increment of heat-treatment duration results in a decrease of PLQY value (17.67%) for P-575-10h sample. This may be attributed to the deformation of the $CsPbBr_3$ QDs as heat treatment exceeds a certain time. The obtained PLQY values in this work are in the same range or better compared to previously reported similar studies [50, 54]. For CdSe and Dy^{3+}+CdSe doped samples heat-treated at 525 °C, an increment in PLQY values is observed when heat-treatment duration rises from 12h to 48h. The dramatic rise in PLQY values between 24h and 36h for Dy^{3+}+CdSe doped samples is possibly due to radiative energy transfer from Dy^{3+} ions to CdSe QDs as there is no similar sign for CdSe doped samples. However, increasing heat-treatment temperature to 535 °C for 12h does not reveal a significant change in PLQY for both samples. This indicates that shorter heat-treatment time could not provide sufficient activation energy for complete crystallization of QDs unless the temperature is raised to 545 °C. Hence, maximum PLQY values of 14.45% and 18.68% are obtained for C-545-12h and DC-525-48h samples, respectively. In other works, Apte et al. [76] calculated PLQY for CdSe QDs in germanate glasses as 21% and Lipatova et al. [77] obtained 15% PLQY in fluorophosphate glasses. Moreover, Han et al. reported that slightly higher PLQY values can be achieved by forming CdS shells around CdSe cores in silicate glasses to overcome notorious surface defects that quench the emission intensity [78, 79]. Obviously, obtained PLQY values for QDs in glass matrices generally fall behind of colloidal systems, which may be due to the interface defects between glass and QDs or formation of structural imperfections in the QDs synthesized by high temperature crystallization route [35, 45]. Since maximum PLQY values are obtained for P-575-8h (40.44%), C-545-12h (14.45%) and DC-525-48h (18.68 %) samples, further studies are realized using these selected GNCs to evaluate their potential in solid state lighting applications.

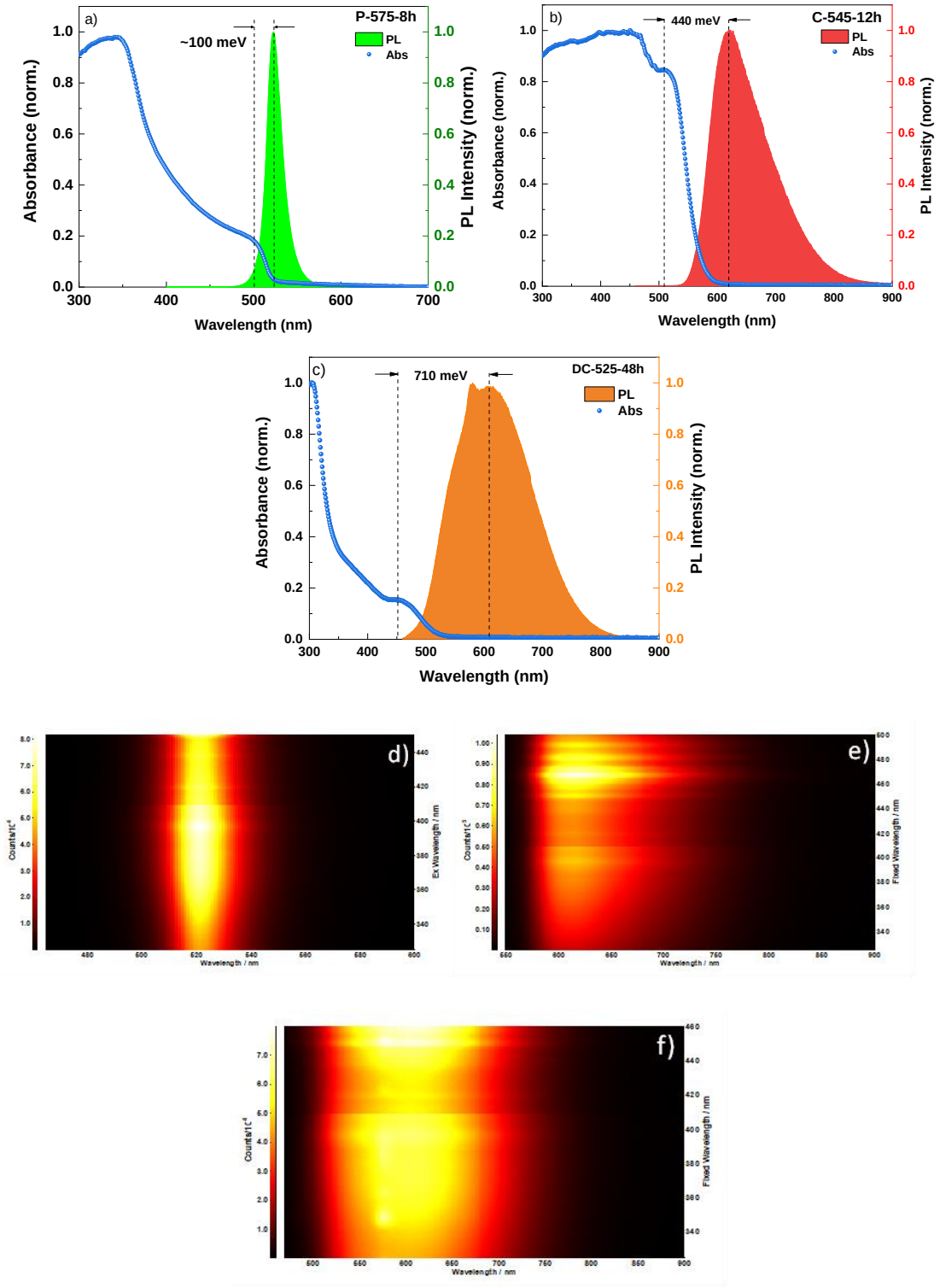


Figure 4.6 (a, b, c) Stokes shift spectra and (d, e, f) two-dimensional excitation-emission mapping for P-575-8h, C-545-12h, and DC-525-48h samples, respectively

The difference between positions of absorption and emission maxima refers to Stokes shift and this value is strongly related with reabsorption and self-quenching effects. Materials possessing larger Stokes shift are more suitable to be coupled

with blue LED chips for the construction of WLEDs [42]. Relatively, large Stokes shifts are estimated as 100, 440, and 710 meV for selected P-575-8h, C-545-12h, and DC-525-48h samples, respectively (see Figure 4.6a-c). Larger Stokes shifts are estimated for CdSe and Dy^{3+}+CdSe doped GNCs compared to $CsPbBr_3$ doped samples due to broader size distribution and surface defects of CdSe QDs [74]. According to excitation-emission mapping plots, $CsPbBr_3$, CdSe and Dy^{3+}+CdSe QDs doped GNCs can be excited in a wide range (see Figure 4.6d-f). This provides a significant flexibility while designing solid-state lighting devices to achieve desired emission color properties. Position and shape of the emission bands are independent from excitation wavelength indicating that the emission is aroused from intrinsic exciton recombination rather than surface defect-originated emission. In addition, PL intensity remains approximately constant in the range of 345-410 nm at its highest for $CsPbBr_3$ doped GNCs supporting the intrinsic exciton recombination emission. On the other hand, peak intensity of CdSe and Dy^{3+}+CdSe doped GNCs shows slight differences with respect to excitation wavelength possibly due to surface defect related fluctuations [54].

PL decay curves of GNCs are illustrated in Figure A.7. Lifetime values are measured in the range of 3.10-8.84 ns, 4.55-11.02 ns, and 3.82-10.98 ns for $CsPbBr_3$, CdSe, and Dy^{3+}+CdSe doped samples, respectively. The lifetime values calculated in the nanosecond scale are indicator of the exciton recombination process and are consistent with colloidal counterparts previously published in the literature [42, 80, 81]. Lifetimes of broad emissions obtained in this work from CdSe and Dy^{3+}+CdSe doped GNCs demonstrate shorter values compared to CdSe/$Cd_{1-x}Zn_xSe$ core/shell QDs reported by Lee et al. In their work, higher lifetime values are originated from the surface passivation and diminishing trap sites of the $Cd_{1-x}Zn_xSe$ shell structure [161]. A slight increment in lifetime values of QDs doped GNCs with increasing heat-treatment temperature or duration is possibly originated due to formation of larger QDs with less surface defects and reduced quenching probability of charge carriers [162].

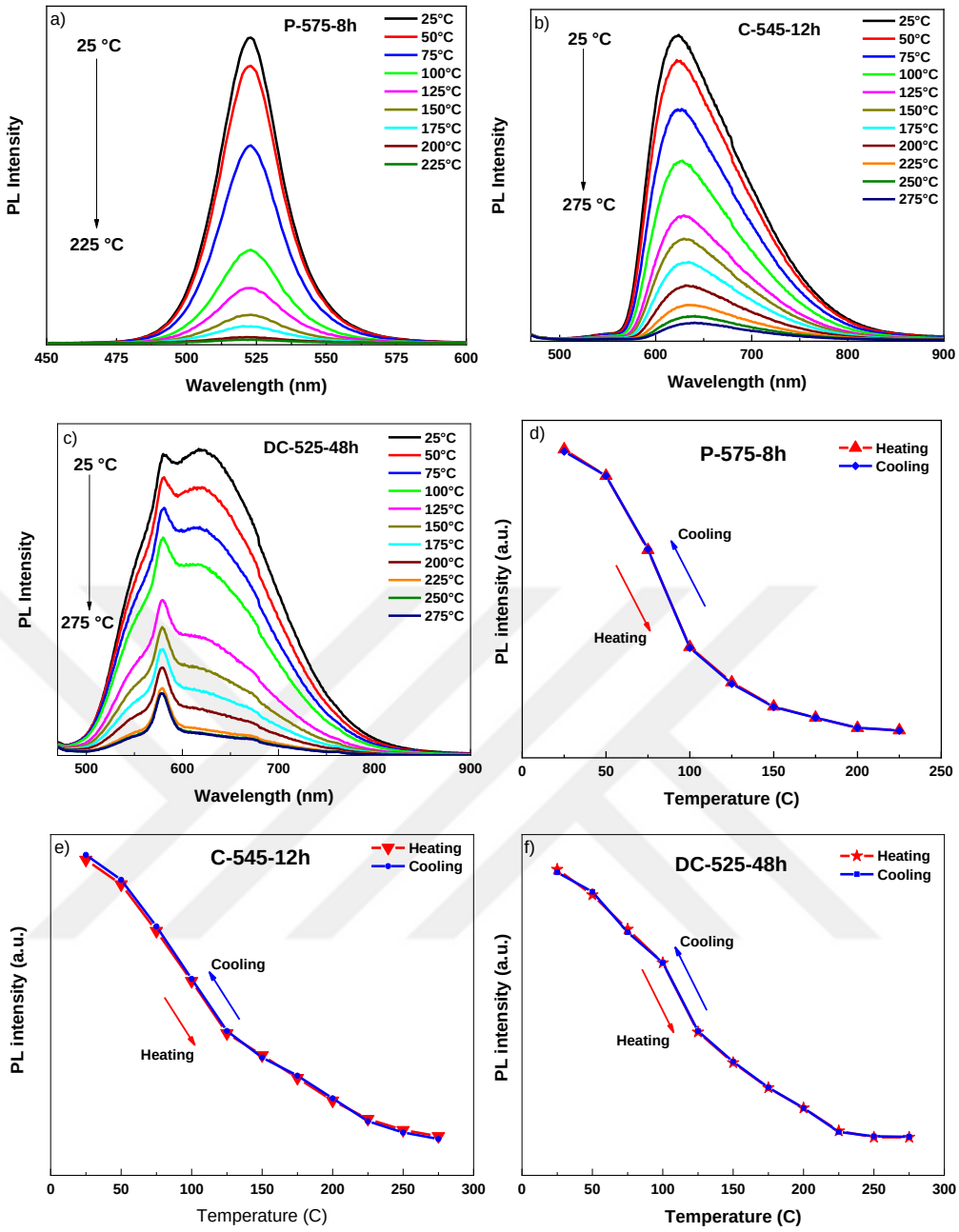


Figure 4.7 (a, b, c) Time-dependent PL spectra and (d, e, f) PL intensities of first heating and last cooling cycles for P-575-8h, C-545-12h, and DC-525-48h samples, respectively

4.3.4 Thermal, chemical and photo stability

Glasses containing necessary ions (e.g., Cs^{+}, Pb^{2+}, Br^{-}, Cd^{2+} and Se^{2-}) to form $CsPbBr_3$ and CdSe QDs can be obtained after melt-quenching process. In this stage, no nucleation occurs due to rapid cooling of the melt which means QDs are not formed at high melting temperatures. Therefore, it is not appropriate to mention their stability at these temperatures. QDs only form when the heat-treatment

process is applied to the as-cast glass samples. Therefore, permanent damage only occurs when the glasses are heated up to temperatures converging to heat-treatment temperature range (525-575 °C for this study) where QDs start to form. However, to better ascertain the thermal stability of selected GNCs temperature-dependent PL spectra up to 275 °C for P-575-8h, C-545-12h, and DC-525-48h samples are recorded (see Figure 4.7). PL intensities show a gradual decrement upon heating for all three samples due to enhanced non-radiative transition of excitons. At 100 °C, $CsPbBr_3$ doped GNCs maintain approximately 30% of their initial PL intensity, while CdSe and Dy^{3+}+CdSe doped GNCs can maintain more than 50%. Therefore, thermal stability feature of QD doped GNCs should be improved significantly before their utilization in practical WLED applications. Moreover, selected samples undergone 10 consecutive heating-cooling cycles and PL intensities of first heating and last cooling cycles are plotted in Figure 4.7d-f. Therefore, compared to colloidal systems and some glass matrices possessing relatively lower T_g values, it can be concluded that selected base glass is a suitable medium for the encapsulation of $CsPbBr_3$ and CdSe QDs with its high T_g values (see Figure A.2) [130]. In addition, thermal stability of QD doped GNCs are also compared to commercially available phosphor based WLED devices. Wu et al, carefully investigated the $Y_3Al_5O_{12}:Ce^{3+}$ + $K_2SiF_6:Mn^{4+}$ based WLED devices and they retained 100% of their PL intensity up to 100 °C [163]. Although QD doped GNCs fall far behind of these results, they are still under development and needs significant improvement before being utilized in practical applications and pave the way for new generation WLED devices.

Table 4.2 Colorimetric properties of selected samples excited with LED chip, constructed WLED devices and LED chip itself

Samples	CIE coordinates (x, y)	CCT (K)	CRI	Color purity (%)	Reference
C-545-12h	0.56, 0.43	N/A	N/A	99.8	Present work
DC-525-48h	0.53, 0.45	N/A	N/A	99	Present work
P-575-8h	0.13, 0.78	N/A	N/A	91.6	Present work
LED chip	0.14, 0.06	N/A	N/A	93.2	Present work
WLED1	0.36, 0.36	4201	76	19.4	Present work
WLED2	0.38, 0.36	3916	85	24.1	Present work
$Y_3Al_5O_{12}:Ce^{3+}$ + $K_2SiF_6:Mn^{4+}$	0.40, 0.40	3536	87.1	N/A	[163]
$Y_3Al_5O_{12}:Ce^{3+}$ + $K_2SiF_6:Mn^{4+}$	0.31, 0.34	6110	70.5	N/A	[164]

Chemical stability of GNCs are tested through immersing selected samples in water and measuring their PLQY values up to 60 days by 20-day intervals (see Figure 4.8). P-575-8h, C-545-12h, and DC-525-48h samples do not show a noticeable decrement in their original PLQY values even after 60 days of immersion. Rigid structure of glasses perfectly prevents the possible chemical reactions that QDs can undergo. On the other hand, colloidal QDs degrade in the presence of moisture and oxygen or even in inert atmospheres far quickly [130]. In this regard, silicate glasses are one of the most appropriate encapsulation materials even compared to some other glass families [143, 165].

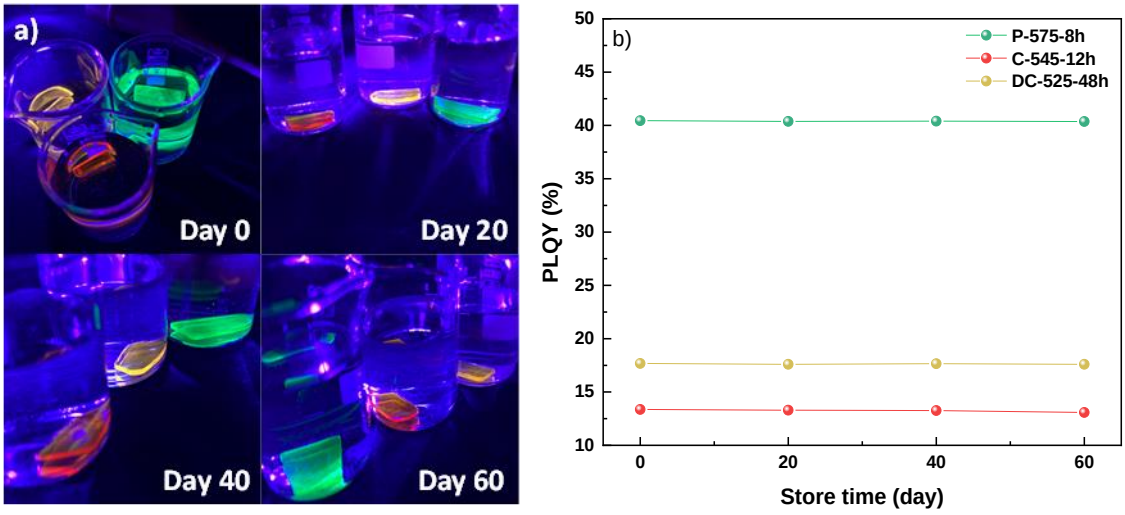


Figure 4.8 a) Macro photos and b) PLQY values of selected P-575-8h (green), C-545-12h (red), and DC-525-48h (yellow) GNCs immersed in water up to 60 days

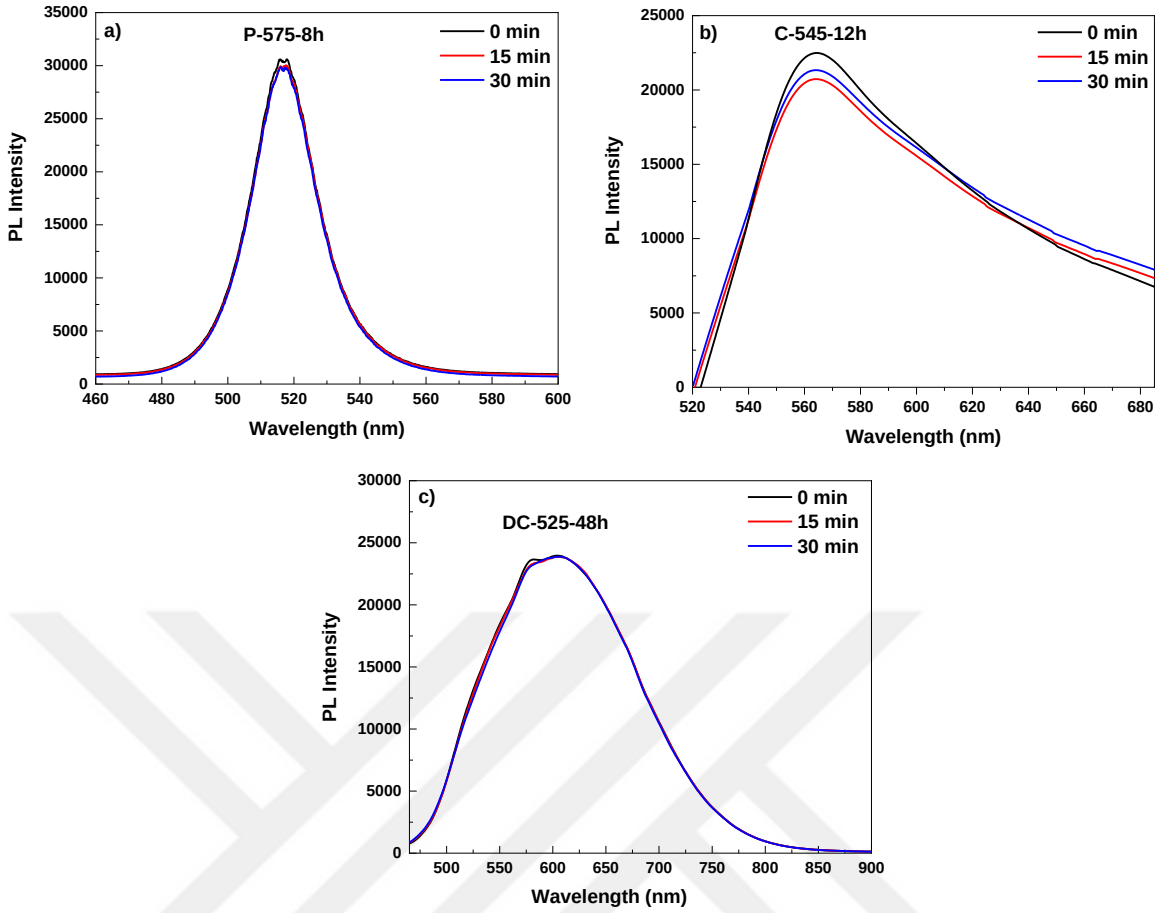


Figure 4.9 PL spectra of a) P-575-8h and b) C-545-12h and c) DC-525-48h samples under 5 W/cm^2 442 nm irradiation up to 30 min

Photostability of the GNCs are tested under 442 nm laser irradiation (5 W/cm^2) up to 30 min (see Figure A.6). As can be seen in Figure 4.9, no significant change in PL intensity is observed due to excellent protection of dense glass structure. No significant change in PL intensity after high-power laser irradiation of P-575-8h and DC-525-48h samples indicate sufficient photo stability feature of GNCs for long term usage in WLED applications. On the other hand, approximately 10% PL intensity drop of C-545-12h sample may be caused by an incident laser power fluctuation as an experimental fault. In other works, Ye et al. demonstrated that $CsPbBr_3$ doped boro-germanate glasses possess reversible PL features up to 2 W/cm^2 power density under 460 nm illumination [130]. Yuan et al. reported highly photostable $CsPbBr_3$ quantum dots encapsulated in tellurite glasses (which are inferior to silicate glasses in terms of stability) under 20 W UV lamp up to 70 hours [143]. Photostability values of glass encapsulated QDs are much higher compared to chemically synthesized counterparts which are in the range of several

hundred milliwatts per square centimeter [131]. Thermal, chemical and photo stability investigations confirm the potential of prepared GNCs in practical solid-sate lighting applications.

4.3.5 Blue LED excited white light generation

Excellent thermal and chemical stability along with favorable PLQY values of prepared GNCs have motivated us to investigate the performance of selected samples as wavelength convertors for solid-state lighting devices (see Table 4.2, Figure 4.10, and Figure 4.11). As demonstrated in Figure 4.10a-d, green-emitting P-575-8h (523 nm), red-emitting C-545-12h (609 nm), and orange-emitting DC-525-48h (575 nm) GNCs can be successfully excited through integrating with a commercial blue (450 nm) LED chip. No significant shift observed in the peak wavelength of emission bands upon LED excitement compared to Xenon excitement inside the PL device. Obviously, bright, and tunable white light generation in terms of CIE coordinates and color temperature can be obtained if the design of a WLED structure is realized meticulously. Hence, two alternative white LED devices (WLED1 and WLED2) are constructed as a proof-of-concept by coupling $CsPbBr_3$ doped glass layer with CdSe and Dy^{3+}+CdSe doped GNC layers on top of a blue LED chip (see Figure 4.10e-f). Emission spectra of constructed setups are given in Figure 4.10g-h. WLED1 and WLED2 schemes demonstrate adjacent color coordinates to pure white as (0.36, 0.36) and (0.38, 0,36), respectively (see Figure 4.11). Impressively, high CRI values are obtained due to broad emission band of CdSe and Dy^{3+}+CdSe QDs as 76 and 85 from WLED1 and WLED2, respectively (see Table 4.2). Obtained CRI values are higher compared to previously reported color converters for WLEDs consisting full perovskites [130, 166] and competitive/superior against Eu^{2+}:$CaAlsiN_3$/Ce^{3+}:YAG/$CsPbBr_3$ [121, 141, 167, 168] and Cd-S-Se/lanthanide combinations [152]. LER values are determined as 87.64 lm/W and 93.53 lm/W for WLED1 and WLED2 setups, respectively. LER values of QD doped GNCs are currently fall behind the WLED devices based on commercially available phosphor materials [163, 164]. Therefore, they should be improved before their utilization in practical applications. EQE values are calculated in a setup where no leakage of blue LED emission and they are found to be 13.42% and 15.51% for WLED1 and WLED2

devices, respectively. Slight difference between LER and EQE values are obtained due different PLQY values of C-545-12h and DC-525-48h samples.

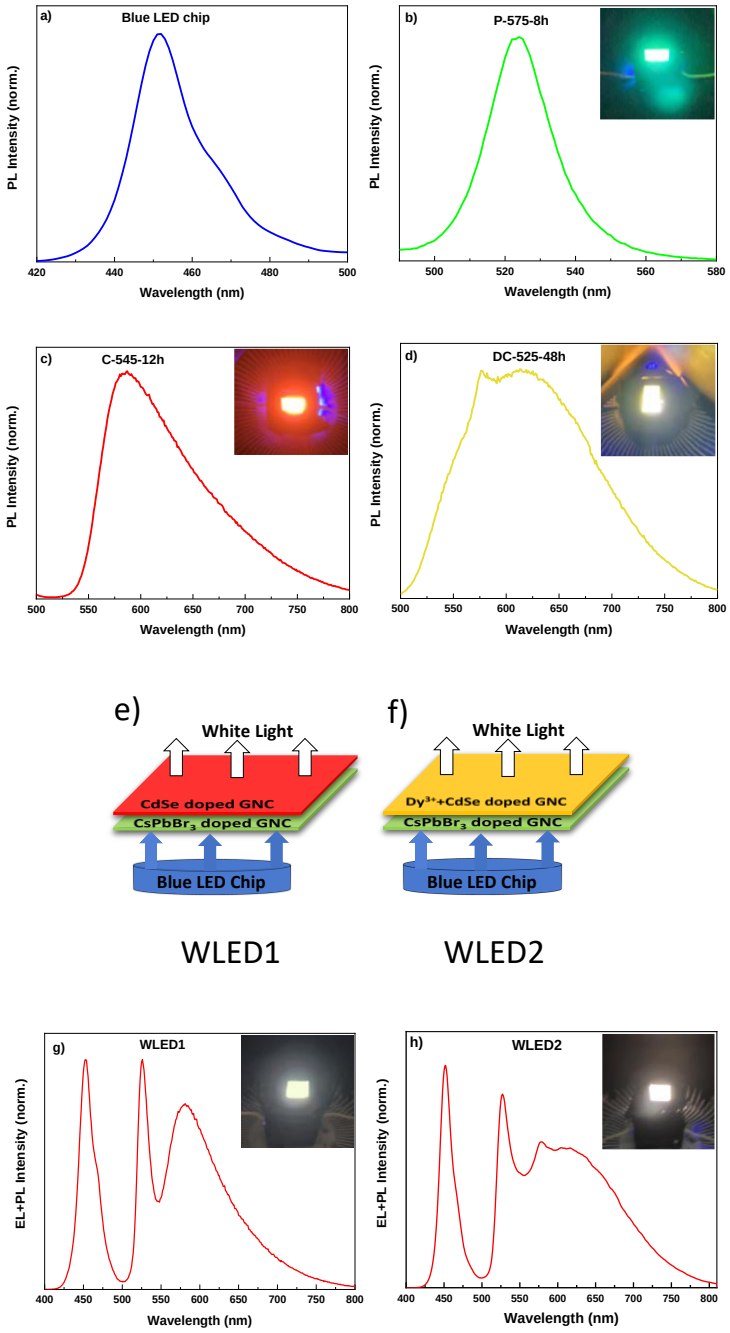


Figure 4.10 Emission spectra of a) blue LED chip, b) P-575-8h, c) C-545-12h, and d) DC-525-48h samples. Schematic illustration of e) WLED1 f) WLED2 devices. EL (electroluminescence) + PL spectra of constructed g) WLED1 and h) WLED2 devices (insets show macro photos of setups)

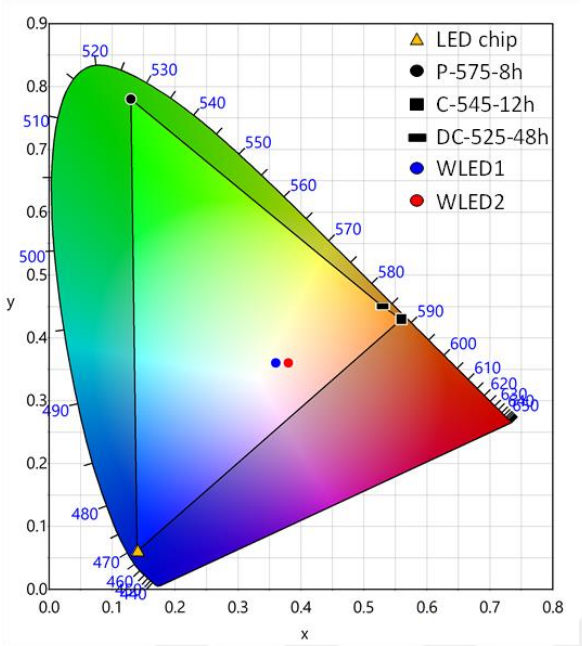


Figure 4.11 CIE diagram showing color coordinates of LED chip, selected samples and constructed WLED devices

4.4 Conclusions

In summary, $CsPbBr_3$ and CdSe / Dy^{3+}+CdSe doped GNCs are synthesized through melt-quenching and controlled crystallization process. GNCs are tested up to 275 °C, 60 days of immersion in water and laser irradiation at 5 W/cm^2 up to 30 min revealing their outstanding stability and applicability as encapsulation medium for QDs. $CsPbBr_3$, CdSe and Dy^{3+}+CdSe doped GNCs demonstrate favorable green, red, and yellow emissions, respectively. Two different WLED devices are constructed through stacking prepared GNCs on top of a blue LED chip to obtain white light. Constructed WLED devices exhibit competitive/superior PLQY and colorimetric properties compared to recently reported similar approaches. Promising results obtained in this study may pave the way new routes to design reliable and high-performance solid-state lighting devices as well as multi-purpose spectral converters in diverse opto-electronic applications.

5
CdSe AND $CsPbBr_3$ QUANTUM DOTS CO-DOPED MONOLITHIC GLASSES AS TUNABLE WAVELENGTH CONVERTORS

O. Kıbrıslı, E. Erol, A. E. Ersundu, and M. Çelikbilek Ersundu, "CdSe and $CsPbBr_3$ quantum dot Co-doped monolithic glasses as tunable wavelength convertors," *Journal of Physics D: Applied Physics,* vol. 55, no. 10, p. 105301, 2021.

5.1 Introduction

Developing tunable wavelength convertors is at the forefront for various applications in display, lighting, and anti-counterfeiting technologies [169]. Altering phase, structure and composition of photoluminescent materials can be a powerful tool for obtaining color tunable emission. Achieving this feature through a monolithic material with fixed composition is quite intricate [170]. At this point, excitation modulation exploiting up-conversion scheme through lanthanide based photoluminescent materials is a promising technique that allows color tunable emission from a material with a fixed composition [24, 171, 172]. However, generally low photoluminescence quantum yield (PLQY) values restrict their further use in advanced technological applications.

Quantum dots (QDs), on the other hand, have taken the center stage in the last decades as multifunctional photoluminescent wavelength convertors owing to their excitons confined in all three dimensions that are comparable or smaller than their Bohr exciton radius. CdSe and $CsPbBr_3$ QDs are well-studied luminescent materials thanks to their favorable properties such as, adjustable size and band gap, high PLQY and relatively low production cost [127, 173]. However, high surface energy of QDs make them vulnerable against oxygen, moisture, and UV rays [129]. Therefore, a robust encapsulation technique is generally incorporated to conserve favorable emission properties of QDs. Herein, polymeric encapsulation is accepted as the most effective way to protect QDs that are synthesized through wet chemistry methods [174]. Nevertheless, polymeric encapsulants cannot meet

desired expectations due to their insufficiency in terms of providing favorable thermal, chemical and photostability features all at once [129]. At this point, glass hosts step forward due to their reliable protection features [175]. There are plenty of research on the synthesis of CdSe or $CsPbBr_3$ QDs in various glass hosts and evaluation of their utilization in various photonic and opto-electronic applications [133, 137, 138, 140, 142, 144, 160, 168, 176, 177]. Recently, PLQY values of $CsPbBr_3$ QDs synthesized in glass hosts are reported to approach 100% and CdSe/$Cd_{1-x}Zn_xSe$ core/shell structures provide PLQY values over 50% when they are successfully engineered in a glass host [127, 173]. Intriguing results revealed out by these studies gave hope to scientists to form CdSe and $CsPbBr_3$ QDs together in an extremely stable monolithic glass host to seek their synergistic potential in state-of-the-art opto-electronic applications. However, formation of multiple QDs in a single glass host that obviously requires different heat-treatment conditions for ideal crystallization and selection of proper glass host and doping ratios make this process a challenging task. Therefore, meticulous effort is needed to design a special glass system together with optimized heat-treatment parameters for revealing ideal emission properties through QDs co-doped glasses. In this work, CdSe and $CsPbBr_3$ QDs are formed together in a monolithic silicate glass for the first time and emission color is tuned by regulating intensity of PL bands of both QDs upon changing excitation wavelength. Leverageable PLQY values obtained for CdSe and $CsPbBr_3$ QDs reveal the high potential of QDs co-doped monolithic glasses for tunable wavelength convertors and pave the way of designing novel opto-electronic devices.

5.2 Experimental procedure

5.2.1 Glass synthesis

CdSe and $CsPbBr_3$ QDs co-doped glasses with the chemical composition of $25Li_2O$-5CaO-10ZnO-$5Al_2O_3$-$55SiO_2$+(1CdO-0.5ZnSe-3CsBr-$6PbBr_2$) (in mol%) are prepared through melt-quenching technique followed by a single step heat-treatment. Additionally, singly CdSe or $CsPbBr_3$ QD doped glasses are prepared for emission properties comparison purposes. Analytical grade starting chemicals of Li_2CO_3, $CaCO_3$, ZnO, Al_2O_3, SiO_2, CdO, ZnSe, CsBr, and $PbBr_2$ purchased from

Alfa Aesar and Sigma Aldrich are blended and mixed in an agate mortar using a pestle until complete homogeneity is achieved. 10 g batches are transferred to alumina crucibles and melted at 1350 °C for 10-20 minutes. The melts are poured into preheated stainless-steel molds and pressed with another steel plate to obtain as-cast samples. Immediately after, the as-cast samples are subjected to annealing below glass transition temperature (T_g) to remove residual stresses originated from rapid quenching. Heat-treatment temperatures are selected above T_g and below crystallization onset temperature (T_c) of as-cast sample for the formation of QDs in glass (see Figure 5.1). Accordingly, as-cast samples are heat-treated in a muffle furnace by altering temperature (525-535 °C) and duration (5-10h) for controlled crystallization of QDs in the glass host. For singly QD doped samples, heat-treatment process is applied at 530 °C for 10h since these parameters result in obtaining homogeneous samples with high PLQY values. Finally, prepared samples are ground and polished to obtain plane parallel surfaces for optical characterizations. Prepared samples and related heat-treatment conditions are summarized in Table 5.1.

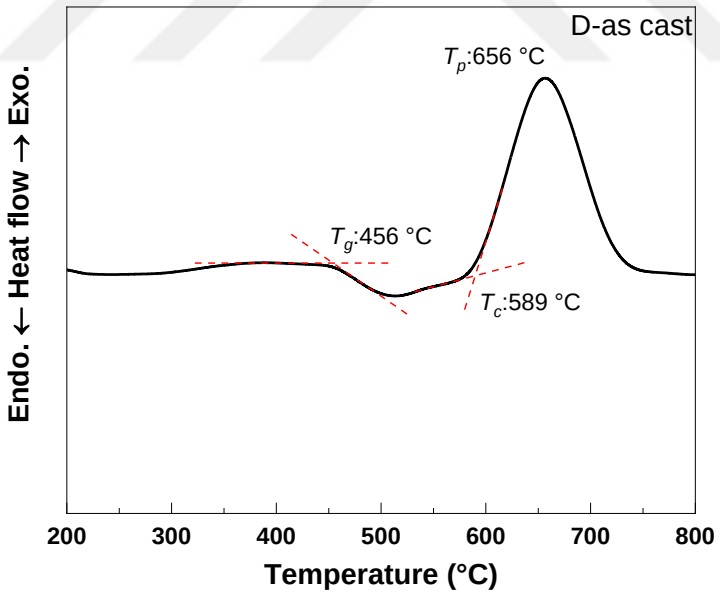


Figure 5.1 DSC thermogram of CdSe and $CsPbBr_3$ QDs co-doped as-cast sample (coded as D-as cast)

Table 5.1 Sample codes and applied heat-treatment conditions

Sample	QDs	Heat-treatment Conditions
C-530-10h	CdSe	530 °C - 10 h
P-530-10h	$CsPbBr_3$	530 °C - 10 h
D-525-5h	CdSe+$CsPbBr_3$	525 °C - 5 h
D-525-10h	CdSe+$CsPbBr_3$	525 °C - 10 h
D-530-5h	CdSe+$CsPbBr_3$	530 °C - 5 h
D-530-10h	CdSe+$CsPbBr_3$	530 °C - 10 h
D-535-5h	CdSe+$CsPbBr_3$	535 °C - 5 h
D-535-10h	CdSe+$CsPbBr_3$	535 °C - 10 h

5.2.2 Characterization studies

Differential scanning calorimetry (DSC) measurements are conducted using Netzsch DSC-204F1 to determine the thermal properties of as-cast sample with a heating rate of 10 °C/min under argon gas atmosphere by placing 25±1 mg powdered sample in a sealed aluminum container. Phase analysis of selected samples are realized through X-ray diffraction (XRD) analysis using a Philips/PANalytical X'pert Pro diffractometer. The average wavelength of Cu $K\alpha_1$ and Cu $K\alpha_2$ radiations (λ = 1.5418 Å) is used at 45 kV and 40 mA in the 2θ range from 10° to 60° with a scanning step size of 0.02°. Raman analysis is performed in Renishaw Invia Raman microscope under 532 nm laser excitation in the 150-1300 cm^{-1} wavenumber range. Raman spectrum of the selected sample (D-530-5h) is collected from 10 different points that are 125 μm deep from the sample surface using a focalized beam and the average values of collective measurements are taken into account. Absorbance spectra are recorded in the UV-Vis region between 300 and 700 nm with a resolution of 1 nm in Edinburgh Instruments FS5 spectrofluorometer. Particle sizes are calculated through effective mass approximation (EMA) as explained in detail in our previous work [175]. Steady-state photoluminescence (PL) and absolute quantum yield (PLQY) measurements are also realized in the same spectrofluorometer (equipped with 150 W xenon lamp) with a signal to noise ratio of water Raman signal >6000:1 and 0.5 nm

spectral resolution. PLQY values are calculated according to the method given in Erol et al. [129].

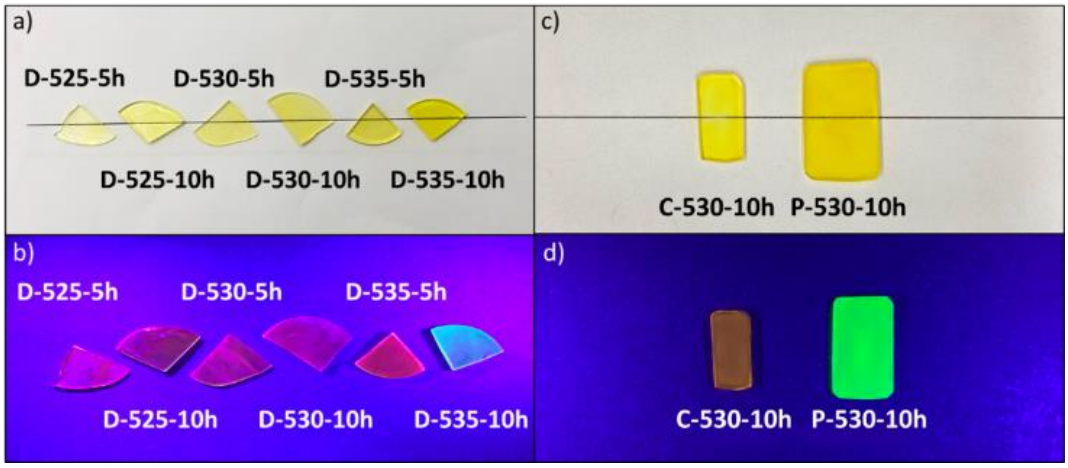


Figure 5.2 Macro photos of prepared glasses a), c) under daylight and b), d) under UV light

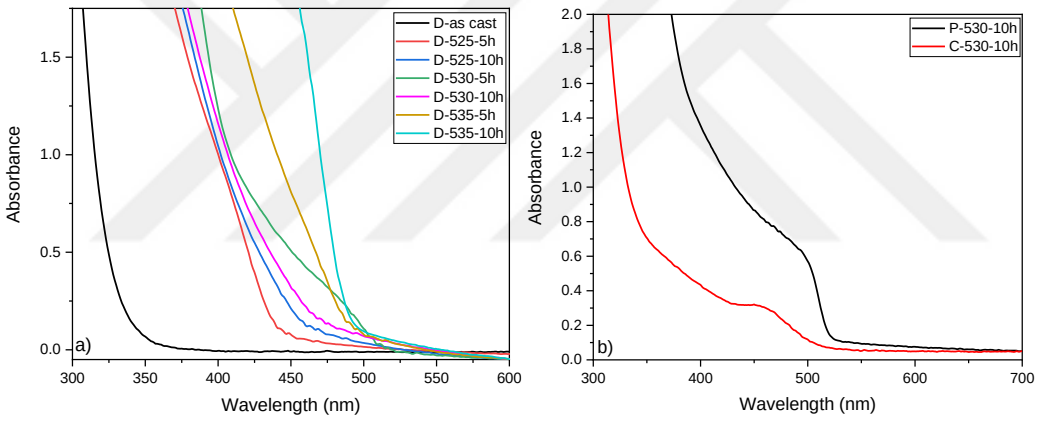


Figure 5.3 Absorbance spectra of QDs a) co-doped and b) singly-doped glass samples

5.3 Results and discussions

Macro photos of prepared samples under daylight and UV light are given in Figure 5.2. CdSe and $CsPbBr_3$ QDs co-doped samples are obtained yellow. The color change in glasses is well-known to be directly connected to visible transmittance and position of absorption edge. As illustrated in Figure 5.3, the absorption edges of QDs co-doped glasses are determined in the range of 333-495 nm and they shift to the red end of the spectrum with increasing heat-treatment temperature and duration resulting in slight darkening of glasses. A similar behavior is also

observed for singly QD doped glasses. In particular, P-530-10h sample is obtained slightly darker compared to C-530-10h sample.

XRD analysis is conducted to check the amorphous nature of as-cast samples and to detect the formation of QDs in a selected heat-treated sample (see Figure 5.4a). Broad halo appearing at approximately 2θ=25° and presence of no sharp peaks confirm the amorphous nature of the glass host. However, selected D-530-5h sample demonstrates sharp diffraction peaks at 2θ values of 21.38° and 30.41° corresponding to (110) and (200) crystalline planes of the cubic $CsPbBr_3$ phase (COD database code: 1533063), respectively.

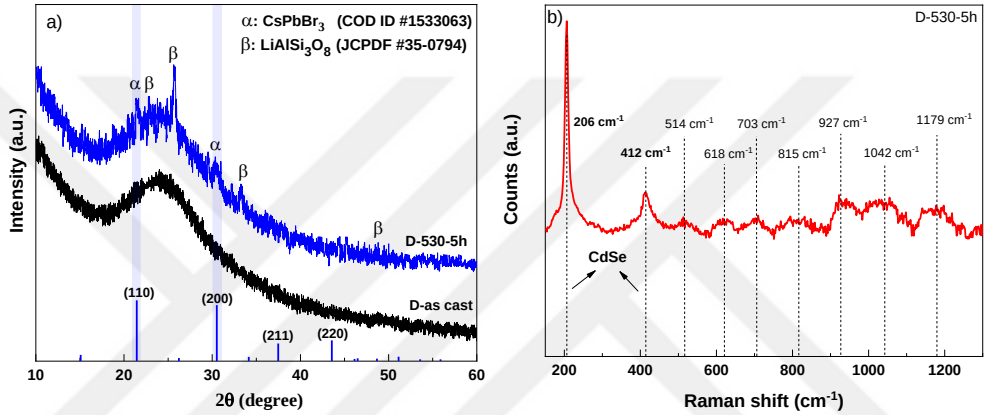


Figure 5.4. a) XRD and b) Raman spectra of selected glass samples

Furthermore, additional peaks at 2θ values of 22.8°, 25.7°, 33.1°, 48.4° are observed and attributed to tetragonal $LiAlSi_3O_8$ phase (JCPDS no. 00-035-0794) indicating significant amount of matrix crystallization. As a matter of fact, $LiAlSi_3O_8$ phase is already reported to demonstrate high transparency, good mechanical strength, low thermal expansion coefficient and high thermal durability [158, 159]. Thus, formation of $LiAlSi_3O_8$ phase would be favorable to exploitation of its advantageous properties. Unfortunately, noisy background of amorphous glass network prevents the detection of CdSe QDs through XRD analysis. Therefore, formation of CdSe QDs are confirmed via Raman analysis [175]. As shown in Figure 5.4b, longitudinal optical mode of CdSe QDs and its overtone are detected at 206 cm^{-1} and 412 cm^{-1}, respectively for selected D-530-5h sample. Additionally, broad peaks are detected due to disordered nature of glass structure. Peaks centered at 514 cm^{-1} and 618 cm^{-1} are assigned to the bending vibrations of Si–O–Si and Al–O–Al bonds. Stretching vibrations of Al–O$^-$

bonds are detected at around 703 and 815 cm^{-1}. The peak at 927 cm^{-1} is caused by stretching vibrations of Al–Si–O bonds. Finally, asymmetric stretching vibrations of Si–O–Si and Al–O–Al bonds and symmetric stretching vibrations of $Si–O^-$ bonds are appointed to the peaks centered at around 1042 and 1179 cm^{-1} (see Table 5.2) [178-180].

First excitonic absorption peaks of CdSe and $CsPbBr_3$ QDs could not be detected for co-doped glasses except for D-530-5h sample (see Figure 5.3). Even though the first excitonic peak is detected for D-530-5h sample, it is not apparent on Tauc plot preventing particle size calculations for QDs co-doped samples. On the other hand, singly QD doped samples demonstrate clearly visible first excitonic absorption peaks. Accordingly, band gap values are determined as 2.62 and 2.39 (see Figure 5.5) and particle sizes are calculated as 1.91 and 5.22 nm for singly CdSe doped C-530-10h sample and singly $CsPbBr_3$ doped P-530-10h sample, respectively. Calculated particle sizes of QDs are smaller than the Bohr exciton radii of CdSe (5.6 nm) and $CsPbBr_3$ (3.5 nm) bulk crystals confirming that the obtained particles are under quantum confinement effect. In addition, authors performed substantial effort to conduct TEM analysis to confirm the formation of QDs in glass host. However, large amount of Li_2O in the glass composition triggers unwanted crystallization and non-conductive nature of glass samples cause charge accumulation under high energy electron beam which ultimately prevent obtaining reliable results.

Table 5.2 Raman peak assignments for selected D-530-5h sample

Center wavenumber (cm^{-1})	Assignment
206 and 412	Longitudinal optical mode of CdSe QDs and its overtone
514 and 618	Bending vibrations of Si–O–Si and Al–O–Al bonds
703 and 815	Stretching vibrations of $Al–O^-$ bonds
927	Stretching vibrations of Al–Si–O bonds
1042 and 1179	Asymmetric stretching vibrations of Si–O–Si and Al–O–Al bonds and symmetric stretching vibrations of $Si–O^-$ bonds

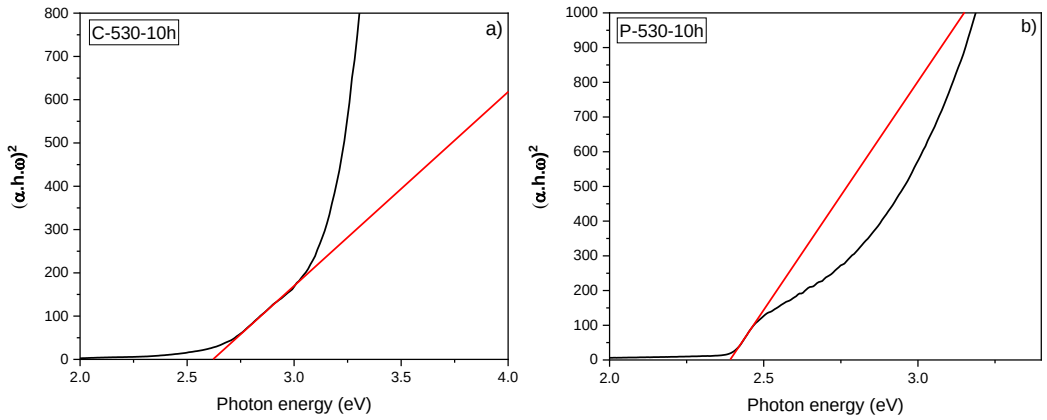


Figure 5.5 Tauc plots of a) C-530-10h and b) P-530-10h samples. Band gaps are calculated as 2.62 eV and 2.39 eV, respectively

Emission spectra of prepared samples are investigated under excitation wavelengths ranging from 325 to 425 nm. Emission band intensity of singly QD doped C-530-10h and P-530-10h samples decrease with increasing excitation wavelength from 325 to 425 nm (see Figure 5.6). The possible reason for this is that QDs are more sensitive to high-energy UV irradiation compared to visible irradiation. However, center wavelengths remain unchanged for both C-530-10h and P-530-10h samples.

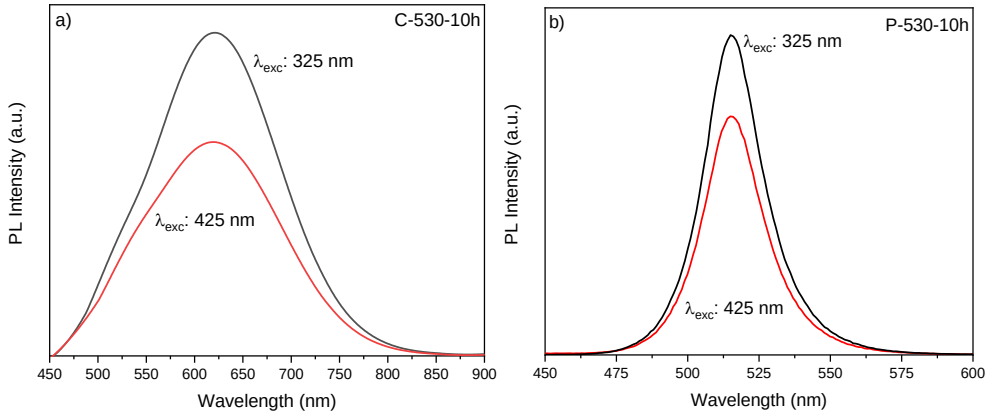


Figure 5.6 Emission spectra of singly QD doped a) C-530-10h and b) P-530-10h samples under 325 and 425 nm excitation

FWHM value is calculated as 24 nm for P-530-10h sample with no significant change upon varying excitation wavelength. On the other hand, FWHM value of CdSe doped sample (C-530-10h) changes between 155 and 173 nm. Broad FWHM values of CdSe QDs compared to $CsPbBr_3$ QDs in singly-doped samples reveal that CdSe QDs possess more surface imperfections compared to $CsPbBr_3$ QDs due to

dual synthesis. Emission band of CdSe QDs are broadened under high energy photon excitation for QDs co-doped samples (see Figure 5.7). Additionally, the weak PL signal of $CsPbBr_3$ QDs (for the $CsPbBr_3$ and CdSe QDs co-doped sample) excited at 325 nm is suppressed (and not detected clearly) due to intense luminescence intensity of CdSe QDs under the same excitation wavelength. FWHM values of emission bands under 325 and 425 nm excitation wavelengths are given in Table 5.3 and they show a decrement with increasing excitation wavelength. Moreover, center wavelengths of emission bands for CdSe QDs significantly blue shift with increasing photon energy, while center wavelengths of emission bands for $CsPbBr_3$ QDs remain constant. Several possible reasons might have triggered these observed behaviors. For instance, increased size distribution may be responsible for broadening of CdSe emission band for QDs co-doped samples [181]. Addition of $CsPbBr_3$ starting materials along with CdSe QDs possibly causes the occurrence of additional emissive sites by interfering with surface morphology of CdSe QDs which ultimately results in blue shifting of emission bands of CdSe QDs [182]. In case of $CsPbBr_3$ QDs, only the intensity of emission bands demonstrates a significant change, while center wavelengths remain constant. Thanks to this strange behavior of CdSe QDs, authors are able to tune the emission color by changing excitation wavelength for only QDs co-doped samples due to formation of more structural imperfections for CdSe QDs in dual synthesis compared to individual synthesis of CdSe and $CsPbBr_3$ QDs in separate glass hosts. Extremum CIE color coordinates for the 325-425 nm excitation wavelength range are given in Table 5.3. All the samples except D-535-10h (see Fig. 7g and 7h) change their color from yellow to red via slightly different routes on CIE color diagram upon varying excitation wavelengths. On the other hand, greenish yellow emission is observed for D-535-10h sample due to overgrowing of $CsPbBr_3$ QDs compared to CdSe QDs. Further structural investigations are needed to understand the different behavior of CdSe and $CsPbBr_3$ QDs when they crystallize in the same glass host.

Table 5.3 FWHM, peak wavelength, color coordinates and PLQY values of prepared glass samples. Excitation wavelengths are indicated on related columns for each feature

Samples	FWHM of CdSe Emission		FWHM of $CsPbBr_3$ Emission		Peak Wavelength of CdSe Emission (nm)		Peak Wavelength of $CsPbBr_3$ Emission (nm)		Color Coordinates (x, y)		PLQY (%)	
	325 nm	425 nm	325 nm	425 nm	325 nm	425 nm	325 nm	425 nm	325 nm	425 nm	345 nm	365 nm
D-525-5h	171	112	N/A	25	544	649	N/A	471	0.35, 0.48	0.47, 0.32	9.61	2.58
D-525-10h	191	120	N/A	33	552	649	N/A	469	0.37, 0.46	0.51, 0.35	5.82	2.05
D-530-5h	181	120	N/A	28	548	644	N/A	472	0.35, 0.45	0.43, 0.31	21.78	16.63
D-530-10h	180	118	N/A	39	560	653	N/A	473	0.38, 0.48	0.48, 0.34	3.86	1.11
D-535-5h	206	119	N/A	29	561	656	N/A	473	0.39, 0.47	0.55, 0.35	6.63	3.18
D-535-10h	177	120	23	N/A	570	665	500	N/A	0.43, 0.52	0.27, 0.49	3.25	1.49
P-530-10h	N/A	N/A	24	24	N/A	N/A	515	515	0.10, 0.71	0.10, 0.73	31.47	27.14
C-530-10h	157	173	N/A	N/A	619	614	N/A	N/A	0.50, 0.48	0.49, 0.48	18.53	15.33

PLQY values of prepared glasses are measured under 345 and 365 nm excitation since these are the most used wavelengths in the literature [130, 166] (see Table 5.3). Highest PLQY value is recorded as 21.78% (under 345 nm excitation) for D-530-5h sample among all QDs co-doped samples. P-530-10h and C-530-10h samples possess relatively higher PLQY values as 31.47% and 18.5% under 345 nm excitation, respectively. Relatively higher PLQY values in singly QD doped samples is probably observed due to less structural imperfection of CdSe and $CsPbBr_3$ QDs in separate glass hosts.

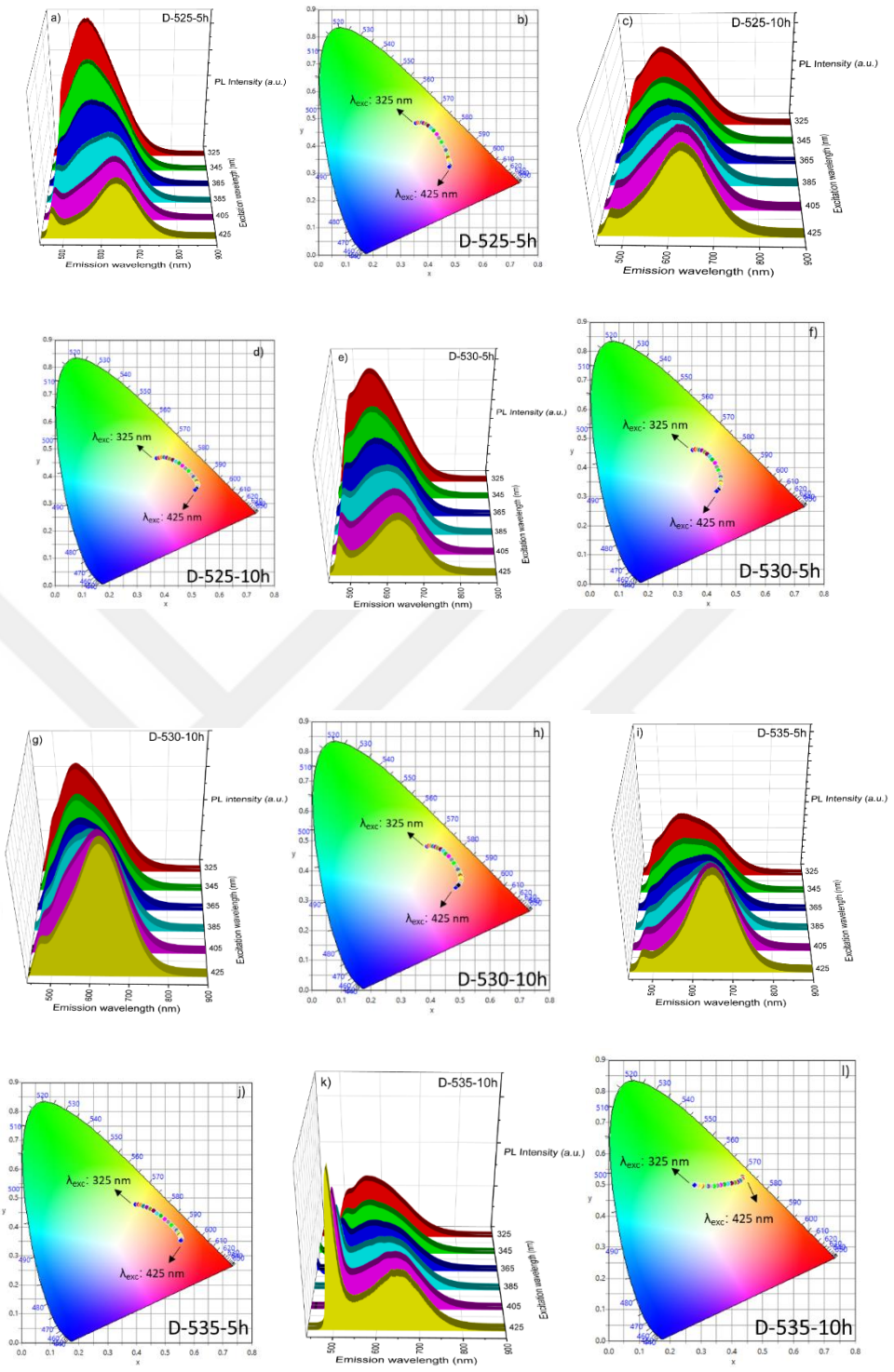


Figure 5.7 Excitation wavelength dependent (325-425 nm) a), c), e), g), i), k) emission spectra and b), d), f), h), j), l) CIE color diagrams of QDs co-doped glass samples. Excitation wavelength intervals are set as 20 nm and 5 nm for emission spectra and CIE color diagram, respectively

5.4 Conclusions

In the present study, synergistic effect of CdSe and $CsPbBr_3$ QDs simultaneously formed in a monolithic glass host is investigated for the first time in terms of emission properties under varying excitation wavelengths. Preliminary results of the novel CdSe and $CsPbBr_3$ QDs co-doped monolithic glasses show that emission color can be easily tuned in a significant color coordinate range (yellow-green to red) by altering excitation wavelength which ultimately indicates the potentiality of such materials to be used as wavelength convertors. Even though favorable PLQY value (21.78%) and significant color tunability is obtained for D-530-5h glass sample, further enhancements are still required to implement this novel material into practical applications. Wide variety of glass families enabling the application of broad range of heat-treatment parameters have high potential waiting to be revealed as beneficial hosts for encapsulation of QDs. The authors believe that the present study will attract researchers to gain full control in synthesis process of QDs co-doped monolithic glasses by further structural analysis and enhance their emission properties to pave their way for next generation photonic and opto-electronic applications.

6
INSTANTANEOUS COLOR TUNING OF UP-CONVERSION EMISSION IN A NOVEL LANTHANIDE DOPED MONOLITHIC GLASS VIA EXCITATION MODULATION

O. Kıbrıslı, N. Vahedigharehchopogh, A. E. Ersundu, and M. Çelikbilek Ersundu, "Instantaneous Color Tuning of Upconversion Emission in a Novel Lanthanide-Doped Monolithic Glass via Excitation Modulation," *The Journal of Physical Chemistry C,* vol. 124, no. 19, pp. 10687-10695, 2020.

6.1 Introduction

Up-conversion (UC) luminescence is a non-linear process, known as anti-stokes emission, in which the consecutive absorption of two or more low energy photons results in the emission of high energy photons. UC concept was first devised by Bloembergen in 1959 [183] but lack of a coherent light source was lingered the generation of up-converted visible emission until the advent of laser. After the breakthrough experiment realized by Auzel in 1966 [15], anti-stokes emission obtained through conversion of NIR (near IR) photons to Vis (visible) photons prompted the development of NIR up-convertors for a vast number of applications [184-188]. UC scheme is usually categorized by energy transfer UC (ETU) or excited state absorption (ESA) that uses physically existing intermediary energy states of lanthanide ions. ETU and ESA have arisen as an alternative for the second harmonic generation (SHG) and two photon absorption (TPA) to generate anti-stokes emission without the requirement of a high-density excitation source or a non-linear optical material [189]. Besides, precise tuning of the relative intensities of emission bands in ETU and ESA schemes is also a noteworthy feature for numerous applications such as, optical information storage [190], anti-counterfeiting [172], bio-imaging [191] color tunable multi-wavelength lasers [192] and laser based volumetric displays [169]. Hence, the color tuning of up-converted emission has been extensively investigated in the frame of structural

adjustment, concentration, size, phase and doping category of the luminescent material [172]. Nonetheless, color tunability of up-converted emission in a fixed material has always been a formidable challenge. Therefore, several studies were reported on non-steady-state excitation of UC nanoparticles to obtain color-tunable emission from a fixed material in various hosts [169, 191, 193-195]. Studies related to color tuning of UC materials by excitation modulation were mostly concentrated on lanthanide doped $NaYF_4$ nano-crystals and applications were ran through their direct uses as aqueous solutions or as nano-crystal embedded polymer based hosts [169, 172, 191, 196]. Additionally, there also exist several fundamental studies in some bulky crystalline hosts [193-195]. However, to the best of our knowledge, there is no such a study on tuning of relative intensities of emission bands in lanthanide doped glasses by excitation modulation. Tuning of emission colors in a fixed oxide glass composition doped with lanthanide ions can give rise to new possibilities and also may promote the already existing applications due to their favorable properties over crystalline and solution based hosts [197]. Of particular interest for volumetric displays, providing high resolution, full-color and high brightness in a long-term stable screen material is always challenging. At this point, laser based volumetric displays step forward with recent developments in holography, laser technology and materials science [169, 198-200]. Yet they are still stuck in laboratories and need further enhancements. In addition, monolithic multi-wavelength (multi-color and white) lasers that cover the visible spectrum, especially red, green and blue colors, have attracted immense interest due to their wide range of applications [192]. Hence, a monolithic laser system that operates selectively at multiple wavelengths has an important practical value in photonics and opto-electronics. Therefore, development of a color-tunable robust luminescent material that can be manufactured in large scale and different forms, e.g. bulk and fiber, with desired mechanical, thermal and chemical durability and efficient luminescence intensity will make a significant contribution to the improvement of laser based volumetric displays and color tunable monolithic multi-wavelength lasers.

Lanthanide ion doped glasses were considerably investigated as luminescent materials for different photonic and opto-electronic applications due to their high transparency in broad wavelengths and easy manufacturing techniques compared to crystals and powders [201]. Besides, low phonon energy is one of the most desirable property expected from an UC host as it reduces non-radiative transition rates [202]. Hereupon, tellurite glasses possess one of the lowest phonon energy (600-850 cm^{-1}) among all oxide glasses [203]. Furthermore, additional favorable properties of tellurite glasses, such as high chemical and thermal stability, good rare-earth ion solubility and suitability for fiber drawing, indicate their potentiality as a versatile hosting medium for lanthanide ion-based UC luminescent materials. In this work, we report a comprehensive investigation on the relation between excitation modulation and emission properties of a $Ho^{3+}/Tm^{3+}/Yb^{3+}$ triply doped monolithic tellurite glass to achieve the precise manipulation of photoluminescence (PL) spectra that is fundamental as well as practical work for ravishing photonic and opto-electronic applications. Radiative properties of the proposed systems are investigated accordingly in terms of PL measurements, Judd-Ofelt (J-O) analysis and quantum yields of related transitions. Instantaneous color change is shown by varying the frequency of excitation source using a galvanometer which is a proof of concept for potentials of proposed systems especially in full-color laser based volumetric displays or color tunable monolithic multi-wavelength lasers.

6.2 Experimental Section

6.2.1 Glass Synthesis

A set of glass samples in the (50-*x*)TeO_2-25WO_3-25Li_2O-*x*RE (*x* in mol%, RE: $Ho^{3+}/Tm^{3+}/Yb^{3+}$) system is fabricated through conventional melt-quenching technique using high purity starting chemicals of TeO_2 (99.99%), WO_3 (99.8%), Li_2CO_3 (99%), Ho_2O_3 (99.9%), Tm_2O_3 (99.9%) and Yb_2O_3 (99.99%). Samples are prepared by keeping the concentration of Yb^{3+} ions as a constant while varying the concentrations of other two RE ions. The compositions and labels of samples are given in Table A.1. For glass synthesis, starting powders are weighed using a high precision scale (10^{-4} g) with extreme care and mixed in an agate mortar with

a pestle for about 15 min to achieve complete homogeneity. Afterwards, the prepared powder mixtures of 7g are placed into a platinum crucible with a lid and melt at 800 °C for 30 min in an electric furnace. Thereafter, the melts are poured into a pre-heated stainless-steel mold and obtained glass samples are immediately annealed below glass transition temperature at 290 °C for 3 h. At the end of the annealing process glass samples are furnace cooled with 1°C/min cooling rate inside the furnace so as to eradicate residual internal stresses originating from fast cooling. All samples go through grinding and polishing processes to obtain plane-parallel surfaces at a thickness of 2 mm. According to steady-state PL spectra measurements, G1 sample is selected for further characterizations due to its more homogeneous spectral distribution and lower concentration quenching effect.

6.2.2 Measurements and Characterization Studies:

Optical absorption spectra of samples are recorded in the UV-Vis-NIR region of electromagnetic spectrum between 380-2100 nm with a resolution of 1 nm using PerkinElmer Lambda 950 spectrophotometer. Line strength values are calculated through absorbance spectra and then fitted to calculate J-O intensity parameters (Ω_2, Ω_4, Ω_6). Root mean square deviations (δ_{rms}) are also calculated to check the quality of the fit. Non-overlapping transitions of Ho^{3+} and Tm^{3+} ions are carefully selected for the precise calculation of integrated areas under absorbance spectra. In addition, $^3H_5$ manifold of the Tm^{3+} ion is excluded from the fit due to its strong magnetic dipole contribution [204]. Radiative transition probabilities (A_{ED} and A_{MD}), branching ratios (β) and lifetime (τ_{cal}) values are calculated through J-O intensity parameters as explained elsewhere [85, 86, 204]. Absorption cross-section values are then calculated using the recorded absorption spectra according to the following equation [205]:

$$\sigma_a(\lambda) = \frac{2.303 \times OD(\lambda)}{NI}, \tag{6.1}$$

where $OD(\lambda)$ is the optical density of recorded absorption spectrum, N the concentration of lanthanide ions and I the thickness of sample. Excited emission cross section values $\sigma_{em}(\lambda_p)$ are calculated using Füchtbauer-Ladenburg theory as follows [206]:

$$\sigma_{em}(\lambda_p) = A \frac{\lambda_P^5 I(\lambda)}{8\pi C n^2 \int \lambda I(\lambda) d\lambda}, \tag{6.2}$$

where, λ_p represents the peak wavelength, n is the refractive index of glass sample, A is the spontaneous emission probability and $\frac{I(\lambda)}{\int \lambda I(\lambda) d\lambda}$ is normalized line shape function of the emission. Furthermore, optical gain cross section $G(\lambda)$ values are determined through absorption and emission cross sections together with population inversion parameter (p) by means of following equation [207]:

$$G(\lambda) = N[p\sigma_{em}(\lambda) - (1-p)\sigma_{abs}]. \tag{6.3}$$

PL measurements are realized using an Edinburgh Instruments FS5 spectrofluorometer with a signal-noise ratio of water Raman signal >6000:1. Glass samples are excited with a 973 nm IR laser operating in CW and pulsed modes at a resolution of 0.5 nm for PL measurements. Excitation characteristics for related experiments are indicated in the results and discussion section. Emission bands at 475, 545 and 660 nm are characteristic for a $Ho^{3+}/Tm^{3+}/Yb^{3+}$ doped system under 980 nm excitation. 475 nm is originated from Tm^{3+} ions, while 545 and 660 nm originated from Ho^{3+} ions. Therefore, decay profiles are obtained by monitoring the emissions at 475 nm, 545 nm and 660 nm with respect to time. Biexponential decay profiles are then fitted according to the following equation [208]:

$$I(t) = A_1 e^{\left(\frac{-t}{\tau_1}\right)} + A_2 e^{\left(\frac{-t}{\tau_2}\right)}, \tag{6.4}$$

where $I(t)$ represents the fluorescence emission intensity at a given time t, τ_1 and τ_2 the luminescence lifetime values and A_1 and A_2 constant decay values. Average lifetimes for each transition are calculated according to the following formula [208]:

$$\tau_{meas} = \frac{A_1\tau_1^2 + A_2\tau_2^2}{A_1\tau_1 + A_2\tau_2}. \tag{6.5}$$

Absolute up-conversion quantum yield (UCQY) values, the ratio of emitted UC photons to absorbed photons of a luminescent material, are measured using the same PL setup. A demountable integrating sphere (150 mm internal spherical cavity, politetrafloroetilen coated) is placed inside the sample chamber with the entrance and exit ports facing perpendicularly to each other. All recorded data for

UCQY are subsequently corrected for the spectral responses of both spectrofluorometer and integrating sphere. Spectral responses of monochromator, detector and integrating sphere in photon flux are determined using a calibrated tungsten lamp. Scattering and emission spectra are recorded separately due to the high power density of excitation source in order to avoid oversaturation of the detector. OD (optical density) 2 filter was inserted before the measurement of scattering radiation from reference and sample. Therefore, scattering spectra are scaled up according to true transmittance of the OD 2 filter at 973 nm. Based on the calibrated spectra, UCQY values are determined with an estimated error of $\pm 5\ \%$ using the following expression [209]:

$$\eta = \frac{number\ of\ emitted\ photons}{number\ of\ absorbed\ photons} = \frac{L_{sample}}{E_{reference} - E_{sample}}, \tag{6.6}$$

where η is the UCQY, L_{sample} is emission intensity determined by integrating the area under calibrated emission spectra and $E_{reference}$ and E_{sample} are the scattering intensities of excitation light not absorbed by reference and sample, respectively. The number of absorbed photons is obtained by the difference in scattering integrated areas between reference and sample.

6.3 Results and Discussion

Compositions of $Ho^{3+}/Tm^{3+}/Yb^{3+}$ triply doped tellurite glasses investigated in this study are determined based on our previous work focusing on the effect of glass composition on the characteristics of PL spectra [210]. A new set of samples containing a mutual sample (G2) with the previous work were synthesized in current study to design a novel monolithic glass for obtaining color tunable emission through excitation modulation (See Table A.1).

Digital images of optically prepared samples are given in Figure A.9. All samples possess high transparency with a pale-yellow color. Notwithstanding, a slightly darker coloration is observed with increasing amount of lanthanide doping. G1 sample that possesses the most intense emissions in Vis region for a homogenous spectral distribution is selected for further investigations by the evaluation of PL spectra (see Figure A.10). Investigation of thermal and optical properties of the prepared glasses is essential as well as the luminescence properties in case of their

usability for practical applications. Therefore, glass transition temperature (T_g) is determined as 330 °C indicating a sufficient temperature limit for the proposed glass in various applications without thermal damage (see Figure A.11). Moreover, low absorbance values recorded in majority of the spectrum given in Figure A.12 denotes for low absorptivity of the proposed glass host until the absorption edge. Supplementary characterizations reveal the applicability of G1 sample for various photonic and opto-electronic applications.

6.3.1 Judd-Ofelt Analysis and Radiative Properties

Thirteen absorption peaks are observed from the absorbance spectrum (see Figure A.12) related to the electronic transitions of Ho^{3+}, Tm^{3+} and Yb^{3+} ions from low energy ground states of $^5I_8$, $^3H_6$ and $^2F_{7/2}$, respectively to the excited energy states centered at 418, 450, 459, 486, 538, 644, 686, 792, 975, 1160, 1212, 1698 and 1972 nm [98]. The electronic transition $^3H_6 \rightarrow {}^3H_5$ at 1212 nm shows both magnetic and electric dipole contributions, while other transitions have only electric dipole contribution. Ω_λ (λ=2, 4, 6) are the Judd-Ofelt intensity parameters and $\|U_\lambda\|^2$ are the doubly reduced matrix elements of the unit tensor operator of the rank λ=2, 4, 6. Doubly reduced matrix elements are not affected by the host or the local environment but only depend on considered lanthanide ion. $^5I_8 \rightarrow {}^5G_6$ transition of Ho^{3+} along with $^3H_6 \rightarrow {}^3H_4$ and $^3H_6 \rightarrow {}^3F_4$ transitions of Tm^{3+} ions are hyper-sensitive and they obey the selection rules $|\Delta S|=0$, $|\Delta L| \leq 2$, and $|\Delta J| \leq 2$. These transitions are described by the Ω_2 parameter and show relatively high line strength values compared to other transitions of the same ion. They possess larger $\|U_2\|$ value than the $\|U_4\|$ and $\|U_6\|$ values, and peak intensities are sensitive to the local environment of the optically active lanthanide ion. Therefore, intensities of these transitions vary significantly from one host to another, while the wavelengths stay almost the same [120].

Line strength defines the probability for considered transition from a specific initial level to all $2J_f + 1$ levels of the final state. The J-O parameters Ω_2, Ω_4, Ω_6 of Ho^{3+} and Tm^{3+} ions and δ_{rms} values are calculated through line strengths (see Table A.2) and are given in Table 6.1 along with available literature data [207, 211-219]. Considerably small δ_{rms} values obtained in this study proves high quality of the fit. Ω_2 parameter is related to the symmetry of the lanthanide ion sites and

strongly affected by the covalency between ligands and lanthanide ions, while Ω_4 and Ω_6 are mostly related with viscosity and rigidity of host medium [212]. Calculated parameters follow the $\Omega_2 > \Omega_4 > \Omega_6$ trend and Ω_2 is quite larger compared to others due to the high asymmetry around Ho^{3+} and Tm^{3+} ions and covalency dominant bonding between lanthanide ions and their surrounding ligands. High asymmetry around the lanthanide ions are originated from the asymmetric nature of tellurite glasses and this results in high oscillator strengths for the hyper-sensitive transitions indicated above [220]. Spectroscopic quality factor Ω_4/Ω_6 (known as Q factor) is an important parameter to estimate stimulated emission to obtain a favorable luminescent material [221]. High spectroscopic quality factor stands for lower rate of energy loss and relatively slower quenching of the oscillation. As depicted in Table 6.1, spectroscopic quality factors for Ho^{3+} and Tm^{3+} ions obtained in this study are larger or in a comparable level with different amorphous, crystalline and colloidal hosts.

Table 6.1. Judd-Ofelt intensity parameters Ω_2, Ω_4, Ω_6, their trend and spectroscopic quality factor (Ω_4/Ω_6) of G1 sample along with the literature data

Samples	Ω_2 [10^{-20} cm^2]	Ω_4 [10^{-20} cm^2]	Ω_6 [10^{-20} cm^2]	Ω_λ trend	Ω_4/Ω_6
Tm^{3+}					
G1	10.90 ± 0.20	2.92 ± 0.17	2.09 ± 0.05	$\Omega_2 > \Omega_4 > \Omega_6$	1.39
Tellurite[207]	9.44	0.22	5.58	$\Omega_2 > \Omega_6 > \Omega_4$	0.03
Tellurite[217]	11.11	3.50	3.60	$\Omega_2 > \Omega_6 > \Omega_4$	0.97
Barium-tellurite[214]	5.32	2.55	1.12	$\Omega_2 > \Omega_4 > \Omega_6$	2.60
Silica-germanate[211]	5.35	3.49	0.70	$\Omega_2 > \Omega_4 > \Omega_6$	4.99
YAG[218]	2.92	17.32	11.73	$\Omega_4 > \Omega_6 > \Omega_2$	1.47
Ho^{3+}					
G1	8.46 ± 0.13	2.74 ± 0.22	0.36 ± 0.06	$\Omega_2 > \Omega_4 > \Omega_6$	7.47
Tellurite[207]	5.59	4.85	2.66	$\Omega_2 > \Omega_4 > \Omega_6$	1.82
Tellurite[212]	10.77	2.07	1.04	$\Omega_2 > \Omega_4 > \Omega_6$	1.99
Silicate[216]	2.87	1.71	0.69	$\Omega_2 > \Omega_4 > \Omega_6$	2.48
Germanotellurite[215]	4.25	2.48	1.31	$\Omega_2 > \Omega_4 > \Omega_6$	1.89
$LiNbO_3$[213]	7.39	11.96	11.39	$\Omega_2 > \Omega_4 > \Omega_6$	1.05
$NaYF_4$[219]	0.34	2.31	1.29	$\Omega_4 > \Omega_6 > \Omega_2$	1.79

J-O parameters are further used to calculate radiative properties, such as radiative transition probabilities, electric dipole (A_{ED}) and magnetic dipole (A_{MD}) transitions, branching ratios (β) and calculated lifetimes (τ_{cal}) and obtained values are given in Table 6.2. Higher radiative transition probability refers to a better opportunity to obtain intense emission [211]. In this work, $^1G_4 \rightarrow {}^3H_6$ (475 nm, Tm^{3+}), $^5F_4$, $^5S_2 \rightarrow {}^5I_8$ (545 nm, Ho^{3+}) and $^5F_5 \rightarrow {}^5I_8$ (660 nm, Ho^{3+}) transitions possess high probability (A_{ED}) compared to other non-radiative transitions. Moreover, the calculated radiative transition probabilities are comparable or larger compared to different Ho^{3+}/Yb^{3+}, Tm^{3+}/Yb^{3+} and $Ho^{3+}/Tm^{3+}/Yb^{3+}$ doped hosts [212, 214-218]. On the other hand, far larger radiative transition probability values are also calculated by favoring less non-radiative energy transfer in a Ho^{3+}/Yb^{3+} and Tm^{3+}/Yb^{3+} co-doped system [207]. Branching ratio (β) is the portion of total

photon flux from upper energy state to lower energy state and it should be higher than 0.5 to consider a host as a good laser gain material [205]. In this study, all three radiative transitions possess β values higher than 0.5. τ_{cal} values are found to be in the μs range that fall in agreement with the previously reported systems in Table 6.2. In addition, $^3H_5 \rightarrow {}^3H_6$ (1252 nm) and $^3F_4 \rightarrow {}^3H_6$ (1800 nm) transitions of Ho^{3+} ion and $^3H_4 \rightarrow {}^3H_6$ (800 nm) transition of Tm^{3+} ion that are not investigated in this work also show favorable lasing properties.

Table 6.2 Radiative properties of G1 sample calculated through Judd-Ofelt analysis for selected transitions

Transitions	λ [nm]	A_{ED} [s^{-1}]	A_{MD} [s^{-1}]	β [10^{-28} cm^3]	τ_{cal} [μs]
Tm^{3+}					
$^1G_4 \rightarrow {}^3H_6$	475	7073.71	-	0.53	75.6
$^1G_4 \rightarrow {}^3F_4$	659	799.86	18.65	0.06	162.5
$^3H_4 \rightarrow {}^3H_6$	800	6440.30	-	0.90	140.1
$^3H_5 \rightarrow {}^3H_6$	1252	1059.46	128.44	0.97	820
$^3F_4 \rightarrow {}^3H_6$	1800	1068.76	-	1	935.7
$^3H_5 \rightarrow {}^3F_4$	3946	31.34	0.30	0.02	31596
$^3F_2 \rightarrow {}^3H_4$	4038	75.47	-	0.009	13181
$^3F_3 \rightarrow {}^3H_4$	5032	16.85	0.46	0.001	57763
Ho^{3+}					
$^5F_4$, $^5S_2 \rightarrow {}^5I_8$	545	5471.59	-	0.72	133.3
$^5F_5 \rightarrow {}^5I_8$	660	3645.97	-	0.77	212.7
$^5I_6 \rightarrow {}^5I_8$	1170	150.02	-	0.74	498.80
$^5I_7 \rightarrow {}^5I_8$	1981	68.04	53.25	1	824.45
$^5F_4 \rightarrow {}^5F_5$	3255	40.72	8.51	0.006	20306
$^5S_2 \rightarrow {}^5F_5$	3420	1.03	-	0.006	964611

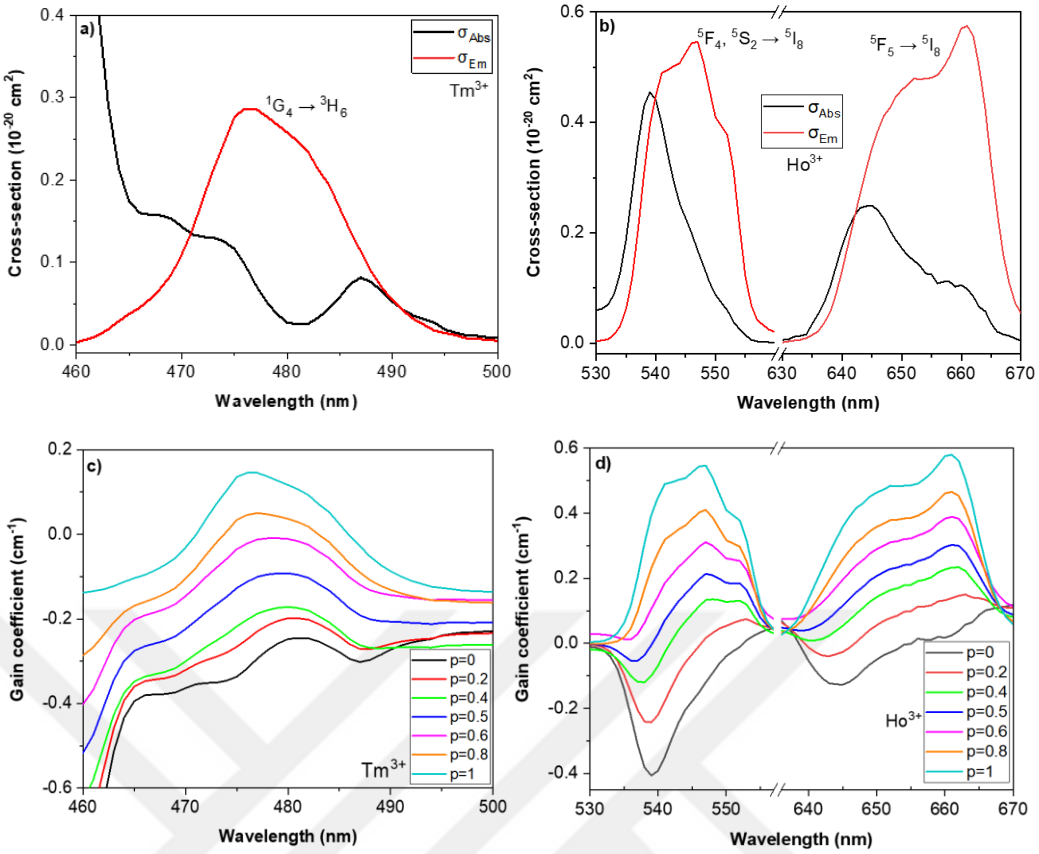


Figure 6.1 Absorption and emission spectra of a) Tm^{3+} and b) Ho^{3+} ions and calculated gain coefficients of c) Tm^{3+} and d) Ho^{3+} ions for red, green and blue emissions in G1 sample

Emission and absorption cross-section parameters are crucial for theoretical simulation and design of a laser. Large emission cross-section is a favorable aspect to obtain high gain and low threshold values [222]. Peak emission cross-sections of the transitions at 475, 545 and 660 nm are found as 0.28 $\times 10^{-20}$ cm^2, 0.54 $\times 10^{-20}$ cm^2 and 0.57 $\times 10^{-20}$ cm^2, respectively (Figures 6.1a-b). As there is no previous report on emission cross-section of a $Ho^{3+}/Tm^{3+}/Yb^{3+}$ triply doped amorphous or crystalline host for Vis region, cross-sections are compared with NIR cross-section values of Ho^{3+}/Yb^{3+}, Tm^{3+}/Yb^{3+} and $Ho^{3+}/Tm^{3+}/Yb^{3}$ doped hosts. Obtained values in this study are in a comparable level with another tellurite system [206] and larger than a $CaLaGa_3O_7$ crystal [223] and a silica-germanate glass host [211]. Gain coefficients are calculated through absorption and emission cross-sections and derived for several population inversion rates, i.e. $0 \leq p \leq 1$ (Figures 6.1c-d). Peak gain coefficients are determined as 0.14 cm^{-1}, 0.54 cm^{-1} and 0.57 cm^{-1} for transitions located at 475, 545 and 660 nm, respectively. Gain coefficient should

be higher than zero to obtain light emission [221]. Positive gain coefficient value is achievable for high population inversion rates for the transition located at 475 nm. Meanwhile, light emission is attainable when $p \geq 0.2$ for the transition located at 545 and 660 nm implying that G1 glass sample has worthwhile gain for laser action at denoted wavelengths together with a proper resonating cavity.

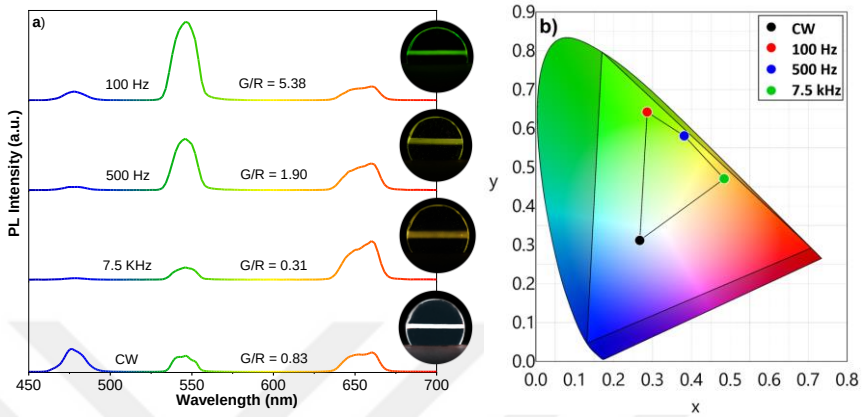


Figure 6.2 (a) Emission spectra of G1 sample under 973 nm laser irradiation showing varying G/R ratios upon different excitation characteristics. Pictures show the colors of the emission upon related excitation. (b) Color coordinates of the obtained emissions with respect to excitation characteristics. Inner triangle-like shape shows the color gamut achievable in the current study and outer triangle defines the Rec. 2020 standard for 4K UHD TVs

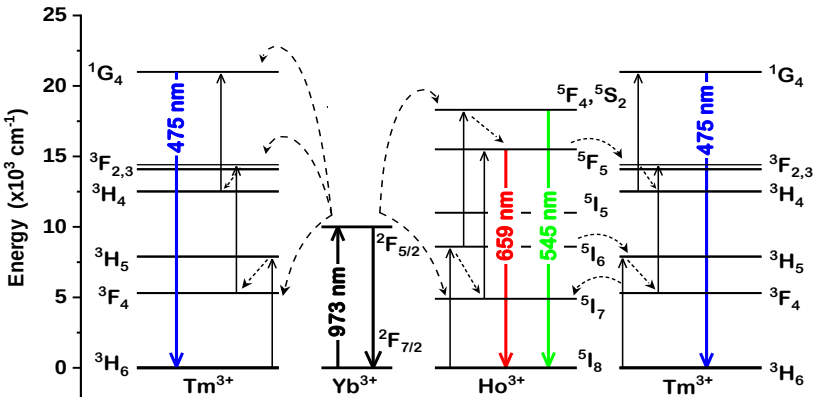


Figure 6.3 Partial Jablonski diagram of Ho^{3+}, Tm^{3+} and Yb^{3+} ions demonstrating radiative and non-radiative transitions along with energy transfer among different ions. Adapted with permission [210] 2019, Elsevier

6.3.2 Modulation of Up-conversion Emission Spectrum

Figure 6.2a presents the PL spectra of $Ho^{3+}/Tm^{3+}/Yb^{3+}$ triply doped tellurite glass under continuous wave (CW) and pulsed excitation. Multi-color emission is observed upon CW and pulsed excitation as a result of up-conversion energy

transfer from Yb^{3+} ion to Ho^{3+} and Tm^{3+} ions. Three intense emission bands are detected at blue (475 nm), green (545 nm) and red (660 nm) regions of the electromagnetic spectrum related to $^1G_4 \rightarrow {}^3H_6$ (Tm^{3+}), $^5F_4$, $^5S_2 \rightarrow {}^5I_8$ (Ho^{3+}) and $^5F_5 \rightarrow {}^5I_8$ (Ho^{3+}) transitions, respectively (see Figure 6.3). Homogenous spectral distribution is observed under CW excitation as the intensities of observed emission bands are approximately in the same level. On the other hand, blue emission is significantly suppressed upon pulsed excitation. A few reasons could have triggered a dramatic intensity drop of blue emission in the proposed system. Firstly, $^1G_4$ state of Tm^{3+} ions that are responsible from blue emission can be populated by three photon absorption process. Therefore, it takes longer time to reach full potential compared to emitting states of Ho^{3+} ions which can be populated by the consecutive absorption of two photons. Secondly, non-radiative energy transfers between $^3F_4$ (Tm^{3+}) and $^5I_7$ (Ho^{3+}) states decelerates population of $^1G_4$ state leading to an intensity drop upon pulsed excitation [169]. Correspondingly, further studies should be done to manipulate intensity of blue emission in order to obtain full control on the PL spectra in $Ho^{3+}/Tm^{3+}/Yb^{3+}$ triply doped tellurite glass. On the other hand, green to red ratios (GRR) are altered by changing the frequency of excitation source that operates with a fixed pulse duration of 115 μs (see Figure 6.2a). GRR values decreased from 5.38 to 0.31 with an increase in frequency from 100 Hz to 7.5 kHz. The key mechanism behind the alteration of GRR is simply due to the different pumping rates between two emitting states of Ho^{3+} that are responsible for green ($^5I_8 \rightarrow {}^5I_6 \rightarrow {}^5F_4$, $^5S_2$) and red ($^5I_8 \rightarrow {}^5I_6 \rightarrow {}^5I_7 \rightarrow {}^5F_5$) emissions (see Figure 6.3). Pulsed excitation with low frequency and short duration hinders energy transfer between intermediary $^5I_6$ and $^5I_7$ states, resulting in a dramatic increment in the intensity of green emission. On the other hand, relatively long pulses with high frequency or CW excitation tends to populate $^5F_5$ state of red emission [224]. Photon UC scheme allows the consecutive absorption of low energy photons in contrast to TPA and SHG [225]. Therefore, GRR tuning is possible through population rate adjustment of related transitions by excitation modulation in terms of pulse duration and/or repetition rate (frequency). In the current study, GRR ratio was changed successfully by frequency modulation of excitation source and green (x = 0.28, y = 0.64),

greenish-yellow (x = 0.38, y = 0.58), pale orange (x = 0.48, y = 0.47) and white (x = 0.26, y = 0.36) emissions (see Figure 6.2b) were observed in a fixed lanthanide doped monolithic oxide glass for the first time. Corresponding color gamut of the emissions from prepared sample is far from embracing Rec. 2020 standard for 4K UHD TVs. Hao et. al. reported wider color gamut is achievable by integrating 915 nm laser and expanding ranges of frequency and pulse width modulation in $Ho^{3+}/Tm^{3+}/Yb^{3+}$ doped $Gd_2(MoO_4)_3$ phosphors [226]. This report shows further studies may also lead the way to achieve a wider color gamut in glass hosts. A tri-colored and plus shaped primitive image (see Figure 6.4) was constructed on the glass sample by using a custom-made galvanometer as a proof of concept for the potentials of the prepared glass as a screen material for laser based volumetric.

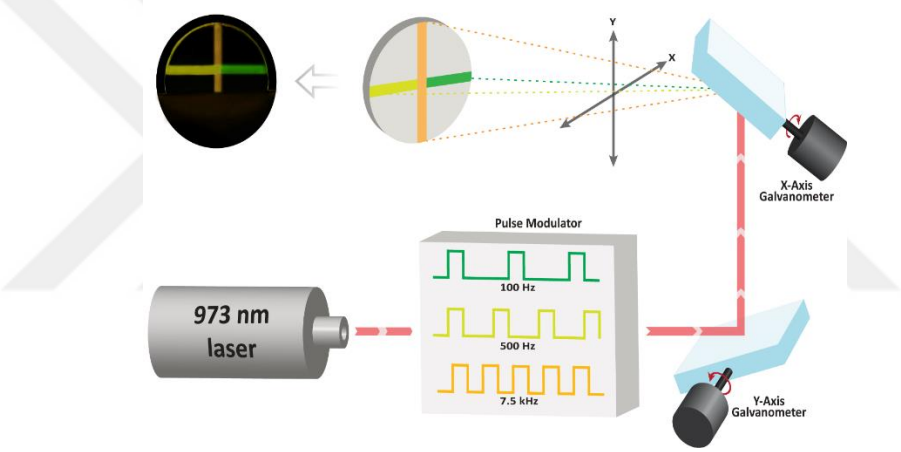


Figure 6.4 Schematic illustration of excitation source, pulse modulator and galvanometer setup. A plus sign was constructed by scanning the glass sample with a 973 nm laser beam. Different colored lines were obtained by instantaneously modulating the pulse frequency

6.3.3 Time Resolved Photoluminescence Spectra

Rising and decay profiles of the Vis emissions obtained by UC process for studied glass system are measured to confirm GRR alteration mechanism through frequency modulation by time resolved PL measurements and corresponding profiles are illustrated in Figure 6.5. 386 μs pulse duration is used for the comprehensive investigation of rising region of time resolved PL spectra of related transitions. Moreover, the pulse duration of 115 μs that is used in emission spectra modulation experiments is indicated on the graph. As it can be seen in the left hand side of Figure 6.5, $^5F_4$, $^5S_2$ (green) states are highly populated upon pulsed

excitation with a 100 Hz repetition rate compared to $^5F_5$ (red) state and vice versa for 1 kHz repetition rate. As visualized in Figure 6.3, population of $^1G_4$ state occurs in three steps and takes relatively longer time due to two non-radiative relaxations. These non-radiative transitions possibly play the main role behind the longer rise time of blue emission since they possess lower branching ratio and longer lifetime values (see Table 6.2). In case of red and green emissions, key point is the non-radiative relaxation between $^5I_6$ and $^5I_7$ states which promotes the red emission. Dominant green emission is achievable upon low frequency excitation, as the suitably adjusted cut off in the excitation pulse prevents the undesirable energy transfer among $^5I_6$ and $^5I_7$ states. On the other hand, high frequency excitation facilitates non-radiative relaxation through $^5I_7$ state and promotes red emission. This mechanism allows us to change GRR value by limiting pulse duration at 115 μs and exploiting highly populated state to obtain desired color through frequency modulation. On the other hand, population rate of $^1G_4$ (blue) state is very low compared to two emitting states of Ho^{3+} that is responsible from green and red emissions. Relatively short pulses such as a few tens of μs with high repetition rate could be used to obtain more intense blue emission compared to green emission. However, even at very low pulse durations, red emission still stays as the most intense emission. Therefore, for the particular system, there is no possibility to populate $^1G_4$ state to intensify blue emission without getting intense red emission. Hence, further enhancements should be done to obtain intensive blue emission by means of changing composition or doping with extra lanthanide ions.

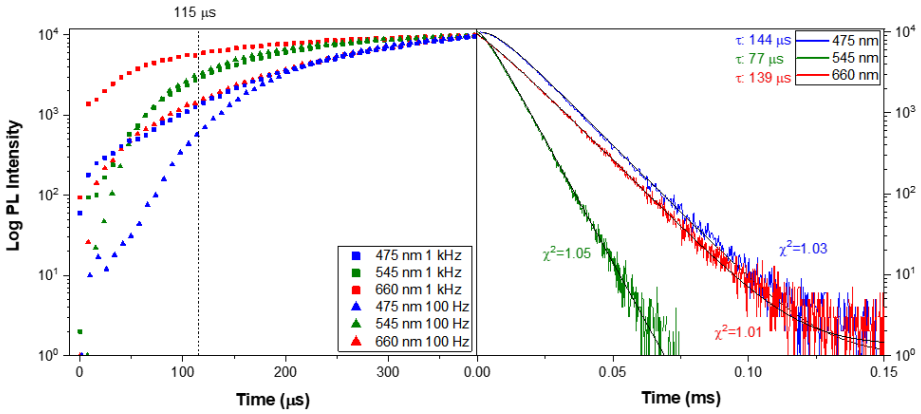


Figure 6.5 Time resolved PL spectra of G1 sample upon two different excitation frequencies for three emission bands. Left hand side illustrates rising and right hand side illustrates decay profiles

Recorded decay profiles are fitted and experimental lifetime values for the emissions located at 475, 545 and 650 nm are determined as 144, 77 and 139 µs, respectively. Decay lifetime of each emission is shorter compared to the rise times as expected from non-linear up-conversion process [227]. The obtained results are compared with crystalline hosts and it is found that lifetime values fall in the µs range which is in a good agreement with the literature [208, 227-229].

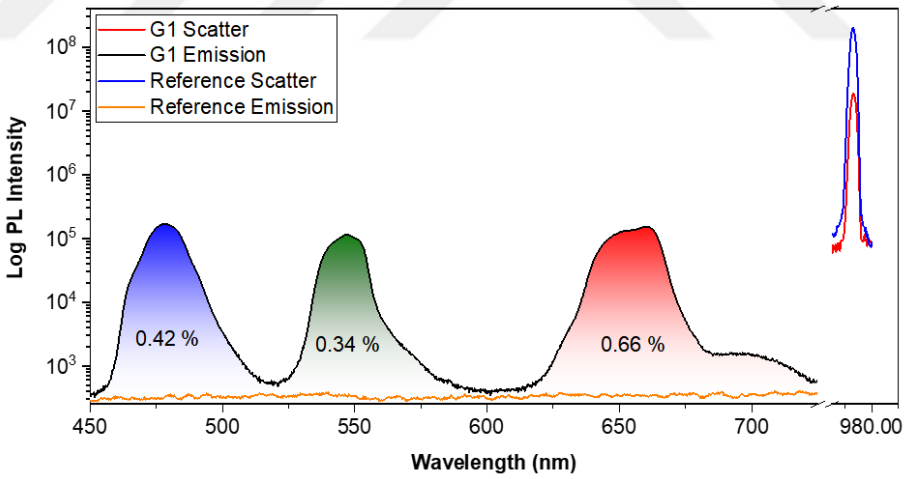


Figure 6.6 PL spectra recorded in the integrated sphere and calculated UCQY values under CW irradiation operating at 13 W cm^{-2} power density

6.3.4 Quantum Yield

It is hard to compare the intensities of PL measurements for different studies because these values are highly dependent on several properties, such as excitation power density, collecting geometry and detector itself. Therefore, investigation of quantum yield is a more convenient way to achieve true

comparison of PL performance of different samples [209]. Calculated up-conversion quantum yield (UCQY) values of each transition as a function of power density and excitation characteristics along with PL spectra are given in Figure 6.6 to visualize the integrated areas used in UCQY calculations. UCQY measurements are performed under 13 W cm^{-2} for CW and 7.5 kHz pulsed excitations, while low frequency measurements are carried out by using power densities of 1.25 W cm^{-2} due to the limitation of PL equipment. Even though applied power density irradiation is low, the obtained UCQY values are remarkable lying in the range of 0.03-0.75 % (See Table A.3). Since UCQY is highly dependent on power density [230], obtained values of each transition are satisfying for applied power densities. Therefore, higher UCQY values are possibly achievable with a more powerful excitation source. The UCQY values for different UC hosts have been reported in several studies. Zhu et. al. reported lower UCQY values in Tm^{3+}/Yb^{3+} co-doped germanate glasses even the measurements were realized at a significantly higher power density values [230]. In another study, Kumar et. al. reported UCQY values below 0.06 % for green and red emissions in Ho^{3+}/Yb^{3+} doped phosphor at 0.5 W cm^{-2} power density [231]. Furthermore, Deng et. al. calculated absolute UCQY for their well-established laser based volumetric display as 0.13 % under 980 nm excitation and 0.09 % under 808 nm excitation at extremely high power densities of 100 W cm^{-2} and 250 W cm^{-2}, respectively. UCQY results of this work are comparable with or better than other reported UC systems (See Table A.3). Additionally, emission intensity enhancement is possible through exploiting plasmon resonance as reported in Wu's remarkable study [232].

6.4 Conclusions

To the best of our knowledge, this is the first work experimentally demonstrating tuning of relative intensities of emission bands by excitation modulation in lanthanide doped glasses. In this framework, GRR ratios of emission spectrum are altered by regulating frequency of excitation source and this alteration is attributed to different population rates of transitions responsible from red and green emissions. Furthermore, radiative properties supported by J-O analysis revealed good radiative transition probabilities along with high branching ratios. Gain coefficient calculations showed that laser action at 475, 545 and 660 nm are

attainable upon proper excitation. Even though the power density of excitation source is low, notable UCQY values are obtained. We believe that our demonstration leads to budding of further tantalizing research on the use of lanthanide doped monolithic glasses in laser based volumetric displays and color tunable multi-wavelength lasers. Consequently, the proposed instantaneous color tuning concept of UC emission via excitation modulation in lanthanide doped glasses can be implemented in a wider variety of processes and technologies where tailorable emission is desired.

7
NONINVASIVE OPTICAL TEMPERATURE SENSING BEHAVIOR OF Ho^{3+} AND Ho^{3+}/Er^{3+} DOPED TELLURITE GLASSES THROUGH UP AND DOWN-CONVERTED EMISSIONS

O. Kıbrıslı, E. Erol, N. Vahedigharehchopogh, E. S. Yousef, M. Çelikbilek Ersundu, and A. E. Ersundu, "Noninvasive optical temperature sensing behavior of Ho^{3+} and Ho^{3+}/Er^{3+} doped tellurite glasses through up and down-converted emissions," *Sensors and Actuators A: Physical,* vol. 315, p. 112321, 2020.

7.1 Introduction

Development of accurate and contactless temperature measurement methods is particularly desired in numerous kinds of scientific research and industrial processes since conventional contact temperature sensors require an electrical circuit that restricts their implementation to the cases where sparks are hazardous, environment is corrosive and magnetic field is strong [233]. Currently, time and length measurements are made in femtosecond and nanometer ranges, respectively. However, the accuracy of temperature measurement is only around tenth of a degree [234]. Among contactless temperature measurement methods, infrared (IR) thermometry is a well-established method that relies on detection of the thermal radiation emitted from subjected sample. However, high absorption coefficient of common glassy materials and water vapor in the IR region prevents IR thermometry measurements using optical windows and in high humidity environments. Additionally, this method suffers from a diffraction limited resolution which results in an optimal spatial resolution of around 5 μm and it is also constrained by pixel size of the sensor [235]. Therefore, fluorescence intensity ratio (FIR) based temperature sensing method has drawn devoted attention due to its captivating features such as, rapid response, self-reference, noninvasive procedure, and high sensitivity [236, 237]. FIR method can be utilized by using thermally coupled (TCL) or non-thermally coupled (NTCL) radiative energy

levels. Population variation in the TCL is controlled by Boltzmann distribution. Therefore, measurement sensitivity is limited by the energy gap between the TCL which is usually restricted to 200-2000 cm^{-1}. In this case, maximum achievable sensitivity is constrained. Moreover, when the energy difference becomes larger, thermalization effect induces a decrement in fluorescence and population intensity of the upper level which ultimately results in complications due to very low fluorescence count levels. For this reason, the use of NTCL emerged as a promising method to achieve higher sensitivity values [238]. TCL or NTCL emission bands of trivalent lanthanide ions, e.g. Dy^{3+} [239], Ho^{3+}[240], Eu^{3+} [241], Nd^{3+} [242], Sm^{3+} [243], Pr^{3+} [244] and Er^{3+} [245], in wide variety of hosts [246-250] have been investigated and their potentiality is proven to be used as FIR based temperature sensors. However, at this point another important subject lies beneath the selection of host material for successful encapsulation of optically active lanthanide ions to achieve long-term durability with favorable optical features.

Among various kind of host materials used for optically active ions, glasses provide unique properties such as, remarkable thermal and chemical stability, ease of manufacturing in fiber and bulk form, easy recycling procedure, versatility, and magnificent transparency. In addition, lack of long-range order creates different available sites for the emissive activators that allows tuning of the emission [251]. Therefore, studies are concentrated on integrating glassy materials into numerous photonic and opto-electronic applications including optical temperature sensing [170, 210, 252-255]. To date, a wide variety of glass systems have been investigated as potential host materials to be used in temperature sensing applications [32, 38, 39, 256-258]. Amongst them, tellurite glasses step forward due to their exquisite set of favorable properties including low melting temperature, high lanthanide ion solubility, good thermal and chemical durability, exceptional IR transmissivity, high dielectric constant, low scattering and absorption losses, high refractive index and relatively low phonon energy [65-67, 129]. It is known that TeO_2 is a conditional glass former; therefore, addition of glass modifiers stabilizes the glass network and contributes to rendering of favorable properties of tellurite glasses. Addition of WO_3 as network

modifiers/intermediate oxides to tellurite glasses enhances chemical and thermal stability and also modifiability of glass composition up to fifth components [259]. Moreover, high optical transmissivity, refractive index and thermal stability properties can be developed by addition of a transition metal oxide compound such as Nb_2O_5 [260, 261]. Furthermore, addition of alkali ions such as K^+ to the tellurite glass network also improves thermal stability and generates non-bridging oxygen sites while enhancing ionic mobility which ultimately results in high lanthanide solubility [71]. Therefore, in this study, TeO_2-K_2TeO_3-WO_3-Nb_2O_5 tellurite glass system is specially designed for the encapsulation of optically active Ho^{3+} and Er^{3+} ions to achieve superior optical features without sacrificing essential durability properties.

Er^{3+} ions are notorious in FIR based temperature sensing due to a pair of TCL in green region of the visible spectrum [253, 262-265]. Ho^{3+} or Ho^{3+}/Yb^{3+} doped phosphors and crystals are also extensively investigated to achieve precise temperature sensing [256, 266-268]. However, there is limited report on the temperature sensing behavior of Ho^{3+} doped glassy materials despite the fact that their high potential in this field [269]. In this work, we report comprehensive investigation of a tellurite glass doped with Ho^{3+} and Ho^{3+}/Er^{3+} ions for FIR based optical temperature sensing. Co-doping of Er^{3+} ions and Ho^{3+} ions reveals the possibility of working in the up-conversion regime due to favorable absorption cross-section of Er^{3+} ions at around 980 nm. Therefore, variations of the emission bands arising in up- and down-converted photoluminescence (PL) spectra of prepared samples are used for temperature sensing. Radiative properties of the proposed samples are investigated in terms of Judd-Ofelt (J-O) analysis and temperature dependent PL measurements. Gradual decrease in the intensity of some of the observed emission bands detected with the increasing temperature and the temperature sensing capability is interpreted in terms of FIR and sensitivity calculations.

7.2 Experimental Section

7.2.1 Glass Synthesis

In this study, a special tellurite glass composition is designed for FIR based optical temperature sensing applications. The base glass is synthesized with the chemical composition of $60TeO_2$-$20K_2TeO_3$-$10WO_3$-$10Nb_2O_5$ (in mol %). 3 mol % from Ho_2O_3 and Ho_2O_3/Er_2O_3 are incorporated to the base glass composition to obtain Ho^{3+} and Ho^{3+}/Er^{3+} doped tellurite glass samples, respectively. Final compositions of the glass samples are checked through EDS technique in a Tescan Maia3 XMU microscope linked with Oxford Xmax 50 energy-dispersive X-ray spectrometer and the results show that final compositions are in a good match with nominal compositions. Therefore, synthesized glass samples are coded as follows: G: Base glass, G-Ho: 3 mol % Ho_2O_3 doped glass, and G-Ho/Er: 3 mol % Ho_2O_3 and 3 mol % Er_2O_3 doped glass.

Glasses are prepared through conventional melt quenching technique by using high purity chemicals. Batches of 50 g are weighed in a precision scale and mixed in an agate mortar with a pestle to ensure homogeneity. Afterwards, well mixed batches are melted in platinum crucible covered with lid at 950 °C for 45 min. The melts are stirred periodically to improve homogeneity. Glass samples are obtained by casting the melts into a graphite mold. Subsequently, samples are transferred into an annealing furnace for 2 h at 320 °C and then cooled inside the furnace down to room temperature for the elimination of internal stresses eradicated as a result of quenching. The prepared samples of a rectangular shape are thoroughly polished to obtain plane-parallel surfaces for the following characterizations.

7.2.2 Measurements and Characterization Studies

Amorphous nature of glass samples is controlled through X-ray diffraction analysis (XRD) using a Philips/PANalytical X'pert Pro powder diffractometer with CuK_α radiation operated at 45 kV and 40 mA in the 2θ scanning range from 20° to 80° with a step size of 0.02°. Density values of prepared glasses are measured by the Archimedes' method using distilled water as the immersing medium with an electronic balance of sensitivity 10^{-4} g. Repetitive measurements up to five times are conducted and average values are calculated with an estimated error of ±1 %.

Refractive indices are determined through Brewster angle method with a resolution of 0.05°/step. Physical properties are calculated according to the expressions reported elsewhere [120]. Thermal properties of glass samples are investigated via differential scanning calorimetry (DSC) analysis in a Netzsch DSC 204F1 (limit of detection: <0.1μV, with an error estimate of ± 1°C) instrument. DSC analysis is conducted with sample weight of 25 ± 1 mg in aluminum pans, under 25 ml/min flowing argon atmosphere with a heating rate of 10 °C/min. Glass transition onset (T_g), crystallization onset and peak temperatures (T_c/ T_p) are determined accordingly. In addition, thermal stability of glasses is assessed through the calculation of thermal stability value: $\Delta T = T_c$-T_g.

Structural investigations are conducted by Fourier transform infrared (FTIR) spectroscopy in the wavenumber range 400-1000 cm^{-1} with a resolution of 1 cm^{-1} in a Bruker Hyperion 3000 spectrometer. Optical absorption spectra of glass samples are monitored using Perkin Elmer Lambda 950 spectrophotometer in the wavelength range 400-2000 nm with a resolution of 0.5 nm. Non-overlapping transitions of Ho^{3+} and Er^{3+} ions are cautiously selected for accurate determination of integrated areas under optical absorbance spectra to calculate experimental (S_{exp}) line strength values. Theoretical line strengths (S_{theo}), S_{exp}, branching ratios (β), radiative transition probabilities (A_{ED} and A_{MD}), lifetime (τ_{cal}) values and J-O parameters are calculated as described elsewhere [85, 86, 204].

PL spectra are measured in an Edinburgh Instruments FS5 spectrofluorometer with a signal-noise ratio of water Raman signal >6000:1. Glass samples are excited with a 150 W Xenon lamp or power tunable (0-2 W) 973 nm IR laser operating in CW mode. Temperature-dependent PL measurements are realized in the range of 298 - 558 K using a heated solid transmission attachment from Pike Technologies placed in the spectrofluorometer. Decay profiles are obtained by monitoring the green and red emissions with respect to time and well fitted with second order exponential equation [120]:

$$I(t) = A_1 e^{\left(\frac{-t}{\tau_1}\right)} + A_2 e^{\left(\frac{-t}{\tau_2}\right)}, \quad (7.1)$$

where $I(t)$ stands for the fluorescence emission intensity at given time t, τ_1 and τ_2 are the luminescence lifetime values and A_1 and A_2 are constant parameters. Obtained χ^2

values are close to unity that indicates the quality of the fit. Average lifetimes of related transitions are determined according to the following formula [120]:

$$\tau_{meas} = \frac{A_1\tau_1^2 + A_2\tau_2^2}{A_1\tau_1 + A_2\tau_2}. \quad (7.2)$$

Experimentally obtained FIR data are fitted through following Arrhenius type equation [270]:

$$FIR = \frac{I_a}{I_b} = Cexp\left(-\frac{\Delta E}{k_B T}\right), \quad (7.3)$$

where I_a and I_b are PL intensities of related transitions, C is a constant, k_B is Boltzmann coefficient and T is absolute temperature.

Absolute (S_A) and relative sensitivity (S_R) values are determined by the first derivative of FIR and 1/FIR through equations 4 and 5, respectively [270]:

$$S_A = \frac{dFIR}{dT} = FIR\left(\frac{\Delta E}{k_B T^2}\right), \quad (7.4)$$

$$S_R = \frac{1}{FIR}\frac{dFIR}{dT} = \frac{\Delta E}{k_B T^2}. \quad (7.5)$$

S_A of selected transition pair are also evaluated through J-O intensity parameters according to the following expression [271]:

$$S_A = \frac{d(FIR)_{a/b}}{dT} \propto \frac{\left[\Omega_2 \times |\langle ij \| U_2 \| kj' \rangle|^2 + \Omega_4 \times |\langle ij \| U_4 \| kj' \rangle|^2 + \Omega_6 \times |\langle ij \| U_6 \| kj' \rangle|^2\right]_a}{[\Omega_2 \times |\langle ij \| U_2 \| kj' \rangle|^2 + \Omega_4 \times |\langle ij \| U_4 \| kj' \rangle|^2 + \Omega_6 \times |\langle ij \| U_6 \| kj' \rangle|^2]_b} \times \frac{\Delta E}{k_B T^2}, \quad (7.6)$$

where $\|U_\lambda\|^2$ (λ = 2, 4, 6) are doubly reduced matrix elements of the transition from ith excited level to ground state k, Ω_2, Ω_4, Ω_6 are the J-O intensity parameters. $\|U_\lambda\|^2$ values are not affected by the local environment or by the host but only depend on considered lanthanide ion. Therefore, necessary values are directly adopted from the astonishing work of Carnall et al [272].

Table 7.1 Physical parameters of synthesized glass samples

Parameter	G	G-Ho	G-Ho/Er
Density, (g/cm^3)	4.86	4.91	4.96
Refractive Index	2.44	2.47	2.51
Molar Volume, V_M (cm^3/mol)	38.594	38.201	37.816
V_O ($cm^3.mol^{-1}$)	19.30	19.10	18.91
OPD ($mol.L^{-1}$)	51.82	52.35	52.89
Molar Refraction, R_m (cm^3)	24.037	24.054	24.148
Reflection Loss, R_L (%)	17.523	17.946	18.507
Molar Electronic Polarizability, α_m ($10^{-24}.cm^3$)	9.538	9.545	9.582
Dielectric Constant, ε	5.954	6.101	6.300
Optical Dielectric Constant, ε^{-1}	4.954	5.101	5.300
Electronic Polarizability, α_e ($Å^3$)	0.953	0.954	0.958
Ionic Concentration, N (10^{20} ions/cm^3)	-	4.694	9.424
Polaron Radius, R_p (Å)	-	5.185	4.110
Inter Ionic Distance, R_i (Å)	-	12.868	10.200
Field Strength, F (cm^{-2}) $\times 10^{16}$	-	2.455	3.908
Metallization Factor, M	0.377	0.370	0.361
Optical Basicity, Λ	0.9450	0.9450	0.9451

7.3 Results and Discussion

7.3.1 Physical, Thermal and Structural Properties

Macro photos of synthesized glass samples revealing high transparency are shown in Figure 7.1. Sample G possesses light yellow color; however, a slight darkening is detected with incorporation of lanthanide ions to the base glass composition. Therefore G-Ho and G-Ho/Er glass samples exhibit yellow and dark amber colors, respectively. Various physical properties calculated from experimentally determined refractive index and density values are listed in Table 7.1. Densities of prepared glass samples show an increment with the addition of lanthanide ions

due to relatively higher molecular weights of Ho_2O_3 (377.9 g/mol) and Er_2O_3 (382.6 g/mol) compared to other compounds in the base glass composition. Increase in the concentration of dopant ions reduces the inter ionic distance which ultimately results in more compact glass network. Tightly packing of glass network causes increment of electronic polarizability, α_e, that describes the magnitude of electrons responding to an electric field. The increase in electronic polarizability value is responsible for the increment of dielectric and optical dielectric constants and so refractive index.

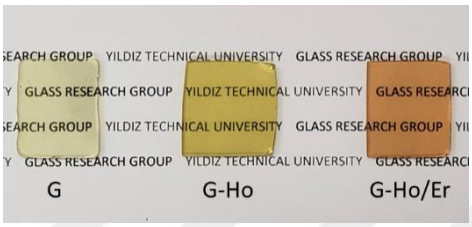


Figure 7.1 Macro photos of transparent samples under daylight

XRD patterns and DSC curves of prepared samples are given in Figure 7.2. XRD measurements reveal amorphous halos without presence of sharp peaks and glass transition reactions are detected from DSC analysis confirming the amorphous nature of prepared glass samples. T_g values are determined as 613, 618 and 629 K for G, G-Ho and G-Ho/Er samples, respectively. The increment in T_g with incorporation of lanthanide ions is assigned to the addition of Ho_2O_3 and Er_2O_3 which possess greater number of cations per mol and higher average cross-link density compared to glass forming compounds [210]. Exothermic peaks associated with crystallization and/or transformation of different phases from glassy matrix are detected at relatively elevated temperatures. Thermal stability, ΔT, provides information about the stability of glasses against crystallization [67]. Calculated ΔT values for G, G-Ho and G-Ho/Er samples are found as 190, 97 and 82 K, respectively. These results reveal that the base glass (G) is extremely stable against crystallization, however incorporation of lanthanide ions to the base glass composition and increasing their content result in a decrease in ΔT values. Nevertheless, obtained thermal stability values for G-Ho and G-Ho/Er samples are still quite adequate for their use in practical applications. Hence, glass samples

prepared in this study are found suitable to be used approximately up to 613 K without any glass relaxation and/or crystallization that can cause complications.

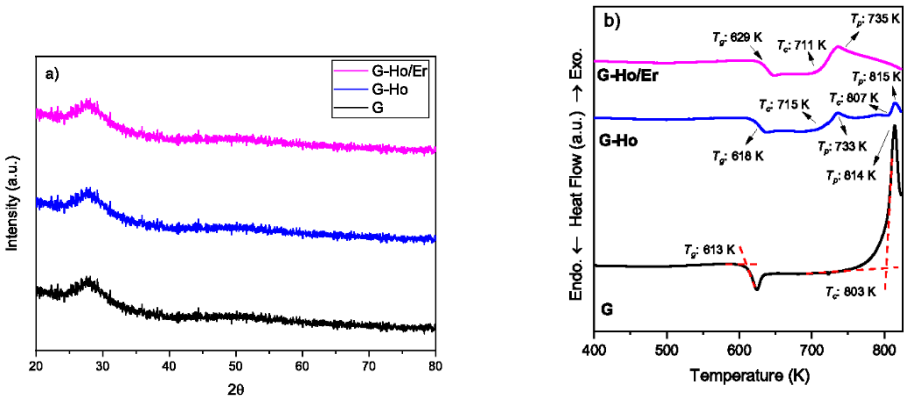


Figure 7.2 a) XRD patterns and b) DSC curves of studied samples confirming their glassy nature

FTIR spectra exhibit broad peaks and shoulders due to lack of long-range periodicity of glass structure (see Figure 7.3). FTIR bands are attributed by considering the reported IR data of each raw material. The relatively narrow band located at around 536 cm^{-1} is arisen due to stretching vibrations of Te–O–W or asymmetric vibrations of Te–O–Te linkages. The peaks at around 615 cm^{-1} and 679 cm^{-1} are due to the stretching vibrations of Te–O–Te linkages in TeO_4 trigonal bipyramid units. Asymmetric stretching vibrations of TeO_3 trigonal pyramid or TeO_{3+1} polyhedral units result in a broad peak at around 783 cm^{-1}. In addition, stretching vibrations of W–O–W linkages create a hardly visible band at around 828 cm^{-1}. According to the previous reports, stretching vibrations of Nb–O linkages of NbO_6 units take place in the range of 850 – 950 cm^{-1} [261, 273]. However, this signal could not be detected due to relatively less amount of Nb_2O_5 content. Consequently, lanthanide incorporation does not make significant changes in the glass structure that can be detectable through FTIR analysis. Therefore, FTIR bands are found to remain at almost same positions upon varying lanthanide ion content.

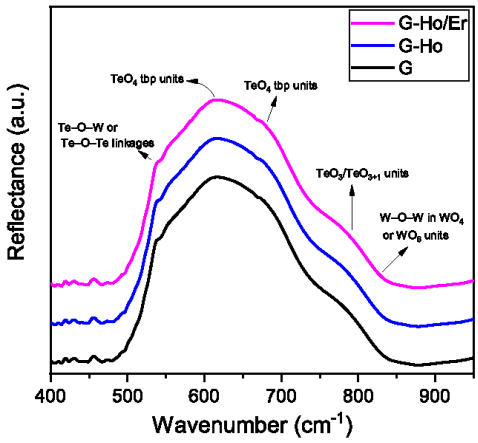


Figure 7.3. FTIR spectra of glass samples revealing broad peaks and shoulders originated from glass structure

7.3.2 Absorption Spectra, Judd-Ofelt Analysis and Radiative Properties

Optical absorption spectra of prepared glass samples are illustrated in the Vis-NIR range (see Figure 7.4). A total of seven absorption peaks related to electronic transitions of Ho^{3+} ions from ground level ($^5I_8$) to the elevated energy states centered at 419, 449, 485, 539, 643, 1154 and 1949 nm are detected for G-Ho sample. Six absorption peaks of Er^{3+} ions between $^4I_{15/2}$ ground state and elevated energy states centered at 489, 519, 650, 798, 975 and 1532 nm are observed along with absorption bands of Ho^{3+} ions for G-Ho/Er sample. The rich energy level structure of Ho^{3+} and Er^{3+} ions make them appealing for various optical purposes.

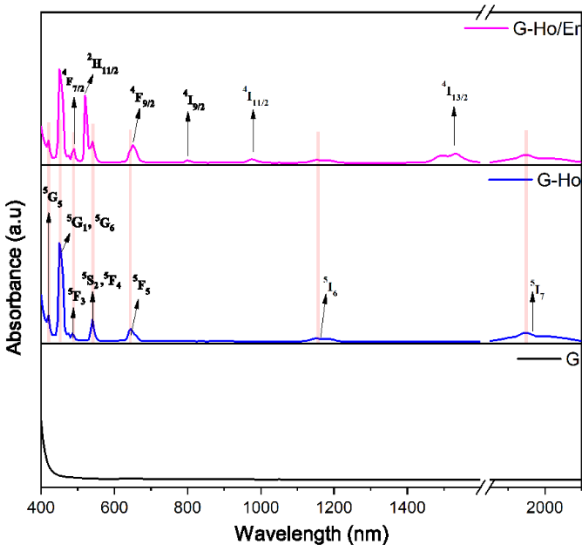


Figure 7.4 Absorbance spectra of glass samples exposing characteristic electronic transitions of Ho^{3+} and Er^{3+} ions along with absorption edge of the glass matrix

J-O analysis is adopted to investigate spectroscopic parameters of G-Ho and G-Ho/Er samples without taking into account the energy transfer and multiphonon de-excitation probabilities. Absorbance spectra are used to calculate S_{exp} and calculated values are given in Table 7.2 along with S_{theo} values. Line strength establishes the probability between a specific initial level to all $2J_f + 1$ levels of the final state. $^5I_8 \rightarrow {}^5G_6$ transition of Ho^{3+} ions and $^4I_{15/2} \rightarrow {}^2H_{11/2}$ transition of Er^{3+} ions possess dominant absorption band due to their hypersensitive nature compared to other transitions. Therefore, they both have significantly higher line strength values as can be seen from Table 7.2 and they obey the selection rules $|\Delta S|=0$, $|\Delta L|\leq 2$, and $|\Delta J|\leq 2$. Line strength values are used to calculate J-O intensity parameters through least square fitting method.

Table 7.2 Linestrengths of the transitions used in Judd-Ofelt analysis

Transition	λ (nm)	S_{exp}	S_{theo}
Ho^{3+}→ Ground state: $^5I_8$ (G-Ho)			
$^5F_1+^5G_6$	450	35.54	35.54
$^5F_4+^5S_2$	538	5.14	5.17
$^5F_5$	644	5.75	5.73
$^5I_6$	1164	2.74	2.70
$^5I_7$	1972	6.52	6.52
δ_{rms}		0.0347	
Er^{3+}→ Ground state: $^4I_{15/2}$ (G-Ho/Er)			
$^2H_{11/2}$	519	16.02	16.03
$^4I_{9/2}$	798	1.00	0.99
$^4I_{11/2}$	973	1.20	1.23
$^4I_{13/2}$	1530	6.62	6.61
δ_{rms}		0.0342	
Ho^{3+}→ Ground state: $^5I_8$ (G-Ho/Er)			
$^5F_1+^5G_6$	450	38.94	38.94
$^5F_4+^5S_2$	538	6.97	7.06
$^5F_5$	644	9.47	9.43
$^5I_6$	1164	2.88	2.81
$^5I_7$	1972	7.21	7.20
δ_{rms}		0.0832	

Ω_2 parameter depicts hypersensitive transitions and relies on short-range effects e.g. covalency of ligand-lanthanide bond and structural distortion in the lanthanide ion environment. Additionally, these transitions possess relatively larger $\|U_2\|$ values compared to $\|U_4\|$ and $\|U_6\|$ values. Peak intensities of hypersensitive transitions are exceedingly sensitive to the local structure of the optically active lanthanide ion. Therefore, minor distortions and/or changes in the local structure may trigger a significant intensity enhancement of these transitions. Ω_4 and Ω_6 parameters are related to bulk (long-range) properties of

the host material such as rigidity and basicity. They retain higher values due to enhanced vibrational amplitude of lanthanide-ligand distance and ionic packing [274]. According to Table 7.3, tellurite glasses of the present study have higher magnitude of J-O intensity parameters compared to previously reported Ho^{3+} and Ho^{3+}/Er^{3+} doped hosts [207, 212, 213, 215, 216, 275-278]. This indicates strongly perceived crystal-field strength by the lanthanide ions which ultimately results in larger fluorescence intensity ratios and higher sensitivities [274]. $\Omega_2 > \Omega_4 > \Omega_6$ and $\Omega_4 > \Omega_2 > \Omega_6$ trends are followed by G-Ho and G-Ho/Er samples, respectively. Ω_2 and Ω_4 parameters are significantly higher compared to others due to covalent environment around lanthanide ions and highly distorted (asymmetric) structure of the tellurite glass. G-Ho and G-Ho/Er samples show high spectroscopic quality factors indicating that favorable emission can be obtained from the investigated samples [170]

Table 7.3 Judd-Ofelt intensity parameters Ω_2, Ω_4, Ω_6 (10^{-20} cm^2), their trend and spectroscopic quality factor (Ω_4/Ω_6) of prepared glass samples along with the literature data

Samples	Ω_2	Ω_4	Ω_6	Ω_λ trend	Ω_4/Ω_6	Reference
Ho^{3+}						
G-Ho	17.97	9.24	3.17	$\Omega_2 > \Omega_4 > \Omega_6$	2.91	Present work
G-Ho/Er	15.19	18.36	2.86	$\Omega_4 > \Omega_2 > \Omega_6$	6.41	Present work
Tellurite	5.59	4.85	2.66	$\Omega_2 > \Omega_4 > \Omega_6$	1.82	[207]
Tellurite	10.77	2.07	1.04	$\Omega_2 > \Omega_4 > \Omega_6$	1.99	[212]
Silicate	2.87	1.71	0.69	$\Omega_2 > \Omega_4 > \Omega_6$	2.48	[216]
Germanotellurite	4.25	2.48	1.31	$\Omega_2 > \Omega_4 > \Omega_6$	1.89	[215]
$LiNbO_3$	7.39	11.96	11.39	$\Omega_4 > \Omega_6 > \Omega_2$	1.05	[213]
Er^{3+}						
G-Ho/Er	8.17	24.18	2.52	$\Omega_4 > \Omega_2 > \Omega_6$	9.59	Present work
Tellurite	5.22	1.55	1.13	$\Omega_2 > \Omega_4 > \Omega_6$	1.37	[275]
Borosilicate	6.69	3.08	3.28	$\Omega_2 > \Omega_6 > \Omega_4$	0.93	[276]
Fluorophosphate	4.14	1.32	1.21	$\Omega_2 > \Omega_4 > \Omega_6$	1.09	[277]
Fluoride	2.68	1.09	0.99	$\Omega_2 > \Omega_4 > \Omega_6$	1.10	[278]

Branching ratios (β), radiative transition probabilities (A_{ED} and A_{MD}) and lifetime (τ_{cal}) values are calculated through J-O intensity parameters (see Table 7.4). Calculations reveal far higher transition probabilities for main radiative transitions at green and red emission bands compared to other non-radiative transitions for both samples. This refers that the favorable emissions are obtainable at the related wavelengths. Additionally, β values of all radiative transitions are greater than 0.50 depicting that sufficient portion of the total photon flux reaches to lower energy state from upper radiative state to acquire such emission intensity comparable to a pleasing laser emission.

Table 7.4 Radiative properties of the prepared glass samples for selected transitions

Transitions	λ (nm)	A_{ED} (s^{-1})	A_{MD} (s^{-1})	β (10^{-28} cm^3)	τ_{cal} (μs)
Ho^{3+} (G-Ho)					
$^5S_2 \rightarrow {}^5I_8$	550	7526.12	-	0.5529	73.5
$^5F_4 \rightarrow {}^5I_8$	550	26584.733	-	0.7801	29.3
$^5F_5 \rightarrow {}^5I_8$	660	15182.46	-	0.7830	51.6
$^5F_4 \rightarrow {}^5F_5$	3255	93.60	8.51	0.0030	9792.4
$^5S_2 \rightarrow {}^5F_5$	3420	3.72	-	0.0003	268482
Er^{3+} (G-Ho/Er)					
$^2H_{11/2} \rightarrow {}^4I_{15/2}$	533	10092.58	-	0.9411	11.6
$^4S_{3/2} \rightarrow {}^4I_{15/2}$	546	23322.64	-	0.6441	88
$^2G_{9/2} \rightarrow {}^4I_{13/2}$	555	21233.18	-	0.4781	34.6
$^4F_{5/2} \rightarrow {}^4I_{13/2}$	643	2422.904	-	0.5738	28.6
$^2K_{15/2} \rightarrow {}^4I_{9/2}$	650	32257.327	-	0.4109	74.8
$^4F_{9/2} \rightarrow {}^4I_{15/2}$	672	15961.07	-	0.7929	24.4
$^4S_{3/2} \rightarrow {}^4F_{9/2}$	3108.5	4.129	-	0.0004	242198.4
$^2H_{11/2} \rightarrow {}^4S_{3/2}$	12562.8	1.204	-	0.0005	830490.6
$^4F_{7/2} \rightarrow {}^2H_{11/2}$	8591.1	1.612	-	0.0003	620187
$^4F_{5/2} \rightarrow {}^4F_{7/2}$	6053.3	8.539	1.555	0.0002	99067.7
$^2G_{7/2} \rightarrow {}^4F_{5/2}$	1692.9	577.797	3.851	0.0036	1198.5
Ho^{3+} (G-Ho/Er)					
$^5S_2 \rightarrow {}^5I_8$	550	6778.84	-	0.5367	79.2
$^5F_4 \rightarrow {}^5I_8$	550	6253.398	-	0.7401	19.3
$^5F_5 \rightarrow {}^5I_8$	660	48587.56	-	0.9450	31.8
$^5F_4 \rightarrow {}^5F_5$	3255	99.95	8.517	0.0021	9219
$^5S_2 \rightarrow {}^5F_5$	3420	6.97	-	0.0006	143396.9

Absolute sensitivity (S_A) of the selected emission band pairs are expressed in terms of J-O intensity parameters as follows:

$$S_{A(546/660)} \propto \frac{\Omega_6 \times 0.22113}{\Omega_4 \times 0.425 + \Omega_6 \times 0.56866} \times \frac{\Delta E}{k_B T^2}, \tag{7.7}$$

$$S_{A(546/533)} \propto \frac{\Omega_6 \times 0.22113}{\Omega_2 \times 0.71255 + \Omega_4 \times 0.41236 + \Omega_6 \times 0.09246} \times \frac{\Delta E}{k_B T^2}. \tag{7.8}$$

Sensitivity of $I_{546/533}$ pair highly depends on Ω_2 and Ω_4, while $I_{546/660}$ relies on Ω_4 parameter. As previously mentioned, calculated J-O intensity parameters follow $\Omega_2 > \Omega_4 > \Omega_6$ or $\Omega_4 > \Omega_2 > \Omega_6$ trends G-Ho and G-Ho/Er samples, respectively and Ω_2 and Ω_4 parameters are significantly higher compared to Ω_6. Therefore, one can predict that $I_{546/660}$ should possess higher S compared to $I_{546/533}$ by evaluating J-O intensity parameters. This estimation has been confirmed by experimental results which will be discussed in section 3.4.

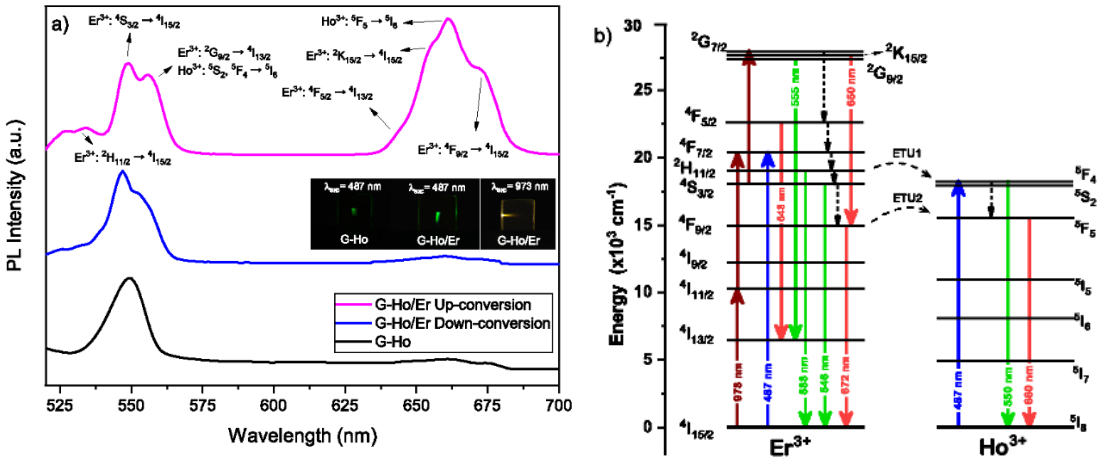


Figure 7.5 a) Room temperature PL spectra of glass samples (inset shows emission colors of samples) b) Possible up- and down-conversion mechanisms in partial Jablonski diagram of Er^{3+} and Ho^{3+} ions

7.3.3 Room-temperature Photoluminescence Measurements

PL spectra of glass samples under 487 and 973 nm light sources are illustrated in Figure 7.5a. Down-conversion scheme gives rise to dominant green emission for both G-Ho and G-Ho/Er samples related to combination of $^4S_{3/2} \rightarrow {}^4I_{15/2}$ (546 nm, Er^{3+}) and $^5S_2$, $^5F_4 \rightarrow {}^5I_8$ (550 nm, Ho^{3+}) radiative transitions. Er^{3+} addition slightly shifts the peak of emission band from 550 nm to 546 nm due to domination of Er^{3+} ions over Ho^{3+} ions. This behavior is also supported by the higher A_{ED} value of $^4S_{3/2} \rightarrow {}^4I_{15/2}$ transition calculated through J-O analysis (see Table 7.4). Under 487 nm excitation, both G-Ho and G-Ho/Er samples give rise to red emissions corresponding to $^4F_{9/2} \rightarrow {}^4I_{15/2}$ (672 nm, Er^{3+}), $^5F_5 \rightarrow {}^5I_8$ (660 nm, Ho^{3+}), $^2K_{15/2} \rightarrow {}^4I_{9/2}$ (650 nm, Er^{3+}) and $^4F_{5/2} \rightarrow {}^4I_{13/2}$ (643 nm, Er^{3+}) transitions. Insufficient population of Ho^{3+}: $^5F_5$ state and Er^{3+}: $^4F_{9/2}$ state are the main reason of weak red emission through down-conversion. On the contrary, G-Ho/Er sample shows an intense red emission overpassing green emission upon 973 nm NIR excitation. Excited energy states ($^2H_{11/2}$ and $^4F_{9/2}$) of Er^{3+} ions populate two main radiative states ($^5S_2$ and $^5F_5$) of Ho^{3+} ions through energy transfer up-conversion (ETU) process. Therefore, intensity of the red emission at around 660 nm is enhanced significantly by the co-work of Er^{3+} and Ho^{3+} ions (see Figure 7.5b). Furthermore, a more finely structured PL spectrum is observed upon 973 nm NIR excitation revealing additional transitions which are indicated in Figure 7.5a.

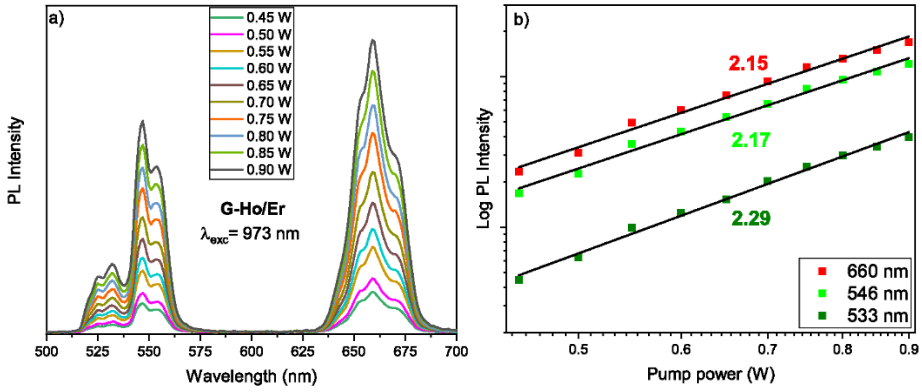


Figure 7.6 a) Pump power dependent PL spectra of G-Ho/Er sample b) Log-Log plot of pump power versus UC emission intensities of G-Ho/Er sample under 973 nm laser irradiation

Figure 7.6 illustrates pump power dependent (from 0.45 to 0.90 W) UC luminescence spectra and Log-Log plot of pump power versus emission intensities at 533, 546 and 660 nm. In general, UC PL emission intensity (I_{UC}) depends on pumping power (P) according to $I_{UC} \propto P^n$ where n is the number of photons needed to populate radiative states of optically active lanthanide ions (see Figure 7.6a). From Figure 7.6b, linear fitting slopes of emission bands at 533, 546 and 660 nm are determined as 2.29, 2.17 and 2.15, respectively. This indicates that two photons involve in populating related radiative state of Ho^{3+} and Er^{3+} ions. As also observed in this study, the character of unsaturated UC emission spectra highly depends on pumping power. Alterations in the intensity of emission bands result a change in FIRs of related transitions and ultimately affect the optical temperature sensing behavior. According to Figure 7.6b, rate of intensity change of 660 and 546 nm emissions are quite similar to each other, while 533 nm show slightly larger rate of change. Therefore, further corrections should be carried out to achieve the highest possible sensitivity in further practical applications of Ho^{3+}/Er^{3+}doped tellurite glasses in the frame of FIR based temperature sensing.

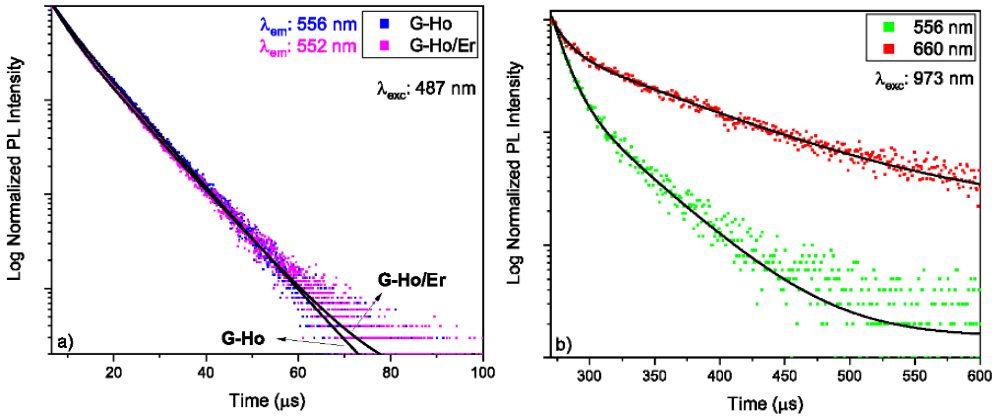


Figure 7.7 Time-resolved PL spectra of prepared samples a) under 487 nm excitation for G-Ho and G-Ho/Er glass samples b) under 973 nm for G-Ho/Er glass sample

Decay profiles of green and red emission in the frame of up and down conversion schemes are given in Figure 7.7. Lifetimes (τ_{exp}) of down-converted green emissions of G-Ho and G-Ho/Er samples are calculated as 7.41 μs and 6.91 μs, respectively. Up-converted green (27.17 μs) and red (85.29 μs) emissions of G-Ho/Er sample possess longer τ_{exp} values compared to down-converted green emissions generated by G-Ho and G-Ho/Er samples. This behavior could be explained by excited state absorption (ESA) through long-lived states of $^4I_{11/2}$ and/or $^4I_{13/2}$ which act as reservoir to populate $^4F_{7/2}$ state. In addition, τ_{cal} values (see Table 7.4) are found to be greater compared to τ_{exp} values due to high error margin of J-O analysis in calculating lifetime values and multiphonon relaxation of lanthanide ions.

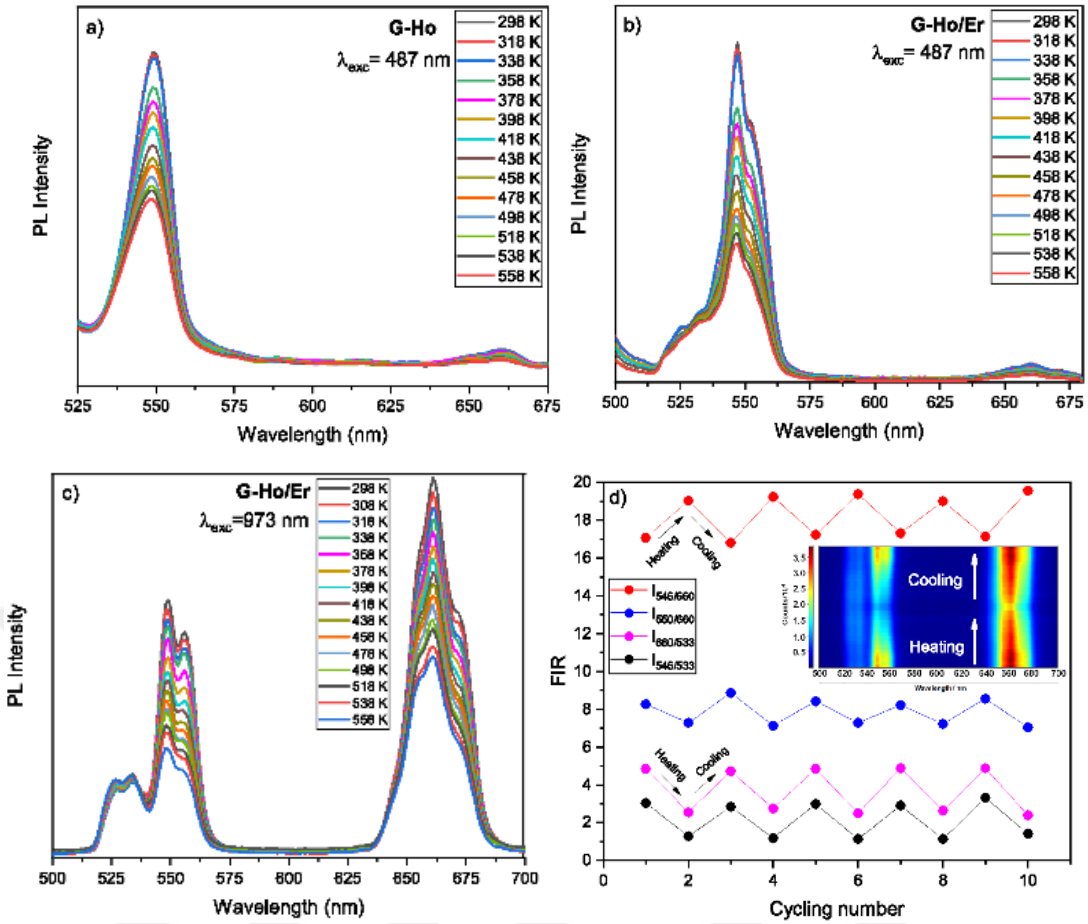


Figure 7.8 Temperature dependent PL spectra of a) G-Ho and b) G-Ho/Er samples under 487 nm excitation and c) G-Ho/Er sample under 973 nm (0.70 W) excitation d) Temperature dependent variation of FIRs alternating between measured maximum and minimum temperatures (inset shows temperature dependent emission mapping of G-Ho/Er sample under 973 nm excitation after 5 heating-cooling cycles)

7.3.4 Optical Temperature Sensing

Temperature dependent up-converted and down-converted emission spectra of G-Ho and G-Ho/Er samples are given in Figure 7.8a-c. Four different emission band pairs ($I_{550/660}$, $I_{660/533}$, $I_{546/533}$ and $I_{546/660}$) are investigated in the frame of up- and down-conversion schemes to explore optical temperature sensing capability of prepared glasses. Therefore, FIR and sensitivity values of the investigated transition pairs are illustrated in Figure 7.9 and Figure 7.10, respectively. As illustrated in Figure 7.8a-c, all observed emission bands keep their positions upon changing temperature. Temperature dependent PL spectra of G-Ho sample show that intensity of $^5F_5 \rightarrow {}^5I_8$ (660 nm) transition appears to be insensitive to temperature change, while intensity of $^5S_2$, $^5F_4 \rightarrow {}^5I_8$ (550 nm) transition gradually

decreases with increasing temperature under 487 nm excitation Additionally, weak down-converted red emission of G-Ho/Er sample at around 660 nm is remain unresponsive to the temperature change (Figure 7.8b) while NIR excitation give rise to dominant and temperature dependent up-converted red emission (Figure 7.8c). Intensity change of $^5S_2$, $^5F_4 \rightarrow ^5I_8$ transition could only be detected in the temperature range of 358 – 558 K where the FIR decreases significantly with increasing temperature which ultimately results in more steeped curve at higher temperatures. FIR of green and red emissions obtained from G-Ho/Er sample increase with a decreasing slope as the temperature increases. As similarly observed in G-Ho sample, gradual intensity change can only be obtained in the temperature range of 358 – 558 K and red emission remain unresponsive to the temperature change.

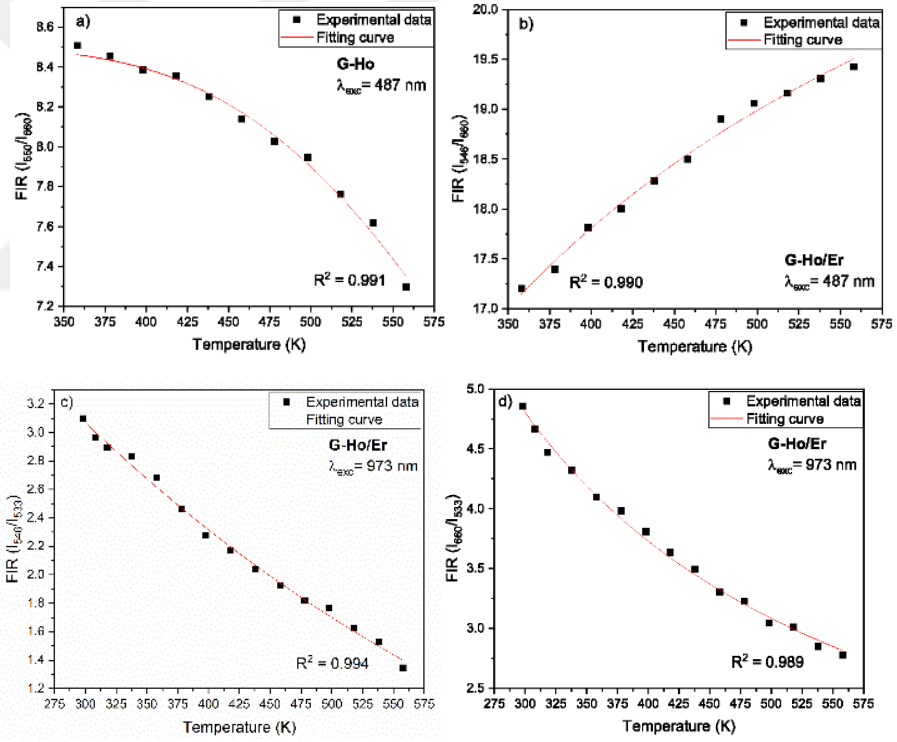


Figure 7.9 Experimentally measured and fitted FIR graphs corresponding to a) $I_{550/660}$ b) $I_{546/660}$ c) $I_{546/533}$ d) $I_{660/533}$ intensity ratios

Reliability of the FIRs after several heating-cooling cycles is investigated and results are given in Figure 7.8d. FIR values restore to their initials after heating to elevated temperatures followed by cooling to RT and the cycle is repeatable and reversible without any considerable change in FIR values. Thus, excellent thermal

stability of the samples is confirmed after five almost identical cycles in terms of emission intensities.

Thermally coupled emission bands centered at 533/546 nm and non-thermally coupled emission bands centered at 660/533 nm are used to calculate the FIRs for G-Ho/Er sample through up-conversion regime. Intensity of the $^{2}H_{11/2}\rightarrow{}^{4}I_{15/2}$ (533 nm, Er^{3+}) transition remain unresponsive to temperature change, while intensities of $^{4}S_{3/2}\rightarrow{}^{4}I_{15/2}$ (546 nm, Er^{3+}) and $^{5}F_{5}\rightarrow{}^{5}I_{8}$ (660 nm, Ho^{3+}) transitions gradually decrease starting from room temperature up to 558 K. Therefore, detectable temperature range is 60 K wider compared to down-conversion scheme. FIR of both emission band pairs exhibit downward tendency with a declining slope, while FIR of $I_{546/533}$ pair possess almost a linear behavior (see Figure 7.9c).

Table 7.5 Absolute sensitivity, S_A, relative sensitivity, S_R, and temperature range of applied intensity ratios along with different Ho^{3+} and Er^{3+} doped materials

Host material	S_A (max) (K^{-1})	S_R (max) (% K^{-1})	Range (K)	Reference
G-Ho ($I_{550/660}$)	0.0111 @ 558 K	0.20 @ 558 K	358 – 558	Present work
G-Ho/Er ($I_{546/660}$)	0.0172 @ 358 K	0.058 @ 358 K	358 – 558	Present work
G-Ho/Er ($I_{546/533}$)	0.0082 @ 298 K	2.48 @ 298 K	298 – 558	Present work
G-Ho/Er ($I_{660/533}$)	0.0145 @ 298 K	0.62 @ 298 K	298 – 558	Present work
Fluorotellurite glass: Er^{3+}	0.0072 @ 547 K	-	83 – 863	[253]
Tellurite glass: Er^{3+}	0.0089 @ 473 K	0.53 @ 198 K	278 – 473	[279]
Fluorotellurite glass: Er^{3+} / Yb^{3+}	0.0048 @ 493 K	-	303 – 603	[270]
Germanate glass: Er^{3+} / Yb^{3+}	0.0036 @ 493 K	-	293 – 493	[280]
Gd_2O_3 nanoparticles: Ho^{3+} / Yb^{3+}	-	0.0080 @ 216 K	140 – 280	[256]
Y_2O_3 phosphors: Ho^{3+} / Yb^{3+}	0.0030 @ 673 K	-	299 – 673	[281]
2CaO-Al_2O_3 glass: Er^{3+}	0.0159 @ 645 K	-	150 – 762	[271]
$CaMoO_4$: Er^{3+} / Yb^{3+}	0.0143 @ 575 K	-	303 – 873	[257]
$CaWO_4$: Ho^{3+}	-	0.0062 @ 750 K	300 – 750	[258]
NbO_3–$SrTiO_3$: Ho^{3+}	0.0096 @ 540 K	-	293 – 683	[240]
$PbTiO_3$: Ho^{3+} / Yb^{3+}	0.0036 @ 298 K	-	298 – 493	[282]
$NaCaPO_4$ glass ceramic: Tb^{3+} / Eu^{3+}	0.0455 @ 293 K	0.66 @ 573 K	293 – 573	[246]
Phosphate glass ceramic: Er^{3+} / Yb^{3+}	0.0057 @ 612 K	1.32 @ 303 K	303 – 753	[247]
Phosphate glass ceramic: Ho^{3+} / Yb^{3+} / Tb^{3+}	0.0022 @ 298 K	0.75 @ 298 K	298 – 648	[248]
Phosphate glass: Tb^{3+} / Eu^{3+}	0.01 @ 753 K	1.16 @ 753 K	303 – 753	[249]
Phosphate glass: Tm^{3+} / Yb^{3+}	-	3.94 @ 303 K	303 – 653	[250]

Sensitivity of the temperature measurement sensors are of great importance as well as sensing range in order to be used in practical applications with desired precision. Therefore, first derivatives of the fitted FIR curves are taken to

determine absolute sensitivities of the proposed procedure (see Figure 7.10). Absolute sensitivity, S_A, can be defined as change rate of FIR per unit temperature. Higher S_A value indicates that conducted measurement possess lower error margin. Determined S_A values of $I_{660/533}$, $I_{546/533}$ and $I_{546/660}$ FIRs exhibit continuous decrease with increasing temperature, while $I_{550/660}$ FIR possesses increasing S_A with increasing temperature. Maximum obtained S_A values for each FIR are given in Table 7.5 along with different FIR based temperature sensing materials. In this study, the highest S_A is achieved as 0.0172 K^{-1} for $I_{546/660}$ FIR at around 358 K. However, for $I_{546/660}$ FIR, the S_A dramatically decreases in a wide range if we consider lower detectable temperatures. For relatively higher temperatures (approximately >450 K), $I_{550/660}$ FIR shows better S_A values (0.0111 K^{-1}) compared to $I_{546/660}$ FIR. The most stable S_A reversal is obtained from $I_{546/533}$ FIR in the range of 0.0082 – 0.0049 K^{-1}. S_R values are calculated to compare sensitivity values of proposed samples with different host materials regardless of their nature. S_R defines change of FIR per degree of temperature in the units of percent change and the highest S_R value is calculated as 2.48% K^{-1} at 298 K for $I_{546/533}$ pair. According to Table 7.5, obtained S_A and S_R values in this study are comparable or better compared to previously reported FIR based temperature sensing luminescent materials [240, 253, 256-258, 270, 271, 279-282].

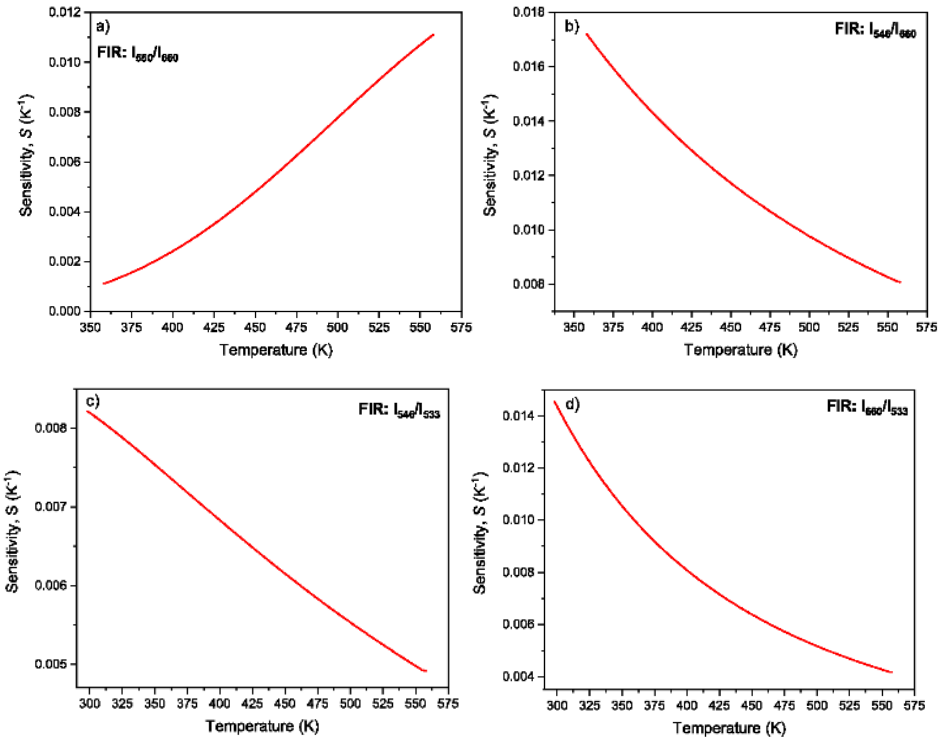


Figure 7.10 Calculated S_A and S_R values corresponding to a) $I_{550/660}$ b) $I_{546/660}$ c) $I_{546/533}$ d) $I_{660/533}$ intensity ratios

7.4 Conclusions

A special tellurite glass composition doped with Ho^{3+} and Er^{3+} ions is designed for obtaining high spectroscopic quality factors to enable favorable emission properties. Thermal characterizations reveal that studied glasses possess noteworthy thermal stability up to approximately 613 K. Four different emission band pairs are comprehensively investigated in the frame of up- and down-conversion regimes. Varying pump power in up-conversion regime slightly altered the rate of change of emission intensities. $I_{546/660}$ pair under 487 nm excitation shows the highest S_A value as 0.0172 K^{-1} at 358 K and $I_{546/533}$ pair under 973 nm excitation reveals the maximum S_R value as 2.48% K^{-1} at 298 K. Temperature change is detectable in the 298 – 558 K range for $I_{546/533}$ and $I_{660/533}$ pairs. Reversibility of the FIRs is confirmed after several heating-cooling cycles. Rich PL spectra of the proposed samples allow the calculation of FIR for different emission band pairs that are exploitable to achieve high sensitivity values in the detectable temperature range. Consequently, obtained results show that prepared glasses

offer promising features to be used as noninvasive optical temperature sensors with high accuracy.

8
RESULTS AND DISCUSSIONS

Lanthanide ions and QDs possess outstanding emission features to be used in various photonic and opto-electronic applications. Colloidal synthesis of lanthanide ion and QD containing luminescent materials are well-matured. However, thermal and chemical stability and photosensitivity of these materials are hindering their integration into further applications. Therefore, robust encapsulation materials are needed to exploit their favorable properties for more advanced applications. In this thesis, specially tailored silicate and tellurite glass matrices were developed and doped with Dy^{3+}, Ho^{3+}, Tm^{3+}, Yb^{3+} and Er^{3+} lanthanide ions and CdSe/$CsPbBr_3$ QDs to obtain photoluminescent glasses and glass nanocomposites. Synthesized glass/glass nanocomposite samples are evaluated to be used in different applications, i.e., solid-state lighting, volumetric display and non-invasive temperature sensing. Generalized results of each core section are given below:

In chapter three, an investigation on Dy^{3+} doped tellurite glasses for solid-state lighting applications are given. Dy^{3+} — that is capable of emitting white light as a mixture of blue and yellow colors — is doped into a tellurite glass matrix in different concentrations. Low phonon energy and favorable optical properties of tellurite glasses are exploited to achieve pure white light generation with competitive color rendering index (CRI) and correlated color temperature (CCT) values by using a single type of lanthanide ion for their evaluation as solid-state lighting materials.

Chapter four presents two alternative white LED device constructions by coupling $CsPbBr_3$ doped silicate-based glass nanocomposite layer with CdSe and Dy^{3+}+CdSe doped layers on top of a blue LED chip to evaluate their potential to be used in solid-state lighting applications. In this work, silicate glasses are chosen as the host material due to difficulties in synthesis of CdSe QDs in tellurite glasses. Significant PLQY enhancement is obtained through co-doping of Dy^{3+} and CdSe

and pure white light emission with excellent color conversion performance and challenging color rendering index values are observed.

Chapter five introduces a novel approach where CdSe and $CsPbBr_3$ QDs are formed together in a silicate glass matrix for the first time to eliminate the disadvantages of multi-layered LED design. In this work, CdSe and $CsPbBr_3$ QDs doped glass nanocomposites demonstrate favorable color tuning ability from yellow-green to red portion of the electromagnetic spectrum with favorable PLQY values under different excitation wavelengths thanks to the energy transfer between different QDs.

In the sixth chapter, instantaneous tuning of emission color in a monolithic tellurite glass doped with $Ho^{3+}/Tm^{3+}/Yb^{3+}$ ions by modulating excitation frequency is experimentally demonstrated for the first time. Emission color changed in the green-red-cool white triangle region and a multicolor plus-shaped image is constructed inside the glass sample using a galvanometer which is underlying their potential to be used in volumetric display applications.

In the seventh chapter, optical temperature sensing behavior of Ho^{3+} and Ho^{3+}/Er^{3+} doped tellurite glasses are investigated in terms of fluorescence intensity ratio (FIR) method in the range of 298 - 558 K. Optical thermometry investigations are carried out through temperature dependent up- and down-converted photoluminescence emissions. The highest possible absolute and relative sensitivities are determined as 0.0172 K^{-1} and 2.48% K^{-1}, respectively indicating the potential of Ho^{3+}/Er^{3+} doped tellurite glasses for their use in noninvasive optical temperature sensing applications.

In this thesis, emission properties are optimized and long-term stability values are obtained for desired applications. Proof-of-concept prototypes for solid-state lighting, volumetric display and non-invasive temperature sensing applications are constructed. The obtained results are promising and highlighting their potentiality to be used in aforementioned applications, however, more research should be conducted in the frame of engineering to achieve their successful integration in commercial products.

In the future studies, PLQY values should be enhanced to match their performance of lanthanide ion and QD doped glasses/glass nanocomposites with their colloidal counterparts. Since it is challenging to synthesize QDs homogeneously in different glass matrices through solid-state synthesis method, more studies are required to obtain necessary information. Investigation of photoluminescent glasses by different research groups will certainly pave the way for their implementation in further opto-electronic applications. In conclusion, this thesis reveals favorable properties and drawbacks of the new generation luminescent glass/glass nanocomposite-based wavelength convertors and also contributes to the integration of these novel materials into high-end applications.

REFERENCES

[1] D. R. Vij, *Luminescence of solids*. New York: Plenum Press, 1998.

[2] E. N. Harvey, *A history of luminescence*. Baltimore: J. H. Furst Company, 1957.

[3] N. T. Kalyani, H. Swart, and S. J. Dhoble, *Principles and applications of organic light emitting diodes*. Duxford: Woodhead Publishing, 2017.

[4] D. M. Jameson, *Introduction to Fluorescence*. Boca Raton: CRC Press, 2014.

[5] J. R. Lakowicz, *Principles of fluorescence spectroscopy*. Singapore: Springer, 2006.

[6] G. D. Gutierrez, "Luminescent organic materials and their application in solar technologies," Ph.D. dissertation, Department of Chemistry, Massachusetts Institute of Technology, Cambridge, 2011.

[7] H. Lin, T. Hu, Y. Cheng, M. Chen, and Y. Wang, "Glass ceramic phosphors: Towards long-lifetime high-power white light-emitting-diode applications–a review," *Laser & Photonics Reviews,* vol. 12, no. 6, p. 1700344, 2018.

[8] M. He, J. Jia, J. Zhao, X. Qiao, J. Du, and X. Fan, "Glass-ceramic phosphors for solid state lighting: A review," *Ceramics International,* vol. 47, no. 3, pp. 2963-2980, 2021.

[9] M. Raukas *et al.*, "Ceramic phosphors for light conversion in LEDs," *ECS Journal of Solid State Science and Technology,* vol. 2, no. 2, pp. R3168-R3176, 2012.

[10] E. Erol, N. Vahedigharehchopogh, O. Kıbrıslı, M. Ç. Ersundu, and A. E. Ersundu, "Recent progress in lanthanide-doped luminescent glasses for solid-state lighting applications—a review," *Journal of Physics: Condensed Matter,* vol. 33, no. 48, p. 483001, 2021.

[11] W. Wang, X. Lei, H. Gao, and Y. Mao, "Near-infrared quantum cutting platform in transparent oxyfluoride glass–ceramics for solar sells," *Optical Materials,* vol. 47, pp. 270-275, 2015.

[12] Q. Y. Zhang and X. Y. Huang, "Recent progress in quantum cutting phosphors," *Progress in Materials Science,* vol. 55, no. 5, pp. 353-427, 2010.

[13] M.-F. Joubert, "Photon avalanche upconversion in rare earth laser materials," *Optical Materials,* vol. 11, no. 2, pp. 181-203, 1999.

[14] D. L. Dexter, "A Theory of Sensitized Luminescence in Solids," *The Journal of Chemical Physics,* vol. 21, no. 5, pp. 836-850, 1953.

[15] F. Auzel, "Upconversion and anti-stokes processes with f and d ions in solids," *Chemical Reviews,* vol. 104, no. 1, pp. 139-174, 2004.

[16] T. Wegh René, H. Donker, D. Oskam Koenraad, and A. Meijerink, "Visible quantum cutting in $LiGdF_4$:Eu^{3+} Through Downconversion," *Science,* vol. 283, no. 5402, pp. 663-666, 1999.

[17] F. Auzel, "History of upconversion discovery and its evolution," *Journal of Luminescence,* vol. 223, p. 116900, 2020.

[18] Y. Arai, T. Yamashidta, T. Suzuki, and Y. Ohishi, "Upconversion properties of Tb^{3+}–Yb^{3+} codoped fluorophosphate glasses," *Journal of Applied Physics,* vol. 105, no. 8, p. 083105, 2009.

[19] K. Prorok, A. Gnach, A. Bednarkiewicz, and W. Stręk, "Energy up-conversion in Tb^{3+}/Yb^{3+} co-doped colloidal α-$NaYF_4$ nanocrystals," *Journal of Luminescence,* vol. 140, pp. 103-109, 2013.

[20] M. Pamei and A. Puzari, "Luminescent transition metal–organic frameworks: An emerging sensor for detecting biologically essential metal ions," *Nano-Structures & Nano-Objects,* vol. 19, p. 100364, 2019.

[21] G. Liu, *Spectroscopic Properties of Rare Earths in Optical Materials*. Heidelberg: Tsinghua University Press.

[22] A. d. Bettencourt-Dias, *Luminescence of Lanthanide Ions in Coordination Compounds and Nanomaterials*. Reno: John Wiley and Sons, 2014.

[23] D. Franke, "Fluorescent materials for short-wave infrared imaging," Ph.D. dissertation, Department of Chemistry, Massachusetts Institute of Technology, Cambridge, 2018.

[24] E. Erol, O. Kıbrıslı, N. Vahedigharehchopogh, M. Çelikbilek Ersundu, and A. E. Ersundu, "The synergistic effect of Er^{3+} and Ho^{3+} on temporal color tuning of upconversion emission in a glass host via a facile excitation modulation technique for anti-counterfeiting applications," *Physical Chemistry Chemical Physics,* vol. 22, no. 44, pp. 25963-25972, 2020.

[25] L. H. C. Andrade *et al.*, "A step forward toward smart white lighting: Combination of glass phosphor and light emitting diodes," *Applied Physics Letters,* vol. 95, no. 8, p. 081104, 2009.

[26] S. Zulfiqar Ali Ahamed, C. Madhukar Reddy, and B. Deva Prasad Raju, "Structural, thermal and optical investigations of Dy^{3+} ions doped lead containing lithium fluoroborate glasses for simulation of white light," *Optical Materials,* vol. 35, no. 7, pp. 1385-1394, 2013.

[27] P. P. Pawar, S. R. Munishwar, and R. S. Gedam, "Intense white light luminescent Dy^{3+} doped lithium borate glasses for W-LED: A correlation between physical, thermal, structural and optical properties," *Solid State Sciences,* vol. 64, pp. 41-50, 2017.

[28] S. Kaur *et al.*, "Blue-yellow emission adjustability with aluminium incorporation for cool to warm white light generation in dysprosium doped borate glasses," *Journal of Luminescence,* vol. 202, pp. 168-175, 2018.

[29] P. P. Pawar, S. R. Munishwar, and R. S. Gedam, "Physical and optical properties of Dy^{3+}/Pr^{3+} Co-doped lithium borate glasses for W-LED," *Journal of Alloys and Compounds,* vol. 660, pp. 347-355, 2016.

[30] N. Deopa and A. S. Rao, "Photoluminescence and energy transfer studies of Dy^{3+} ions doped lithium lead alumino borate glasses for w-LED and laser applications," *Journal of Luminescence,* vol. 192, pp. 832-841, 2017.

[31] T. A. Lodi, M. Sandrini, A. N. Medina, M. J. Barboza, F. Pedrochi, and A. Steimacher, "Dy:Eu doped CaBAl glasses for white light applications," *Optical Materials,* vol. 76, pp. 231-236, 2018.

[32] L. Shamshad, G. Rooh, K. Kirdsiri, N. Srisittipokakun, H. J. Kim, and J. Kaewkhao, "Development of Li_2O-SrO-GdF_3-B_2O_3 oxyfluoride glass for white light LED application," *Journal of Molecular Structure,* vol. 1125, pp. 601-608, 2016.

[33] P. Suthanthirakumar and K. Marimuthu, "Investigations on spectroscopic properties of Dy^{3+} doped zinc telluro-fluoroborate glasses for laser and white LED applications," *Journal of Molecular Structure,* vol. 1125, pp. 443-452, 2016.

[34] P. P. Pawar, S. R. Munishwar, S. Gautam, and R. S. Gedam, "Physical, thermal, structural and optical properties of Dy^{3+} doped lithium alumino-borate glasses for bright W-LED," *Journal of Luminescence,* vol. 183, pp. 79-88, 2017.

[35] V. K. Rai, S. B. Rai, and D. K. Rai, "Optical studies of Dy^{3+} doped tellurite glass: Observation of yellow-green upconversion," *Optics Communications,* vol. 257, no. 1, pp. 112-119, 2006.

[36] L. Jyothi, G. Upender, R. Kuladeep, and D. N. Rao, "Structural, thermal, optical properties and simulation of white light of titanium-tungstate-tellurite glasses doped with dysprosium," *Materials Research Bulletin,* vol. 50, pp. 424-431, 2014.

[37] J. Hu *et al.*, "Tunable luminescence of Dy^{3+} single-doped and Dy^{3+}/Tm^{3+} co-doped tungsten borate glasses," *Optical Materials,* vol. 38, pp. 108-112, 2014.

[38] G. C. Ram *et al.*, "Investigation of luminescence and laser transition of Dy^{3+}ion in P_2O_5–PbO–Bi_2O_3–R_2O_3(R = Al, Ga, In) glasses," *Optical Materials,* vol. 66, pp. 189-196, 2017.

[39] F. Zaman, J. Kaewkhao, N. Srisittipokakun, N. Wantana, H. J. Kim, and G. Rooh, "Investigation of luminescence and laser transition of Dy^{3+} in Li_2O-Gd_2O_3-Bi_2O_3-B_2O_3 glasses," *Optical Materials,* vol. 55, pp. 136-144, 2016.

[40] S. Ruengsri, N. Srisittipokakun, F. Zaman, G. Rooh, and J. Kaewkhao, "Optical and luminescence properties of Dy^{3+} doped in soda lime borate glasses," in *Key Engineering Materials* vol. 702, ed, 2016, pp. 51-56.

[41] G. Venkataiah and C. K. Jayasankar, "Dy^{3+}-doped tellurite based tungsten-zirconium glasses: Spectroscopic study," *Journal of Molecular Structure,* vol. 1084, pp. 182-189, 2015.

[42] B. Li, D. Li, E. Y. B. Pun, and H. Lin, "Dy^{3+} doped tellurium-borate glass phosphors for laser-driven white illumination," *Journal of Luminescence,* vol. 206, pp. 70-78, 2019.

[43] M. Walas *et al.*, "Tailored white light emission in Eu^{3+} /Dy^{3+} doped tellurite glass phosphors containing Al^{3+} ions," *Optical Materials,* vol. 79, pp. 289-295, 2018.

[44] R. Vijayakumar, R. Nagaraj, P. Suthanthirakumar, P. Karthikeyan, and K. Marimuthu, "Silver (Ag) nanoparticles enhanced luminescence properties of Dy^{3+} ions in borotellurite glasses for white light applications," *Spectrochimica Acta Part A: Molecular and Biomolecular Spectroscopy,* vol. 204, pp. 537-547, 2018.

[45] T. Lewandowski *et al.*, "Structural and luminescent study of TeO_2-BaO-Bi_2O_3-Ag glass system doped with Eu^{3+} and Dy^{3+} for possible color-tunable phosphor application," *Optical Materials,* vol. 79, pp. 390-396, 2018.

[46] C. Hua, L. Shen, E. Y. B. Pun, D. Li, and H. Lin, "Dy^{3+} doped tellurite glasses containing silver nanoparticles for lighting devices," *Optical Materials,* vol. 78, pp. 72-81, 2018.

[47] H. Algarni, M. Reben, S. Almoeed, R. Maâlej, and E. S. Yousef, "Luminescence emission of Tm-Dy ions codoped tellurite glasses under visible light excitation," *Optik,* vol. 160, pp. 340-347, 2018.

[48] C. Wang *et al.*, "Mid-infrared photo-luminescence and energy transfer around 2.8μm from Dy^{3+}/Tm^{3+} co-doped tellurite glass," *Infrared Physics & Technology,* vol. 85, pp. 128-132, 2017.

[49] C. Wang *et al.*, "Investigation of broadband mid-infrared emission and quantitative analysis of Dy-Er energy transfer in tellurite glasses under different excitations," *Optics Express,* vol. 25, no. 23, pp. 29512-29525, 2017.

[50] S. Balaji, A. R. Allu, K. Biswas, G. Gupta, D. Ghosh, and K. Annapurna, "Bandwidth enhancement of MIR emission in Yb^{3+}/Er^{3+}/Dy^{3+} triply doped fluoro-tellurite glass," *Laser Physics Letters,* vol. 14, no. 3, p. 035804, 2017.

[51] V. P. Tuyen *et al.*, "Dy^{3+} ions as optical probes for studying structure of boro-tellurite glasses," *Journal of Luminescence,* vol. 178, pp. 27-33, 2016.

[52] Y. Ma, X. Li, F. Huang, and L. Hu, "2.9μm emission properties and energy transfer mechanism in Dy^{3+}/Tm^{3+}-codoped tellurite glass," *Materials Science and Engineering: B,* vol. 196, pp. 23-27, 2015.

[53] M. N. Ami Hazlin, M. K. Halimah, and F. D. Muhammad, "Absorption and emission analysis of zinc borotellurite glass doped with dysprosium oxide nanoparticles for generation of white light," *Journal of Luminescence,* vol. 196, pp. 498-503, 2018.

[54] M. Reza Dousti and S. Raheleh Hosseinian, "Enhanced upconversion emission of Dy^{3+}-doped tellurite glass by heat-treated silver nanoparticles," *Journal of Luminescence,* vol. 154, pp. 218-223, 2014.

[55] B. D. O. Richards, T. Teddy-Fernandez, G. Jose, D. Binks, and A. Jha, "Mid-IR (3–4 μm) fluorescence and ASE studies in Dy^{3+} doped tellurite and germanate glasses and a fs laser inscribed waveguide," *Laser Physics Letters,* vol. 10, no. 8, p. 085802, 2013.

[56] W. A. Pisarski, J. Pisarska, L. Żur, and T. Goryczka, "Structural and optical aspects for Eu^{3+} and Dy^{3+} ions in heavy metal glasses based on $PbO–Ga_2O_3–XO_2$ (X=Te, Ge, Si)," *Optical Materials,* vol. 35, no. 5, pp. 1051-1056, 2013.

[57] B. C. Jamalaiah, "Intense yellow luminescence from Dy^{3+}-doped TeO_2-WO_3-GeO_2glasses: Structural and optical characterization," *Journal of Physics Condensed Matter,* vol. 30, no. 33, 2018, Art. no. 335701.

[58] P. Karthikeyan, S. Arunkumar, K. Annapoorani, and K. Marimuthu, "Investigations on the spectroscopic properties of Dy^{3+} ions doped Zinc calcium tellurofluoroborate glasses," *Spectrochimica Acta - Part A: Molecular and Biomolecular Spectroscopy,* vol. 193, pp. 422-431, 2018.

[59] T. Honma, Y. Benino, T. Fujiwara, T. Komatsu, R. Sato, and V. Dimitrov, "Electronic polarizability, optical basicity, and interaction parameter of La_2O_3 and related glasses," *Journal of Applied Physics,* vol. 91, no. 5, pp. 2942-2950, 2002.

[60] X. Zhao, X. Wang, H. Lin, and Z. Wang, "Electronic polarizability and optical basicity of lanthanide oxides," *Physica B: Condensed Matter,* vol. 392, no. 1-2, pp. 132-136, 2007.

[61] K. V. Raju, S. Sailaja, M. B. Reddy, P. Giridhar, C. N. Raju, and B. S. Reddy, "Effect of Concentration on the Photoluminescence Properties of Sm^{3+} and Dy^{3+}: Cadmium Lithium Boro Tellurite Glasses," *Journal of Nanoscience and Nanotechnology,* vol. 12, no. 2, pp. 1662-1666, 2012.

[62] P. Giridhar, S. Sailaja, M. B. Reddy, K. V. Raju, C. N. Raju, and B. S. Reddy, "Spectroscopic studies of RE^{3+}(RE = Eu, Tb, Sm & Dy): Lithium lead boro tellurite glasses," *Ferroelectrics Letters Section,* vol. 38, no. 1-3, pp. 1-10, 2011.

[63] K. V. Krishnaiah, K. U. Kumar, and C. K. Jayasankar, "Spectroscopic properties of Dy^{3+}-doped oxyfluoride glasses for white light emitting diodes," *Materials Express,* vol. 3, no. 1, pp. 61-70, 2013.

[64] R. T. Alves *et al.*, "Dy^{3+}/Tb^{3+}-codoped tunable warm light-emitting fluorogermanate glass phosphor," *Optical Engineering,* vol. 55, no. 11, 2016, Art. no. 117103.

[65] A. E. Ersundu, G. Karaduman, M. Elikbilek, N. Solak, and S. Aydin, "Effect of rare-earth dopants on the thermal behavior of tungsten-tellurite glasses," *Journal of Alloys and Compounds,* vol. 508, no. 2, pp. 266-272, 2010.

[66] A. E. Ersundu, M. Çelikbilek, N. Solak, and S. Aydin, "Glass formation area and characterization studies in the CdO-WO_3-TeO_2 ternary system," *Journal of the European Ceramic Society,* vol. 31, no. 15, pp. 2775-2781, 2011.

[67] M. Çelikbilek Ersundu and A. E. Ersundu, "Structure and crystallization kinetics of lithium tellurite glasses," *Journal of Non-Crystalline Solids,* vol. 453, pp. 150-157, 2016.

[68] H. R. V *et al.*, "Spectroscopic studies of Dy^{3+} ion doped tellurite glasses for solid state lasers and white LEDs," *Spectrochimica Acta Part A: Molecular and Biomolecular Spectroscopy,* vol. 188, pp. 516-524, 2018.

[69] K. Damak, E. S. Yousef, C. Rüssel, and R. Maâlej, "White light generation from Dy^{3+} doped tellurite glass," *Journal of Quantitative Spectroscopy and Radiative Transfer,* vol. 134, pp. 55-63, 2014.

[70] M. Çelikbilek, A. E. Ersundu, and S. Aydin, "Preparation and characterization of TeO_2-WO_3-Li_2O glasses," *Journal of Non-Crystalline Solids,* vol. 378, pp. 247-253, 2013.

[71] M. Çelikbilek, A. E. Ersundu, E. O. Zayim, and S. Aydin, "Thermochromic behavior of tellurite glasses," *Journal of Alloys and Compounds,* vol. 637, pp. 162-170, 2015.

[72] I. Z. Hager, R. El-Mallawany, and A. Bulou, "Luminescence spectra and optical properties of TeO_2–WO_3–Li_2O glasses doped with Nd, Sm and Er rare earth ions," *Physica B: Condensed Matter,* vol. 406, no. 4, pp. 972-980, 2011.

[73] G. F. Ansari, S. K. Mahajan, and J. Parashar, "Intense upconversion luminescence of Yb^{3+}-Er^{3+} in Li_2O content tungsten-tellurite glasses," *Journal of Fluorescence,* vol. 21, no. 4, pp. 1337-1342, 2011.

[74] I. Z. Hager and R. El-Mallawany, "Preparation and structural studies in the (70 - X)TeO_2-20WO_3-10Li_2O-xLn_2O_3 glasses," *Journal of Materials Science,* vol. 45, no. 4, pp. 897-905, 2010.

[75] W. A. Capanema *et al.*, "The structure and optical dispersion of the refractive index of tellurite glass," *Optical Materials,* vol. 33, no. 11, pp. 1569-1572, 2011.

[76] M. K. Halimah, M. F. Faznny, M. N. Azlan, and H. A. A. Sidek, "Optical basicity and electronic polarizability of zinc borotellurite glass doped La^{3+}ions," *Results in Physics,* vol. 7, pp. 581-589, 2017.

[77] J. Schroeder, "Brillouin scattering and pockels coefficients in silicate glasses," *Journal of Non-Crystalline Solids,* vol. 40, no. 1-3, pp. 549-566, 1980.

[78] P. Chimalawong, J. Kaewkhao, C. Kedkaew, and P. Limsuwan, "Optical and electronic polarizability investigation of Nd^{3+}-doped soda-lime silicate glasses," *Journal of Physics and Chemistry of Solids,* vol. 71, no. 7, pp. 965-970, 2010.

[79] E. A. Davis and N. F. Mott, "Conduction in non-crystalline systems V. Conductivity, optical absorption and photoconductivity in amorphous semiconductors," *Philosophical Magazine,* vol. 22, no. 179, pp. 903-922, 1970.

[80] R. Vijayakumar, G. Venkataiah, and K. Marimuthu, "Structural and luminescence studies on Dy^{3+} doped boro-phosphate glasses for white LED's and laser applications," *Journal of Alloys and Compounds,* vol. 652, pp. 234-243, 2015.

[81] W. T. Carnall, P. R. Fields, and K. Rajnak, "Electronic energy levels in the trivalent lanthanide aquo ions. I. Pr^{3+}, Nd^{3+}, Pm^{3+}, Sm^{3+}, Dy^{3+}, Ho^{3+}, Er^{3+},

and Tm^{3+}," *The Journal of Chemical Physics,* vol. 49, no. 10, pp. 4403-4406, 1968.

[82] S. P. Sinha, "Chapter 2 - Complexes of the rare earths," in *Complexes of the Rare Earths*, S. P. Sinha, Ed.: Pergamon, 1966, pp. 17-23.

[83] C. S. McCamy, "Correlated color temperature as an explicit function of chromaticity coordinates," *Color Research & Application,* vol. 17, no. 2, pp. 142-144, 1992.

[84] L. Yuliantini *et al.*, "Yellow and blue emission from $BaO-(ZnO/ZnF_2)–B_2O_3–TeO_2$ glasses doped with $Dy^{3+}$for laser medium and scintillation material applications," *Optical Materials,* vol. 85, pp. 382-390, 2018.

[85] B. R. Judd, "Optical absorption intensities of rare-earth ions," *Physical Review,* vol. 127, no. 3, pp. 750-761, 1962.

[86] G. S. Opelt, "Intensities of crystal spectra of rare-earth ions," *Journal of Chemical Physics,* vol. 37, no. 3, pp. 511-520, 1962.

[87] C. K. Jayasankar and E. Rukmini, "Optical properties of Sm^{3+} ions in zinc and alkali zinc borosulphate glasses," *Optical Materials,* vol. 8, no. 3, pp. 193-205, 1997.

[88] B. M. Walsh, "Judd-Ofelt theory: principles and practices," in *Advances in Spectroscopy for Lasers and Sensing*, Dordrecht, 2006, pp. 403-433: Springer Netherlands.

[89] K. Jha and M. Jayasimhadri, "Structural and emission properties of Eu^{3+}-doped alkaline earth zinc-phosphate glasses for white LED applications," *Journal of the American Ceramic Society,* vol. 100, no. 4, pp. 1402-1411, 2017.

[90] I. Khan *et al.*, "Photoluminescence and white light generation of Dy_2O_3 doped $Li_2O-BaO-Gd_2O_3-SiO_2$ for white light LED," *Journal of Alloys and Compounds,* vol. 774, pp. 244-254, 2019.

[91] N. Vijaya, K. Upendra Kumar, and C. K. Jayasankar, "Dy^{3+}-doped zinc fluorophosphate glasses for white luminescence applications," *Spectrochimica Acta - Part A: Molecular and Biomolecular Spectroscopy,* vol. 113, pp. 145-153, 2013.

[92] C. B. Annapurna Devi, S. Mahamuda, M. Venkateswarlu, K. Swapna, A. Srinivasa Rao, and G. Vijaya Prakash, "Dy^{3+} ions doped single and mixed alkali fluoro tungsten tellurite glasses for LASER and white LED applications," *Optical Materials,* vol. 62, pp. 569-577, 2016.

[93] T. Sekiya, N. Mochida, and S. Ogawa, "Structural study of WO_3-TeO_2 glasses," *Journal of Non-Crystalline Solids,* vol. 176, no. 2-3, pp. 105-115, 1994.

[94] R. El-Mallawany and I. A. Ahmed, "Thermal properties of multicomponent tellurite glass," *Journal of Materials Science,* vol. 43, no. 15, pp. 5131-5138, 2008.

[95] S. Arunkumar, G. Venkataiah, and K. Marimuthu, "Spectroscopic and energy transfer behavior of Dy^{3+} ions in $B_2O_3TeO_2PbOPbF_2Bi_2O_3CdO$ glasses for laser and WLED applications," *Spectrochimica Acta Part A: Molecular and Biomolecular Spectroscopy,* vol. 136, pp. 1684-1697, 2015.

[96] K. A. Aly, R. El-Mallawany, Y. B. Saddeek, A. Dahshan, and A. M. Abd Elnaeim, "DTA and FTIR of $70TeO_2–(25 − x)MnO_2–xV_2O_5–5Fe_2O_3$ tellurite glass systems," *Journal of Thermal Analysis and Calorimetry,* vol. 131, no. 2, pp. 1857-1865, 2018.

[97] V. O. Sokolov, V. G. Plotnichenko, and E. M. Dianov, "Structure of WO_3-TeO_2 glasses," *Inorganic Materials,* vol. 43, no. 2, pp. 194-213, 2007.

[98] W. T. Carnall, G. L. Goodman, K. Rajnak, and R. S. Rana, "A systematic analysis of the spectra of the lanthanides doped into single crystal LaF_3," *Journal of Chemical Physics,* vol. 90, no. 7, pp. 3443-3457, 1989.

[99] C. K. Jørgensen and B. R. Judd, "Hypersensitive pseudoquadrupole transitions in lanthanides," *Molecular Physics,* vol. 8, no. 3, pp. 281-290, 1964.

[100] V. Uma, K. Maheshvaran, K. Marimuthu, and G. Muralidharan, "Structural and optical investigations on Dy^{3+}doped lithium tellurofluoroborate glasses for white light applications," *Journal of Luminescence,* vol. 176, pp. 15-24, 2016.

[101] C. K. Jørgensen and R. Reisfeld, "Judd-Ofelt parameters and chemical bonding," *Journal of The Less-Common Metals,* vol. 93, no. 1, pp. 107-112, 1983.

[102] R. R. Jacobs and M. J. Weber, "Dependence of the $^4F_{3/2}$ - $^4I_{11/2}$ Induced-Emission Cross Section for Nd^{3+} on Glass Composition," *IEEE Journal of Quantum Electronics,* vol. 12, no. 2, pp. 102-111, 1976.

[103] E. Kaewnuam, N. Wantana, H. J. Kim, and J. Kaewkhao, "Development of lithium yttrium borate glass doped with Dy^{3+} for laser medium, W-LEDs and scintillation materials applications," *Journal of Non-Crystalline Solids,* vol. 464, pp. 96-103, 2017.

[104] J. Kaewkhao, N. Wantana, S. Kaewjaeng, S. Kothan, and H. J. Kim, "Luminescence characteristics of Dy^{3+}doped Gd_2O_3-CaO-SiO_2-B_2O_3 scintillating glasses," *Journal of Rare Earths,* vol. 34, no. 6, pp. 583-589, 2016.

[105] B. Klimesz, G. Dominiak-Dzik, M. Zelechower, and W. Ryba-Romanowski, "Optical study of GeO_2-PbO-PbF_2 oxyfluoride glass single doped with lanthanide ions," *Optical Materials,* vol. 30, no. 10, pp. 1587-1594, 2008.

[106] R. J. Amjad, M. R. Sahar, S. K. Ghoshal, M. R. Dousti, and R. Arifin, "Synthesis and characterization of Dy^{3+} doped zinc-lead-phosphate glass," *Optical Materials,* vol. 35, no. 5, pp. 1103-1108, 2013.

[107] O. Ravi, C. M. Reddy, B. S. Reddy, and B. D. P. Raju, "Judd-Ofelt analysis and spectral properties of Dy^{3+} ions doped niobium containing tellurium

calcium zinc borate glasses," *Optics Communications,* vol. 312, pp. 263-268, 2014.

[108] N. Maruyama, T. Honma, and T. Komatsu, "Enhanced quantum yield of yellow photoluminescence of Dy^{3+} ions in nonlinear optical $Ba_2TiSi_2O_8$ nanocrystals formed in glass," *Journal of Solid State Chemistry,* vol. 182, no. 2, pp. 246-252, 2009.

[109] X. Wan, Y.-q. Lin, S.-l. Tie, and J.-y. Shen, "Luminescence and energy transfer in Dy^{3+}/Tb^{3+} co-doped $CaO–Al_2O_3–B_2O_3–RE_2O_3$ glass," *Journal of Non-Crystalline Solids,* vol. 357, no. 19, pp. 3424-3429, 2011.

[110] X. F. Wang, X. H. Yan, Y. Xuan, J. Zheng, and W. Y. He, "Green-white-yellow tunable luminescence from Dy^{3+}-Tb^{3+}-Eu^{3+} doped transparent glass ceramics containing $GdSr_2F_7$ nanocrystals," *Applied Physics A: Materials Science and Processing,* vol. 113, no. 1, pp. 41-46, 2013.

[111] D. Ramachari, L. R. Moorthy, and C. K. Jayasankar, "Energy transfer and photoluminescence properties of Dy^{3+}/Tb^{3+} co-doped oxyfluorosilicate glass-ceramics for solid-state white lighting," *Ceramics International,* vol. 40, no. 7 PART B, pp. 11115-11121, 2014.

[112] C. Zhu, J. Wang, M. Zhang, X. Ren, J. Shen, and Y. Yue, "Eu-, Tb-, and Dy-doped oxyfluoride silicate glasses for LED applications," *Journal of the American Ceramic Society,* vol. 97, no. 3, pp. 854-861, 2014.

[113] U. Caldiño, G. Muñoz H, I. Camarillo, A. Speghini, and M. Bettinelli, "Down-shifting by energy transfer in Tb^{3+}/Dy^{3+} co-doped zinc phosphate glasses," *Journal of Luminescence,* vol. 161, pp. 142-146, 2015.

[114] J. Juárez-Batalla, A. N. Meza-Rocha, G. Muñoz H, and U. Caldiño, "Green to white tunable light emitting phosphors: Dy^{3+}/Tb^{3+} in zinc phosphate glasses," *Optical Materials,* vol. 64, pp. 33-39, 2017.

[115] G. Lakshminarayana *et al.*, "Optical absorption, luminescence, and energy transfer processes studies for Dy^{3+}/Tb^{3+}-codoped borate glasses for solid-state lighting applications," *Optical Materials,* vol. 72, pp. 380-391, 2017.

[116] Z. He *et al.*, "Influence of compositional variation on optical and structural properties of Tb^{3+} and Dy^{3+} doped phosphosilicate glasses," *Journal of Non-Crystalline Solids,* vol. 500, pp. 260-265, 2018.

[117] L. Zur *et al.*, "Influence of acceptor concentration on crystallization behavior and luminescence properties of lead borate glasses co-doped with Dy^{3+} and Tb^{3+} ions," *Journal of Alloys and Compounds,* vol. 749, pp. 561-566, 2018.

[118] M. Khan, *Understanding LED Illumination*. Boca Barton: CRC Press, 2014.

[119] Y. Cheng, C. Shen, L. Shen, W. Xiang, and X. Liang, "Tb^{3+}, Eu^{3+} co-doped $CsPbBr_3$ QDs glass with highly stable and luminous adjustable for white LEDs," *ACS Applied Materials & Interfaces,* vol. 10, no. 25, pp. 21434-21444, 2018.

[120] O. Kıbrıslı, A. E. Ersundu, and M. Ç. Ersundu, "Dy^{3+} doped tellurite glasses for solid-state lighting: An investigation through physical, thermal,

structural and optical spectroscopy studies," *Journal of Non-Crystalline Solids,* vol. 513, pp. 125-136, 2019.

[121] R. Yuan *et al.*, "Eu^{3+}-doped $CsPbBr_{1.5}I_{1.5}$ quantum dots glasses: A strong competitor among red fluorescence solid materials," *Journal of the American Ceramic Society,* vol. 101, no. 11, pp. 4927-4932, 2018.

[122] H. V. Demir, S. Nizamoglu, T. Erdem, E. Mutlugun, N. Gaponik, and A. Eychmüller, "Quantum dot integrated LEDs using photonic and excitonic color conversion," *Nano Today,* vol. 6, no. 6, pp. 632-647, 2011.

[123] J. Liang *et al.*, "All-inorganic perovskite solar cells," *Journal of the American Chemical Society,* vol. 138, no. 49, pp. 15829-15832, 2016.

[124] S. Akin, Y. Altintas, E. Mutlugun, and S. Sonmezoglu, "Cesiumlead based inorganic perovskite quantum-dots as interfacial layer for highly stable perovskite solar cells with exceeding 21% efficiency," *Nano Energy,* vol. 60, pp. 557-566, 2019.

[125] X. Sheng *et al.*, "Cesium lead Halide perovskite quantum dots as a photoluminescence probe for metal ions," *Advanced Materials,* vol. 29, no. 37, p. 1700150, 2017.

[126] M. Green, "Semiconductor quantum dots as biological imaging agents," *Angewandte Chemie International Edition,* vol. 43, no. 32, pp. 4129-4131, 2004.

[127] J. Lin *et al.*, "Perovskite quantum dots glasses based backlit displays," *ACS Energy Letters,* vol. 6, no. 2, pp. 519-528, 2021.

[128] Y. Duan, P. Li, Y. Lu, S. Xu, and J. Zhang, "Origin of bimodal luminescence in Cs_4PbBr_6 quantum dots glass ceramic," *Ceramics International,* 2021.

[129] E. Erol, O. Kıbrıslı, M. Çelikbilek Ersundu, and A. E. Ersundu, "Size-controlled emission of long-time durable $CsPbBr_3$ perovskite quantum dots embedded tellurite glass nanocomposites," *Chemical Engineering Journal,* vol. 401, p. 126053, 2020.

[130] Y. Ye *et al.*, "Highly luminescent cesium lead halide perovskite nanocrystals stabilized in glasses for light-emitting applications," *Advanced Optical Materials,* vol. 7, no. 9, p. 1801663, 2019.

[131] F. Palazon, Q. A. Akkerman, M. Prato, and L. Manna, "X-ray lithography on perovskite nanocrystals films: from patterning with anion-exchange reactions to enhanced stability in air and water," *ACS Nano,* vol. 10, no. 1, pp. 1224-1230, 2016.

[132] C. Sun *et al.*, "Efficient and stable white LEDs with silica-coated inorganic perovskite quantum dots," *Advanced Materials,* vol. 28, no. 45, pp. 10088-10094, 2016.

[133] Y. Wang *et al.*, "Solution-Grown $CsPbBr_3/Cs_4PbBr_6$ Perovskite Nanocomposites: Toward Temperature-Insensitive Optical Gain," *Small,* vol. 13, no. 34, p. 1701587, 2017.

[134] F. Krieg *et al.*, "Colloidal $CsPbX_3$ (X = Cl, Br, I) Nanocrystals 2.0: Zwitterionic Capping Ligands for Improved Durability and Stability," *ACS Energy Letters,* vol. 3, no. 3, pp. 641-646, 2018.

[135] Y. Wei, Z. Cheng, and J. Lin, "An overview on enhancing the stability of lead halide perovskite quantum dots and their applications in phosphor-converted LEDs," *Chemical Society Reviews,* vol. 48, no. 1, pp. 310-350, 2019.

[136] X. Li *et al.*, "$CsPbX_3$ quantum dots for lighting and displays: room-temperature synthesis, photoluminescence superiorities, underlying origins and white light-emitting diodes," *Advanced Functional Materials,* vol. 26, no. 15, pp. 2435-2445, 2016.

[137] M. Xia *et al.*, "Surface Passivation of CdSe Quantum Dots in All Inorganic Amorphous Solid by Forming $Cd_{1-x}Zn_xSe$ Shell," *Scientific Reports,* vol. 7, no. 1, p. 42359, 2017.

[138] S. Wageh, A. S. Eid, S. El-Rabaie, and A. A. Higazy, "CdSe nanocrystals in novel phosphate glass matrix," *Physica E: Low-dimensional Systems and Nanostructures,* vol. 40, no. 10, pp. 3049-3054, 2008.

[139] X. Xiang *et al.*, "$CsPb(Br,I)_3$ embedded glass: Fabrication, tunable luminescence, improved stability and wide-color gamut LCD application," *Chemical Engineering Journal,* vol. 378, p. 122255, 2019.

[140] K. Han, S. Yoon, and W. J. Chung, "CdS and CdSe quantum dot-embedded silicate glasses for led color converter," *International Journal of Applied Glass Science,* vol. 6, no. 2, pp. 103-108, 2015.

[141] S. Liu, G. Shao, L. Ding, J. Liu, W. Xiang, and X. Liang, "Sn-doped $CsPbBr_3$ QDs glasses with excellent stability and optical properties for WLED," *Chemical Engineering Journal,* vol. 361, pp. 937-944, 2019.

[142] P. Li *et al.*, "Nanocrystalline structure control and tunable luminescence mechanism of Eu-doped $CsPbBr_3$ quantum dot glass for WLEDs," *Nanoscale,* vol. 12, no. 12, pp. 6630-6636, 2020.

[143] S. Yuan, D. Chen, X. Li, J. Zhong, and X. Xu, "In situ crystallization synthesis of $CsPbBr_3$ perovskite quantum dot-embedded glasses with improved stability for solid-state lighting and random upconverted lasing," *ACS Applied Materials & Interfaces,* vol. 10, no. 22, pp. 18918-18926, 2018.

[144] D. Chen *et al.*, "$CsPbX_3$ (X = Br, I) perovskite quantum dot embedded low-melting phosphosilicate glasses: controllable crystallization, thermal stability and tunable emissions," *Journal of Materials Chemistry C,* vol. 6, no. 25, pp. 6832-6839, 2018.

[145] D. Carta, D. M. Pickup, J. C. Knowles, I. Ahmed, M. E. Smith, and R. J. Newport, "A structural study of sol–gel and melt-quenched phosphate-based glasses," *Journal of Non-Crystalline Solids,* vol. 353, no. 18, pp. 1759-1765, 2007.

[146] X. Zhang *et al.*, "Highly Thermally Stable Single-Component White-Emitting Silicate Glass for Organic-Resin-Free White-Light-Emitting

Diodes," *ACS Applied Materials & Interfaces,* vol. 6, no. 4, pp. 2709-2717, 2014.

[147] Z. Xu *et al.*, "Effect of topological structure on photoluminescence of PbSe quantum dot-doped borosilicate glasses," *Journal of the American Ceramic Society,* vol. 101, no. 4, pp. 1508-1515, 2018.

[148] X. Di *et al.*, "Use of long-term stable $CsPbBr_3$ perovskite quantum dots in phospho-silicate glass for highly efficient white LEDs," *Chemical Communications,* vol. 53, no. 80, pp. 11068-11071, 2017.

[149] S. Liu, Y. Luo, M. He, X. Liang, and W. Xiang, "Novel $CsPbI_3$ QDs glass with chemical stability and optical properties," *Journal of the European Ceramic Society,* vol. 38, no. 4, pp. 1998-2004, 2018.

[150] K. Li *et al.*, "Efficient red photoluminescence from Al^{3+} and Cu^{+} co-doped CdS QDs embedded silicate glasses," *Chemical Engineering Journal,* vol. 410, p. 128324, 2021.

[151] M. Xia, C. Liu, J. Han, and X. Zhao, "Formation of $CdS/Cd_{1-x}Zn_xS$ sandwich-structured quantum dots with high quantum efficiency in silicate glasses," *Journal of Luminescence,* vol. 186, pp. 30-33, 2017.

[152] K. Han, W. B. Im, J. Heo, and W. J. Chung, "Compositional dependency of Cd-S-Se quantum dots within silicate glass on color conversion for a white LED," *Journal of the American Ceramic Society,* vol. 102, no. 4, pp. 1703-1709, 2019.

[153] Y. Liu, W. Chen, J. Zhong, and D. Chen, "Upconversion luminescence in Yb/Ln (Ln = Er, Tm) doped oxyhalide glasses containing $CsPbBr_3$ perovskite nanocrystals," *Journal of the European Ceramic Society,* vol. 39, no. 14, pp. 4275-4282, 2019.

[154] M. Xia, J. Luo, C. Chen, H. Liu, and J. Tang, "Semiconductor quantum dots-embedded inorganic glasses: Fabrication, luminescent properties, and potential applications," *Advanced Optical Materials,* vol. 7, no. 21, p. 1900851, 2019.

[155] L. E. Brus, "Electron–electron and electron-hole interactions in small semiconductor crystallites: The size dependence of the lowest excited electronic state," *The Journal of Chemical Physics,* vol. 80, no. 9, pp. 4403-4409, 1984.

[156] W. W. Yu, L. Qu, W. Guo, and X. Peng, "Experimental Determination of the Extinction Coefficient of CdTe, CdSe, and CdS Nanocrystals," *Chemistry of Materials,* vol. 15, no. 14, pp. 2854-2860, 2003.

[157] T. Erdem and H. V. Demir, "Color science of nanocrystal quantum dots for lighting and displays," *Nanophotonics,* vol. 2, no. 1, pp. 57-81, 2013.

[158] E. Kleebusch, C. Patzig, T. Höche, and C. Rüssel, "A modified B_2O_3 containing Li_2O-Al_2O_3-SiO_2 glass with ZrO_2 as nucleating agent - Crystallization and microstructure studied by XRD and (S)TEM-EDX," *Ceramics International,* vol. 44, no. 16, pp. 19818-19824, 2018.

[159] E. Kleebusch, C. Patzig, M. Krause, Y. Hu, T. Höche, and C. Rüssel, "The effect of TiO_2 on nucleation and crystallization of a Li_2O-Al_2O_3-SiO_2 glass investigated by XANES and STEM," *Scientific Reports,* vol. 8, no. 1, p. 2929, 2018.

[160] Y. K. Lee, Y. G. Choi, J. Heo, and W. J. Chung, "Compositional Dependence of CdSe Quantum Dot Formation on Silicate Host Glass Composition," *Journal of the American Ceramic Society,* vol. 96, no. 12, pp. 3868-3871, 2013.

[161] D. Chen *et al.*, "Promoting photoluminescence quantum yields of glass-stabilized $CsPbX_3$ (X = Cl, Br, I) perovskite quantum dots through fluorine doping," *Nanoscale,* vol. 11, no. 37, pp. 17216-17221, 2019.

[162] Q. Wu, C. Liao, J. Pan, X. Ye, W. You, and L. Xia, "HF-free molten salt route for synthesis of highly efficient and water-resistant $K_2SiF_6:Mn^{4+}$ for warm white LED," *Journal of the American Ceramic Society,* vol. 103, no. 12, pp. 6901-6912, 2020.

[163] F. Zheng *et al.*, "Reliability of fluoride phosphor $K_2XF_6:Mn_4+$ ($K_2SiF_6:Mn^{4+}$, $K_2(Si,Ge)F_6:Mn^{4+}$, $K_2TiF_6:Mn^{4+}$) for LED application," *Journal of Materials Science: Materials in Electronics,* vol. 29, no. 24, pp. 21061-21071, 2018.

[164] B. Ai, C. Liu, J. Wang, J. Xie, J. Han, and X. Zhao, "Precipitation and Optical Properties of $CsPbBr_3$ Quantum Dots in Phosphate Glasses," *Journal of the American Ceramic Society,* vol. 99, no. 9, pp. 2875-2877, 2016.

[165] Z. Zhang *et al.*, "Novel red-emitting $CsPb_{1-x}Ti_xI_3$ perovskite QDs@glasses with ambient stability for high efficiency white LEDs and plant growth LEDs," *Chemical Engineering Journal,* vol. 378, p. 122125, 2019.

[166] D. Chen, S. Yuan, J. Chen, J. Zhong, and X. Xu, "Robust $CsPbX_3$ (X = Cl, Br, and I) perovskite quantum dot embedded glasses: nanocrystallization, improved stability and visible full-spectral tunable emissions," *Journal of Materials Chemistry C,* vol. 6, no. 47, pp. 12864-12870, 2018.

[167] L. Ding, S. Liu, Z. Zhang, G. Shao, W. Xiang, and X. Liang, "Stable Zn-doped $CsPbBr_3$ NCs glasses toward an enhanced optical performance for WLED," *Ceramics International,* vol. 45, no. 17, Part B, pp. 22699-22706, 2019.

[168] K. Han, J. Heo, and W. J. Chung, "The effect of rare earth on color conversion properties of Cd–S–Se quantum dot embedded silicate glasses for white LED," *Optical Materials,* vol. 111, p. 110545, 2021.

[169] R. Deng, F. Qin, R. Chen, W. Huang, M. Hong, and X. Liu, "Temporal full-colour tuning through non-steady-state upconversion," *Nature Nanotechnology,* vol. 10, no. 3, pp. 237-242, 2015.

[170] O. Kıbrıslı, N. Vahedigharehchopogh, A. E. Ersundu, and M. Çelikbilek Ersundu, "Instantaneous color tuning of upconversion emission in a novel lanthanide-doped monolithic glass via excitation modulation," *The Journal of Physical Chemistry C,* vol. 124, no. 19, pp. 10687-10695, 2020.

[171] N. Vahedigharehchopogh, O. Kıbrıslı, E. Erol, M. Çelikbilek Ersundu, and A. E. Ersundu, "A straightforward approach for high-end anti-counterfeiting

applications based on NIR laser-driven lanthanide doped luminescent glasses," *Journal of Materials Chemistry C,* vol. 9, no. 6, pp. 2037-2046, 2021.

[172] Y. Han *et al.*, "Upconversion modulation through pulsed laser excitation for anti-counterfeiting," *Scientific Reports,* vol. 7, no. 1, p. 1320, 2017.

[173] J. Roncali, "Luminescent solar collectors: quo vadis?," vol. 10, no. 36, p. 2001907, 2020.

[174] P. Aryal *et al.*, "Rapid and convenient crystallization of quantum dot $CsPbBr_3$ inside a phosphate glass matrix," *Journal of Alloys and Compounds,* vol. 866, p. 158974, 2021.

[175] O. Kıbrıslı, E. Erol, M. Çelikbilek Ersundu, and A. E. Ersundu, "Robust $CsPbBr_3$ and CdSe / Dy^{3+}+CdSe quantum dot doped glass nanocomposite hybrid coupling as color converter for solid-state lighting applications," *Chemical Engineering Journal,* vol. 420, p. 130542, 2021.

[176] H. Lee, W. J. Park, and J. Heo, "Continuous-wave laser irradiation to form $Cd_{1-x}Zn_xSe$ shell on CdSe QDs in silicate glasses," *Journal of the American Ceramic Society,* vol. 102, no. 8, pp. 4555-4561, 2019.

[177] P. J. Pacheco-Liñán, I. Bravo, M. L. Nueda, J. Albaladejo, and A. Garzón-Ruiz, "Functionalized CdSe/ZnS quantum dots for intracellular pH measurements by fluorescence lifetime imaging microscopy," *ACS Sensors,* vol. 5, no. 7, pp. 2106-2117, 2020.

[178] B. Jia, M. Li, X. Yan, Q. Wang, and S. He, "Structure investigation of CaO-SiO_2-Al_2O_3-Li_2O by molecular dynamics simulation and Raman spectroscopy," *Journal of Non-Crystalline Solids,* vol. 526, p. 119695, 2019.

[179] P. Glatz, M. Comte, L. Cormier, L. Montagne, B. Doumert, and G. G. Moore, "Different roles of phosphorus in the nucleation of lithium aluminosilicate glasses," *Journal of Non-Crystalline Solids,* vol. 493, pp. 48-56, 2018.

[180] S. Ross, A.-M. Welsch, and H. Behrens, "Lithium conductivity in glasses of the Li_2O–Al_2O_3–SiO_2 system," *Physical Chemistry Chemical Physics,* vol. 17, no. 1, pp. 465-474, 2015.

[181] K. Xu and J. Heo, "New functional glasses containing semiconductor quantum dots," *Physica Scripta,* vol. T139, p. 014062, 2010.

[182] Y.-P. Sun *et al.*, "Quantum-sized carbon dots for bright and colorful photoluminescence," *Journal of the American Chemical Society,* vol. 128, no. 24, pp. 7756-7757, 2006.

[183] N. Bloembergen, "Solid state infrared quantum counters," *Physical Review Letters,* vol. 2, no. 3, pp. 84-85, 1959.

[184] W. Xu *et al.*, "Broadband plasmonic antenna enhanced upconversion and its application in flexible fingerprint identification," *Advanced Optical Materials,* vol. 6, no. 6, p. 1701119, 2018.

[185] J. Zhou, Q. Liu, W. Feng, Y. Sun, and F. Li, "Upconversion luminescent materials: Advances and applications," *Chemical Reviews,* vol. 115, no. 1, pp. 395-465, 2015.

[186] M. L. Debasu, D. Ananias, I. Pastoriza-Santos, L. M. Liz-Marzán, J. Rocha, and L. D. Carlos, "All-in-one optical heater-thermometer nanoplatform operative from 300 to 2000 K based on Er^{3+} emission and blackbody radiation," *Advanced Materials,* vol. 25, no. 35, pp. 4868-4874, 2013.

[187] B. M. van der Ende, L. Aarts, and A. Meijerink, "Lanthanide ions as spectral converters for solar cells," *Physical Chemistry Chemical Physics,* vol. 11, no. 47, pp. 11081-11095, 2009.

[188] E. Downing, L. Hesselink, J. Ralston, and R. Macfarlane, "A three-color, solid-state, three-dimensional display," *Science,* vol. 273, no. 5279, p. 1185, 1996.

[189] F. Wang *et al.*, "Tuning upconversion through energy migration in core–shell nanoparticles," *Nature Materials,* vol. 10, no. 12, pp. 968-973, 2011.

[190] Y. Lu *et al.*, "Tunable lifetime multiplexing using luminescent nanocrystals," *Nature Photonics,* vol. 8, no. 1, pp. 32-36, 2014.

[191] C. F. Gainer, G. S. Joshua, C. R. De Silva, and M. Romanowski, "Control of green and red upconversion in $NaYF_4$:Yb^{3+},Er^{3+} nanoparticles by excitation modulation," *Journal of Materials Chemistry,* vol. 21, no. 46, pp. 18530-18533, 2011.

[192] F. Fan, S. Turkdogan, Z. Liu, D. Shelhammer, and C. Z. Ning, "A monolithic white laser," *Nature Nanotechnology,* vol. 10, no. 9, pp. 796-803, 2015.

[193] A. Watras, P. J. Dereń, R. Pązik, and K. Maleszka-Bagińska, "Upconversion luminescence properties of nanocrystallite $MgAl_2O_4$ spinel doped with Ho^{3+} and Yb^{3+} ions," *Optical Materials,* vol. 34, no. 12, pp. 2041-2044, 2012.

[194] A. Rapaport, J. Milliez, M. Bass, A. Cassanho, and H. Jenssen, "Role of pump duration on temperature andefficiency of up-conversion in fluoride crystalsco-doped with ytterbium and thulium," *Optics Express,* vol. 12, no. 21, pp. 5215-5220, 2004.

[195] H. Naruke, T. Mori, and T. Yamase, "Luminescence properties and excitation process of a near-infrared to visible up-conversion color-tunable phosphor," *Optical Materials,* vol. 31, no. 10, pp. 1483-1487, 2009.

[196] D. V. Pominova *et al.*, "Pulsed periodic laser excitation of upconversion luminescence for deep biotissue visualization," *Laser Physics,* vol. 26, no. 8, p. 084001, 2016.

[197] A. Jha *et al.*, "Rare-earth ion doped TeO_2 and GeO_2 glasses as laser materials," *Progress in Materials Science,* vol. 57, no. 8, pp. 1426-1491, 2012.

[198] I. T. Lima and V. R. Marinov, "Volumetric display based on two-photon absorption in quantum dot dispersions," *Journal of Display Technology,* vol. 6, no. 6, pp. 221-228, 2010.

[199] K. Kumagai, I. Yamaguchi, and Y. Hayasaki, "Three-dimensionally structured voxels for volumetric display," *Optics Letters,* vol. 43, no. 14, pp. 3341-3344, 2018.

[200] K. Kumagai, D. Suzuki, S. Hasegawa, and Y. Hayasaki, "Volumetric display with holographic parallel optical access and multilayer fluorescent screen," *Optics Letters,* vol. 40, no. 14, pp. 3356-3359, 2015.

[201] J. Zhao *et al.*, "Selective preparation of Ag species on photoluminescence of Sm^{3+} in borosilicate glass via Ag^{+}-Na^{+} ion exchange," *Journal of the American Ceramic Society,* vol. 103, no. 2, pp. 955-964, 2020.

[202] Z. Zhou *et al.*, "Tb^{3+}/Yb^{3+} heavily-doped tellurite glasses with efficient green light emission," *Journal of Non-Crystalline Solids,* vol. 356, no. 50, pp. 2896-2899, 2010.

[203] J. S. Wang, E. M. Vogel, and E. Snitzer, "Tellurite glass: a new candidate for fiber devices," *Optical Materials,* vol. 3, no. 3, pp. 187-203, 1994.

[204] B. M. Walsh, N. P. Barnes, D. J. Reichle, and S. Jiang, "Optical properties of Tm^{3+} ions in alkali germanate glass," *Journal of Non-Crystalline Solids,* vol. 352, no. 50, pp. 5344-5352, 2006.

[205] M. Seshadri, L. C. Barbosa, and M. Radha, "Study on structural, optical and gain properties of 1.2 and 2.0μm emission transitions in Ho^{3+} doped tellurite glasses," *Journal of Non-Crystalline Solids,* vol. 406, pp. 62-72, 2014.

[206] L. X. Li, W. C. Wang, C. F. Zhang, J. L. Liu, Q. Y. Zhang, and Z. H. Jiang, "Exploration of the new tellurite glass system for efficient 2 μm luminescence," *Journal of Non-Crystalline Solids,* vol. 508, pp. 15-20, 2019.

[207] M. Seshadri, L. C. Barbosa, C. M. B. Cordeiro, M. Radha, F. A. Sigoli, and Y. C. Ratnakaram, "Study of optical absorption, visible emission and NIR–vis luminescence spectra of Tm^{3+}/Yb^{3+}, Ho^{3+}/Yb^{3+} and Tm^{3+}/Ho^{3+}/Yb^{3+} doped tellurite glasses," *Journal of Luminescence,* vol. 166, pp. 8-16, 2015.

[208] J. Sarkar, S. Mondal, S. Panja, I. Dey, A. Sarkar, and U. K. Ghorai, "Multicolour tuning and perfect white emission from novel $PbWO_4$:Yb^{3+}:Ho^{3+}:Tm^{3+} nanophosphor," *Materials Research Bulletin,* vol. 112, pp. 314-322, 2019.

[209] A.-H. Li and G. Chen, "Controlling lanthanide-doped upconversion nanoparticles for brighter luminescence," *Journal of Physics D: Applied Physics,* vol. 53, no. 4, p. 043001, 2019.

[210] N. Vahedigharehchopogh, O. Kıbrıslı, A. E. Ersundu, and M. Çelikbilek Ersundu, "Color tunability and white light generation through up-conversion energy transfer in Yb^{3+} sensitized Ho^{3+}/Tm^{3+} doped tellurite glasses," *Journal of Non-Crystalline Solids,* vol. 525, p. 119679, 2019.

[211] W. Cao *et al.*, "Analysis of mid-infrared photoluminescence around 2.85 μm in Yb^{3+}/Ho^{3+} co-doped synthetic silica-germanate glass," *Infrared Physics & Technology,* vol. 89, pp. 363-368, 2018.

[212] M. Azam and V. K. Rai, "Ho^{3+}-Yb^{3+} codoped tellurite based glasses in visible lasers and optical devices: Judd-Ofelt analysis and frequency upconversion," *Solid State Sciences,* vol. 66, pp. 7-15, 2017.

[213] L. Dai, Z. Yan, S. Jiao, C. Xu, and Y. Xu, "Effect of [Li]/[Nb] ratios on the absorption and up-conversion emission spectra in In:Yb:Ho:$LiNbO_3$ crystal," *Journal of Alloys and Compounds,* vol. 644, pp. 502-505, 2015.

[214] S. Bose and R. Debnath, "Strong crystal-field effect and efficient phonon assisted $Yb^{3+}\rightarrow Tm^{3+}$ energy transfer in a (Yb^{3+}/Tm^{3+}) co-doped high barium–tellurite glass," *Journal of Luminescence,* vol. 155, pp. 210-217, 2014.

[215] B. Zhou, L. Tao, C. Yat-Yin Chan, W. Jin, Y. H. Tsang, and E. Yue-Bun Pun, "Near- and mid-infrared photoluminescence in Ho^{3+} doped and Ho^{3+}–Yb^{3+} codoped low-phonon-energy germanotellurite glasses," *Journal of Luminescence,* vol. 137, pp. 132-137, 2013.

[216] G. Bai, Y. Guo, Y. Tian, L. Hu, and J. Zhang, "Light emission at 2 μm from Ho–Tm–Yb doped silicate glasses," *Optical Materials,* vol. 33, no. 8, pp. 1316-1319, 2011.

[217] Q. J. Huang, Q. P. Wang, J. Chang, X. Y. Zhang, Z. J. Liu, and G. Y. J. L. P. Yu, "Optical parameters and upconversion fluorescence in Tm^{3+}/Yb^{3+} codoped tellurite glass," vol. 20, no. 4, pp. 865-870, 2010.

[218] W. Xu *et al.*, "Infrared to visible upconversion fluorescence in Yb,Tm:YAG single crystal," *Optics Communications,* vol. 272, no. 1, pp. 182-185, 2007.

[219] A. Pilch *et al.*, "The concentration dependent up-conversion luminescence of Ho^{3+} and Yb^{3+} co-doped β-$NaYF_4$," *Journal of Luminescence,* vol. 182, pp. 114-122, 2017.

[220] K. Siva Rama Krishna Reddy, K. Swapna, M. Venkateswarlu, S. Mahamuda, and A. S. Rao, "Thermal, up-conversion and near-infrared luminescence studies of Erbium ions doped alkaline-earth boro tellurite glasses," *Solid State Sciences,* vol. 97, p. 106016, 2019.

[221] S. Sun *et al.*, "$Li_2Gd_4(MoO_4)_7$ crystal preparation and spectral properties applied to 2.0 μm lasers," *CrystEngComm,* vol. 20, no. 41, pp. 6472-6481, 2018.

[222] K. Yoshimoto, Y. Ezura, M. Ueda, A. Masuno, and H. Inoue, "2.7 μm mid-infrared emission in highly erbium-doped lanthanum gallate glasses prepared via an aerodynamic levitation technique," *Advanced Optical Materials,* vol. 6, no. 8, p. 1701283, 2018.

[223] Y. Liu *et al.*, "Crystal growth and spectroscopic analysis of Tm, Ho singly-doped and Tm/Ho co-doped $CaLaGa_3O_7$ NIR laser crystals," *Optical Materials,* vol. 75, pp. 744-750, 2018.

[224] M. Bettinelli, "Bright colours ahead," *Nature Nanotechnology,* vol. 10, no. 3, pp. 203-204, 2015.

[225] B. Zhou, B. Shi, D. Jin, and X. Liu, "Controlling upconversion nanocrystals for emerging applications," *Nature Nanotechnology,* vol. 10, no. 11, pp. 924-936, 2015.

[226] H. Hao, H. Lu, G. Ao, Y. Song, Y. Wang, and X. Zhang, "Tunable emission color of $Gd_2(MoO_4)_3$:Yb^{3+}, Ho^{3+}, Tm^{3+} phosphors via different excitation condition," *Dyes and Pigments,* vol. 148, pp. 298-305, 2018.

[227] G. Gao, D. Busko, R. Joseph, I. A. Howard, A. Turshatov, and B. S. Richards, "Highly Efficient La_2O_3:Yb^{3+},Tm^{3+} Single-Band NIR-to-NIR Upconverting Microcrystals for Anti-Counterfeiting Applications," *ACS Applied Materials & Interfaces,* vol. 10, no. 46, pp. 39851-39859, 2018.

[228] X. Tan *et al.*, "Highly efficient up-conversion green emission in Ho/Yb co-doped yttria-stabilized zirconia single crystals," *Journal of Luminescence,* vol. 209, pp. 95-101, 2019.

[229] J.-Y. Su, X.-Y. Zhang, X. Li, and M.-L. Qu, "Synthesis and luminescence properties of Yb^{3+}, Tm^{3+} and Ho^{3+} co-doped $SrGd_2(WO_4)_2(MoO_4)_2$ nano-crystal," *Advanced Powder Technology,* 2019.

[230] S. Wilhelm, "Perspectives for upconverting nanoparticles," *ACS Nano,* vol. 11, no. 11, pp. 10644-10653, 2017.

[231] G. A. Kumar, M. Pokhrel, and D. K. Sardar, "Absolute quantum yield measurements in Yb/Ho doped M_2O_2S (M=Y, Gd, La) upconversion phosphor," *Materials Letters,* vol. 98, pp. 63-66, 2013.

[232] Y. Wu *et al.*, "Upconversion superburst with sub-2 μs lifetime," *Nature Nanotechnology,* vol. 14, no. 12, pp. 1110-1115, 2019.

[233] S. Balabhadra *et al.*, "Boosting the sensitivity of Nd^{3+}-based luminescent nanothermometers," *Nanoscale,* vol. 7, no. 41, pp. 17261-17267, 2015.

[234] P. Li, M. Jia, G. Liu, A. Zhang, Z. Sun, and Z. Fu, "Investigation on the fluorescence intensity ratio sensing thermometry based on nonthermally coupled levels," *ACS Applied Bio Materials,* vol. 2, no. 4, pp. 1732-1739, 2019.

[235] P. Löw, B. Kim, N. Takama, and C. Bergaud, "High-Spatial-Resolution Surface-Temperature Mapping Using Fluorescent Thermometry," vol. 4, no. 7, pp. 908-914, 2008.

[236] X. Zhu *et al.*, "Temperature-feedback upconversion nanocomposite for accurate photothermal therapy at facile temperature," *Nature Communications,* vol. 7, no. 1, p. 10437, 2016.

[237] K. Okabe, N. Inada, C. Gota, Y. Harada, T. Funatsu, and S. Uchiyama, "Intracellular temperature mapping with a fluorescent polymeric thermometer and fluorescence lifetime imaging microscopy," *Nature Communications,* vol. 3, no. 1, p. 705, 2012.

[238] H. Hao, H. Lu, G. Ao, Y. Song, Y. Wang, and X. Zhang, "Improving sensing sensitivity of Er/Yb co-doped $NaYF_4$ nanorods via selecting non-thermally-coupled levels," *Journal of Materials Science: Materials in Electronics,* vol. 28, no. 24, pp. 18551-18557, 2017.

[239] Z. Boruc, M. Kaczkan, B. Fetlinski, S. Turczynski, and M. Malinowski, "Blue emissions in Dy^{3+} doped $Y_4Al_2O_9$ crystals for temperature sensing," *Optics Letters,* vol. 37, no. 24, pp. 5214-5216, 2012.

[240] J. Lin *et al.*, "Outstanding optical temperature sensitivity and dual-mode temperature-dependent photoluminescence in Ho^{3+}-doped (K,Na)NbO_3–$SrTiO_3$ transparent ceramics," vol. 102, no. 8, pp. 4710-4720, 2019.

[241] V. K. Rai, A. Pandey, and R. Dey, "Photoluminescence study of Y_2O_3:Er^{3+}-Eu^{3+}-Yb^{3+} phosphor for lighting and sensing applications," vol. 113, no. 8, p. 083104, 2013.

[242] N. Rakov and G. S. Maciel, "Nd^{3+}-Yb^{3+} doped powder for near-infrared optical temperature sensing," *Optics Letters,* vol. 39, no. 13, pp. 3767-3769, 2014.

[243] K. M. Girish, S. C. Prashantha, R. Naik, and H. Nagabhushana, "Zn_2TiO_4: A novel host lattice for Sm^{3+} doped reddish orange light emitting photoluminescent material for thermal and fingerprint sensor," *Optical Materials,* vol. 73, pp. 197-205, 2017.

[244] S. Zhou, G. Jiang, X. Wei, C. Duan, Y. Chen, and M. Yin, "Pr^{3+}-doped -$NaYF_4$ for temperature sensing with fluorescence intensity ratio technique," *Journal of Nanoscience and Nanotechnology,* vol. 14, no. 5, pp. 3739-3742, 2014.

[245] J. J. Leal *et al.*, "Effect of TiO_2 on the thermal and optical properties of Er^{3+}/Yb^{3+} co-doped tellurite glasses for optical sensor," *Journal of Luminescence,* vol. 208, pp. 342-349, 2019.

[246] L.-Q. Yao, G.-H. Chen, T. Yang, S.-C. Cui, Z.-C. Li, and Y. Yang, "Energy transfer, tunable emission and optical thermometry in Tb^{3+}/Eu^{3+} co-doped transparent $NaCaPO_4$ glass ceramics," *Ceramics International,* vol. 42, no. 11, pp. 13086-13090, 2016.

[247] Y. Chen, X. Liu, J. Xu, T. Yang, Z. Li, and G. Chen, "Yb^{3+}/Tb^{3+}/Ho^{3+}: phosphate nanophase embedded glass ceramics: enhanced upconversion emission and temperature sensing behavior," *Journal of Materials Science: Materials in Electronics,* vol. 30, no. 1, pp. 778-785, 2019.

[248] Y. Chen *et al.*, "Upconversion luminescence, optical thermometric properties and energy transfer in Yb^{3+}/Tm^{3+} co-doped phosphate glass," *Optical Materials,* vol. 81, pp. 78-83, 2018.

[249] Y. Chen, G. H. Chen, X. Y. Liu, and T. Yang, "Enhanced up-conversion luminescence and optical thermometry characteristics of Er^{3+}/Yb^{3+} co-doped transparent phosphate glass-ceramics," *Journal of Luminescence,* vol. 195, pp. 314-320, 2018.

[250] Y. Chen *et al.*, "Down-conversion luminescence and optical thermometric performance of Tb^{3+}/Eu^{3+} doped phosphate glass," *Journal of Non-Crystalline Solids,* vol. 484, pp. 111-117, 2018.

[251] X. Zhang *et al.*, "Tunable luminescent properties and concentration-dependent, site-preferable distribution of Eu^{2+} ions in silicate glass for

white leds applications," *ACS Applied Materials & Interfaces,* vol. 7, no. 18, pp. 10044-10054, 2015.

[252] J. L. Liu, Y. B. Xiao, S. J. Huang, L. Y. Mao, W. C. Wang, and Q. Y. Zhang, "The glass-forming region and 2.7 μm emission of Er^{3+}-doped $TeO_2-Ta_2O_5-ZnO$ tellurite glass," *Journal of Non-Crystalline Solids,* vol. 522, p. 119564, 2019.

[253] M. Haouari, A. Maaoui, N. Saad, and A. Bulou, "Optical temperature sensing using green emissions of Er^{3+} doped fluoro-tellurite glass," *Sensors and Actuators A: Physical,* vol. 261, pp. 235-242, 2017.

[254] S. Hashim *et al.*, "Luminescence characteristics of $Li_2O–MgO–B_2O_3$ doped with Dy^{3+} as a solid TL detector," *Radiation Physics and Chemistry,* vol. 116, pp. 138-141, 2015.

[255] O. Kıbrıslı and A. E. Ersundu, "The effect of UV exposure and heat treatment on crystallization behavior of photosensitive glasses," *Applied Physics A,* vol. 124, no. 5, p. 375, 2018.

[256] Z. Liu, H. Deng, and D. Chen, "Temperature dependent upconversion properties of Yb^{3+}:Ho^{3+} co-doped Gd_2O_3 nanoparticles prepared by pulsed laser ablation in water," *Ceramics International,* vol. 45, no. 10, pp. 13235-13241, 2019.

[257] F. Huang, Y. Gao, J. Zhou, J. Xu, and Y. Wang, "Yb^{3+}/Er^{3+} co-doped $CaMoO_4$: a promising green upconversion phosphor for optical temperature sensing," *Journal of Alloys and Compounds,* vol. 639, pp. 325-329, 2015.

[258] L. Li, F. Qin, Y. Zhou, Y. Zheng, H. Zhao, and Z. Zhang, "Using the upconversion luminescence of the $CaWO_4$:$Yb^{3+}–X^{3+}$ (X = Er/Ho/Tm) phosphors for ratiometric thermal sensing," *Journal of Luminescence,* vol. 202, pp. 301-308, 2018.

[259] A. E. Ersundu, M. Çelikbilek, and S. Aydin, "Characterization of B_2O_3 and/or WO_3 containing tellurite glasses," *Journal of Non-Crystalline Solids,* vol. 358, no. 3, pp. 641-647, 2012.

[260] S. Dai, J. Wu, J. Zhang, G. Wang, and Z. Jiang, "The spectroscopic properties of Er^{3+}-doped $TeO_2–Nb_2O_5$ glasses with high mechanical strength performance," *Spectrochimica Acta Part A: Molecular and Biomolecular Spectroscopy,* vol. 62, no. 1, pp. 431-437, 2005.

[261] N. Elkhoshkhany, R. Essam, and E. S. Yousef, "Influence of La_2O_3 on the structural, optical and thermal properties of $TeO_2–ZnO–Li_2O–Nb_2O_5$ glass," *Journal of Non-Crystalline Solids,* vol. 536, p. 119994, 2020.

[262] V. Klinkov, V. Aseev, A. Semencha, and E. Tsimerman, "Temperature sensor based on upconversion luminescence of Er^{3+}-doped fluoroaluminate glasses," *Sensors and Actuators A: Physical,* vol. 277, pp. 157-162, 2018.

[263] G. Sui *et al.*, "Theoretical evaluation on laser cooling of ZBLAN:Er^{3+} glass with in situ optical temperature sensing," *Sensors and Actuators B: Chemical,* vol. 220, pp. 362-368, 2015.

[264] W. A. Pisarski, J. Janek, J. Pisarska, R. Lisiecki, and W. Ryba-Romanowski, "Influence of temperature on up-conversion luminescence in Er^{3+}/Yb^{3+} doubly doped lead-free fluorogermanate glasses for optical sensing," *Sensors and Actuators B: Chemical,* vol. 253, pp. 85-91, 2017.

[265] A. Pandey *et al.*, "Enhanced upconversion and temperature sensing study of Er^{3+}–Yb^{3+} codoped tungsten–tellurite glass," *Sensors and Actuators B: Chemical,* vol. 202, pp. 1305-1312, 2014.

[266] A. Kumar, S. P. Tiwari, K. Kumar, and J. C. G. E. da Silva, "Magnetic tuning in upconversion emission enhanced through Ag^{+} ions co-doped in GdF_3: Ho^{3+}/Yb^{3+} phosphor and a real-time temperature sensing demonstration," *Journal of Alloys and Compounds,* vol. 776, pp. 207-214, 2019.

[267] N. An, L. Ye, R. Bao, L. Yue, and L.-G. Wang, "Up-conversion luminescence characteristics and temperature sensing of Y_2O_3: Ho^{3+}/Yb^{3+} single crystal fiber," *Journal of Luminescence,* vol. 215, p. 116657, 2019.

[268] X. Wang *et al.*, "Can temperature be accurately sensed by red-green emission ratio in $YNbO_4$: Ho^{3+}/Yb^{3+} phosphor under 980 nm excitation?," *Journal of Alloys and Compounds,* vol. 754, pp. 222-226, 2018.

[269] A. K. Singh, "Ho^{3+}:TeO_2 glass, a probe for temperature measurements," *Sensors and Actuators A: Physical,* vol. 136, no. 1, pp. 173-177, 2007.

[270] J. Yang, P. Lin, E. Y. B. Pun, J. Yuan, X. Zhao, and H. Lin, "Quantification of upconversion photon and thermosensitive feedback in Er^{3+}/Yb^{3+} doped fluorotellurite glasses," *Journal of Luminescence,* vol. 222, p. 117184, 2020.

[271] S. F. León-Luis *et al.*, "$2CaO{\cdot}Al_2O_3$:Er^{3+} glass: An efficient optical temperature sensor," *Journal of Luminescence,* vol. 179, pp. 272-279, 2016.

[272] W. T. Carnall, H. Crosswhite, and H. M. Crosswhite, "Energy level structure and transition probabilities in the spectra of the trivalent lanthanides in LaF_3," 1978.

[273] N. Elkhoshkhany, S. Y. Marzouk, and S. Shahin, "Synthesis and optical properties of new fluoro-tellurite glass within (TeO_2-ZnO-LiF-Nb_2O_5-NaF) system," *Journal of Non-Crystalline Solids,* vol. 472, pp. 39-45, 2017.

[274] S. F. León-Luis, U. R. Rodríguez-Mendoza, P. Haro-González, I. R. Martín, and V. Lavín, "Role of the host matrix on the thermal sensitivity of Er^{3+} luminescence in optical temperature sensors," *Sensors and Actuators B: Chemical,* vol. 174, pp. 176-186, 2012.

[275] R. Rolli, M. Montagna, S. Chaussedent, A. Monteil, V. K. Tikhomirov, and M. Ferrari, "Erbium-doped tellurite glasses with high quantum efficiency and broadband stimulated emission cross section at 1.5 μm," *Optical Materials,* vol. 21, no. 4, pp. 743-748, 2003.

[276] M. Rajesh, M. R. Babu, N. J. Sushma, and B. D. P. Raju, "Influence of Er^{3+} ions on structural and fluorescence properties of SiO_2-B_2O_3- Na_2Co_3-NaF-

CaF_2 glasses for broadband 1.53 μm optical amplifier applications," *Journal of Non-Crystalline Solids,* vol. 528, p. 119732, 2020.

[277] G. L. Agawane, K. Linganna, J.-H. In, and J. H. Choi, "High emission cross-section Er^{3+}-doped fluorophosphate glasses for active device application," *Optik,* vol. 198, p. 163228, 2019.

[278] S. Ivanova and F. Pellé, "Strong 1.53 μm to NIR-VIS-UV upconversion in Er-doped fluoride glass for high-efficiency solar cells," *Journal of the Optical Society of America B,* vol. 26, no. 10, pp. 1930-1938, 2009.

[279] D. Manzani, J. F. d. S. Petruci, K. Nigoghossian, A. A. Cardoso, and S. J. L. Ribeiro, "A portable luminescent thermometer based on green up-conversion emission of Er^{3+}/Yb^{3+} co-doped tellurite glass," *Scientific Reports,* vol. 7, no. 1, p. 41596, 2017.

[280] M. Kochanowicz, D. Dorosz, J. Zmojda, J. Dorosz, and P. Miluski, "Influence of temperature on upconversion luminescence in tellurite glass co-doped with Yb^{3+}/Er^{3+} and Yb^{3+}/Tm^{3+}," *Journal of Luminescence,* vol. 151, pp. 155-160, 2014.

[281] A. Pandey and V. K. Rai, "Improved luminescence and temperature sensing performance of Ho^{3+}–Yb^{3+}–Zn^{2+}:Y_2O_3 phosphor," *Dalton Transactions,* vol. 42, no. 30, pp. 11005-11011, 2013.

[282] Z. Xiao *et al.*, "Hydrothermal synthesis and up-conversion luminescence of Ho^{3+}/Yb^{3+} Co-doped $PbTiO_3$," vol. 645, no. 18-19, pp. 1111-1117, 2019.

A

SUPPORTING INFORMATION

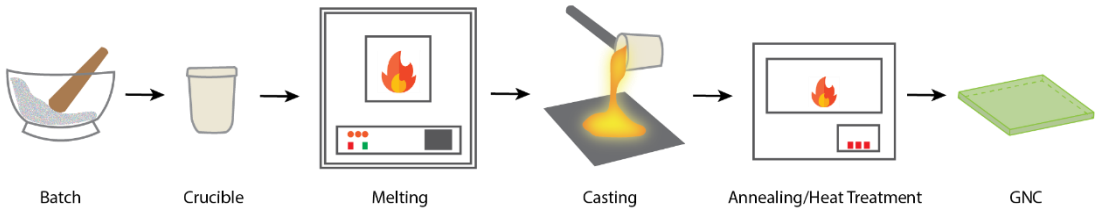


Figure A.1 Schematic representation of GNC synthesis

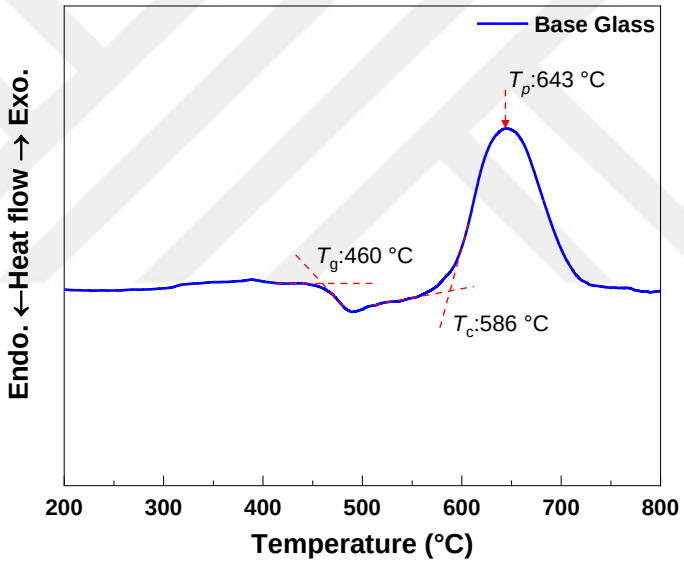


Figure A.2 Thermal analysis result of base glass indicating glass transition temperature (T_g), crystallization onset temperature (T_c) and crystallization peak (T_p) temperature

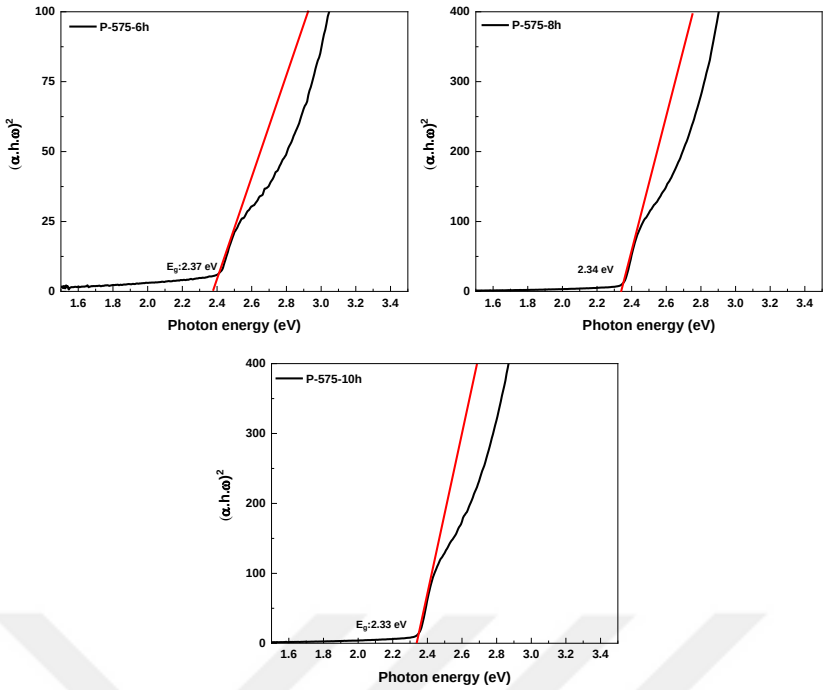
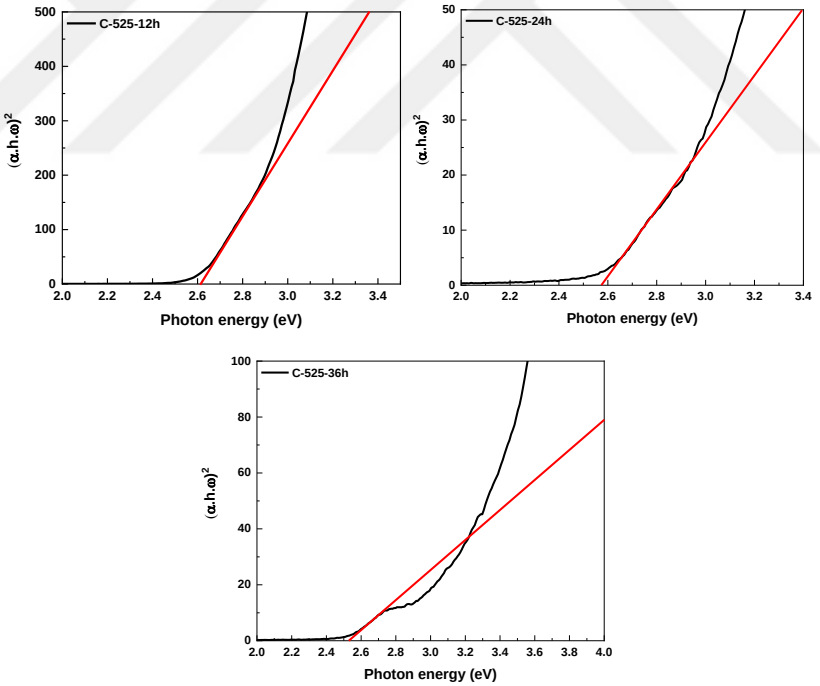


Figure A.3 Tauc plots of $CsPbBr_3$ doped glass nanocomposites (Tauc plot of P-575-4h could not be given due to the absence of first excitonic absorption peak)



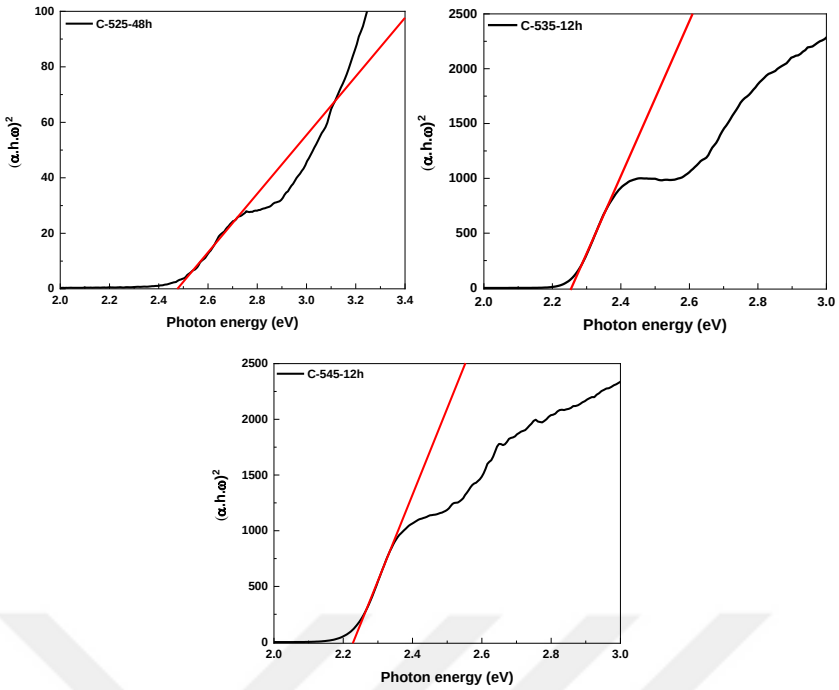


Figure A.4 Tauc plots of CdSe doped glass nanocomposites

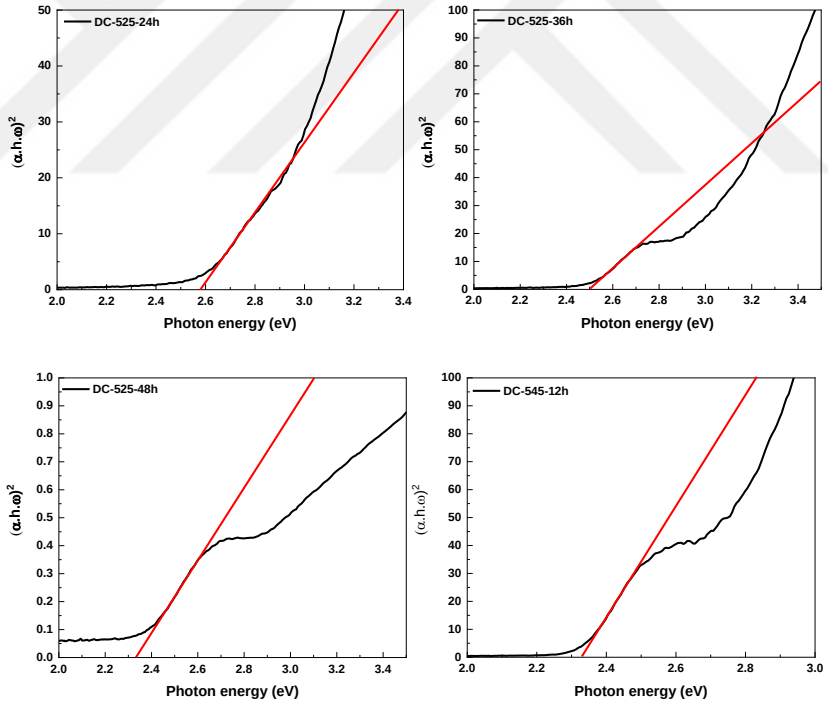


Figure A.5 Tauc plots of Dy^{3+}+CdSe doped glass nanocomposites (Tauc plots of DC-525-12h and DC-535-12h samples could not be given due to the absence of first excitonic absorption peaks)

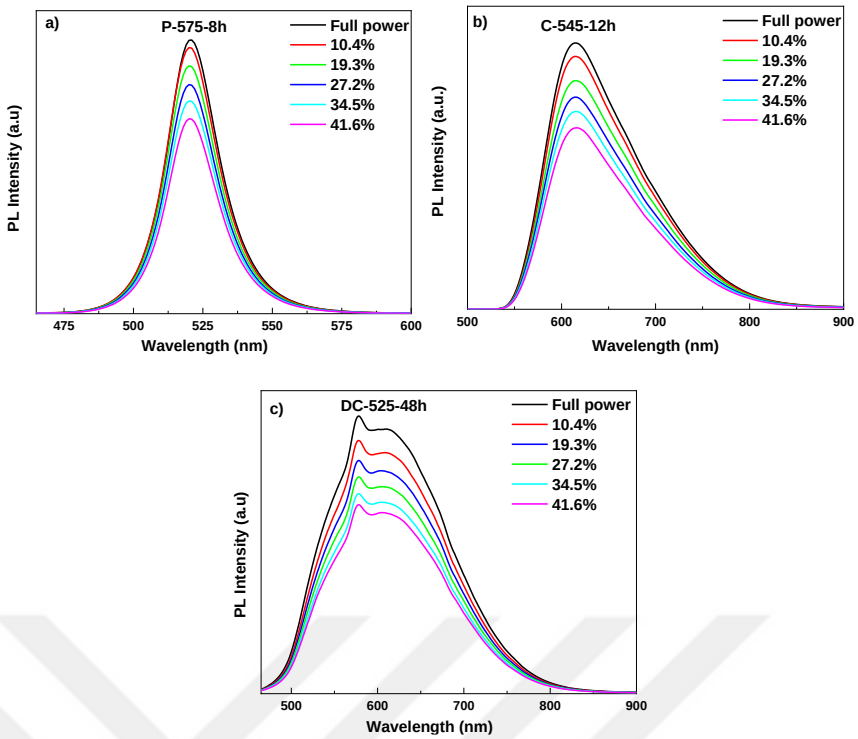


Figure A.6 Excitation power dependent PL spectra of a) P-575-8h b) C-545-12h c) DC-525-48h samples. Measurements are conducted in a closed spectrofluorometer setup with attenuator filters to adjust power density. Percentage values indicate how much the power density attenuated for that measurement. No significant change is observed in the line shape of PL spectra besides their intensity decreased according to attenuation applied

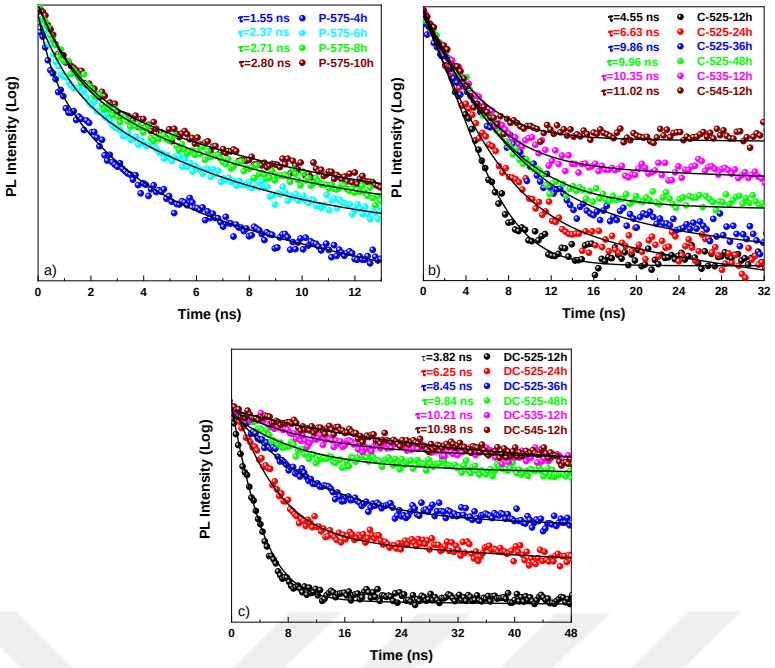
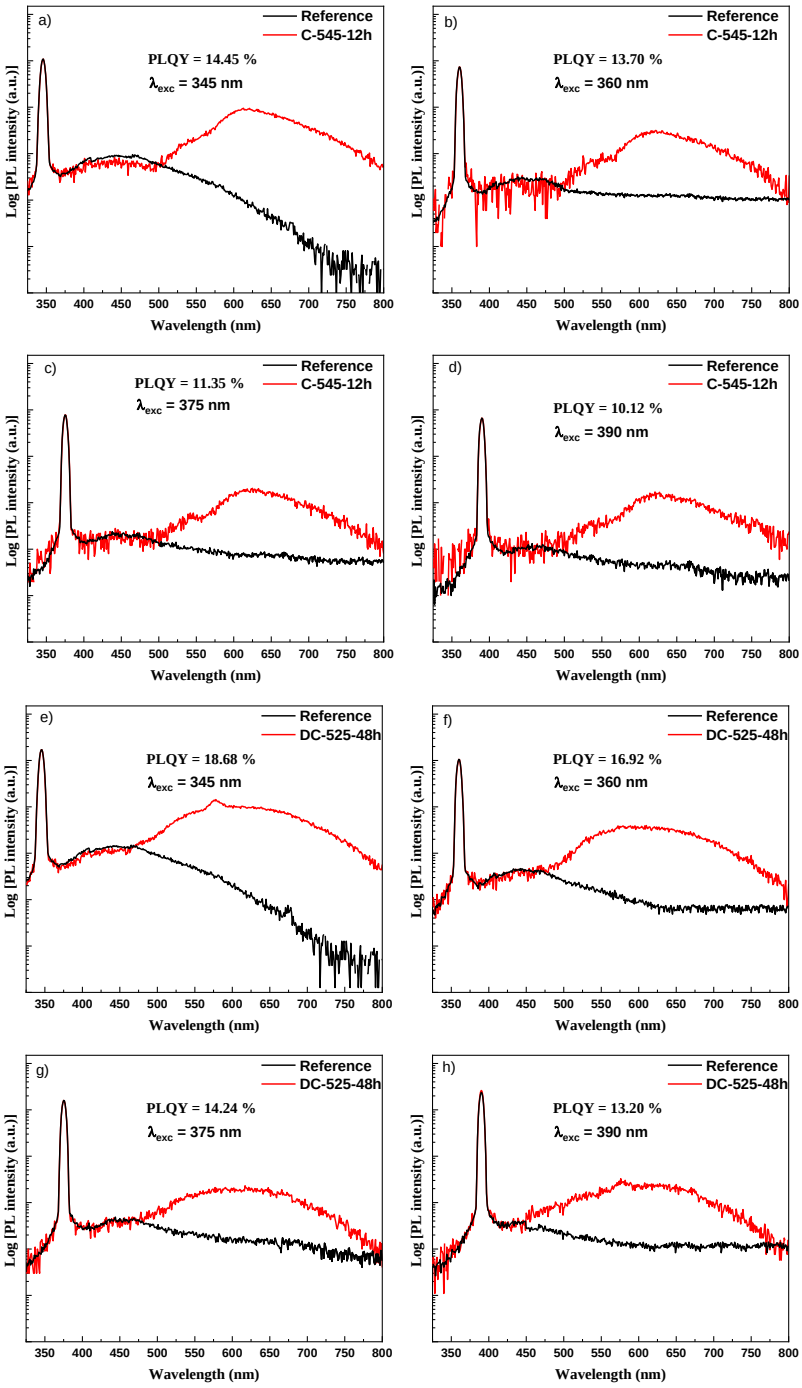


Figure A.7 Time-resolved PL traces of a) $CsPbBr_3$ b) CdSe and c) Dy^{3+}+CdSe doped GNCs


a)
Reference
C-545-12h
PLQY = 14.45 %
λexc = 345 nm
b)
PLQY = 13.70 %
λexc = 360 nm
c)
PLQY = 11.35 %
λexc = 375 nm
d)
PLQY = 10.12 %
λexc = 390 nm
e)
DC-525-48h
PLQY = 18.68 %
λexc = 345 nm
f)
PLQY = 16.92 %
λexc = 360 nm
g)
PLQY = 14.24 %
λexc = 375 nm
h)
PLQY = 13.20 %
λexc = 390 nm
Log [PL intensity (a.u.)]
Wavelength (nm)
350 400 450 500 550 600 650 700 750 800

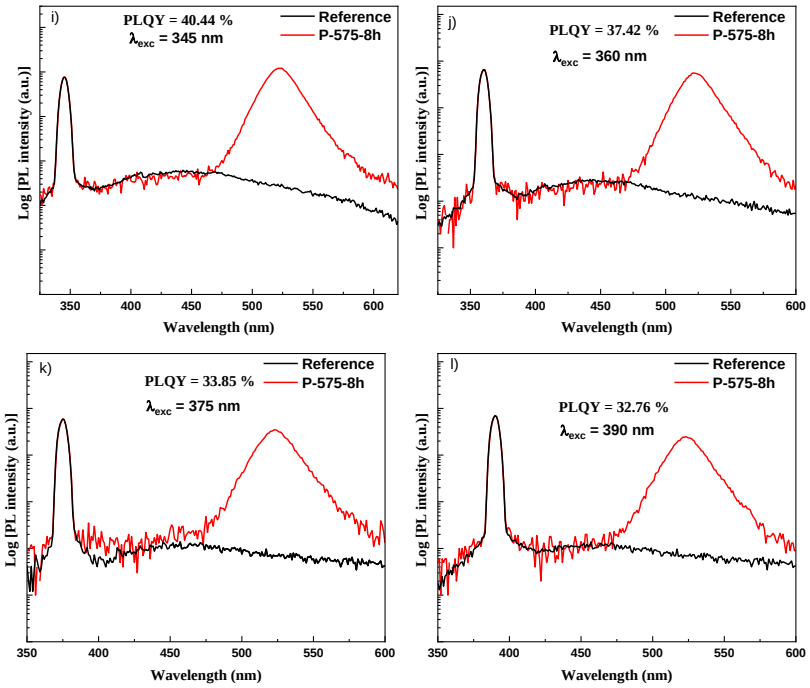


Figure A.8 PLQY mapping of selected C-545-12h, DC-525-48h and P-575-8h glass nanocomposites. Samples are excited at a), e), i) 345 nm, b), f), j) 360 nm, c), g), k) 375 nm and d), h), l) 390 nm wavelengths. Excitation wavelengths and PLQY values are indicated in each plot

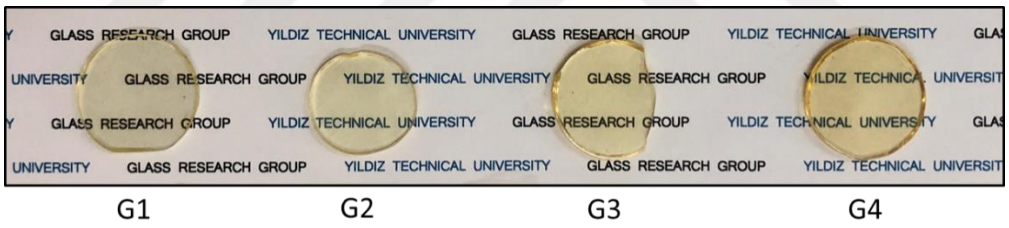


Figure A.9 Macro photos of glass samples prepared in different compositions

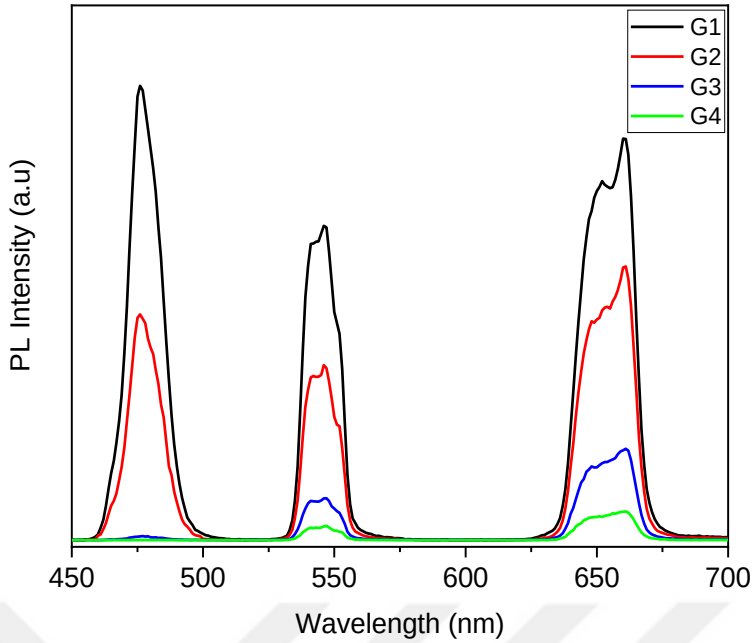


Figure A.10 PL spectra of glass samples under CW irradiation operating at 13 W cm^{-2} power density

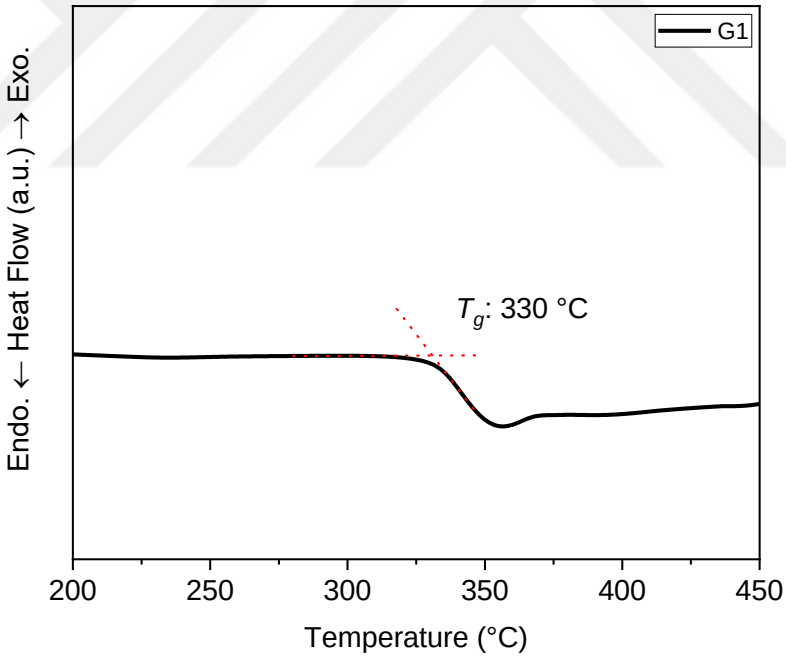


Figure A.11 Thermal analysis of G1 sample indicating its T_g (glass transition temperature)

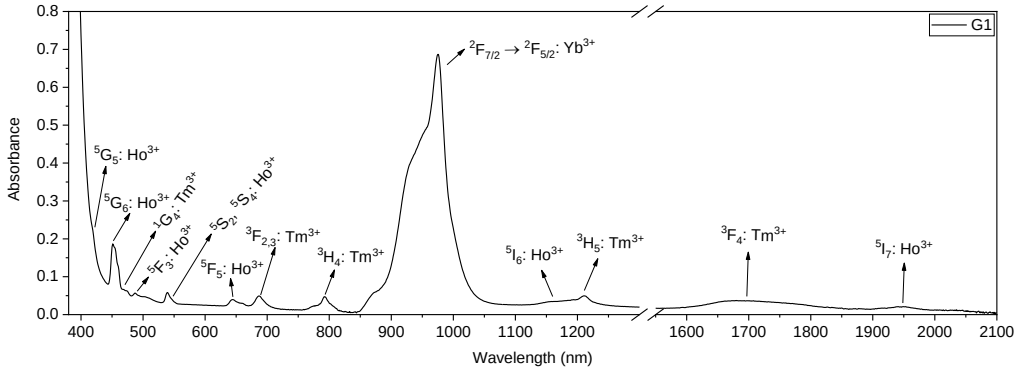


Figure A.12 UV-Vis-NIR absorbance spectrum of G1 sample indicating excited states of observed transitions

Table A.1 Compositions of $Ho^{3+}/Tm^{3+}/Yb^{3+}$ triply doped tellurite glass samples

Sample label	TeO_2	WO_3	Li_2O	Ho_2O_3	Tm_2O_3	Yb_2O_3
	[mol %]					
G1	47.75	25	25	0.05	0.2	2
G2	47.70	25	25	0.1	0.2	2
G3	47.25	25	25	0.25	0.5	2
G4	46.50	25	25	0.5	2	2

Table A.2 Line strengths of the transitions used in Judd-Ofelt analysis

Transition	λ [nm]	S_{exp} [10^{-20} cm^2]	S_{theo} [10^{-20} cm^2]
Tm^{3+}→ Ground state: $^3H_6$			
$^1G_4$	468	0.7202	0.7710
$^3F_2$+$^3F_3$	686	3.2228	3.2225
$^3H_4$	792	4.1477	4.1495
$^3F_4$	1698	8.4844	8.4791
δ_{rms}		0.0511	
Ho^{3+}→ Ground state: $^5I_8$			
$^5G_6$	450	15.2347	15.2353
$^5F_3$	485	0.1662	0.1273
$^5F_4$	538	0.9039	1.0012
$^5F_5$	644	1.4227	1.3777
$^5I_7$	1972	1.1749	1.1409
δ_{rms}		0.0841	

Table A.3 Calculated quantum yield values under different irradiation characteristics

Excitation Character	Power Density [W cm^{-2}]	Quantum Yield [%]		
		475 nm	545 nm	660 nm
CW	13	0.42	0.34	0.66
7.5 kHz	13	0.52	0.39	0.75
500 Hz	1.25	0.06	0.26	0.17
100 Hz	<0.30	0.03	0.23	0.05

PUBLICATIONS FROM THE THESIS

Conference Papers

1. Kıbrıslı O., Çelikbilek Ersundu M., Ersundu A. E., "Development of Rare Earth Ion Doped New Generation Glasses for White Light Emitting LEDs" 33rd Şişecam Glass Symposium, İstanbul, Turkey 2018

2. Kıbrıslı O., Çelikbilek Ersundu M., Ersundu A. E., "Effect of CdSe and ZnSe on Spectroscopic Properties of White Light Emitting Dy^{3+}-Doped Tellurite Glasses" 25th International Congress on Glass, Boston, USA 2019

Papers

1. O. Kıbrıslı, A. E. Ersundu, and M. Ç. Ersundu, "Dy^{3+} doped tellurite glasses for solid-state lighting: An investigation through physical, thermal, structural and optical spectroscopy studies," *Journal of Non-Crystalline Solids,* vol. 513, pp. 125-136, 2019.

2. O. Kıbrıslı, E. Erol, N. Vahedigharehchopogh, E. S. Yousef, M. Çelikbilek Ersundu, and A. E. Ersundu, "Noninvasive optical temperature sensing behavior of Ho^{3+} and Ho^{3+}/Er^{3+} doped tellurite glasses through up and down-converted emissions," *Sensors and Actuators A: Physical,* vol. 315, p. 112321, 2020.

3. O. Kıbrıslı, N. Vahedigharehchopogh, A. E. Ersundu, and M. Çelikbilek Ersundu, "Instantaneous Color Tuning of Upconversion Emission in a Novel Lanthanide-Doped Monolithic Glass via Excitation Modulation," *The Journal of Physical Chemistry C,* vol. 124, no. 19, pp. 10687-10695, 2020.

4. O. Kıbrıslı, E. Erol, A. E. Ersundu, and M. Çelikbilek Ersundu, "CdSe and $CsPbBr_3$ quantum dot Co-doped monolithic glasses as tunable wavelength convertors," *Journal of Physics D: Applied Physics,* vol. 55, no. 10, p. 105301, 2021.

5. O. Kıbrıslı, E. Erol, M. Çelikbilek Ersundu, and A. E. Ersundu, "Robust $CsPbBr_3$ and CdSe / Dy^{3+}+CdSe quantum dot doped glass nanocomposite hybrid coupling as color converter for solid-state lighting applications," *Chemical Engineering Journal,* vol. 420, p. 130542, 2021.

Projects

1. YTU Scientific Research Project (BAP) No: FDK-2021-4543 “Development of $CsPbBr_3$ Quantum Dot and Lanthanide Ions Co-doped Glass Nanocomposites for Solid-State Lighting Applications”, Researcher, (2021– 2023).

2. The Scientific and Technological Research Council of Turkey (TUBITAK) - Research Project No: 120N750 “Full-color tunable emission of lanthanide-doped

monolithic glasses upon single beam irradiation for laser-based volumetric displays", Research Scholar, (2021– 2023).

3. YTU Scientific Research Project (BAP) No: FDK-2020-3935 "Development of Quantum Dot and Rare Earth Element Co-Doped Tellurite Nanocomposite Glasses and Investigating Their Luminescence and Color Properties", Researcher, (2020-2022).

4. YTU Scientific Research Project (BAP) No: FBA-2018-3382 "Investigation of Luminescence Properties of Ho_2O_3, Er_2O_3, Tm_2O_3 Containing Multicomponent Glasses for LED Applications" , Researcher, (2018 – 2020).

5. The Scientific and Technological Research Council of Turkey (TUBITAK) - Research Project No: 117M206 "Investigation of Quantum Dot and Rare Earth Element Co-Doping Effect on Luminescence and Color Properties of Tellurite Nanocomposite Glasses for High Luminous Efficiency White LEDs", Research Scholar, (2017 – 2020).

Awards

1. Scientific and Technological Research Council of Turkey (TUBITAK), BIDEB 2214 Visiting Researcher Scholarship for PhD Students (2021 – 2022)

2. 25th International Congress on Glass, Boston, Registration Fee Grant for Students (2019)

3. Scientific and Technological Research Council of Turkey (TUBITAK), BIDEB 2211-C Ph.D. Scholarship for Underlying Research Fields (2019 – 2022)

4. The Council of Higher Education (YOK), 100/2000 Ph.D. Scholarship (2017 – 2021)